Millimeter Wave Hybrid Photonic Wireless Links for High-Speed Wireless Access and Mobile Fronthaul

Rommel, Simon; Delgado Mendinueta, J.M.

Publication date:
2017

Document Version
Publisher's PDF, also known as Version of record

Millimeter Wave Hybrid Photonic Wireless Links for High-Speed Wireless Access and Mobile Fronthaul

PhD Thesis

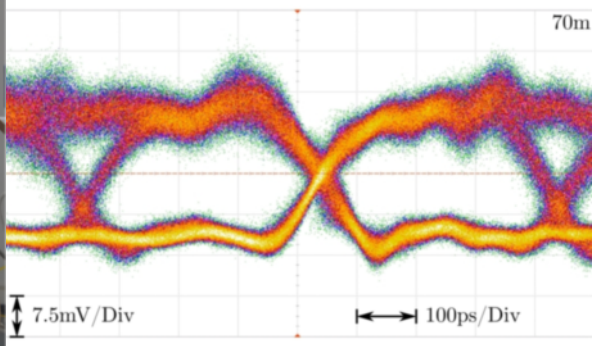

Simon Rommel
December 2017

DTU Fotonik
Department of Photonics Engineering

Millimeter Wave Hybrid Photonic Wireless Links for High-Speed Wireless Access and Mobile Fronthaul

Simon Rommel

Supervisors:
Professor Idelfonso Tafur Monroy,
Dr. Juan José Vegas Olmos and
Dr. José Manuel Delgado Mendinueta

Delivery Date: 20th October 2017

DTU Fotonik
Department of Photonics Engineering
Technical University of Denmark
Building 343, Ørsteds Plads
2800 Kgs. Lyngby
DENMARK

DTU Fotonik
Department of Photonics Engineering

Abstract

As the introduction of the fifth generation of mobile services (5G) is set to revolutionize the way people, devices and machines connect, the changes to the underlying networks and technologies are no less drastic. The massive increase in user and data capacity, as well as the decrease in latency require a complete re-thinking of radio access networks – one important aspect of which is the introduction of millimeter wave communications, which is expected to play a key role. Millimeter wave hybrid photonic wireless links seamlessly merge the wired optical and wireless radio network segments and combine the best of both technologies, offering very large capacity and bridging long distances with optical fiber, while retaining the flexibility and easy deployment of wireless communications.

The research in this thesis experimentally investigates millimeter wave (mmW) hybrid photonic wireless links, demonstrating their potential and pushing their implementation beyond the state of the art. While touching upon a multitude of aspects, the contributions can mostly be classified in three larger groups: first, the demonstration of mmW radio-over-fiber (RoF) links in various configurations of reduced complexity, real-time enabled and almost ready for deployment. Second, the use of advanced modulation formats to increase the capacity and spectral efficiency of mmW RoF links, to enhance their robustness against channel impairments and to allow flexible resource allocation. Therein, a significant increase of spectral efficiency is achieved for RoF links in W-band using multi-band carrierless amplitude phase modulation (multiCAP), the first experimental validation of wavelet coding for robustness against frequency fading is performed, and the combination of multiCAP with non-orthogonal multiple access for flexible user and resource allocation is suggested and experimentally demonstrated. Third, the integration of mmW RoF links with optical networks and the resulting impact on the design and architecture of the remote station, performing heterodyne up-conversion, is considered, demonstrating real-time transmis-

sion with a fully reconfigurable remote station. The thesis further contains work on optical vector network analysis as an efficient tool for the characterization of optical space division multiplexing fibers and components – as a prerequisite for their future use in mmW RoF links and radio access networks.

In summary, the work presented in this thesis has regarded a multitude of aspects of millimeter wave hybrid photonic wireless links, expanding upon the state of the art and showing their feasibility for use in fifth generation mobile and high speed wireless access networks – hopefully bringing them a small step closer to adoption in deployed networks.

Resumé

Introduktionen af den femte generation af mobiltjenester (5G) er sat til at revolutionere måden mennesker, enheder og maskiner forbindes, og ændringerne i de underliggende netværk og teknologier er ikke mindre drastiske. Den massive stigning i bruger- og datakapacitet samt fald i latens kræver en fuldstændig omstrukturering af radioadgangsnetværkerne. Et vigtigt aspekt af dette er indførelsen af millimeterbølgekommunikation, som forventes at spille en central rolle. Hybride millimeterbølge-fotoniske trådløse forbindelser fletter de ledede optiske og trådløse radionetværkssegmenter sammen og kombinerer det bedste af begge teknologier, hvilket tilbyder meget stor kapacitet og overlader lange transportafstande til optiske fibre, samtidig med at fleksibiliteten og den nemme udbredelse af trådløs kommunikation opretholdes.

Forskningen i denne afhandling er baseret på en eksperimentel undersøgelse af hybride millimeterbølge-fotoniske trådløse forbindelser, der demonstrerer deres potentiale og skubber deres implementering ud over det nyeste inden for teknikken. Afhandlingen omhandler en lang række aspekter, men bidragene kan for det meste klassificeres i tre hovedgrupper: Den første gruppe viser en demonstration af millimeterbølgeradio over fiberforbindelser i forskellige konfigurationer med reduceret kompleksitet, real-time implementering og som næsten er klar til implementering. Den anden gruppe bruger avanceret modulering for at øge kapaciteten og den spektrale effektivitet af millimeterbølgeradio via fiberforbindelser for at øge deres robusthed mod kanalforringelser og tillader fleksibel ressourcefordeling. Der opnås en signifikant forøgelse af den spektrale effektivitet for radio over fiberforbindelser i W-bånd ved anvendelse af multibånds bærerfri amplitude-fase modulering, og den første eksperimentelle validering af wavelet-kodning for robusthed mod frekvensfading udføres, og kombinationen af multibånds bærerfri amplitudefase modulering med ikke-ortogonal multiple adgang til fleksibel bruger og ressourceallokering foreslås og demonstreres eksperimentel. I den tredje

gruppe overvejes integrationen af millimeterbølgeradio over fiberforbindelser med optiske netværk og den resulterende indvirkning på fjernstationens, der udfører heterodyne opkonvertering, design og arkitektur, og demonstrerer realtidsoverførsel med en fuldt omkonfigurerbar fjernstation. Afhandlingen indeholder endvidere arbejde med optisk vektornetværksanalyse som et effektivt værktøj til karakterisering af optiske rumfordelings multipleksede fibre og -komponenter – som en forudsætning for deres fremtidige brug i millimeterbølgeradio over fiberforbindelser og radioadgangsnettet.

Som opsummering har arbejdet, der præsenteres i denne afhandling, betragtet og udvidet på en lang række aspekter af hybride millimeterbølge-fotoniske trådløse forbindelser, der udvider den nyeste teknologi og viser deres gennemførlighed til brug i den femte generation af mobilnetværk og højhastighedstjenester til trådløs adgang – hvilket forhåbentlig bringer dem et lille skridt tættere på adoption i implementerede netværk.

Acknowledgments

I would like to express my gratitude to everyone that contributed to this thesis and the work therein – whether they were directly involved as colleagues, supervisors or co-authors, gave insight and broad guidance as collaborators, provided assistance and support in various functions or were 'simply' part of making the whole experience and the time throughout enjoyable as friends and family.

Specifically, I thank my supervisors Prof. Idelfonso Tafur Monroy, Dr. Juan José Vegas Olmos and Dr. José Manuel Delgado Mendinueta. Idelfonso for his trust, belief and guidance throughout, JJ for opening doors and showing opportunities, Mendi for the great experience I had at NICT.

Thanks are also due to all my co-authors around the world, without whom little of this would have been possible – it was and is an honour and pleasure to work with you.

A major thank you belongs to my colleagues, especially those I spent so many hours in the lab with at DTU and NICT, many of whom have become friends and will be part of the onward path.

For the funding of my PhD studies, thanks go to the Independent Research Fund Denmark, for support with various travel grants to the Otto Mønsteds Fond.

Finally, the biggest thank you goes to my family and friends, who put up with me being all over the world, never anywhere for long and never 'at home'. Thank you for being there.

Thank you! Danke! Tak!

Gentofte, October 2017

Simon Rommel

Summary of original work

This thesis is based on the following original publications:

[PAPER1] **S. Rommel**, L. C. P. Cavalcante, A. G. Quintero, J. J. Vegas Olmos, and I. Tafur Monroy. "Channel characterization for high-speed W-band wireless communication links". In: *Opto-Electronics and Communications Conference 2015*. July 2015, paper PWe.17. DOI: 10.1109/OECC.2015.7340310.

[PAPER2] L. C. P. Cavalcante, **S. Rommel**, S. Rodriguez, J. J. Vegas Olmos, and I. Tafur Monroy. "On the capacity of radio-over-fiber links at the W-band". In: *Optical and Quantum Electronics* 48.5 (May 2016), paper 279. DOI: 10.1007/s11082-016-0554-6.

[PAPER3] **S. Rommel**, L. C. P. Cavalcante, A. K. Mishra, J. J. Vegas Olmos, and I. Tafur Monroy. "Requirements for Bend Insensitive Fiber in Millimeter-Wave Fronthaul Systems". In: *2015 International Topical Meeting on Microwave Photonics*. Oct. 2015, paper TuP-29. DOI: 10.1109/MWP.2015.7356674.

[PAPER4] **S. Rommel**, L. C. P. Cavalcante, J. J. Vegas Olmos, and I. Tafur Monroy. "Low RF Complexity Photonically Enabled Indoor and Building-to-Building W-Band Wireless Link". In: *Asia Communications and Photonics Conference 2015*. Nov. 2015, paper AM1B.7. DOI: 10.1364/ACPC.2015.AM1B.7.

[PAPER5] **S. Rommel**, L. C. P. Cavalcante, A. G. Quintero, A. K. Mishra, J. J. Vegas Olmos, and I. Tafur Monroy. "W-band photonic-wireless link with a Schottky diode envelope detector and bend insensitive fiber". In: *Optics Express* 24.11 (May 2016), pp. 11312–11322. DOI: 10.1364/OE.24.011312.

[PAPER6] **S. Rommel**, S. Rodriguez, L. Chorchos, E. P. Grakhova, A. K. Sultanov, J. P. Turkiewicz, J. J. Vegas Olmos, and I. Tafur Monroy. "225m Outdoor W-Band Radio-over-Fiber Link Using an Optical

SFP+ Module". In: *Optical Fiber Communication Conference 2016*. Mar. 2016, paper Th2A.16. DOI: 10.1364/OFC.2016.Th2A.16.

[PAPER7] **S. Rommel**, S. Rodriguez, L. Chorchos, E. P. Grakhova, A. K. Sultanov, J. P. Turkiewicz, J. J. Vegas Olmos, and I. Tafur Monroy. "Outdoor W-Band Hybrid Photonic Wireless Link Based on an Optical SFP+ Module". In: *IEEE Photonics Technology Letters* 28.21 (Nov. 2016), pp. 2303–2306. DOI: 10.1109/LPT.2016.2592326.

[PAPER8] **S. Rommel**, L. Yi, M. Shi, I. Tafur Monroy, and J. J. Vegas Olmos. "Demonstration of 4Gbit/s Duobinary Ka-Band Hybrid Photonic-Wireless Transmission". In: *Asia Communications and Photonics Conference 2015*. Nov. 2015, paper ASu1J.2. DOI: 10.1364/ACPC.2015.ASu1J.2.

[PAPER9] **S. Rommel**, J. J. Vegas Olmos, and I. Tafur Monroy. "15Gbit/s Duobinary Transmission Over a W-Band Radio-over-Fiber Link". In: *Advances in Wireless and Optical Communications 2016*. Nov. 2016, pp. 197–200. DOI: 10.1109/RTUWO.2016.7821883.

[PAPER10] **S. Rommel**, R. Puerta, J. J. Vegas Olmos, and I. Tafur Monroy. "Capacity Enhancement for Hybrid Fiber-Wireless Channels with 46.8Gbit/s Wireless Multi-CAP Transmission over 50m at W-Band". In: *Optical Fiber Communication Conference 2017*. Mar. 2017, paper M3E.5. DOI: 10.1364/OFC.2017.M3E.5.

[PAPER11] R. Puerta, **S. Rommel**, J. J. Vegas Olmos, and I. Tafur Monroy. "Optically Generated Single Side-Band Radio-over-Fiber Transmission of 60Gbit/s over 50m at W-Band". In: *Optical Fiber Communication Conference 2017*. Mar. 2017, paper M3E.4. DOI: 10.1364/OFC.2017.M3E.4.

[PAPER12] L. C. P. Cavalcante, **S. Rommel**, R. Dinis, L. G. Q. Silveira, L. F. Q. Silveira, and I. Tafur Monroy. "Performance Evaluation of Wavelet-Coded OFDM on a 4.9 Gbps W-Band Radio-over-Fiber Link". In: *Journal of Lightwave Technology* 35.14 (July 2017), pp. 2803–2809. DOI: 10.1109/JLT.2017.2701358.

[PAPER13] J. A. Altabas, **S. Rommel**, R. Puerta, D. Izquierdo, I. Garcés, J. A. Lazaro, J. J. Vegas Olmos, and I. Tafur Monroy. "Non-Orthogonal Multiple Access and Carrierless Amplitude Phase Modulation for 5G Mobile Networks". In: *43rd European Conference on Optical Communication*. Sept. 2017, paper Tu.1.B.2. *(inpress)*.

[PAPER14] J. A. Altabas, **S. Rommel**, R. Puerta, D. Izquierdo, I. Garcés, J. A. Lazaro, J. J. Vegas Olmos, and I. Tafur Monroy. "Non-Orthogonal Multiple Access and Carrierless Amplitude Phase Modulation for Flexible Multi-User Provisioning in 5G Mobile Networks". In: *Journal of Lightwave Technology* (2017). DOI: 10.1109/JLT.2017.2761541. *(inpress)*.

[PAPER15] L. Chorchos, **S. Rommel**, S. Spolitis, J. P. Turkiewicz, I. Tafur Monroy, and J. J. Vegas Olmos. "W-Band Real-Time Transmission Utilizing a Reconfigurable RAU for NG-PON Networks". In: *Advances in Wireless and Optical Communications 2016*. Nov. 2016, pp. 66–69. DOI: 10.1109/RTUWO.2016.7821857.

[PAPER16] L. Chorchos, **S. Rommel**, J. P. Turkiewicz, I. Tafur Monroy, and J. J. Vegas Olmos. "Reconfigurable Radio Access Unit for DWDM to W-Band Wireless Conversion". In: *IEEE Photonics Technology Letters* 29.6 (Mar. 2017), pp. 489–492. DOI: 10.1109/LPT.2017.2656894.

[PAPER17] S. Rodriguez, **S. Rommel**, J. J. Vegas Olmos, and I. Tafur Monroy. "Reconfigurable radio access unit to dynamically distribute W-band signals in 5G wireless access networks". In: *Optical Switching and Networking* 24 (Apr. 2017), pp. 21–24. DOI: 10.1016/j.osn.2016.10.002.

[PAPER18] S. Rodriguez, A. Morales, **S. Rommel**, J. J. Vegas Olmos, and I. Tafur Monroy. "Real-time Measurements of an Optical Reconfigurable Radio Access Unit for 5G Wireless Access". In: *Optical Fiber Communication Conference 2017*. Mar. 2017, paper W1C.3. DOI: 10.1364/OFC.2017.W1C.3.

[PAPER19] **S. Rommel**, J. M. Delgado Mendinueta, W. Klaus, J. Sakaguchi, J. J. Vegas Olmos, Y. Awaji, I. Tafur Monroy, and N. Wada. "Characterization of a Fiber-Coupled 36-Core 3-Mode Photonic Lantern Spatial Multiplexer". In: *OSA Advanced Photonics Congress (Photonic Networks and Devices)*. July 2017, paper NeW3B.2. DOI: 10.1364/NETWORKS.2017.NeW3B.2.

[PAPER20] **S. Rommel**, J. M. Delgado Mendinueta, W. Klaus, J. Sakaguchi, J. J. Vegas Olmos, Y. Awaji, I. Tafur Monroy, and N. Wada. "Analysis of Few-Mode Multi-Core Fiber Splice Behavior Using an Optical Vector Network Analyzer". In: *43rd European Conference on Optical Communication*. Sept. 2017, paper W.3.B.5. *(inpress)*.

[PAPER21] **S. Rommel**, J. M. Delgado Mendinueta, W. Klaus, J. Sakaguchi, J. J. Vegas Olmos, Y. Awaji, I. Tafur Monroy, and N. Wada. "Few-mode fiber, splice and SDM component characterization by spatially-diverse optical vector network analysis". In: *Optics Express* 25.19 (Sept. 2017), pp. 22347–22361. DOI: 10.1364/OE.25.022347.

Other scientific publications associated with the project:

[A1] R. Puerta, **S. Rommel**, J. J. Vegas Olmos, and I. Tafur Monroy. "Up to 35 Gbps Ultra-Wideband Wireless Data Transmission Links". In: *27th Annual IEEE International Symposium on Personal, Indoor and Mobile Radio Communication 2016*. Sept. 2016, paper WeD7.2. DOI: 10.1109/PIMRC.2016.7794775.

[A2] R. Puerta, **S. Rommel**, J. J. Vegas Olmos, and I. Tafur Monroy. "10Gb/s Ultra-Wideband Wireless Transmission Based on Multi-Band Carrierless Amplitude Phase Modulation". In: *17th Annual Wireless and Microwave Technology Conference 2016*. Apr. 2016. DOI: 10.1109/WAMICON.2016.7483847.

[A3] L. C. P. Cavalcante, L. F. Q. Silveira, **S. Rommel**, J. J. Vegas Olmos, and I. Tafur Monroy. "Performance analysis of wavelet channel coding in COST207-based channel models on simulated radio-over-fiber systems at the W-band". In: *Optical and Quantum Electronics* 48.1 (Jan. 2016), paper 28. DOI: 10.1007/s11082-015-0284-1.

[A4] **S. Rommel**, E. P. Grakhova, A. Jurado-Navas, A. K. Sultanov, J. J. Vegas Olmos, and I. Tafur Monroy. "Pulse Shaping for High Data-Rate Ultra-Wideband Wireless Transmission Under the Russian Spectral Emission Mask". In: *International Journal of Communication Systems* 31.1 (Jan. 2018), paper e3388. DOI: 10.1002/dac.3388.

[A5] **S. Rommel**, B. Cimoli, G. Silva Valdecasa, J. B. Jensen, T. K. Johansen, J. J. Vegas Olmos, and I. Tafur Monroy. "Real-time 2.5 Gbit/s ultra-wideband transmission using a Schottky diode-based envelope detector". In: *Microwave and Optical Technology Letters* 59.3 (Mar. 2017), pp. 606–609. DOI: 10.1002/mop.30352.

[A6] R. Puerta, **S. Rommel**, J. A. Altabas, L. Pyndt, R. Idrissa, A. K. Sultanov, J. J. Vegas Olmos, and I. Tafur Monroy. "Multiband carrierless amplitude/phase modulation for ultrawideband high data rate wireless communications". In: *Microwave and Optical Technology Letters* 58.7 (July 2016), pp. 1603–1607. DOI: 10.1002/mop.29866.

[A7] E. P. Grakhova, **S. Rommel**, A. Jurado-Navas, A. K. Sultanov, J. J. Vegas Olmos, and I. Tafur Monroy. "First experimental impulse-radio ultra-wideband transmission under the Russian spectral emission mask". In: *Electronics Letters* 52.10 (May 2016), pp. 877–879. DOI: 10.1049/el.2016.0635.

[A8] W. Klaus, **S. Rommel**, J. M. Delgado Mendinueta, J. Sakaguchi, P. Mitchell, N. Psaila, J. J. Vegas Olmos, I. Tafur Monroy, Y. Awaji, and N. Wada. "Numerical analysis of misalignment effects in few-mode multi-core fiber systems". In: *IEEE Photonics Conference*. Oct. 2017, pp. 283–284. DOI: 10.1109/IPCon.2017.8116107.

[A9] **S. Rommel**, J. M. Delgado Mendinueta, W. Klaus, J. Sakaguchi, J. J. Vegas Olmos, Y. Awaji, I. Tafur Monroy, and N. Wada. "Impulse Response of a 36-Core Few-Mode Photonic Lantern Hybrid Spatial-Multiplexer". In: *4th International Symposium on Extremely Advanced Transmission Technologies*. June 2017, p. 38.

[A10] U. Armendariz, **S. Rommel**, S. Rodriguez, C. B. Olsen, I. Tafur Monroy, and J. J. Vegas Olmos. "Evaluation and Performance Analysis of 3D Printing Technique for Ka-Band Antenna Production". In: *46th European Microwave Conference 2016*. Oct. 2016, pp. 1259–1262. DOI: 10.1109/EuMC.2016.7824579.

[A11] U. Armendariz, **S. Rommel**, S. Rodriguez, I. Tafur Monroy, J. J. Vegas Olmos, and C. B. Olsen. "Additive manufacturing of Ka-band antennas for wireless communications". In: *4M/IWMF 2016 [11th International Conference on Multi-Material Micro Manufacture (4M) / 10th International Workshop on Microfactories (IWMF)]*. Sept. 2016, paper 701. DOI: 10.3850/978-981-11-0749-8_701.

[A12] A. Ruiz Salazar, **S. Rommel**, E. Anufriyev, I. Tafur Monroy, and J. J. Vegas Olmos. "Rapid Prototyping by 3D Printing for Advanced Radio Communications at 80 GHz and Above". In: *4M/IWMF 2016 [11th International Conference on Multi-Material Micro Manufacture (4M) / 10th International Workshop on Microfactories (IWMF)]*. Sept. 2016, paper 735. DOI: 10.3850/978-981-11-0749-8_735.

[A13] E. P. Grakhova, **S. Rommel**, A. Jurado Navas, A. K. Sultanov, J. J. Vegas Olmos, and I. Tafur Monroy. "Pulse Shaping for High Capacity Impulse Radio Ultra-Wideband Wireless Links Under the Russian Spectral Emission Mask". In: *27th Annual IEEE International Symposium on Personal, Indoor and Mobile Radio Communication 2016*. Sept. 2016, paper WeD7.1. DOI: 10.1109/PIMRC.2016.7794775.

[A14] **S. Rommel**, B. Cimoli, G. Silva Valdecasa, J. B. Jensen, T. K. Johansen, J. J. Vegas Olmos, and I. Tafur Monroy. "Ultra Wideband Signal Detection with a Schottky Diode Based Envelope Detector". In: *37th Progress In Electromagnetics Research Symposium 2016*. Aug. 2016, p. 5054. DOI: 10.1109/PIERS.2016.7735832.

[A15] L. Chorchos, **S. Rommel**, J. P. Turkiewicz, I. Tafur Monroy, and J. J. Vegas Olmos. "Remote Access Unit for Optic-to-Wireless Conversion". In: *37th Progress In Electromagnetics Research Symposium 2016*. Aug. 2016, p. 2375. DOI: 10.1109/PIERS.2016.7734974.

[A16] A. Ruiz Salazar, **S. Rommel**, E. Anufriyev, J. J. Vegas Olmos, and I. Tafur Monroy. "Convergence of photonics and electronics for Terahertz wireless communications". In: *21st European Conference on Networks and Optical Communications 2016*. June 2016, paper S7.1. DOI: 10.1109/NOC.2016.7507005. *(Invited)*.

[A17] L. Chorchos, **S. Rommel**, J. P. Turkiewicz, and J. J. Vegas Olmos. "Reconfigurable remote access unit for W-band radio-over-fiber transmission". In: *Proc. SPIE – Photonics Applications in Astronomy, Communications, Industry, and High-Energy Physics Experiments*. Vol. 10031. May 2016, paper 100311D. DOI: 10.1117/12.2249350.

[A18] X. Lu, A. Tatarczak, **S. Rommel**, S. Rodriguez, J. J. Vegas Olmos, and I. Tafur Monroy. "Microwave Photonics Technologies Supporting High Capacity and Flexible Wireless Communications Systems". In: *Asia Communications and Photonics Conference 2015*. Nov. 2015, paper ASu1J.5. DOI: 10.1364/ACPC.2015.ASu1J.5. *(Invited)*.

[A19] A. Tatarczak, X. Lu, **S. Rommel**, S. Rodriguez, J. J. Vegas Olmos, and I. Tafur Monroy. "Radio-over-fiber transmission using vortex modes". In: *2015 International Topical Meeting on Microwave Photonics*. Oct. 2015, paper TuP-31. DOI: 10.1109/MWP.2015.7356677.

[A20] **S. Rommel**, L. C. P. Cavalcante, J. J. Vegas Olmos, and I. Tafur Monroy. "Microwave Photonics Techniques Supporting Flexible Wireless Communications Links". In: *36th Progress In Electromagnetics Research Symposium 2015*. July 2015, paper 2P8b-7. *(Invited)*.

Other scientific publications:

[O1] K. Hasanuzzaman, S. Spolitis, T. Salgals, J. Braunfelds, A. Morales, L. González, R. Simon, R. Puerta, P. Asensio, V. Bobrovs, S. Iezekiel, and I. Tafur Monroy. "Minimization of Crosstalk in Multicore Optical Fibre Link using Real-time FPGA-based Approach". In: *Asia Communications and Photonics Conference*. Nov. 2017. *(inpress)*.

[O2] S. Echeverri-Chacón, A. Morales, S. Rodríguez, **S. Rommel**, S. Vazquez, J. J. Vegas Olmos, J. J. Mohr, S. B. Christensen, and I. Tafur Monroy. "Short Range Inter-Dataceneter Transmission with Carrier Delivery and Remote Modulation for 112 Gb/s PM-QPSK Signals". In: *19th International Conference on Transparent Optical Networks*. July 2017, paper Mo.C3.3. DOI: 10.1109/ICTON.2017.8024765.

[O3] V. S. Lyubopytov, A. Tatarczak, X. Lu, R. V. Kutluyarov, **S. Rommel**, A. K. Sultanov, and I. Tafur Monroy. "Analysis of Optical Fiber Complex Propagation Matrix on the Basis of Vortex Modes". In: *2016 International Conference Laser Optics*. June 2016, paper ThR4-p02. DOI: 10.1109/LO.2016.7549769.

[O4] V. S. Lyubopytov, A. Tatarczak, X. Lu, R. V. Kutluyarov, **S. Rommel**, A. K. Sultanov, and I. Tafur Monroy. "Optical-domain Compensation for Coupling between Optical Fiber Conjugate Vortex Modes". In: *11th Conference on Lasers and Electro-Optics Pacific Rim 2015*. Aug. 2015, paper PDP.T12.

Contents

Chapter 1

Introduction

Telecommunications, i.e., the transport of information over long distances, has been an enabling technology as well as one of the characteristic pillars of the 'information age' of humanity, where the handling of information and its omnipresence are the defining elements [1, 2]. Together with the rise and rapid development of digital information storage and processing or computation, telecommunications has completely reshaped society and industry in only a few decades and has impacted and transformed all facets of life [1–3] to the point where, today, we live in a world where computerized automation has fully arrived in the 'industry 3.0' [2, 4], where data is heralded as 'the new oil' [5], i.e., where big data drives innovation and changes in the industry, and where, with the (industrial) internet of things (IoT), the next industrial revolution – the shift to the 'industry 4.0', where machines, systems, processes etc. connect to form intelligent production and value chains – is within sight [4, 6, 7].

Similarly, the rise and spread of the internet – to the point where today the availability of a (high-speed) data connection is taken for granted at any time, any place and under all circumstances [8, 9] – has entirely transformed private and social life [10–12]. From the early internet, making information available instantly, replacing paper mail with email and introducing online shopping, via the rise of internet telephony and early social networks, to today's world of on-demand, high quality video and audio streaming, video chat and conferencing, instant messaging and the omnipresence of social networks and platforms with user-generated content, the internet has entirely remodeled the way we interact with each other [12, 13].

One key element in enabling the fourth industrial revolution and to allow continuation of the growth in mobile data usage is the evolution of

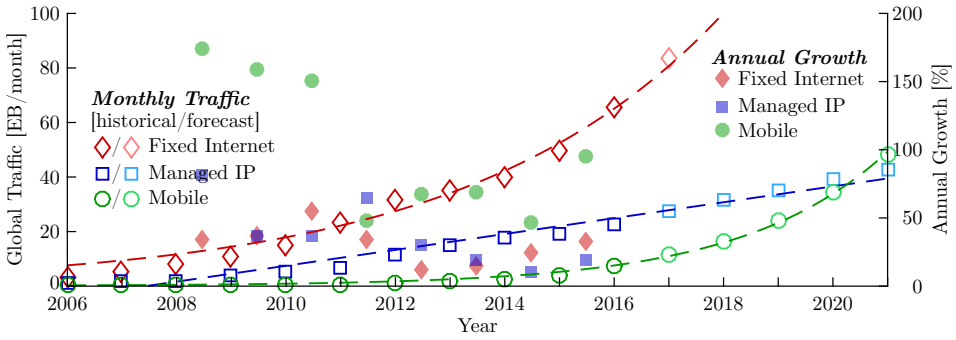

Figure 1.1: Historical and forecast volume and growth of worldwide internet and mobile data traffic.[1,2]

the mobile networks [14–16], where the fourth generation (4G) introduced high-speed mobile data and allowed for larger user densities [17]. The fifth generation (5G) and beyond of mobile networks, however, will require more radical, sweeping changes, not only to allow major growth in capacity, user density and network efficiency, but also to fulfill a multitude of new requirements arising from applications newly entering the picture in mobile communications [15, 16, 18]. It is within this framework that the research presented in this thesis was carried out, hoping that it may contribute a small part to these next generations of mobile networks – and, as such, to the development of the technologies underlying and enabling the advancement of society.

1.1 Motivation

The immense growth of worldwide data traffic and the emergence of new applications are two of the key driving factors informing the requirements set for the next generation(s) of mobile network standards [15]. Global data traffic has grown exponentially over the last decade and is forecast to continue such growth [19]. Mobile traffic in particular has grown at twice the rate of all other traffic [19, 20] and, with a forecast compound annual growth rate (CAGR) of 46.3 %, is forecast to more than double every two years, as seen in Fig. 1.1 and Table 1.1. This rapid growth is enabled by the continued proliferation of 4G mobile networks, bringing a threefold increase in the average downstream data rate to 6.8 Mbit/s in 2016 – and with 4G connections already carrying 69 % of mobile data traffic, even though only constituting 26 % of all mobile connections [20].

Traffic Type	Compound Annual Growth Rate		
	Historical		Forecast
	2006–2011	2011–2016	2016–2021
Fixed Internet	47.5%	23.1%	23.2%
Managed IP	50.2%	27.3%	13.1%
Mobile	143.3%	64.5%	46.3%

Table 1.1: Historical and forecast CAGR of worldwide internet and mobile data traffic.[1,2]

Similarly, the number of devices connected to the mobile networks is growing rapidly – by 500 M devices a year – and has reached a total of 8.0 B devices in 2016 and is forecast to grow to as many as 11.6 B connected devices [20]. The majority of this growth is driven by machine-to-machine (M2M) connections in the IoT, accounting for only 780 M devices in 2016, but as many as 3.3 B by 2021 [20]. The growth of the number of M2M connections introduces a new set of challenges to the mobile networks and their standardization, as these connections may differ significantly from typical (smart-)phone connections in their requirements for data rate, latency, mobility and power consumption – e.g., with the requirements from low-power wide-area (LPWA) connections [21], forecast to constitute 7 % of all mobile connections by 2021, being almost diametrically opposite to those of video conferencing: the latter requiring high-bandwidth and low latency, while the former typically are low-bandwidth, can tolerate large latencies, but are constrained by power consumption [20, 21].

To support such growth, the standardization efforts for 5G networks have set a number of ambitious targets, designed to match the user experience of fixed networks [22]:

capacity: The ubiquitously available, user-experienced, data rate is set to increase 10× to 100 Mbit/s, while peak user data rates are to increase 20× to 20 Gbit/s. These are supported by both an increase of average spectral efficiency (SE) to 3 bit/s/Hz and, more significantly a 100× increase of area traffic capacity to 100 Mbit/s/m^2.

[1] Source of historic traffic data for the years 2007–2015: 'Cisco Visual Networking Index: Forecast and Methodology' yearly editions 2007 to 2015. Source of traffic data for the year 2016 and traffic forecast data for the years 2017–2021: 'Cisco Visual Networking Index: Forecast and Methodology, 2016–2021' [19]. Forecast 2018–2021, Fixed Internet: 2018: 103.0 EB/month, 2019: 127.0 EB/month, 2020: 155.1 EB/month, 2021: 187.4 EB/month.

[2] Annual growth data derived from historical traffic data 2007 to 2016. Fitted curves: exponential fit on 'Fixed Internet' and 'Mobile' traffic, linear fit on 'Managed IP' traffic.

user density: The number of connections per area, i.e., the connection density, should increase by a factor of 10, to 10^6 devices/km^2 – again supported by the increase in area traffic capacity.

mobility: The maximum supported movement speed of the mobile user is set to increase from 350 km/h to 500 km/h, supporting even the highest speed trains.

latency: To support tactile applications in the IoT, as well as high-speed mobility, the latency requirements are set to become much more stringent, supporting latencies as low as 1 ms.

energy efficiency: Network energy efficiency is set to scale at a similar factor as area traffic capacity, i.e., by 100×.

These targets require substantial changes in all segments of the mobile network – between the mobile user and the remote radio head (RRH) it mandates a move to higher radio frequency (RF) carriers to accommodate the larger required bandwidths, from the RRH to the network it requires a re-consideration of where data is converted from radio to baseband and eventually processed, i.e., a re-design of the front- and backhaul interfaces between RRH and central office (CO) in a centralized radio access network (C-RAN) [23–25]. Together with the need for much smaller – and hence more – cells to support the required user densities and capacities per area and new, more flexible and less uniform, deployment strategies [26–28], these result in the need for a flexible functional split between the RRH, an intermediate distributed unit (DU), and the central unit (CU) in the CO [24, 25, 29]. As the connections between these will carry different types and volumes of signals, their implementation may vary – however, the link between CO and DU will typically be optical fibers, bridging potentially large (tens of kms) distances and supporting the high-capacity demanded by backhaul, while the link between DU and RRH may often need to be wireless to allow flexible and easy deployment of the RRH, independent of access to an optical fiber [23, 28].

To support the massive front- and/or backhaul capacities required, or to directly carry analog radio signals to the DU/RRH, these wireless links will need to use RF carriers in the lower millimeter wave (mmW) frequency range between 30 GHz and 100 GHz, where large amounts of spectrum are available lightly licensed or even unlicensed [30]. Similarly, to support peak user data rates of tens of Gbit/s, the use of mmW carriers is inevitable, even directly to the mobile user – as is the case in direct wireless access

and indoor distribution [30, 31]. Together, these make mmW hybrid photonic wireless links an essential technology in future mobile networks and high-speed wireless access – and consequently an important research topic.

1.2 Outline of the thesis

This thesis is structured in four chapters: Chapter 1 introduced and motivated the use of mmW radio-over-fiber (RoF) in mobile networks of the fifth generation and beyond, provides this outline and in its last section gives a short summary of the contributions by the original work presented in this thesis. Chapters 2 and 3 provide the necessary background on hybrid mmW photonic wireless links and their integration in mobile networks respectively, while setting the original contributions into perspective to the state of the art. Finally, chapter 4 concludes the thesis and provides an outlook on future work.

In chapter 2, first, the generation of mmW signals using photonics is discussed, giving an idea of the general setup of RoF links, before their achievable capacity is estimated by characterizing the mmW wireless channel (sections 2.1 and 2.2). Chapter 2 further compares a series of possible link implementations, analyzing possible reductions in link complexity and their connection to link deployment (section 2.3), before discussing modulation formats for optimization of capacity, robustness and flexibility (section 2.4).

Chapter 3 deals with the integration of mmW RoF links into existing networks and its place in the radio access network (RAN), briefly discussing the integration with passive optical networks (PONs) and looking at reconfigurable architectures for the RRH (sections 3.1 and 3.2). The final section of chapter 3, section 3.3, looks further ahead, beyond the immediate impact of the introduction of mmW carriers, towards the challenges and possibilities of introducing optical space division multiplexing (SDM) to RoF links.

1.3 Summary of contributions by original work

The contributions of the work in this thesis are spread across a few challenges connected to mmW RoF links. A first contribution comes from **PAPER1** and **PAPER2**, characterizing the mmW wireless channel in W-band and estimating the achievable capacity and wireless reach. **PAPER3**–**PAPER7** regard deployability of mmW RoF links, implementing setups with reduced complexity in the optical and RF domains, showing simple

configurations to achieve multi-gigabit capacity over large distances and demonstrating real-time transmission.

PAPER8–PAPER14 use advanced modulation formats to extend the state of the art in mmW RoF links, by showing increases in capacity and spectral efficiency through the use of duobinary modulation and multi-band carrierless amplitude phase modulation (multiCAP) – the latter achieving record spectral efficiencies for W-band mmW links longer than 10 m –, and by experimentally demonstrating both wavelet coding and the combination of non-orthogonal multiple access (NOMA) and multiCAP for the first time, allowing increased link robustness and flexibility.

Network integration of mmW RoF links and reconfigurability of the up-conversion unit are the focus of **PAPER15–PAPER18**, contributing RRH architectures that allow integration with wavelength division multiplexing (WDM) PONs, flexible selection of WDM channel and RF carrier frequency and switching between multiple antennas or sectors – in sum adding a layer of flexibility to the RAN, which by design is ready for the introduction of software-defined networks (SDN).

Finally, a look ahead is taken to the use of optical SDM for mmW RoF links and RANs, discussing and using spatially diverse optical network analysis as a means to fully characterize SDM components, fibers and systems in **PAPER19–PAPER21** – thus providing a prerequisite for their eventual use for mmW RoF which requires a more complete understanding of their propagation properties.

Chapter 2

Millimeter wave hybrid photonic wireless links

Hybrid photonic wireless communication links, comprising both fiber optical and wireless radio transmission – hence also commonly known as radio-over-fiber (RoF) links –, are ideally suited to solve many of the challenges faced by the front- and backhaul for next-generation mobile networks and in high-speed wireless access [23, 29]. They cover a range of scenarios – as shown in Fig. 2.1 – as high-capacity point to point links for links between buildings and across obstacles and for mobile front-/backhaul, and for wireless distribution in offices, shopping centers, stadiums or other large indoor areas.

A generic millimeter wave (mmW) RoF link, as shown in Fig. 2.2, consists of the transport of a signal through on optical fiber, optical to electrical (O/E) conversion and subsequent radiation and detection of the radio frequency (RF) signal. Therein, the O/E conversion, i.e., the transition from fiber optics to an RF signal at mmW frequencies, is the key step to unlock-

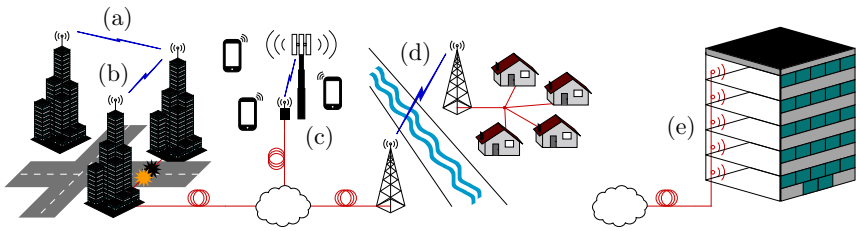

Figure 2.1: Scenarios for the use of mmW RoF links: (a) high-speed connection to buildings without fiber access, (b) protection against fiber breaks, (c) mobile front-/backhaul, (d) bridging obstacles and (e) indoor high-speed wireless distribution.

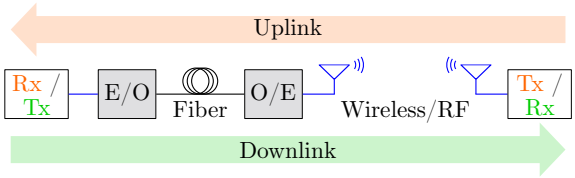

Figure 2.2: Schematic of a generic RoF link, indicating up- and downlink directions, involved E/O and O/E conversions and transmission media. Acronyms: Rx: receiver, Tx: transmitter, E/O: electrical to optical conversion, O/E: optical to electrical conversion.

ing the advantages of hybrid photonic wireless links. While it is possible to transport only the baseband signals in the optical fiber and, after detection, up-convert it to the desired RF frequency electronically, this suffers from system bandwidth limitations and increased complexity at mmW frequencies. On the other hand, the use of analogue RoF, where the RF signal is generated directly by beating on the optical detector, not only allows using the large modulation bandwidths readily available in optics, but also enables centralizing critical equipment – e.g., network control, RF oscillators etc. – and simplifying the remote stations. Thus, by combining fiber optics, photonic up-conversion and wireless transmission, such hybrid photonic wireless links benefit from the advantages of both worlds – fiber optics bring the ability to easily bridge large distances and use very large modulation bandwidths, while wireless links allow for easy, fast and flexible deployment – and additionally simplify deployment of centralized networks [24, 29, 32].

This chapter discusses a number of aspects of mmW hybrid photonic wireless links, starting with an introduction of the relevant photonic techniques in section 2.1 to establish a basis for the further sections that discuss specific aspects and the contributions by the original work in this thesis. Thereafter, section 2.2 discusses the mmW wireless channel, its characterization and estimation of the achievable capacity and reach, before section 2.3 looks at possibilities for complexity reduction of RoF setups and finally section 2.4 discusses modulation formats to increase capacity and spectral efficiency, improve link robustness and allow flexible resource allocation.

2.1 Techniques for millimeter wave hybrid photonic wireless links

The use of photonics for the generation, manipulation and detection of radio and wireless signals has been widely studied under the label of microwave

photonics (MWP) [33–35] and with the advances of the last decades in the design and fabrication of larger bandwidth modulators and photodiodes has extended this field to cover the whole millimeter wave frequency range. The large set of technologies for the manipulation of microwave signals in photonics is of significant interest to RoF communications links, especially for optically controlled beam forming and steering, they will however not be further regarded in this section, as their application falls firmly in to the category of 'future work' – they will hence be mentioned in section 4.2. Conversely, the generation and detection of mmW signals – especially the former – with the help of photonics are central to the work presented in this thesis and are thus briefly discussed in the following.

2.1.1 Photonic up-conversion for for millimeter wave generation

The generation of micro- and millimeter wave signals by optical means has been widely studied and a large number of schemes developed – they are however all based on the beating of two optical signals, spaced at the desired RF frequency and carrying the modulation data, on a photodiode (PD).[1] In the following, the mathematical principle will be briefly presented to illustrate the concept, before a number of generation schemes are discussed in their advantages and disadvantages.

In the simplest and most general case of optical heterodyning, where a baseband modulated optical signal beats with an independent and free running local oscillator (LO) laser, the two signal and LO optical fields $E_{\mathrm{S}}(t)$ and $E_{\mathrm{LO}}(t)$ can be expressed as:[2]

$$E_{\mathrm{S}}(t) = \sqrt{P_{\mathrm{S}}}s(t)\,\mathrm{e}^{-j(\omega_{\mathrm{S}}t+\phi_{\mathrm{S}}(t))} \tag{2.1}$$

$$E_{\mathrm{LO}}(t) = \sqrt{P_{\mathrm{LO}}}\,\mathrm{e}^{-j(\omega_{\mathrm{LO}}t+\phi_{\mathrm{LO}}(t))}, \tag{2.2}$$

where $s(t)$ is the baseband modulation signal (real or complex), P_{S} and P_{LO} are the respective optical powers and ω_{S}, ω_{LO}, $\phi_{\mathrm{S}}(t)$, and $\phi_{\mathrm{LO}}(t)$ are the optical frequencies and phases. The electrical output E_{PD} of the PD is then

[1] The generation of mmW signals by electrical means is of course possible and is combined with optical fiber transmission in so-called digitized RoF, where the optical transmission is a digital baseband transmission only – such links are not regarded in this thesis.

[2] For the sake of brevity, polarization has been disregarded in this discussion and all involved optical signals are assumed to be co-polarized to ensure efficient beating on the PD.

proportional to the square of the combined optical fields:

$$E_{\mathrm{PD}} \propto \left| \frac{1}{\sqrt{2}} E_{\mathrm{S}}(t) + \frac{1}{\sqrt{2}} E_{\mathrm{LO}}(t) \right|^2 \tag{2.3}$$
$$= \wr(0) + s^2(t)\wr(0) + E_{\mathrm{RF}} + \wr(\omega_{\mathrm{S}} + \omega_{\mathrm{LO}}) + s^2(t)\wr(2\omega_{\mathrm{S}}) + \wr(2\omega_{\mathrm{LO}}),$$

where $\wr(\omega)$ indicates terms oscillating at frequency ω and E_{RF} is the difference frequency term, i.e., is $\wr(|\omega_{\mathrm{S}} - \omega_{\mathrm{LO}}|)$, and is the desired RF signal, given as:

$$E_{\mathrm{RF}} = \sqrt{P_{\mathrm{S}} P_{\mathrm{LO}}}\, s(t) \cos\left(|\omega_{\mathrm{S}} - \omega_{\mathrm{LO}}|\right), \tag{2.4}$$

with $\omega_{\mathrm{RF}} = |\omega_{\mathrm{S}} - \omega_{\mathrm{LO}}|$ and $\phi_{\mathrm{RF}} = \phi_{\mathrm{S}}(t) - \phi_{\mathrm{LO}}(t)$, the RF carrier frequency and total phase respectively. All the terms denoted with $\wr(\omega)$ in Eq. (2.3) are terms of no interest for mmW signal generation – and are, in the case of the $\wr(0)$ terms, which are a voltage offset and a squared baseband copy of the signal $s(t)$, easily removed using a filter or the passband response of the radiating antenna, while the sum- and double frequency terms are at twice the optical frequencies and thus much too high to be passed by the PD. Heterodyning of two optical tones is thus an easy way to generate mmW RF signals and is commonly referred to as photonic up-conversion, as it can preserve any modulation present on the optical signals. The exact properties of the signal and its susceptibility to impairments, however, heavily depend on the scheme employed for generation of the two optical tones.

An overview of the most common schemes for RoF signal generation is given in Figs. 2.3(a)–(f), while Figs. 2.3(A)–(C) further show three heterodyning schemes, characterized by the optical signal present in the transmission fiber. The scheme with an independent LO laser at the remote station in Fig. 2.3(C), corresponds closest to the above mathematical discussion and suffers least from fiber-induced impairments, as only the modulated signal is present in the transmission fiber. It does however, in the same way as the two incoherent generation schemes in Figs. 2.3(a)–(b), result in the RF signal carrying the combined phase noise of both lasers – and thus likely a phase noise that is outside of ITU regulations for radio carriers [36], unless the lasers are of narrow linewidth and tightly controlled [37].

The self-heterodyne schemes in Figs. 2.3(c)–(f), where the light from a single laser is split into two optical tones by modulating it with a sinusoid, provide significantly better phase stability [37, 38] at the cost of a more complex generation setup. In these schemes an external modulator is driven with a sinusoid (Figs. 2.3(c)–(d)) or a modulated RF signal (Fig. 2.3(e)) to generate the two tones. In these schemes it is essential to

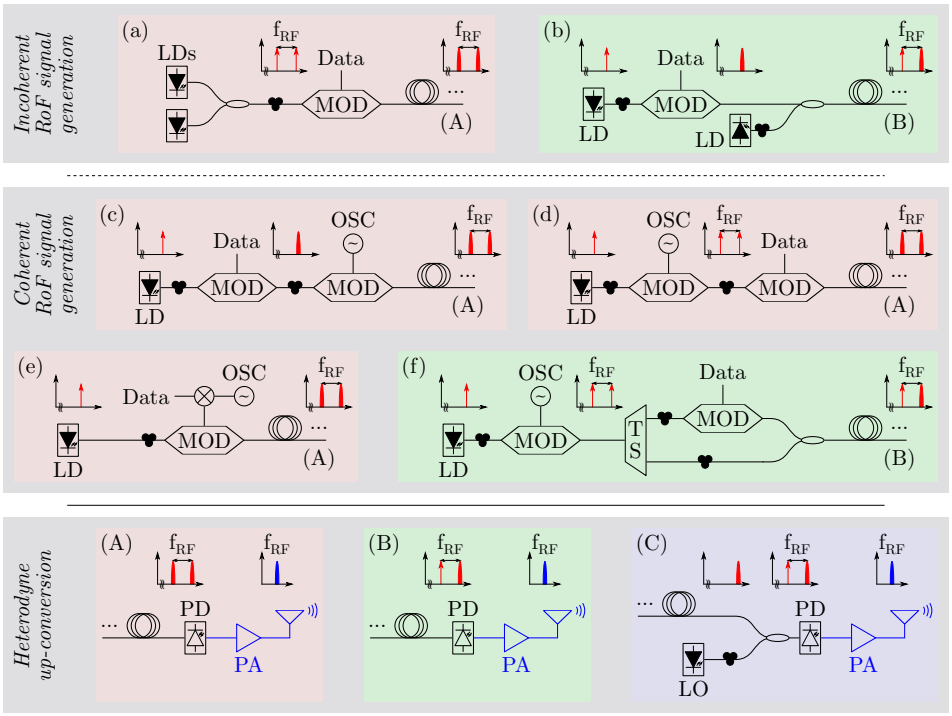

Figure 2.3: ROF signal generation and corresponding heterodyne up-conversion schemes. Signal generation: (a)–(b) incoherent schemes with two free running lasers, (c)–(f) coherent schemes based on a single laser and two-tone generation. Heterodyne up-conversion by beating on the PD: (A) with two modulated optical tones in the transmission fiber, (B) with one modulated and one CW tone in the transmission fiber, (C) with only the modulated tone in the fiber and a local free running LO laser. Insets: qualitative rendition of optical and electrical spectra, illustrating presence and modulation of signal components. Acronyms: LD: laser diode, MOD: optical modulator, OSC: oscillator, TS: tone separation (i.e., dual band-pass filter with separate outputs), PD: photodiode, PA: power amplifier, LO: local oscillator (laser).

employ carrier suppressed modulation to avoid dispersion induced RF power fading[3] [38–40], resulting from the two sides experiencing different amounts of chromatic dispersion and thus their beating signals with the carrier being out of phase. The use of carrier suppressed modulation further reduces the required oscillator frequency (and thus modulation bandwidth), as the RF frequency resulting from direct beating of the two tones is double the oscillator frequency [39, 40].

The presented schemes in Fig. 2.3 further differ in their ability to pre-

[3]For this reason, only carrier suppressed modulation is shown in the insets in Fig. 2.3.

serve the phase information of the modulation signal, i.e., their applicability for the up-conversion of complex modulation formats, rather than intensity modulation only. For the schemes where both optical lines are modulated, i.e., those matching Fig. 2.3(A), the heterodyne mixing may cause the loss of phase information [41, 42], making them unsuitable for up-conversion of complex modulation formats.[4] The schemes where only one optical tone is modulated, i.e., those matching Fig. 2.3(B), do not suffer from in-band beat noise generated by direct beating of multiple sidebands and thus preserve phase information and allow the transport of complex modulation formats, such as phase shift keying (PSK), quadrature amplitude modulation (QAM) etc. The scheme in Fig. 2.3(f) thus remains as the main candidate to achieve low phase noise, not be affected by RF fading and allow complex modulation formats.

Finally, a range of other generation schemes has been suggested, including dual wavelength lasers [43], mode-locked lasers [44] and optical frequency combs [45] – the evaluation of their performance, however, follows the above principles in that coherence of the involved tones largely determines phase noise, in that dispersion induced RF power fading must be avoided and in that the presence of unwanted sidebands impacts the use of complex modulation formats.

Of the original works presented in this thesis, the majority (PAPER3–PAPER5, PAPER8–PAPER10, PAPER12–PAPER14) uses the self-heterodyne scheme with only one modulated tone as shown in Fig. 2.3(f), while the works focused on architectural aspects (PAPER15–PAPER18) employ a LO laser at the up-conversion site as in Fig. 2.3(C). PAPER11 augments the self-homodyne scheme by introducing optical single-sideband modulation on the single modulated tone to limit the spectral occupation of the generated RF signal.

2.1.2 Detection and down-conversion of millimeter wave signals

The detection and down-conversion of mmW RF signals, i.e., the recovery of the transported baseband signal, are the direct complement to up-conversion and radiation of the RF signal. Contrary to up-conversion however, for down-conversion electrical means are the main method of choice – although a number of photonics based schemes were suggested, including di-

[4]The scheme of Fig. 2.3(e) may be salvaged by shifting the baseband data to an intermediate frequency (IF), before combining it with the RF, so as to shift the desired signal away from the beat noise [41].

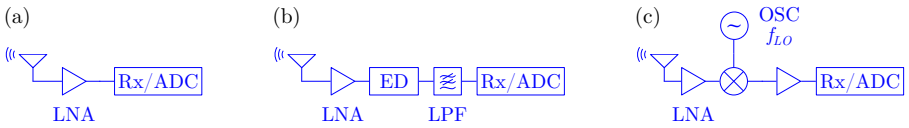

Figure 2.4: mmW signal detection and down-conversion schemes: (a) direct reception/digitization of the mmW RF signal, (b) envelope detection of the RF signal and reception/digitization in baseband, (c) down-conversion to IF by mixing with an LO and reception/digitization of the IF signal. Acronyms: LNA: low noise amplifier, ED: envelope detector, Rx: receiver, ADC: analog to digital converter, LPF: low pass filter, OSC: oscillator.

rect remodulation, optical envelope detection and optical down-conversion to IF [46–48] –, either converting to an IF or directly to baseband. Once at IF or baseband, the signal can easily be modulated onto an optical carrier for transmission through fiber [49, 50] or directly treated by the receiver.

For electrical down-conversion, three main schemes may be discerned and are shown in Fig. 2.4. The first, in Fig. 2.4(a), forgoes any actual down-conversion and directly samples and digitizes the full RF signal – requiring an analog to digital converter (ADC) with a large enough bandwidth and sampling rate to fit the mmW RF signal. As in mmW signals the modulation bandwidth is small compared to the carrier frequency, this is highly inefficient and not cost effective. Employing envelope detection as in Fig. 2.4(b), on the other hand, converts the signal directly to baseband, limiting the required ADC bandwidth to the minimum – at the cost of losing phase information and thus being applicable to intensity modulated RF signals only. Down-conversion to an IF by mixing with a LO, as shown in Fig. 2.4(c), preserves phase information, while reducing the required ADC bandwidth and is thus the preferred option if high spectral efficiency (SE) – and thus complex modulation – is required. While the required ADC bandwidth and ability to work with complex modulation formats are the key discerning factors between the three schemes, other considerations may be required – e.g., the possible increase of noise resulting from envelope detection and the added phase noise from the LO when down-mixing to IF.

The original works presented in this thesis cover all three down-conversion schemes, with the experiment at the lowest RF frequency in PAPER8 the only one to employ direct digitization, while the other two schemes are employed in many more cases. Envelope detection is used in PAPER3–PAPER7 and PAPER15–PAPER18, while down-mixing to an IF and subsequent digital conversion to baseband are employed in PAPER9–PAPER14.

2.2 Channel characterization and capacity and reach estimation

The transition away from the overcrowded conventional wireless bands at and below 6 GHz towards mmW RF carriers is key to enabling the large data rates foreseen for font- and backhaul in fifth generation (5G) mobile networks and high-speed wireless access – it does however come with a series of new challenges with regards to the wireless channel [29, 30, 51]. The characterization of the channel and the evaluation of the applicability of existing channel models is thus essential to allow an estimate of the achievable capacities and transmission distances – and thus to evaluate the potential of mmW hybrid photonic wireless links [26, 29].

The wireless channel exhibits a significantly higher path loss at mmW frequencies and has potentially large atmospheric absorption – the use of highly directive antennas is thus typical in mmW links. Together with a reduced penetration through obstacles, the latter significantly alters channel characteristics with regards to multi-path propagation and frequency selectivity [52]. Indoor and outdoor channel characterization efforts were performed in the lower regions of the mmW range, around 30 GHz [51, 52] and 60 GHz [31, 52, 53] – the latter especially with regards to the increased atmospheric absorption in this frequency range [26, 30]. **PAPER1** contributes an indoor channel measurement across the whole W-band, i.e., from 75 GHz to 110 GHz, confirming good applicability the Friis and generic empirical path loss model (GEPL) models [54, 55] and measuring both frequency and time response of the channel. The measurements show multi-path components at 30 dB and more below the line of sight (LOS) signal and thus suggest the wireless channel in W-band to be predominantly LOS for a distance of 4 m, when employing antennas with 24 dBi gain each.

PAPER2 estimates the achievable channel capacity, based on a modified version of Shannon's capacity limit [56, 57] and a survey of a series of transmission experiments. Extracting a set of common system parameters from [PAPER4, PAPER6] and [58–62], it estimates the achievable capacity depending on distance, bandwidth, antenna gains and transmitted power, as shown in Fig. 2.5. It thus confirms the large achievable data rates in mmW RoF links and derives a metric to relate actual link implementations to the achievable capacity, providing a means to evaluate their efficiency in employing spectral resources.

To analyze the achievable reach with the RF components available today and using a simple link setup with envelope detection, the series of experi-

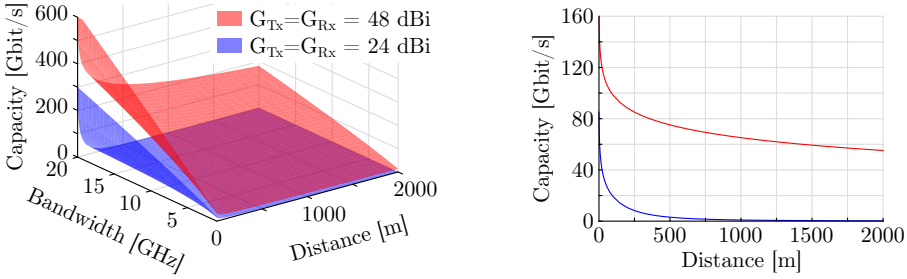

Figure 2.5: Estimated mmw channel capacity over distance and bandwidth for different antenna gains and with a transmitted power of 10 dBm. Acronyms: $G_{\mathrm{Tx}}/G_{\mathrm{Rx}}$: transmitter and receiver antenna gain.

ments from PAPER4, PAPER5 and PAPER6 is compared to a reach estimate mainly based in free space path loss in **PAPER7**, finding good agreement. **PAPER4** and **PAPER5** show experimental results for a RoF link with wireless transmission in W-band (i.e., between 75 GHz and 110 GHz) over 10 m to 70 m, while **PAPER6** and **PAPER7** extend the wireless reach in an outdoor experiment through the use of a slightly modified setup with additional amplification at the transmitter. This confirms the wireless link to be entirely LOS and predominantly limited by the available power – with a reach of almost 2500 m predicted with a transmitted power of only 20 dBm.

2.3 Link complexity and deployment

Analyzing the complexity of mmw hybrid photonic wireless links, its impact on different deployment scenarios and evaluating possible preconditions for their deployment, requires both an understanding of the possibilities offered by links of different complexity and an analysis of the requirements from the network in different deployment scenarios [24, 26–28, 63]. As the variety of the latter is still much too large to allow a comprehensive analysis, a number of particular issues have been selected and were addressed by the original works discussed in this section.

First, **PAPER3** regards the inclusion of bend-insensitive fiber (BiF) in the fiber link, as the latter will be required for on-premise fiber installation and optical wiring of – and within – the antenna, where fiber bends with small radii are likely to occur. Measuring the bend-loss of single mode fiber (SMF) and a set of BiF samples, it confirms a difference of multiple dB in loss from macro bends, even for a small number of turns, and evaluates their effect on a mmw RoF link, finding the inclusion of BiF to have no

detrimental effects on signal quality, while providing significantly larger tolerance to small-radius bends.

Second, **PAPER4** shows a mmW RoF link, in which the RF section has been reduced to a minimum, by employing a passive RF transmitter and using envelope detection at the receiver to directly down-convert the signal to baseband. Evaluating performance with carriers between 75 GHz and 87 GHz over distance from 10 m to 70 m, it demonstrates the simplified link to achieve good performance over significant distances and to be only limited by transmitter power and available laboratory space. **PAPER5** combines the results of PAPER1, PAPER3 and PAPER4 and sets them into perspective with the corresponding scenarios.

Third, **PAPER6** and **PAPER7** extend the wireless distance to 225 m, with only the addition of a medium power amplifier (MPA) at the transmitter, while otherwise maintaining the simplified RF setup. It further simplifies the optical setup, by replacing the RoF signal generation based on two tone generation and modulation of one tone – as in Fig. 2.3(f) and (B) – with a free running LO laser at the O/E conversion stage – as in Fig. 2.3(C). It shows that such simplification comes at the price of increase frequency variation of the generated RF signal over time – with variations larger than mandated by ITU-R regulations, but easily within the acceptable range for direct envelope detection with negligible penalty. Simplification of the optical setup will thus require additional control electronics or a relaxation of frequency purity standards – which for a highly directive, purely LOS, mmW link may be acceptable.

Finally, to demonstrate the path towards deployment for low complexity links, **PAPER15** implements real-time transmission of 2.5 Gbit/s signals over a link similar to that in [PAPER3–PAPER5], using a commercial clock and data recovery module.

2.4 Modulation formats for flexible and high capacity links

The choice of modulation format is a key element in the design of any communications link and defines its achievable SE, i.e., capacity per bandwidth used, has a large impact on signal processing complexity, on the ability to adaptively allocate resources and – especially in the case of broadcast transmission such as wireless and mobile – the access to the medium and thus number of users that can be accommodated [63, 64]. Modulation formats are thus a central point of study in mmW RoF links, both for the increase in

capacity and spectral efficiency, and for allowing flexible provisioning and ensuring efficient usage of resources [26, 30, 63, 64].

Of the original works in this thesis, PAPER8–PAPER10 and PAPER11 focused on increasing capacity by adopting modulation formats beyond on-off keying (OOK), while PAPER12 introduces wavelet coding to increase the robustness of orthogonal frequency division multiplexing (OFDM) against deep fading and PAPER13 and PAPER14 combine non-orthogonal multiple access (NOMA) with carrierless amplitude phase modulation (CAP) for flexibility in bandwidth and resource assignment.

2.4.1 Advanced modulation formats for capacity and spectral efficiency increase

Simple, intensity only, modulation formats, such as OOK, duo- or polybinary modulation and m-ary pulse amplitude modulation (PAM), allow straightforward implementation without the need for recovery of a carrier and typically dominate whenever the availability of spectrum is not a major limiting factor. Complex modulation formats, such as m-ary PSK or m-ary QAM, allow transmission of multiple bits per symbol and thus increased SE, at the cost of requiring carrier frequency and phase recovery, i.e., higher complexity. Advanced modulation formats, such as OFDM, and CAP, allow multi-carrier/-band operation and offer increased robustness against certain channel impairments and may allow further increases in SE.

As increasing capacity is one of the main drivers for the introduction of mmW RoF links, demonstrating and increasing the capacity achievable in such links has been a focus of research in recent years. However, overall capacity should not be the main figure of merit, as any achieved capacity must be set in relation to the employed bandwidth and complexity of the system – the latter especially with regards to the use of multiple parallel links and/or antenna polarization multiplexing. The disparity between overall achieved capacity and achieved effective[5] SE is illustrated in Fig. 2.6 which plots capacity and SE for a selection of recent experimental demonstrations of mmW RoF links.[6] As can be seen, capacities above 400 Gbit/s

[5] Calculation of the effective SE takes into account the actual spectral occupation of the RF signal and the capacity loss from forward error correction (FEC) overhead. Effective SE figures will thus differ from figures quoted in the respective papers, as the latter typically quote SE without accounting for the double-sideband nature of RF transmission in most experimental demonstrations.

[6] It should be noted that an overview over all experimental demonstrations even in the short span of a few years is practically impossible and thus the shown selection

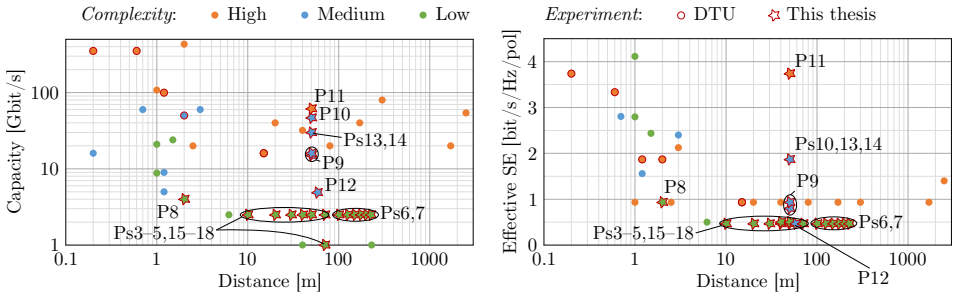

Figure 2.6: Overview of capacity and effective SE over distance of recent mmW RoF experiments.[8,9] Acronyms: SE: spectral efficiency.

have been achieved over a few meters, while for longer distances the mark of 100 Gbit/s is yet to be broken. Similarly and more drastically noticeable, the achieved effective SE was limited to values below 1 bit/s/Hz/pol until very recently[7] for any transmission above 3 m wireless distance.

2.4.1.1 Duobinary signaling

Duobinary signaling, where correlation between adjacent symbols is introduced on purpose to reduce signal bandwidth [80–82], is used in **PAPER8** and **PAPER9** to double spectral efficiency, while maintaining a low link complexity. Introducing correlation by adding $M-1$ adjacent bits, creates a signal of M levels with reduced bandwidth, allowing an increase in SE at the cost of increased requirements on signal to noise ratio (SNR) and the necessity of signal precoding [80]. In **PAPER8**, duobinary signaling is used to demonstrate the transmission of 4 Gbit/s over limited bandwidths in the Ka-band, while in **PAPER9** a series of duobinary signals with data rates up to 16 Gbit/s are transmitted over 50 m in W-band.

naturally is incomplete. It does however include the most significant demonstrations, i.e., those breaking records with respect to distance, capacity or SE, and the majority of demonstrations from the most relevant conferences of recent years; it does not include experimental demonstrations with carriers below 30 GHz and above 300 GHz, i.e., outside the mmW range, nor does it include demonstrations purely in electronics, i.e., without the involvement of fiber optics.

[7] Specifically until OFC 2017, with the publication of [PAPER10, PAPER11] and [65].

[8] Includes experimental transmission rates and spectral efficiency from the following references: [59–62, 65–79], and the following original works: [PAPER3–PAPER18].

[9] An overview of the included data in tabular form is provided in Appendix A.

2.4.1.2 Multi-band carrierless amplitude phase modulation

CAP is similar to QAM in that it allows transmission of two independent data streams over the two orthogonal in-phase (I) and quadrature (Q) signal components [83–86]. Contrary to QAM, modulation is not achieved by modulating a sine and cosine of the same frequency, but through filtering with two orthogonal filters. The latter result from multiplying two orthogonal carriers of the same frequency with a pulse shaping function – typically a root raised cosine (RRC), which, with matched filtering at the receiver, gives a raised cosine (RC) and thus minimizes inter symbol interference (ISI) – used to limit spectral occupation [85, 86]. Extending CAP into multi-band carrierless amplitude phase modulation (multiCAP), by using multiple pairs of orthogonal filters generated with carriers of different frequencies [84, 85, 87], allows the use of bit and power loading, as is typical for multi-band modulations [84, 85, 88, 89] and further allows different baud rates in different bands [90]. In combination, these allow multiCAP to adapt to the available bandwidth and given channel conditions with high flexibility and thus allow an increase in capacity, SE and/or link reach [73, 85, 87, 91] – including a number of recent capacity records in both the wireless and optical worlds [73, 91, A1, A2].

PAPER10 and **PAPER11** employ multiCAP to increase SE – and thus achievable capacity within a limited bandwidth – for mmW RoF links in W-band. Using a setup based on two tone generation with one modulated tone, **PAPER10** demonstrates the flexibility of multiCAP in adapting to channel conditions, with both bit and power loading exploited heavily. Transmission of 46.8 Gbit/s is achieved using nine bands with a baud rate of 1.3 GBd, constellation sizes between 8-PSK and 32-QAM and power loading with differences up to 2.5 dB. While not breaking any outright capacity record, it was the first[10] demonstration to achieve such capacities in a limited bandwidth and without the use of antenna multiplexing and thus presented a significant increase of SE over previous experiments with similar transmission distances.

By introducing optically generated single sideband modulation, **PAPER11** reduces the occupied RF bandwidth by a factor of two and thus drastically boosts SE. Single-sideband modulation is achieved by modulating one of the two generated tones in an I/Q modulator, driven with the signal and a Hilbert-filtered copy to suppress the upper side band. Using

[10] It was the first demonstration of such SE and capacity – although published at the same time as PAPER11, which surpasses both.

three bands of 5 GBd with 16-QAM constellations and applying power loading to achieve similar performance in all bands, transmission of 60 Gbit/s is achieved over 50 m wireless distance in W-band. Taking into account the capacity loss from a FEC with 7 % overhead, this results in an effective SE of 3.74 bit/s/Hz/pol – by far the highest shown for any transmission beyond 10 m, as is seen in Fig. 2.6.

2.4.2 Modulation formats for robust and flexible links

While increasing capacity is an important use of advanced modulation formats, their characteristics may be tailored to suit specific channels or to allow easy and granular assignment of resources and capacity [64, 92, 93]. Channel coding in combination with the modulation formats may allow further adaptation to specific channel impairments [92–94], e.g., in the case of OFDM, against Doppler effects [95] and deep fading – as shown in PAPER12. Similarly NOMA can be tailored to allow flexible adaptation of the number of users and capacity per user [64, 96–98] – and when combined with multiCAP, as in PAPER13 and PAPER14 allows even more flexibility, without sacrificing capacity.

2.4.2.1 Wavelet coded orthogonal frequency division multiplexing

Wavelet coding has been suggested for zero-redundancy channel coding, especially in fading channels [95, 99–101], where it achieves significant performance gains, while maintaining a simple receiver structure [95, 100, A3]. A sequence of independent and equiprobable information bits is encoded on a sequence of correlated and non-equiprobable symbols, by spreading the information of the bits among many symbols based on a wavelet coefficient matrix (WCM) [95, 100]. As the resulting number of symbols is larger than the number of initial symbols – and hence would require a larger constellation –, symbols are mapped in a many-to-one fashion to simpler and optimized, non-uniform constellations to avoid performance degradation from constellation crowding [100, 101]. At the receiver, decoding may be performed by a simple bank of correlators, thanks to the properties of the WCM, allowing low complexity decoding [99, 101].

While often analyzed in simulations [95, 100, A3], **PAPER12** was the first experimental demonstration of wavelet coding, showing transmission of wavelet coded OFDM. Comparing two wavelet coding schemes with different WCM sizes to uncoded binary phase shift keying (BPSK) and convolutional

coded quadrature phase shift keying (QPSK) – all of the same spectral efficiency –, bit error rate (BER) performance is analyzed over a W-band LOS RoF link of 58 m. The obtained results show that neither convolutional coding, nor wavelet coding with a small WCM manage to offset the resulting increase in constellation size, i.e., convolutional coding with 100 % overhead can not offset the move from BPSK to QPSK and wavelet coding with a 2×8 WCM cannot offset the move to a non-uniform 9-PSK. Wavelet coding with a larger, 2×128 WCM, on the other hand, does outperform uncoded BPSK, even though it requires an 11-PSK constellation, even after many-to-one wavelet symbol mapping. Showing coding gain even in a relatively benign, purely LOS link without any Doppler effects and with only sparse fading, suggests wavelet coding may provide large coding gains under more challenging channel conditions, as suggested by simulations, – but at the same time points towards the requirement for more research on applicable WCM sizes and feasible symbol constellations for actual implementations.

2.4.2.2 Non-orthogonal multiple access and carrierless amplitude phase modulation

In communications over a shared access medium, the number of achievable users, the available capacity per user and the overall system capacity directly depend on the user allocation scheme [64, 96–98, 102]. While traditional user allocation schemes are based on ensuring orthogonality between users – e.g., through the use of different time slots, frequencies or codes [64] –, NOMA allows increasing the number of possible users of a shared medium, by giving up on orthogonality between users [64, 96–98]. As an increasing user density is one of the challenges for 5G mobile networks and beyond, NOMA is considered a candidate for advanced multiple access [64, 103]. Although both power and code domain multiplexing are considered for NOMA, power domain multiplexing is especially interesting for downlink wireless access, as it efficiently and adaptively accommodates users with different received levels of SNR, e.g., from being at different distances or with and without a LOS to the transmitter [97, 102, 104]. In order to multiplex users, their constellations are weighted and added, forming the transmitted superconstellation. At the receiver, successive interference cancellation (SIC) is employed to recover the signal of interest – i.e., if the signal with the largest weight is not the signal of interest, it is decoded first and deducted from the received signal, allowing decoding of the signal with the second largest weight; this process is iteratively repeated until the desired signal is the one with the largest remaining weight [97, 104].

While demonstrations of NOMA exist [104, 105], it has never been combined with multiCAP to obtain the flexibility and adaptability of both. **PAPER13** and **PAPER14** propose such a combination and evaluate its performance in a W-band RoF link. **PAPER13** demonstrates combined NOMA-CAP transmission with six bands and up to two users per band, allowing flexible allocation of capacity between one to twelve users, while achieving a total system capacity of 30 Gbit/s and maintaining good SE. It evaluates BER performance with different power ratios between the users and estimates allowable distance combinations when multiplexing two users per band. **PAPER14** extends the discussion of user power weight ratio and allowable distances, setting it into perspective with the application scenarios. The combination of NOMA and CAP thus shows constant and large system capacity, while able to dynamically adapt to different user densities and scenarios.

Chapter 3

Network integration of hybrid photonic wireless links

Hybrid photonic wireless links not only unlock the enormous capacities discussed in the previous chapter, but also enable significant gains in the implementation of advanced radio access network architectures. The continuing centralization of processing resources from the radio access networks in the central office (CO) and resulting simplification of the radio access unit (RAU) – or remote radio head (RRH) as it is now known – poses new requirements on the connection between the two [24, 25, 106]. As complex functions such as radio frequency (RF) signal generation and demodulation are centralized at the CO, the link to the RRH no longer transports the data signal in baseband, but must transport either a digitized RF signal or the analogue RF signal directly, making transport through optical fiber essential to provide the required capacities [25, 28, 106]. The RRH, at the same time, becomes increasingly simple – potentially completely passive – and performs only the function of optical to electrical (O/E) conversion and amplification and radiation of the RF signal [106, 107]. The continuing shift in network paradigm and the additional requirements for the introduction of fifth generation (5G) mobile services require a re-design of the mobile front- and backhaul with millimeter wave (mmW) hybrid photonic wireless links at its heart [32, 108, 109]. As the signal generation, transport and conversion to RF are closely interlinked for such links, their design must regard not only architectures for the separate network components, but must consider their interrelations and their integration into existing deployed fiber systems or shared deployment with new fiber access networks [32, 106, 107, 110].

In this chapter, section 3.1 briefly reviews the integration of mmW

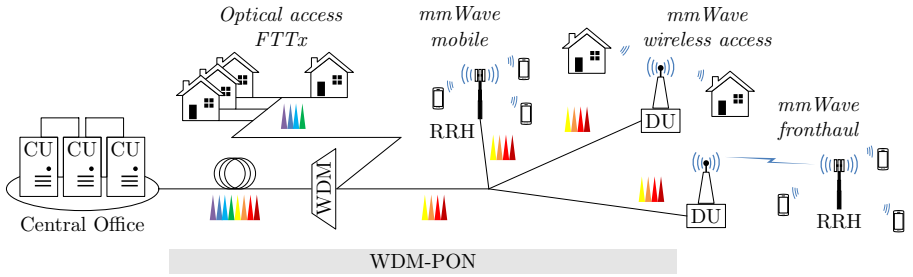

Figure 3.1: Network architecture for mmW wireless access and fronthaul over a shared PON. Acronyms: WDM: wavelength division multiplexing, PON: passive optical network, FTTx: fiber to the x, CU: central unit, DU: distributed unit, RRH: remote radio head.

radio-over-fiber (RoF) links with existing passive optical network (PON) structures and section 3.2 discusses a few considerations with regards to RAU/RRH architectures and their reconfigurability. Finally, section 3.3 looks far ahead to the potential use of optical space division multiplexing (SDM) for flexible and advanced radio access networks (RANs) and discusses a series of works on detailed characterization of SDM components and systems as a prerequisite to their use for mmW RoF links.

3.1 Integration with passive optical networks

As fiber deployment is costly and time consuming [111], it is a possible bottleneck for the roll out of mmW RoF links – making integration with already deployed or co-roll out with fiber networks for other services an interesting option [106, 107, 112]. As PONs are being more widely deployed, integration of mmW RoF links with current and future versions of PONs was suggested – as a wavelength multiplexed overlay to next generation passive optical network (NG-PON) [106, 113, 114], or for integration with future dense wavelength division multiplexing (DWDM) or ultra dense wavelength division multiplexing (UDWDM) fiber access networks [110, 115, 116]. An exemplary centralized radio access network (C-RAN) architecture based on wavelength division multiplexing (WDM)-PON is shown in Fig. 3.1, enabling direct fiber to the x (FTTx), as well as mmW wireless access, fronthaul and mobile services.

In such a network, O/E conversion, i.e., heterodyne up-conversion, is performed either by the distributed unit (DU) or at the RRH and these must therefore be designed to be able to operate in a WDM environment. **PAPER15** and **PAPER16** demonstrate such configurations, where the

DU/RRH receives a DWDM signal from the CO, selects the required channel and up-converts it to RF with the help of a local local oscillator (LO). While the WDM signal in these experiments was based on narrow linewidth external cavity lasers (ECLs), the same configuration is possible with a WDM signal generated by cheaper sources – such as, e.g., commercial enhanced small form-factor pluggable (SFP+) modules, as was shown in **PAPER6** and **PAPER7**. Real-time transmission of a 2.5 Gbit/s signal is demonstrated over 50 m in W-band, showing the impact of the presence of adjacent channels on bit error rate (BER) performance, even though channel selection is performed by an optical filter with >20 dB suppression of the unwanted channels. Featuring a tunable filter, in connection with a tunable LO, makes the DU/RRH reconfigurable, as discussed in the next section.

3.2 Reconfigurable remote radio head architectures

As traffic patterns, network load and user positions change over time, reconfigurability is key to maintain service and to enable the introduction of software-defined networks (SDN) and network function virtualization (NFV) [32, 112, 113]. While centralization of complex equipment at the CO naturally enables reconfigurability of some aspects, for others reconfigurability must be within DU/RRH – e.g., to select a different channel from the WDM signal, change RF frequency or direct the signal to another sector or antenna.

PAPER15 and **PAPER16** allow both WDM channel selection and variable RF frequency by featuring a tunable optical filter for channel selection and a finely tunable LO for up-conversion to control RF frequency. **PAPER17**, on the other hand, introduces switching between different antenna sectors and antennas by including an optical switch inside the DU and demonstrates packet switched RoF transmission.

PAPER18 combines all three degrees of flexibility, i.e., tunable filtering and a tunable LO for channel selection and RF frequency tuning, and optical switching for control over sector or antenna, into a fully reconfigurable DU/RRH. Free WDM channel selection allows efficient resource usage on the optical side and ensures maximum integrability with any type of deployed network, while, similarly, tunability of the RF frequency ensures efficient and flexible radio resource usage. The switching between sectors or antennas enables, e.g., support of high capacity mobility, where a user – or group of users, e.g., on a high speed train – moves through a cell served by a single RRH or through a larger area served by multiple RRHs connected to

the same DU through mmW fronthaul.

Finally, all of the aforementioned reconfigurable DU/RRH implementations featured intelligent control by connected and SDN-ready controllers, hence not only adding an extra layer of flexibility to the C-RAN network, but making it readily available to be included in SDN concepts.

3.3 Optical space division multiplexing

While the use of the spatial domain is common in radio communications and is widely commercially deployed as multiple-input multiple-output (MIMO) systems to increase diversity or extend capacity [23, 26, 117, 118], its use in fiber optics is relatively new and not yet commercially adopted. It has however, progressed at an immense rate and allowed spectacular increases in transmission capacity per fiber, by moving from one spatial channel in single mode fiber (SMF) to more than one hundred in few-mode multi-core fibers (FM-MCFs) [119–122]. As the availability of a large number of channels is of interest also in RANs, the use of optical SDM has been suggested for mmW RoF, both through the use of multi-core fibers (MCFs) [113, 123] and few-mode fibers (FMFs) [60, 124, 125].

While, in the majority, the spatial channels in these fibers have so far been treated as separate channels [60, 113, 124], they offer a range of possibilities when regarded as related channels with potentially different characteristics [123, 125]. In order to make such usage feasible however, a deep and detailed understanding of the effects along the fiber and in any multiplexer (MUX) and de-multiplexer (DMUX) is required. Optical vector network analysis – based on swept-wavelength interferometry – allows getting such an understanding, by allowing fast and precise measurement of the transfer function of fibers, components or systems [126–128]. As a step towards a deeper understanding of optical SDM fibers and components – and thus their potential future use for mmW RoF links –, the following will introduce the concept of optical vector network analysis and include three three original works, where the latter is described and employed for the characterization of a spatial MUX and effects in FM-MCFs, although they are not directly related to mmW hybrid photonic wireless links.

Optical vector network analysis allows measurement of the complex transfer function $\boldsymbol{H}(\omega)$ of an optical device under test (DUT), by placing the latter in one arm of an interferometric structure and interrogating it with a wavelength swept laser [126, 127]. The beating of the output of the interferometer on a photodiode (PD) then generates interference fringes

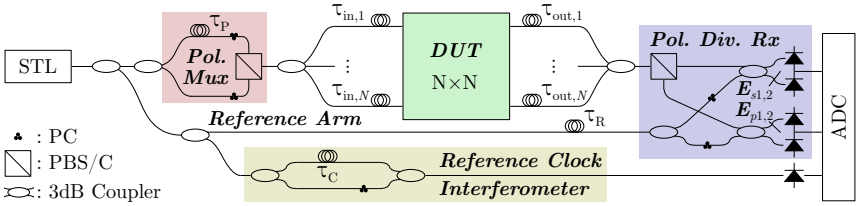

Figure 3.2: Typical setup for a spatially diverse OVNA. Acronyms: STL: swept tunable laser, PC: polarization controller, PBS/PBC: polarization beam splitter/combiner, DUT: device under test, ADC: analog to digital converter.

that contain all information about the transfer function of the DUT [126, 127]. Polarization resolved measurement may be achieved, by extending the interferometric structure with a polarization multiplexer, where one polarization is delayed with respect to the other, as the additional delay will cause the rise of an additional beat frequency [127]. By extension of the same concept, a spatially diverse optical vector network analyzer (OVNA) may be built, by introducing artificial delays at every in- and output and ensuring all possible combinations of delays are distinct and their spacing is larger than the duration of the impulse response of the device [128]. A typical setup for a spatially diverse OVNA is given in Fig. 3.2, showing the two arms of the interferometer – the arm containing the DUT, polarization multiplexer and additional delays and the reference arm – and the polarization diverse receiver. It further shows an auxiliary interferometer structure used to linearize the sweep of the laser – i.e., to correct for any deviations in sweep speed and to convert the linear sweep in wavelength performed by the laser, to a linear sweep in frequency as required for analysis.

To extract the device response from the recorded interferogram, a number of signal processing steps, is required after the aforementioned sweep linearization by re-sampling and re-timing the signal. First, the elements $h_{j,k}(t)$ of the impulse response matrix $\boldsymbol{h}(t)$ are extracted from the Fourier transform of the interferogram by temporal windowing, followed by a separate inverse Fourier transform of each element to reconstruct the frequency response matrix $\boldsymbol{H}(\omega)$ of the DUT. Finally, from the transfer function, singular value decomposition (SVD) [129] allows deriving the modal gains/losses – and thus insertion loss (IL) and mode-dependent loss (MDL) –, while direct analysis of the impulse response or principle state of polarization analysis [130] allow derivation of differential modal group delay (DMD) [131]. The full signal processing chain is shown in Fig. 3.3.

Implementing and using an OVNA, **PAPER19** characterizes a photonic

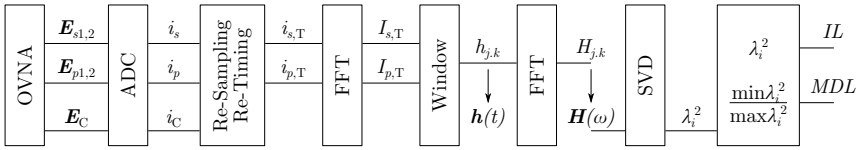

Figure 3.3: Signal processing for optical vector network analysis. Acronyms: FFT: fast Fourier transform, SVD: singular value decomposition, IL: insertion loss, MDL: mode-dependent loss.

lantern spatial MUX for a 36-core 3-mode FM-MCF, measuring its impulse response and calculating IL and MDL. Analysis of the impulse response shows two groups of cores in opposite halves of the fiber, showing strong and negligible mode-mixing respectively, which – in combination with analysis of fiber DMD – is found to result from a fusion splice between the fiber pigtail of the MUX and a short length of FM-MCF. Further, detailed analysis of the effect of splices in FM-MCFs and their impact on system IL and MDL is shown in **PAPER20**: comparison of multiple splices to a reference measurement without any splice, shows the splices to have significant impact on system MDL – in a non-predictable manner, as system MDL is the result of a concatenation of many elements with MDL, with different and unknown associated eigenmodes.[1] The latter confirms that splices may impact system MDL positively or negatively as predicted by previous simulations [133, 134], but, contrary to these simulations, finds no correlation between observed splice IL and impact on system MDL.

Finally, **PAPER21**, for the first time, gives a comprehensive discussion of spatially diverse optical vector network analysis, including a full discussion of the mathematical principle, setup and required signal processing. It expands on the results of PAPER19 and PAPER20 by including the cleaved fiber facet, present in all measurements, in the analysis and provides further discussion on the relevance of the impact of fusion splices in FM-MCF.

Overall, **PAPER19, PAPER20** and **PAPER21** demonstrate that optical vector network analysis is a powerful tool for characterization of SDM systems and components, providing precise measurement of the linear parameters of the DUT. Especially with regards to DMD, a high temporal resolution on the order of 5 ps was achieved, providing detailed knowledge of modal propagation – and thus establishing one of the pre-requisites for the design of SDM components, fibers and systems for use in mmW RoF.

[1] This is due to the fiber being a weakly coupled system and analyzing only few MDL elements – in a strongly coupled system with many MDL elements, the distribution of overall MDL can be described by means of a Gaussian unitary ensemble [132].

Chapter 4

Conclusions and outlook on future work

4.1 Conclusions

The introduction of millimeter wave (mmW) communications is foreseen to play a key role in fifth generation (5G) mobile networks to support the massive growth in capacity, both directly towards the user and even more for wireless fronthaul. The combination with photonics in mmW hybrid photonics wireless links allows taking advantage of the best of both worlds, seamlessly combining transport of large capacity signals over fiber with their up-conversion to mmW radio frequency (RF) carriers. This thesis addressed a range of issues in such mmW radio-over-fiber (RoF) links, from characterizing the wireless channel, over demonstrating low complexity link implementations that may allow rapid deployment and links employing advanced modulation formats for enhanced spectral efficiency (SE), robustness and flexible resource deployment, to regarding integration with fiber optic networks and corresponding architecture considerations.

The research on channel characterization in PAPER1 complements previous research on channel characterization and modeling, by providing measured channel responses in W-band, showing the link is predominantly line of sight (LOS) and confirming applicability of existing models. An estimation of channel capacity and reach was derived in PAPER2 and PAPER7, by combining a modified version of Shannon's capacity limit with an estimation of power budget and receiver sensitivity, providing a tool to evaluate how efficiently any actual link implementation is in its resource usage.

Regarding complexity reduction and deployability, bend-insensitive fiber

(BiF) was shown to allow fiber installation in tight spaces without any impact on signal quality [PAPER3] and links with reduced complexity in both the RF and optical domains were implemented and analyzed for their performance, including an outdoor demonstration over 225 m and real-time transmission [PAPER4–PAPER7, PAPER15, PAPER18].

Further contributions were made with regards to advanced modulation formats, using duobinary signaling to increase SE without necessarily increasing complexity [PAPER8, PAPER9] and achieving large increases in SE, by using multi-band carrierless amplitude phase modulation (multiCAP) and optically generated single sideband modulation [PAPER10, PAPER11]. Wavelet coding was experimentally demonstrated for the first time in PAPER12, as a novel coding scheme to increase the robustness of orthogonal frequency division multiplexing (OFDM) against channel impairments, showing improved performance even under benign channel conditions, suggesting larger gains under more difficult channel conditions. With the introduction of NOMA-CAP, i.e., the combination of multiCAP with non-orthogonal multiple access (NOMA), in PAPER13 and PAPER14, a system allowing flexible allocation of users and capacity was demonstrated, while maintaining maximum overall system capacity and good SE.

Looking at the larger picture, beyond a single mmW RoF link, the research in PAPER15 and PAPER16 showed the integration with passive optical networks (PONs) trough the use of wavelength overlays or dense wavelength division multiplexing (DWDM), demonstrating an architecture that provides unrestricted WDM channel selection and RF frequency tunability through a tunable optical filer and local local oscillator (LO). Expanding on the idea of a reconfigurable remote radio head (RRH), PAPER17 suggested optical switching in the RRH for sector or antenna selection and PAPER18 combined all three degrees of flexibility into a fully reconfigurable RRH, with a controller ready for the introduction of software-defined networks (SDN).

Finally, space division multiplexing in the optical domain was regarded as a step ahead, characterizing a spatial multiplexer (MUX) and mode-mixing effects in few-mode multi-core fiber (FM-MCF) using spatially diverse optical vector network analysis [PAPER19, PAPER20] and providing the first comprehensive discussion of the latter as a means to fully characterize space division multiplexing (SDM) fibers, components and systems in PAPER21 – providing a prerequisite for their use in mmW RoF links.

Overall, this thesis has expanded upon the state of the art of mmW RoF links in a series of aspects, bringing them closer to deployment, by demonstrating real-time transmission with low complexity, showing their potential,

by demonstrating an increase in SE by more than a factor of three and by increasing robustness and flexibility with the first experimental demonstrations of wavelet coded OFDM and NOMA-CAP, and finally showcasing how they enable new radio access network (RAN) architectures, through seamless integration with PONs and dynamic, reconfigurable RRH architectures.

4.2 Outlook on future work

Although research on mmW hybrid photonic wireless links has been very active in the last decade and substantial progress has been made in countless experimental demonstrations towards their deployability and use in 5G networks, many issues require further research – from improving the hardware capabilities in both the optical and RF parts, improving the generation of mmW by optical means, over enabling additional RF functionality based on photonics, further increasing capacity and SE, taking a more holistic view on architectures and network integration, network control and management, to considerations of energy consumption, miniaturization and reliability. One key technology underlying and informing many, if not all, of these issues is photonic integration and co-integration with RF electronics, naturally bringing with it smaller footprints in size and energy consumption and opening a door to many innovative concepts on how photonics can support and enable additional RF functionality, such as, e.g., beam forming, steering and control.

On the most immediate front, there are gains to be obtained from improved hardware – with focus less on increased bandwidth, but rather on noise performance, linearity and modulation efficiency. Such advances may be one step towards improving SE, which at this time is far from what is common at lower RF frequencies – although increases in SE are also still to be found in more efficient and adaptive modulation formats and especially through the introduction of multiple-input multiple-output (MIMO). The development of real-time solutions for down-conversion and carrier and phase recovery, is a further area where improvements are required and will have significant impact on performance and deployability of mmW RoF links.

The introduction of MIMO and related RF technologies is maybe the most interesting and central area where photonics can have direct impact. Massive MIMO with two-dimensional arrays of antennas is seen as a key technology to overcome the challenges of mmW RF, allowing beam shaping and steering as well as improved channel estimates and perceived channel characteristics [26, 29]. To support the required large number of antennas,

photonics allows the generation of many parallel signals and with co-integration of passive photonics, optical to electrical (O/E) conversion and potentially even the antenna itself, allows massive numbers of antennas on small footprints [135, 136]. In the world of analogue RoF, integrated photonics further allows treatment of the optical signals, e.g., through filtering or with the introduction of differential delays – the latter being the key to beam steering [137] –, in both ways well understood from microwave photonics and with novel concepts specifically targeted to solve the challenges of mmW RF [33–35, 138, 139]. Here, the use of optical SDM in the fiber between signal generation and O/E conversion provides further flexibility and opens the path to completely new concepts and ideas [123] – including, for instance, optical remote power delivery through multi-core fibers (MCFs) [140].

On the layer of network layout and design, the introduction of mmW communications and especially the use of beam shaping and steering, bring a change to, or even loss of, the notion of a mobile cell, as obstacles become opaque and thus blocking becomes a major limit to base station selection and association [26, 29]. Further research is thus required on strategies for base station deployment, ensuring coverage and sufficient capacity, while maintaining acceptable cost and complexity [28, 29]. Similarly, strategies for coordination of traffic and dynamic offloading between cells of different sizes and technologies, to whichever provides best service or lowest cost – depending on user and/or network requirements – must be developed [26, 27]. The latter will require the introduction of software-defined radio (SDR), SDN and network function virtualization (NFV), all of which have further roles to play, but which must be combined in a holistic approach to obtain their maximum benefit [141, 142].

Last, but certainly not least and ever more pressing as the usage of mobile data grows, energy consumption and resource usage must be considered. Foreseeing many more mobile devices and, more importantly, with smaller and more densely deployed cells, a multiplication of the number of base stations and access points, maintaining the energy consumption per base station, while increasing capacity, will not be sufficient and ways must be found to drastically reduce energy consumption [63].

Even after many of the above have been addressed, the jury is still out on whether analog mmW RoF will have its place in mobile networks of the fifth or even sixth generation or if digitized RoF can be salvaged for use with mmW carriers through the introduction of eCPRI [143] and the like. There can however, be no doubt that analog mmW RoF has shown

immense capabilities and by doing so has significantly raised the bar for any competing technology – nor can there be doubt that analog mmW RoF will find applications, be they niche or mass deployment.

Finally, in the larger picture, the largest 'gains' may be obtained from a shift in mindset, temporarily putting aside the ways and habits of research in photonics and optical fiber communications and opening up further to the unique challenges of radio communications, absorbing and embracing thought patterns from RF research. As the combination of photonics and RF technology in mmW RoF offers unique possibilities, it is a better and richer understanding of the methods and approaches of *both* worlds, that will actually unlock them.

PAPER1: Channel characterization for high-speed W-band wireless communication links

S. Rommel, L. C. P. Cavalcante, A. G. Quintero, J. J. Vegas Olmos, and I. Tafur Monroy. "Channel characterization for high-speed W-band wireless communication links". In: *Opto-Electronics and Communications Conference 2015*. July 2015, paper PWe.17. DOI: 10.1109/OECC.2015.7340310

Channel Characterization for High-Speed W-Band Wireless Communication Links

Simon Rommel, Lucas Costa Pereira Cavalcante,
J. J. Vegas Olmos, Idelfonso Tafur Monroy
DTU Fotonik, Department of Photonics Engineering
Technical University of Denmark
Kgs. Lyngby, 2800, Denmark
sirem@fotonik.dtu.dk

Alexander Galvis Quintero
GIDATI, Telecommunications Engineering Faculty
Universidad Pontificia Bolivariana
Medellín, Colombia
alex_galvis@comsoc.org

***Abstract*—We present and discuss results from an experimental characterization of the W-band indoor wireless channel, including both large and small scale fading phenomena as well as corresponding channel parameters and their impact on system performance.**

I. Introduction

The ubiquity of mobile devices such as smartphones and tablet computers and the emergence of bandwidth intensive applications—e.g. high-definition video—thereon has created a demand for high-speed wireless data communications at speeds of tens of gigabits per second. With frequency bands below 10 GHz already overcrowded and the available bandwidth therein severely limited, higher frequency bands with broader transmission bandwidths and wireless carriers in the millimeter-wave (mm-wave) region become attractive [1], [2]. Furthermore ultra-wide band (UWB) wireless links are gaining increasing focus in relation to the 'Internet of things' and as an option for replacing short-distance data buses [3].

Optical generation of mm-wave signals and data transmission in the V-band (50 GHz to 75 GHz) [4], [5], W-band (75 GHz to 110 GHz) [6], [7] and even sub-THz [1], [8] have been demonstrated, but it is commonly noted that for increased data-rates and higher transmission quality a better understanding of the wireless channel is a necessity. Most investigations of wireless channel characteristics and corresponding models have focused on frequencies in and below V-band or concerned themselves only with estimations of path loss [9], [10].

In this paper we show a characterization of the indoor wireless channel in the W-band, including large- and small-scale fading analysis. The paper is organized as follows: Section II reviews some applicable channel modelling theory, Section III presents the experimental results and finally Section IV concludes the paper.

II. Wireless Channel Modelling

Characterization of propagation phenomena affecting communication signals in wireless systems is an important issue since it forms the base for defining the signal processing required to enhance the system performance. Fading channel manifestations can be classified in two groups: large-scale fading and small-scale fading [11]. The former is mainly due to the distance between the antennas and the environment in which the system operates, resulting in signal attenuation. This attenuation is characterized statistically by calculating its mean in dependence on distance (path loss) and variations around this mean (shadowing). A variety of models for path loss estimation exist [12], two of which will be used for comparison in this paper. The free-space loss model (FSL, referred to as Friis model) defines path loss as in (1), where d is the distance between transmitting and receiving antenna, f the carrier frequency and c the speed of light in vacuum.

$$FSL_{[dB]} = 10\log\left(\left(4\pi df/c\right)^2\right) = 20\log\left(4\pi df/c\right) \qquad (1)$$

Another widely model used is the generic empirical path loss model (GEPL) in (2) where n is the path loss exponent, d_0 is a reference distance and L_0 is the loss measured at d_0 or estimated using the Friis model.

$$GEPL_{[dB]} = 10n\log\left(d/d_0\right) + L_0 \qquad (2)$$

Shadowing is a random variable with log-normal distribution and manifested as a loss value additive to path loss, making it easy to calculate from experimental data [12].

The small-scale fading behavior of a channel is described by a number of characteristics: the frequency response of the channel and its comparison with the signal spectrum determine if the fading is frequency-selective or not. The time response of the channel shows how multipath phenomena affect reception and communication in general. The main parameters to characterize small-scale fading are coherence bandwidth (B_c), root mean squared delay (τ_{rms}), Doppler shift (f_d) and coherence period (T_c) [11], [12].

III. Experimental Results

A. Measurement Setup

The setup employed for the channel characterization is depicted in Fig. 1 and consists of a Vector Signal Generator (VSG) followed by a frequency sextupler on the transmitting side for W-band signal generation, while at the receiving side the signal is down-converted using a harmonic mixer driven by a 4 GHz to 6 GHz local oscillator (LO) and received with an electrical spectrum analyzer (ESA). Pyramidal horn antennas with a gain of 25 dBi are employed for radiation and capture at the transmitter and receiver respectively. Given the experimental setup and operating band, it is difficult to obtain

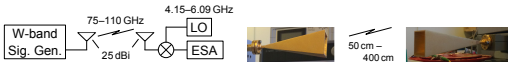

Fig. 1. Experimental setup for the channel characterization

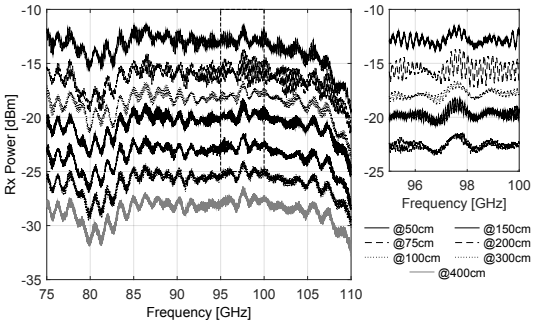

Fig. 2. Received power over frequency at different distances; inset: close up, showing the aggregated effect of path loss, shadowing and small-scale fading

the frequency response of the antennas in order to perform a rigorous decoupling and hence a flat response over the entire sounded band was assumed.

The spectrum of the W-band is swept with a resolution of 1 MHz, using a single-tone method as described in [13]. Received power levels are recorded for analysis and channel characterization at distances between 0.5 m and 4 m. The received power over distance and frequency is shown in Fig. 2, giving a clear indication of the distance dependency of path loss; the frequency limitations of the employed equipment cause the reduced performance at the higher end of the analyzed frequency range.

B. Large-Scale Fading Analysis

A comparison between experimentally obtained W-band path loss values and those predicted by Friis model is shown in Fig. 3(a) and (b) for distance and frequency dependence respectively. For the distance dependency of path loss the general behavior is in good agreement with theoretical curves, but a certain offset is observed. The error has a mean of 2.1 dB and 4.3 dB at 75 GHz and 110 GHz respectively, which is a good approximation considering that Friis model is a very optimistic model even for a point-to-point wireless link.

From the experimental data the path loss exponent (n) and shadowing parameter (σ_S) were calculated, using the procedure described in [12]. Best approximations for the observed path loss at 75 GHz and 110 GHz are obtained from GEPL with $n \approx 2.2$ and $n \approx 2.5$ respectively, confirming the expectations for an indoor environment and a directive link [12]. Experimental data shows that under these conditions distance impacts path loss more than frequency; going from 0.5 m to 4 m implies an increase in path loss between 13.1 dB and 16.2 dB depending on frequency. The shadowing parameter σ_S is found to be very small at 0.05 dB and 0.12 dB for 75 GHz and 110 GHz respectively, owing to the short distances and high directivity of the link.

The observed frequency dependency of path loss in Fig. 3(b) also confirms the theoretical predictions, indicating an increase in path loss of 3.8 dB at 0.5 m, 3.3 dB at 2 m and 1.9 dB at 4 m if the frequency is increased from 75 GHz to 110 GHz. Such frequency dependent variations in path loss can easily be compensated in a transmission system employing narrow-band signals, but the simple large-scale analysis is insufficient to describe the channel effects on wide and ultra-wide band signals as expected for future W-band transmission systems.

C. Small-Scale Fading Analysis

Signal bandwidths for W-band systems—especially such exploiting the advantages of photonic upconversion—will be of several GHz and hence the required channel can be considered as UWB. Such channels are characterized by a multipath-rich profile, but considerably lower power levels for each multipath component. After obtaining the S_{21} parameter from the measurements, analysis using the IFFT and the Hermitian method [13] is performed and the frequency response of the channel calculated. Fig. 4(a) and (c) show the frequency response (single sideband) for distances of 0.5 m and 4 m. The frequency response of the channel is very uniform over the whole band, except for the area near the operational limits of the devices and in the region around 80 GHz. The average magnitude of the channel response at 0.5 m is −68 dB and is strongly determined by path loss, due to the high directivity of the link. The regular behavior of the small-scale fading component smoothly defines an approximate coherence bandwidth of $B_c = 2$ GHz (see Fig. 4(a)) and indicates a theoretical delay of $\tau_{rms} = 0.5$ ns [13].

It is however necessary to also regard the time response of the channel as shown in Fig. 4(b) and (d) where magnitude has been normalized and which represents a good approximation to the power delay profile (PDP) of the channel [13]. The time response has a very good time-resolution (fractions of a nanosecond), which—translated into space domain—makes it possible to distinguish reflective surfaces on a scale of centimeters [13]. If a threshold of −60 dB is assumed to select the multipath components that are significant, by calculation $\tau_{rms} = 0.16$ ns and $B_c = 6.3$ GHz are obtained for $d = 0.5$ m and $\tau_{rms} = 0.40$ ns and $B_c = 2.5$ GHz for $d = 4$ m. At greater link distances, distances traveled by different multi-path components are larger and delays grow (more reflective surfaces affecting propagation), whereby the coherence bandwidth decreases. This behavior significantly impacts system performance since any signal with a bandwidth larger than the coherence bandwidth will be affected by frequency selectivity. Thus for signals with several GHz of bandwidth mitigation of channel effects is a necessity. A modulated signal with 6 GHz bandwidth might see quasi flat fading at a transmission distance of 0.5 m, but at 4 m would encounter severely frequency selective fading, causing an irreducible degradation of signal-to-noise ratio (SNR) and bit error rate. The threshold of −60 dB may—considering path loss and receiver sensitivity—be low for the present link and consequently all significant multipath components might belong to the first tap in the PDP (resulting in a coherence bandwidth ∼25 GHz); with the introduction of point to multipoint transmission however coherence bandwidths become significantly smaller than those calculated.

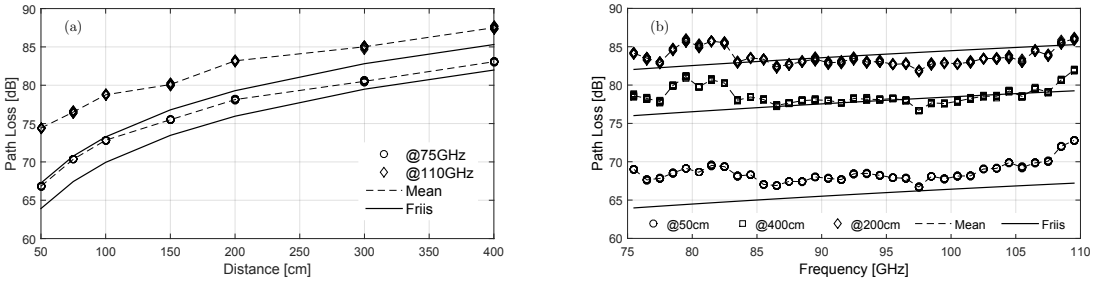

Fig. 3. Path loss over (a) distance and (b) frequency compared to predictions based on the Friis transmission equation

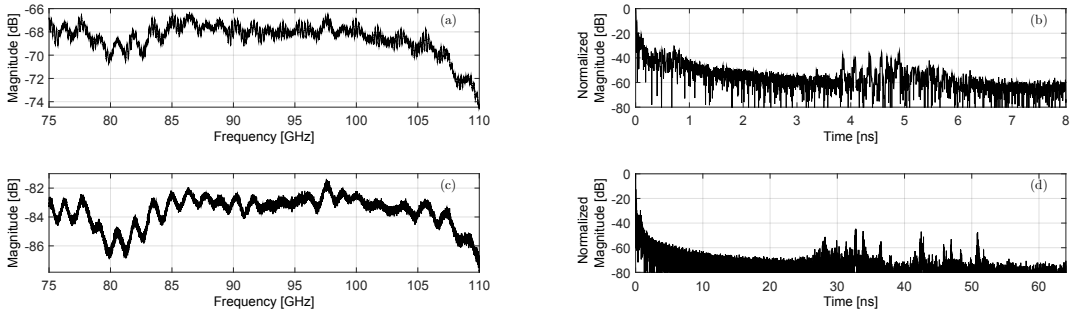

Fig. 4. Wireless channel frequency ((a), (c)) and time ((b), (d)) response at 50 cm ((a), (b)) and 400 cm ((c), (d)) transmission distance

IV. Conclusions

Channel characterization for a mm-wave link in W-band was performed, including path loss, shadowing and multipath parameter calculations from experimental data. It is clear that some mitigation techniques must be applied even for a highly directive link, taking into account the large signal bandwidths required for high data rate transmissions. SNR degradation caused by path loss and shadowing must be compensated, potentially by applying some type of diversity to obtain additional uncorrelated estimates of the signal. To overcome the observed frequency selectivity, pre-processing (spread spectrum, OFDM) may be performed or equalization will be needed. In the case of photonic upconversion, the effects of the optical channel must be regarded in combination with those of the wireless channel discussed here.

Acknowledgments

This work was supported by mmW-SPRAWL, EC IPHOBAC-NG and Science without Borders.

References

[1] T. Nagatsuma *et al.*, "Millimeter- and THz-wave photonics towards 100-Gbit/s wireless transmission," in *Proc. 23rd Annu. Meeting IEEE Photon. Soc.*, Nov. 2010, pp. 385–386.

[2] M. García Larrodé *et al.*, "Transparent transport of wireless communication signals in radio-over-fibre systems," in *Proc. 10th Eur. Conf. on Netw. and Opt. Comm.*, Jul. 2005, pp. 83–90.

[3] S. Hamada, A. Tomiki, T. Toda, and T. Kobayashi, "Wireless connections within spacecrafts to replace wired interface buses," in *IEEE Aerospace Conference*, Mar. 2013.

[4] W.-J. Jiang *et al.*, "40 Gb/s RoF signal transmission with 10 m wireless distance at 60 GHz," in *OFC/NFOEC 2012*, Mar. 2012, p. OTu2H.1.

[5] A. Lebedev *et al.*, "Simultaneous 60-GHz RoF transmission of lightwaves emitted by ECL, DFB, and VCSEL," *IEEE Photon. Technol. Lett.*, vol. 26, no. 7, pp. 733–736, Apr. 2014.

[6] X. Pang, A. Lebedev, J. J. Vegas Olmos, and I. Tafur Monroy, "Multigigabit W-band (75-110 GHz) bidirectional hybrid fiber-wireless systems in access networks," *J. Lightw. Technol.*, vol. 32, no. 23, pp. 3983–3990, Dec. 2014.

[7] X. Li *et al.*, "Fiber-wireless transmission system of 108 Gb/s data over 80 km fiber and 2x2 multiple-input multiple-output wireless links at 100 GHz W-band frequency." *Opt. Lett.*, vol. 37, no. 24, pp. 5106–5108, Dec. 2012.

[8] S. Koenig *et al.*, "100 Gbit/s wireless link with mm-wave photonics," in *OFC/NFOEC 2013*, Mar. 2013, p. PDP5B.4.

[9] H. Xu, V. Kukshya, and T. S. Rappaport, "Spatial and temporal characteristics of 60-GHz indoor channels," *IEEE J. Sel. Areas Commun.*, vol. 20, no. 3, pp. 620–630, Apr. 2002.

[10] A. P. Garcia *et al.*, "60 GHz in-cabin real-time channel sounding," in *ChinaCOM 2009*, Aug. 2009, pp. 1–5.

[11] B. Sklar, "Rayleigh fading channels in mobile digital communication systems - Part I: characterization," *IEEE Commun. Mag.*, vol. 35, no. 7, pp. 90–100, Jul. 1997.

[12] T. S. Rappaport, *Wireless Communications: Principles and Practice*, 2nd ed. Prentice Hall, 2002.

[13] I. Oppermann, M. Hämäläinen, and J. Iinatti, Eds., *UWB: Theory and Applications*. Wiley, 2004.

PAPER2: On the capacity of radio-over-fiber links at the W-band

L. C. P. Cavalcante, **S. Rommel**, S. Rodriguez, J. J. Vegas Olmos, and I. Tafur Monroy. "On the capacity of radio-over-fiber links at the W-band". In: *Optical and Quantum Electronics* 48.5 (May 2016), paper 279. DOI: 10.1007/s11082-016-0554-6

Opt Quant Electron (2016) 48:279
DOI 10.1007/s11082-016-0554-6

On the capacity of radio-over-fiber links at the W-band

Lucas Cavalcante[1] · Simon Rommel[1] · Sebastian Rodriguez[1] · J. J. Vegas Olmos[1] · Idelfonso T. Monroy[1]

Received: 24 November 2015 / Accepted: 6 April 2016

Abstract In this work we discuss on the channel capacity of mm-wave Radio-over-Fiber (RoF) experimental transmissions at the W-band (75–110 GHz) over distances up to 300 m and bandwidth up to 20 GHz. In addition to an updated state-of-the-art on RoF demonstrations at such a promising frequency range, we provide a set of trade-off maps in terms of crucial resources on the design of W-band RoF links. The proposed framework offers a unified view for answering how fundamental spectrum resources can be optimally utilized, and how far we are from overcoming the challenge of offering seamless convergence between optical-fibers and wireless links.

Keywords Radio-over-Fiber · W-band · Channel capacity

1 Introduction

A driving force in the communication technology is the role of bandwidth. It refers to the physical means by which a signal carries information (Internet Society 2010). This notion plays a critical role as the information infrastructure is developed. Like any other commodity, bandwidth can be plentiful or scarce relative to the need for it. With the growth of telecommunications and computing, communication bandwidth has become increasingly scarce.

Migration towards millimeter-wave radio frequencies (RF) (30–300 GHz) and integration between fiber-optic and wireless communications systems in the 'last mile' is currently considered as the most promising solution for alleviating the bandwidth shortage of the access interface. Therefore, the lower capacity of wireless systems needs to be

✉ Lucas Cavalcante
luca@fotonik.dtu.dk

[1] Department of Photonics Engineering, Technical University of Denmark, Ørsted Plads, Bld. 343, 2800 Kongens Lyngby, Denmark

Published online: 13 April 2016

increased to match the continuously increasing bandwidth of fiber-optic access systems. As W-band signal generation becomes more practical and affordable by the use of photonic technologies, and RF oscillators and modulators with superior RF properties become available, more attention has been given to RoF systems based on such a frequency range. However, whilst in ongoing expansion, the state-of-the-art in W-band RoF reports still lacks a unified framework for evaluation of how efficiently the radio links and spectrum resources are being utilized.

One way to inquire about such an important aspect is to consider Shannon's capacity limit theorem to assess on the tradeoff between bandwidth and Signal-to-Noise-Ratio (SNR) of band-limited systems (Shannon 1948). Based on that hypothesis, recent reports on capacity analysis of mm-wave wireless links provide guidelines for link design supporting transmission capacity beyond 100 Gbps (Dogadaev and Monroy 2011; Dogadaev et al. 2012). They provide recommendations on the required values of signal bandwidth, input power to a transmitter, antenna gain, and link distances in order to achieve 100 Gbps wireless transmissions taking into account the role of crucially relevant aspects on the design of RoF systems such as antenna directivity, frequency spectrum, modulation formats etc.

Still, such a variety of design parameters can be allocated in an uncountable number of ways. And to the best of our knowledge there's no objective criterion to evaluate how efficiently such resources are being utilized with regards to how much capacity it is provided with them. In this work we propose an analysis framework for wireless systems based on a modification of the Shannon limit. We also perform a proof of concept by investigating several of the most recent reports on the state-of-the-art of W-band RoF demonstrations. Our findings confirm the prediction that a combination of advanced modulation formats and spatial diversity are crucial factors for combating capacity losses.

2 Methodology

The current investigation aims to compare how efficiently the radio spectrum has been utilized in some of most recent experimental W-band RoF demonstrations. According to Beas et al. (2013) the overall performance assessment of a RoF system must take into account the figures of merit of different subsystems, namely:

a. Cost, simplicity, and power consumption of the central station (CS) and the base stations (BS);
b. Available RF power after optical distribution and photo-detection;
c. Phase noise due to spectral instability of the mm-wave carriers, in case of coherent setups that depend on phase information;
d. Transmission integrity, evaluated in terms of bit-error-rate (BER) and error vector magnitude (EVM) metrics;
e. Capability of the system to increase coverage and capacity to meet usage demand without a significant cost increase.

It is hence a corollary that no single parameter can account for grading the performance of RoF systems in a unifying manner. However, a slight modification to Shannon limit is proposed in Struzak (2002) to account for losses in capacity due to lack of spectrum isolation leading to diminished SNR of a specific link. Defined as the *isolation parameter*, such an index can be used to show how various design factors of a communication link can

be combined to control its capacity loss, and how much the link should be isolated to keep such losses within acceptable limits. Regarding specifically the wireless channel, which is the bottleneck for seamless convergence of hybrid fiber-wireless solutions, as previously discussed, such an isolation parameter can be employed as a measure of effective use of the radio links and spectrum resources.

According to the Shannon limit (Shannon 1948), the maximum amount of information that can be transmitted with an arbitrarily small error rate equals the product of the transmission time and channel capacity defined as

$$C = B\log_2(1+q), \tag{1}$$

where B is the channel bandwidth (in hertz), and $q = S/N$ is the signal-to-noise power ratio at the receiver input. This equation has universally been accepted as useful reference to which various practical communication systems can be compared, even if they do not strictly follow all the conditions assumed by its formulation.

It is proposed in Struzak (2002) to differentiate between two components of the noise at the receiver input: the intrinsic noise N and the environmental interference noise I. The intrinsic or residual noise N is the noise that would be observed if all environmental radiation sources were removed or switched off, or if the link were absolutely isolated. The environmental noise component I is the difference between the total noise and the residual noise. Then, the isolation index a is defined as the power ratio of the intrinsic noise to the total noise:

$$a = \frac{N}{I+N}. \tag{2}$$

It is a dimensionless variable, conveniently confined between one and zero. One represents a hypothetical isolated radio link with $\mathrm{I/N} \rightarrow 0$, whose operation does not depend on the environment. Zero represents a link whose operation is completely dominated by the environmental noise component, leading to $\mathrm{N/I} \rightarrow 0$. All practical cases fall between these extremes. As the original Shannon's formula don't consider the environmental noise, Eq. (1) can be modified so instead of $q = \mathrm{S/N}$, the channel capacity could be expressed in terms of $aq = \mathrm{S/(N + I)}$. Thus:

$$C^* = B\log_2(1+aq). \tag{3}$$

Just as Shannon's original formula, Eq. (3) represents the upper limit imposed on the link capacity. The capacity is largest when the link is fully isolated, i.e. $a \rightarrow 1$, approaching the original Shannon limit. For instance, a radio link with $a \rightarrow 1$ and signal equaling intrinsic noise ($q = 1$) is theoretically capable of transmitting of one bit of information per second per hertz. However, for $a = 0.1$ its capacity drops to $\log_2(1.1) = 0.14$.

From (1) and (3) it follows that the *capacity loss* can be defined as the difference between the potential capacity of the radio link and its actual capacity:

$$\Delta C = C - C^* = B\log_2\frac{(1+q)}{(1+aq)}. \tag{4}$$

Equation (4) can be used then to define the *relative capacity loss* as

$$\frac{\Delta C}{C} = 1 - \frac{\log_2(1+aq)}{\log_2(1+q)}, \tag{5}$$

a dimensionless numerical value confined between 0 and 1 that decreases with the isolation index of the link. This equation will be used further on for the calculus of the isolation

parameter for recent experimental demonstrations of RoF systems on the W-Band frequency range.

The SNR in the far field region of a line-of-sight (LOS) wireless link with one transmitter and one receiver can be computed in dB using the link power budget (Proakis and Manolakis 2007; Rommel et al. 2015) as:

$$q = P_T + G_T + G_R - L_{FS} - IL - (N_0 + 10log_{10}B + NF), \tag{6}$$

where P_T is the total transmitter power of a signal with bandwidth B, G_T and G_R are antenna gains on the transmitter and receiver sides correspondingly. IL represents implementations losses, N_0 is the Johnson–Nyquist noise and NF represents the system's noise figure (may these three latter terms, here assumed as constants, not to be confused with the intrinsic and environmental noises, N and I, for the calculation of the index a as in Eq. (2)). Path loss L_{FS} can be determined by the Log-distance path loss model for the free space propagation as function of the distance d between transmitter and receiver antennas, and the propagating frequency f, according to:

$$PL = 20\log_{10}\frac{4\pi f d_0}{c} + 10n\log_{10}\frac{d}{d_0}, \tag{7}$$

where d_0 is a reference point situated in far field, c is the speed of light, and n is the path loss exponent, set as 2 in free space.

Using Eq. (7) in Eq. (6), and Eq. (6) in Eq. (1), one can calculate, using the Shannon limit as an upper bound, how much capacity can be achieved for a given link as a function of the terms listed in Table 1.

If one fixes three of those, say items (a), (c) and (f), the result is a tridimensional space with basis given by parameters (b), (d), and the actual computed capacity. In such a space, Shannon's capacity limit can be visualized as a tridimensional surface. The combination of specific parameters corresponding to experimental setups can be regarded as points, of which orthogonal projections onto the 'capacity surfaces' will arise as the *capacity losses*, as defined in Eq. (4). These values can be used to calculate the index a, following Eq. (5), according to:

$$a = \frac{1}{q}\left[(1+q)^{\left(1-\frac{\Delta C}{C}\right)} - 1\right]. \tag{8}$$

Once the a parameter for a specific link is known, one can calculate the theoretical increase in frequency band ΔB that would be required in order to compensate for the equivalent capacity loss ΔC. Although such an increase is not always possible in practice, ΔB may serve as criterion in evaluating alternative frequency plans, spectrum management rules, and frequency assignment algorithms from the viewpoint of efficient use of the available

Table 1 Required parameters for the calculation of channel capacity

Variable	Parameter	Variable name
a	Transmitted power	P_T (dBm)
b	Signal bandwidth	B (GHz)
c	Antenna gains	G_T, G_R (dBi)
d	Achieved range	d (m)
e	Propagation frequency	f_C (Hz)

spectrum resources. Through Eq. (4), the capacity loss ΔC can be related to an equivalent bandwidth loss ΔB by:

$$\Delta B = \frac{\Delta C}{\log_2(1+aq)}. \tag{9}$$

We expect that alongside with a common ground for measuring how efficiently the spectrum of W-band RoF experiments is being utilized, such a framework can also be used for predicting the outcome of virtually any wireless-based setup in terms of spectrum efficiency under different conditions of SNR.

3 Results and discussion

Previous studies on the capacity analysis for high-speed mm-wave hybrid fiber-wireless communications [4; 4] discussed the great potential of mm-wave, particularly for the W-Band, to provide 100 Gbps wireless links using existing technology. However, the state-of-the-art in W-band RoF still lacks a unified framework for the evaluation of the efficiency of spectral use. Based on such a hypothesis that the efficiency of a linkcan be parametrized in terms of major common attributes, multiple reports on W-band RoF demonstration have been investigated upon the methodology described in the previous section.

In the next sub-section we provide a case-study for the proposed method. We utilized a recent experimental demonstration performed in our facilities of 15 km fiber plus 100–225 m wireless transmission of 2.5 Gbps NRZ signal on a carrier at 86 GHz. We proceed by generalizing the analysis over the most recent reports on W-Band RoF transmissions, followed by a discussion of the observed results.

3.1 Case-study

Figure 1 shows the experimental setup for the W-band RoF transmission based on optical baseband generation and heterodyne photonic up-conversion with low complexity in the radio-frequency domain. A 2.5 Gbit/s $2^{15}-1$ bit long pseudo-random bit sequence (PRBS15) non-return-to-zero (NRZ) signal from a pulse pattern generator (PPG) is used to modulate an optical signal which is amplified and transmitted through a combination of

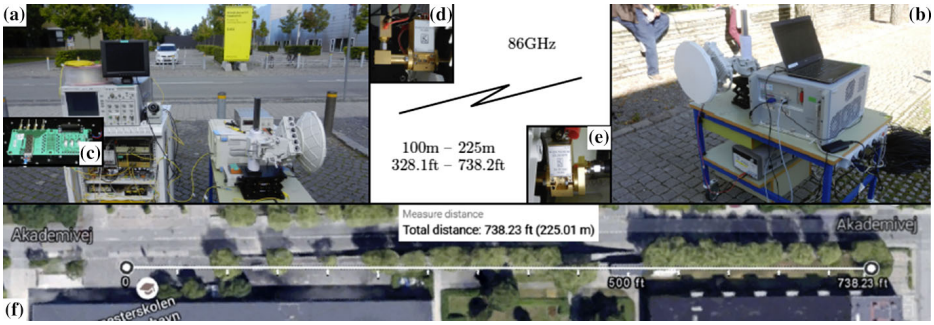

Fig. 1 Experimental setup for 100–225 m wireless transmission of 2.5 Gbps NRZ at 86 GHz using pair of 48 dBi parabolic antennas and heterodyne photonic up-conversion. Default parameters shown in Table 1

10 km ITU-T G.652 standard single-mode fiber (SMF) and 5 km ITU-T G.657.B3 bend insensitive fiber (BIF). The resulting 86 GHz RF signal is amplified by 8 dB after photo-detection before being transmitted over distances of 100–225 m using a pair of parabolic antennas with a gain of 48 dB each. At the receiver side a low noise amplifier (LNA) provides a 40 dB gain before signal down-conversion by a Schottky diode based envelope detector (ED) with a nominal 3 dB bandwidth of 3 GHz. The baseband signal is filtered with a 1.8 GHz Bessel filter to limit noise bandwidth and recorded on a digital storage oscilloscope (DSO). Error free transmission was achieved at all distances with recorded sequences of a total length >25 Mbit, suggesting a BER on the order of 10^{-7} or lower. Following the schematics presented in Tables 1 and 2 contains a summary of the parameters' values for this setup.

Such a set of values can be used to calculate the value of a just as described in the previous section according to Eq. (8). The result is $a = 0.0033$, which can be considered a relatively low value among the evaluated setups in this work, as will be discussed with more details in the next sub-section. It can be explained by the fact that because we had observed a considerably low BER, we could therefore have used even wider bandwidths, more complex modulation formats, farther link range, and lower transmitted power or antenna gains, yet having error free transmission. From this point of view, such a low a parameter suggests an inefficient use of the available bandwidth regarding the abundant conditions in terms of SNR.

3.2 Application

Among a wide variety of experiments, we chose to further consider those with distance ranges above 2 m (with exception of a world record with 1.7 km range (Xu et al. 2015)), and signal bandwidth below 35 GHz (so it could be framed solely within the W-band range), resulting in a set of seven setups to be evaluated. Although we could not obtain information about the exact values on some of the parameters for all the reports, we expect that approximated assumptions based on standard technology commonly found in the state-of-the-art should not lead to broad fluctuations of the index a on more than 0.1 order of magnitude. Table 3 contains a summary of the default parameters for these setups.

Figure 2 displays the computation of channel capacity in terms of channel bandwidths B from 1 GHz to 20 GHz and transmission distances d from 1 m to 300 m, assuming operational frequency f_C of 86 GHz and transmitted power P_T of 0 dB, according to Eqs. (1), (6) and (7). Using Shannon limit as an upper bound, the two observed surfaces stand for illustrating the achievable capacity by adopting antenna gains of 25 and 48 dBi.

Table 2 Default parameters for the experimental setup shown in Fig. 1

Variable	Parameter	Variable name	Value
a	Transmitted power	P_T (dBm)	0
b	Signal bandwidth	B (GHz)	5
c	Antenna gains	G_T, G_R (dBi)	48
d	Achieved range	d (m)	225
e	Propagation freq.	f_C (Hz)	86
–	Thermal noise	N_0 (dBm/Hz)	174
–	Implem. losses	I_L (dB)	6
–	Noise figure	NF (dB)	6

Table 3 Summary of the default parameters for the seven analyzed experimental setups

	{i} Rommel et al. (2015)	{ii}	{iii} Li et al. (2015a)	{iv} Li et al. (2015b)	{v} Diamantopoulos et al. (2015)	{vi} (Pang et al. (2013)	{vii} Xu et al. (2015)
P_T (dB)	0	0	2	0[a]	0	0	2[a]
G_T,G_R (dBi)	48	48	48	23	25[a]	25	25
max. d (m)	70	225	300	3	2.5	15	80
f_C (GHz)	87	86	95.5	92.5	103.5	81.4	87
B (GHz)	5	5	20	10	20	16	10
C (Gbps)	2.5 NRZ	2.5 NRZ	20 QPSK per Pol., per Carr.	10 QPSK per Pol.	40 16-QAM OFDM	16 QPSK	10 QPSK per Pol.
a (n.d.)	0.0023	0.0033	0.0101	0.0170	0.0326	0.0447	0.2987

Values for *thermal noise*, *implementation losses* and *noise figure*, assumed as $N_0 = 174$ dBm/Hz, $I_L = 6$ dB and $NF = 6$ dB, respectively, for all of them

[a] Value not reported; assumed value based on standard technology commonly found in state-of-the-art

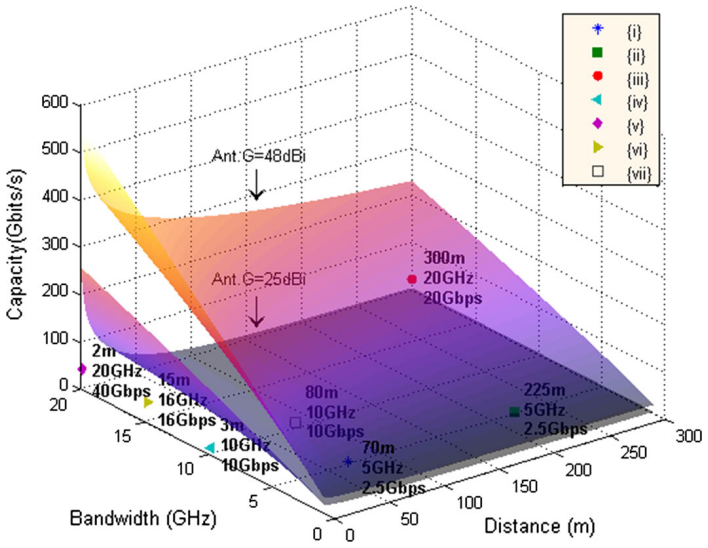

Fig. 2 Channel capacity for operational frequency of 86 GHz, and 0 dBm transmitted power. Distances up to 300 m are converted into SNR values. Baseband bandwidths up to 20 GHz are considered

Clearly, the higher the gain provided by the antennas, higher the achievable capacity of the link. The points {i–vii} are plotted according to their attributes, as listed in Table 3, following the tuple (d, B, C). The case-study setup, for instance, can be observed as the point represented by the legend {ii}, at the coordinates (225, 5, 2.5), meaning a distance of

225 m, an utilized bandwidth of 5 GHz, and a delivered capacity of 2.5 Gbps. Such a "map" allows visualization of how fundamental resources can be optimally utilized and how far the state-of-the-art is from overcoming the challenge of offering seamless convergence between optical-fibers and wireless links.

Proceeding with the analysis, as described in the Sect. 2, the values of the index a for all the evaluated setups have been obtained. It is possible from there to assess their rates of relative capacity loss $\Delta C/C$ and loss in spectral efficiency $\Delta C/B$ (bits/s/Hz) as functions of SNR for fixed values of a, as shown in Fig. 3a, b, respectively. In both cases, the highest blue curve represents the experiment {i}, in which the lowest value of a has been obtained, whereas the lowest red curve represents the experiment {vii}, in which the highest value of a has been obtained.

As previously noted in the Sect. 3.1, the relatively low value of a for the setup {i}, as for the setup {ii}, can be explained by the fact that because a considerably low BER had been observed, one could therefore have used even wider bandwidths, more complex modulation formats, farther link range, and lower transmitted power or antenna gains, yet having error free transmission. From this point of view, such a low a parameter suggests an inefficient use of the available bandwidth regarding the abundant conditions in terms of SNR. In the same sense, the higher-order modulation format for the experiment {v} results it a higher value for a than for the experiments {i–iv}, but the short distance link can explain why it's lower than for the experiments {vi, vii}.

Regarding Fig. 3a, without loss of generality, one can notice by observing any particular curve the general trend of less capacity being lost as higher SNR becomes available. For limited values of SNR, say up to 30 dB (see vertical black lines), one can conclude that insofar as the index a decreases less the increasing of SNR can compensate for capacity loss. Now regarding Fig. 3b, one can clearly observe that lower the index a, higher is the loss in spectral efficiency with the increasing of SNR.

In general, we conclude that a high index a should be regarded as a fundamental parameter for granting that any wireless-based link should be considered as efficiently utilizing its resources. Of course, no single parameter can account for scoring the performance of RoF systems in a unifying manner due to its large complexity. Nevertheless, this approach may help in rational use of limited resources of the radio frequency spectrum and in solving problems of spectrum management that suffer from a lack of appropriate

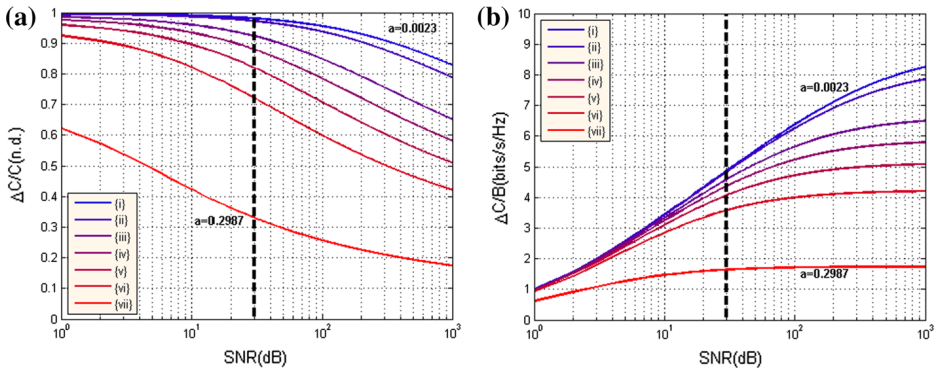

Fig. 3 **a** $\Delta C/C$ for $q = 1{:}1000$ over different values of a; **b** $\Delta C/B$ for $q = 1{:}1000$ over different values of a. *Black vertical lines* corresponding to the threshold of 30 dB SNR

objective criteria. If such a viewpoint is accepted, frequency plans will require revision to minimize spectrum misuse.

4 Conclusions

Previous research has addressed the analysis on the capacity of W-band RoF links without accounting for how efficiently fundamental resources on wireless links are being deployed. In this work we integrate a modification of the Shannon limit with the power budget for free space propagation in order to generate a grading system to assess wireless-based system efficiency. The results are compatible with those from other parameters as level of modulation formats and spatial diversity, achievable range, power savings by use of directive links etc., although within a composite single-unit metric. This approach may help in rational use of limited resources of the radio frequency spectrum and in solving problems of spectrum management that suffer from a lack of appropriate objective criteria. To the best of our knowledge there is to date no report on any unified framework for W-band RoF design analysis. If such a viewpoint is accepted, frequency plans will require revision to minimize spectrum waste. However, some limitations are worth noting. The method suggested in this work is based on a coarse binary logic of whether the transmission has or not been transmitted under the proposed limits for BER. We believe that such an important factor should have more weight on the calculation of the proposed index, allowing the contribution offered by DSP techniques and coding schemes to be considered.

Acknowledgments Lucas Cavalcante thanks the Science without Borders program. This work was partly funded by the DFF FTP mmW-SPRAWL and EC IPHOBAC-NG projects.

References

Beas, J., Castanon, G., Aldaya, I., Aragon-Zavala, A., Campuzano, G.: Millimeter-wave frequency radio over fiber systems: a survey. IEEE Commun. Surv. Tutor. **15**(4), 1593–1619 (2013)

Diamantopoulos, N.P., Inudo, S., Yoshida, Y., Maruta, A., Kanno, A., Dat, P.T., Kawanishi, T., Maruyama, R., Kuwaki, N., Matsuo, S., Kitayama, K.: Mode-division multiplexed W-band RoF transmission for higher-order spatial multiplexing. Optical Fiber Communication Conference, p. W4G.2 (2015)

Dogadaev, A., Lavrinenko, A.V., Monroy, I.T.: Capacity analysis for high-speed terahertz wireless communications. International Conference on Infrared, Millimeter, and Terahertz Waves, pp. 1–2 (2012)

Dogadaev, A., Monroy, I.T.: Challenges and capacity analysis of 100 Gbps optical fibre wireless links in 75–110 GHz band. IEEE Photonics Conference, pp. 268–269, p. TuJ2 (2011)

Internet Society: "Growing Pains: Bandwidth on the Internet", Briefing Papers (2010). http://www.internetsociety.org/growing-pains-bandwidth-internet

Li, C.-H., Wu, M.-F., Lin, C.-H., Lin, C.-T.: W-band OFDM RoF system with simple envelope detector down-conversion. Optical Fiber Communication Conference, p. W4G.6 (2015b)

Li, X., Yu, J., Zhang, Z., Xu, Y.: Field trial of 80-Gb/s PDM-QPSK signal delivery over 300-m wireless distance with MIMO and antenna polarization multiplexing at W-band. Optical Fiber Communication Conference Post Deadline Paper, p. Th5A.5 (2015a)

Pang, X., Vegas Olmos, J.J., Lebedev, A., Monroy, I.T.: A 15-meter multi-gigabit W-band bidirectional wireless bridge in fiber-optic access networks. IEEE International Topical Meeting on Microwave Photonics, pp. 37–40 (2013)

Proakis, J.G., Manolakis, D.K.: Digital Signal Processing, 4th edn. Pearson Prentice Hall, New York (2007)

Rommel, S., Cavalcante, L., Vegas Olmos, J.J., Monroy, I. T., Quintero, A.: Channel characterization for high-speed W-band wireless links. Proceedings of OECC (2015)

Rommel, S., Cavalcante, L., Olmos, J.J.V., Monroy, I.T. (2015) Low RF complexity photonically enabled indoor and building-to-building W-band wireless link. Asia Communications and Photonics Conference, pp. 8–10 (2015)
Shannon, C.E.: A mathematical theory of communication. Bell Syst. Tech. J. **27**, 379–423, 623–656 (1948)
Struzak, R.: On spectrum congestion and capacity of radio links. Ann. Oper. Res. **107**(4), 339–347 (2002)
Xu, Y., Yu, J., Li, X., Xiao, J., Zhang, Z.: Experimental investigation on fiber-wireless MIMO system with different LO at W band. IEEE Photonics J. **7**(2), 1–8 (2015)

PAPER3: Requirements for Bend Insensitive Fiber in Millimeter-Wave Fronthaul Systems

S. Rommel, L. C. P. Cavalcante, A. K. Mishra, J. J. Vegas Olmos, and I. Tafur Monroy. "Requirements for Bend Insensitive Fiber in Millimeter-Wave Fronthaul Systems". In: *2015 International Topical Meeting on Microwave Photonics*. Oct. 2015, paper TuP-29. DOI: 10.1109/MWP.2015.7356674

Requirements for Bend Insensitive Fiber in Millimeter-Wave Fronthaul Systems

Simon Rommel, Lucas Costa Pereira Cavalcante,
J. J. Vegas Olmos, Idelfonso Tafur Monroy
Department of Photonics Engineering
Technical University of Denmark
Kgs. Lyngby, 2800, Denmark
sirem@fotonik.dtu.dk

Arvind K. Mishra

Centre of Excellence
Sterlite Technologies Limited
E1-E3, MIDC, Waluj, Aurangabad, 431 136, India

***Abstract*—The impact of fiber bending on mm-wave radio-over-fiber transmission is investigated and the need for bend insensitive fiber for front-haul installation confirmed. A 70m W-band hybrid photonic-wireless link including bend insensitive fiber is demonstrated with BER<10^{-6} at 5mm bending radius.**

I. Introduction

The increasing use of bandwidth intensive applications on mobile consumer devices such as smartphones and tablet computers has created a demand for high-speed wireless data communications at gigabit speeds that need to be supported by future 5G mobile networks. Millimeter-wave (mm-wave) radio-over-fiber (RoF) links have been identified as a key candidate for the required mobile front- and backhaul as well as direct gigabit-class wireless broadband services [1]–[5], as a viable alternative to baseband, digitized, packet encapsulated grey optic solutions [5], [6].

RoF links in the different mm-wave bands have been demonstrated with wireless transmission distances ranging from a few to multiple hundred meters and with a variety of optical generation, upconversion and radio-frequency (RF) detection setups [4], [7], [8]. The transmission fiber itself has received attention mostly with regard to transmission impairments due to dispersion and fiber nonlinearities [9] or the combination of single- and multi-mode fibers [7] and—more recently—as a means for capacity increase by combining spatial multiplexing in the fiber with the well known concept of multiple-input multiple-output (MIMO) RF transmission [3].

The practical consideration of on-premise fiber installation and optical wiring of—and within—the antenna has however been neglected, although it is obvious that—analogous to the case of fiber-to-the-x [10]—fiber bends with small radii are likely to occur. With the introduction of MIMO transmission and antenna arrays especially as well as their housing in compact, weather resistant and easy to mount outdoor units, radii well below $10\,\mathrm{mm}$ will be common and macrobending induced losses may thus play a significant role.

In this paper we assess the performance of a W-band RoF link with $15\,\mathrm{km}$ optical and $70\,\mathrm{m}$ wireless transmission. Significantly we include $5\,\mathrm{km}$ of bend insensitive fiber (BIF), we show that for radii below $15\,\mathrm{mm}$ BIF is a necessity and demonstrate how the use of different fibers from the set of specifications defined by ITU-T G.657 may allow different numbers of bends at different radii. Finally we discuss the trade-off between the available power budget, required tolerance to fiber bending and the cost of including BIF.

II. Experimental Setup

The experimental setup is depicted in Fig. 1 and employs photonic upconversion at the transmitter, consisting of an external cavity laser (ECL) at $\lambda = 1550\,\mathrm{nm}$ for signal generation, followed by a Mach-Zehnder modulator (MZM) driven with a sinusoidal at $f_{RF}/2$ to generate two spectral lines spaced at f_{RF}. The signal is amplified and an arrayed waveguide grating (AWG) used to separate the two lines while suppressing the central line, allowing one line to be modulated in a second MZM. The latter is driven at data rates of $1\,\mathrm{Gbit/s}$ and $2.5\,\mathrm{Gbit/s}$ by a $2^{15}-1$ bit long pseudo-random bit sequence (PRBS15) non-return-to-zero (NRZ) signal from a pulse patter generator (PPG). The lines are recombined, amplified and transmitted through $10\,\mathrm{km}$ of ITU-T G.652 standard single-mode fiber (SMF) and one of three spool samples of $5\,\mathrm{km}$ Sterlite bending insensitive fiber. In order to test the effects of macrobending, the different fibers are wound for 1 to 10 turns around mandrels with radii between $5\,\mathrm{mm}$ and $15\,\mathrm{mm}$ while monitoring the resulting incident power on the photodiode (PD) with a $1\,\%$ tap and recording bit-error rate (BER) values after wireless transmission. It should be noted that the impact of macrobending and the performance analysis of the BIF are independent of the choice of signal generation scheme.

The beating of the two signal lines on the PD generates the radio-frequency (RF) signal at $f_{RF} = 84\,\mathrm{GHz}$ which is transmitted wirelessly over a distance of $70\,\mathrm{m}$ with a pair of parabolic antennas—with a gain of $48\,\mathrm{dBi}$ each. A low noise amplifier (LNA) with $40\,\mathrm{dB}$ gain restores the signal level before the receiver which consists of a Schottky diode based envelope detector (ED) and digital storage oscilloscope (DSO). With only a single LNA and the use of envelope detection rather than down-conversion with an electrical mixer the need for a local oscillator at the receiver is alleviated and the complexity in the RF domain is kept to a minimum. Finally BER values are determined through offline processing, consisting of simple thresholding and error counting over four recorded sequences with a combined length $>10\,\mathrm{Mbit}$.

Fig. 2 gives an overview of the laboratory setup with optical signal generation, bending test and receive antenna co-located

978-1-4673-9368-3/15/$31.00 ©2015 IEEE

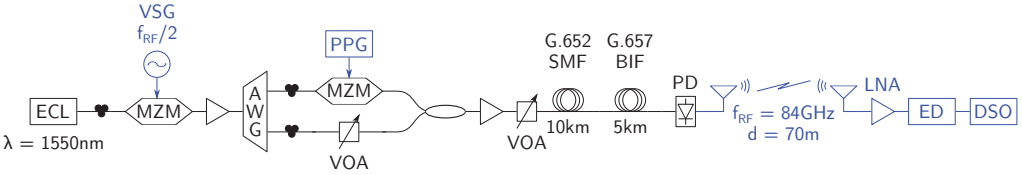

Fig. 1. Experimental setup for radio-over-fibre transmission including bend insensitive fibre. ECL: external cavity laser, VSG: vector signal generator, MZM: Mach-Zehnder modulator, AWG: arrayed waveguide grating, PPG: pulse pattern generator, VOA: variable optical attenuator, PD: photodiode, LNA: low noise amplifier, ED: envelope detector, DSO: digital storage oscilloscope

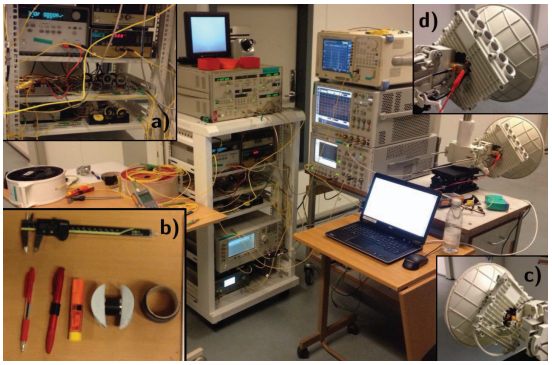

Fig. 2. Portable laboratory setup with photonic upconversion. Insets: a) Rack-mounted optical setup, b) Mandrels of different radii, c) Transmit antenna with PD, d) Receive antenna with LNA and ED

for experiment convenience while the transmit antenna and attached PD are remotely fed through an optical fiber.

III. Experimental Results

In this work the performance of a hybrid optical-wireless link is analyzed in the presence of fiber bends similar to what would be found in a fiber installation at a radio-access-unit or the antennae of a wireless broadband access link. First the macrobending loss performance of the different fibers under test is compared to the specification for bend insensitive fiber (BIF) of ITU-T G.657, with results shown in Fig. 3. The tested sample A shows marcobending losses significantly—as much as an order of magnitude at radii of 10 mm and 15 mm—below those of SMF and well below those required by ITU-T G.657.A1. Samples B and C show similar performance at a bending radius of 5 mm with sample C showing a five times lower loss at 7.5 mm radius; both show loss figures below the requirements set by G.657.A2/B2 and sample C further meets the loss requirements of G.657.B3.

As the number of bends in an installation may easily add up to the equivalent of five to ten turns, these loss figures indicate that while at a radius of 15 mm the bending loss introduced by SMF may be tolerable, category G.657.A1 fiber will be required at 10 mm and A2/B2 or B3 fiber for even smaller radii in order to remain within typical system power budgets.

Fig. 4 a) and Fig. 5 a) show the dependency of system BER performance on the optical power P_{PD} incident on the PD at 1 Gbit/s and 2.5 Gbit/s respectively. Setting $P_{PD} = 6$ dBm

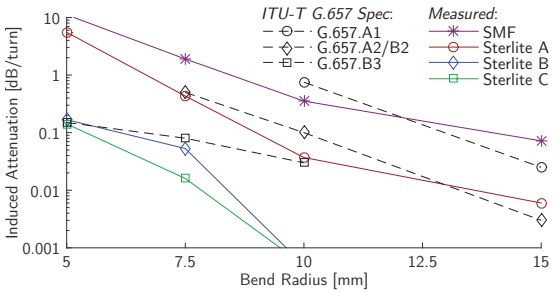

Fig. 3. Comparison of macrobending losses of Sterlite BIF fiber samples at 1550 nm with ITU-T G.657 A1, A/B2 and B3 specifications

as reference power and assuming a required maximum BER of 10^{-6} gives an allowable margin of just below 2 dB for loss induced by fiber bending, with a near negligible penalty for going from 1 Gbit/s to 2.5 Gbit/s.

With the same BER limit and data rates the combinations of fibers, radii and numbers of turns that have been found to be allowable while maintaining system performance are shown in Fig. 4 b) and Fig. 5 b) respectively.[1] The benefit obtained by the use of G.657 fibers is immediately visible at both data rates and it is evident that especially for small radii category A2/B2 and B3 fiber will be a necessity. The observed maximum allowable combinations together with the loss/turn values from Fig. 3 adhere to the allowable loss margin of about 2 dB derived from Fig. 4 a) and Fig. 5 a). While no difference between sample B and C fibers is observed in either Fig. 4 b) or Fig. 5 b), an extrapolation of the number of turns up to the found acceptable loss margin suggests respective allowable numbers of turns of 11 and 14 at 5 mm and 38 and 126 at 7.5 mm, clearly showing the benefit of a fiber with bending loss as low as found for sample C when considering complex installations.

While the margin of 2 dB for allowable bending loss is specific to the assessed system and link, the trade-off it highlights is a general one, requiring assessment of system parameters such as the available power budget, logistical challenges such as the required tolerance to bending and ease of installation as well as economical considerations such as the additional cost of BIF. Due to the drastic differences in loss however these considerations are likely to be between the different types of

[1] Setting a BER limit of 10^{-3} does not significantly alter the picture with only a single data point being changed for each of the data rates as indicated by the $\triangledown$ in Fig. 4 b) and $\triangle$ in Fig. 5 b).

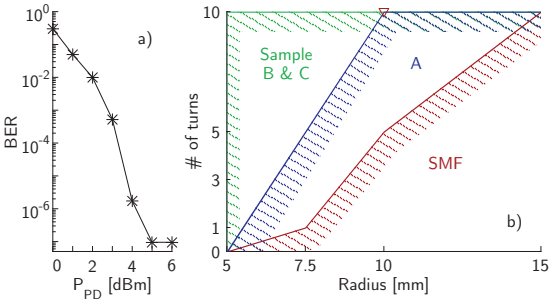

Fig. 4. a) BER vs P_{PD} at 1 Gbit/s without bending, b) Allowable radii and numbers of turns for a system performance with BER $< 10^{-6}$ at 2.5 Gbit/s ($\triangledown$: BER $= 2.0 \cdot 10^{-4}$ for 10 turns @ 10 mm with SMF fiber)

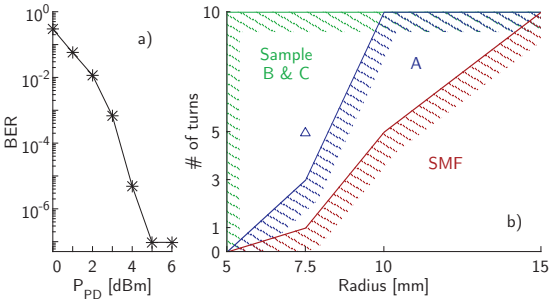

Fig. 5. a) BER vs P_{PD} at 2.5 Gbit/s without bending, b) Allowable radii and numbers of turns for a system performance with BER $< 10^{-6}$ at 2.5 Gbit/s ($\triangle$: BER $= 2.5 \cdot 10^{-6}$ for 5 turns @ 7.5 mm with sample A)

BIF rather than whether or not BIF will be included for the last stretch of fiber in the on-site and antenna installation.

IV. Conclusions

We assessed the performance of a W-band hybrid fiber-wireless link with 70 m wireless and 15 km fiber transmission distance under the inclusion of 5 km of bend insensitive fiber (BIF), matching the scenarios for mobile fronthaul or wireless broadband access.

A selection of BIFs were verified to adhere to and actually outperform the requirements set by ITU-T G.657. With these the impact of fiber bending at radii between 5 mm and 15 mm on system performance has been analyzed and the trade-off between available power budget and required tolerance to bending has been discussed both with respect to the presented system as well as in general terms.

The observed loss difference between SMF and BIF suggests the inclusion of BIF as a key enabler for RoF solutions for next generation mobile fronthaul and wireless broadband access where fiber bending is unavoidable due to on-site and antenna installation. The demonstrated benefit of BIF is available to RoF in any frequency band and may be harnessed in combination with wavelength division multiplexing.

Acknowledgments

The authors wish to thank Siklu Communication Ltd. for providing the W-band antennas.

This work was partly funded by the DFF FTP mmW-SPRAWL and EC IPHOBAC-NG projects. L. Cavalcante thanks the Brazilian government for supporting his research through the Science without Borders program.

References

[1] M. García Larrodé, A. M. J. Koonen, J. J. Vegas Olmos, G. J. Rijckenberg, L. Dang Bao, and I. Niemegeers, "Transparent transport of wireless communication signals in radio-over-fibre systems," in *Proc. 10th Eur. Conf. on Netw. and Opt. Comm.*, London, Jul. 2005, pp. 83–90.

[2] J. E. Mitchell, "Integrated wireless backhaul over optical access networks," *J. Lightw. Technol.*, vol. 32, no. 20, pp. 3373–3382, Oct. 2014.

[3] M. Morant, A. Macho, and R. Llorente, "Optical fronthaul of LTE-advanced MIMO by spatial multiplexing in multicore fiber," in *Proc. OFC 2015*, Los Angeles, Mar. 2015, paper W1F.6.

[4] K.-i. Kitayama, T. Kuri, J. J. Vegas Olmos, and H. Toda, "Fiber-wireless networks and radio-over-fibre technique," in *Proc. CLEO/QELS 2008*, San Jose, May 2008, paper CThR4.

[5] T. Pfeiffer, "Next generation mobile fronthaul architectures," in *Proc. OFC 2015*, Los Angeles, Mar. 2015, paper M2J.7.

[6] N. Shibata, T. Tashiro, S. Kuwano, N. Yuki, J. Terada, and A. Otaka, "Mobile front-haul employing ethernet-based TDM-PON system for small cells," in *Proc. OFC 2015*, Los Angeles, Mar. 2015, paper M2J.1.

[7] A. Lebedev, J. J. Vegas Olmos, X. Pang, S. Forchhammer, and I. Tafur Monroy, "Demonstration and comparison study for V- and W-band real-time high-definition video delivery in diverse fiber-wireless infrastructure," *Fiber and Integrated Optics*, vol. 32, no. 2, pp. 93–104, Mar. 2013.

[8] S. Koenig *et al.*, "100 Gbit/s wireless link with mm-wave photonics," in *Proc. OFC 2013*, Anaheim, 2013, paper PDP5B.4.

[9] C. Lim, A. Nirmalathas, M. Bakaul, K.-L. Lee, D. Novak, and R. Waterhouse, "Mitigation strategy for transmission impairments in millimeter-wave radio-over-fiber networks," *J. Opt. Netw.*, vol. 8, no. 2, pp. 201–214, Feb. 2009.

[10] D. Z. Chen, W. R. Belben, J. B. Gallup, C. Mazzali, P. Dainese, and T. Rhyne, "Requirements for bend insensitive fibers for Verizon's FiOS and FTTH applications," in *Proc. OFC/NFOEC 2008*, San Diego, Feb. 2008, paper NTuC2.

PAPER4: Low RF Complexity Photonically Enabled Indoor and Building-to-Building W-Band Wireless Link

S. Rommel, L. C. P. Cavalcante, J. J. Vegas Olmos, and I. Tafur Monroy. "Low RF Complexity Photonically Enabled Indoor and Building-to-Building W-Band Wireless Link". In: *Asia Communications and Photonics Conference 2015*. Nov. 2015, paper AM1B.7. DOI: 10.1364/ACPC.2015.AM1B.7

Low RF Complexity Photonically Enabled Indoor and Building-to-Building W-Band Wireless Link

Simon Rommel, Lucas C. P. Cavalcante, J. J. Vegas Olmos, Idelfonso Tafur Monroy
Department of Photonics Engineering, Technical University of Denmark, 2800 Kgs. Lyngby, Denmark
sirem@fotonik.dtu.dk

Abstract: We demonstrate W-band wireless transmission over distances covering both indoor and building-to-building scenarios with a setup of reduced complexity in the RF domain, employing a passive wireless transmitter and envelope detection at the receiver.

OCIS codes: (060.5625) Radio frequency photonics; (060.4510) Optical communications.

1. Introduction

The introduction and increasing use of a variety of bandwidth intensive services and applications—including e-health monitoring, distance learning, high resolution video streaming and holographic video conferencing—on portable consumer devices has lead to an increased demand for high-speed wireless connections. The high bandwidth requirements of such applications are beyond the capacity of the already congested conventional wireless bands and a migration to higher frequency bands supporting greater transmission bandwidths—such as the millimeter-wave (mmW) region—is necessary [1–4].

While currently the V-band and especially carriers at 60 GHz are the dominant focus for Gbit/s indoor wireless [3] this region is affected by a large peak in atmospheric absorption [1], severely limiting it to short-range transmissions. The W-band (75 GHz to 110 GHz) however does not share this limitation and may thus be a candidate for both indoor and building-to-building transmission scenarios [3, 5] as shown in Fig. 1.

Long distance Gbit/s class W-band wireless transmission has been demonstrated with high complexity in both the optical and radio frequency (RF) parts of the system, while on the contrary recent demonstrations with reduced complexity and employing envelope detection have not reached beyond 10 m wireless transmission [6, 7].

In this paper we demonstrate W-band wireless transmission with a reduced-complexity setup employing a passive wireless transmitter and a Schottky diode based envelope detection receiver. We analyze system performance and requirements for error free transmission and their dependency on both wireless distance and RF carrier frequency. By investigating RF carriers between 75 GHz and 87 GHz and wireless distances of 20 m to 70 m we cover the lower half of the W-band for both indoor and building-to-building scenarios as shown in Fig. 1.

2. Experimental Setup

The W-band transmission setup with low complexity in the radio-frequency (RF) domain is depicted in Fig. 3 while Fig. 2 shows the corresponding laboratory setup. Photonic up-conversion is employed at the transmitter, consisting of an external cavity laser (ECL) at $\lambda = 1550$ nm for signal generation, followed by a Mach-Zehnder modulator (MZM) driven with a sinusoidal at $f_{RF}/2$ to generate two spectral lines spaced at f_{RF}. While the wavelength of the ECL is constant, the driving frequency for the MZM is varied in order to generate line spacings between 75 GHz and 87 GHz.

The signal is amplified and an arrayed waveguide grating (AWG) separates the two lines while suppressing the original signal, allowing one line to be modulated in a second MZM. The latter is driven at data rates of 2 Gbit/s and 2.5 Gbit/s by a $2^{15} - 1$ bit long pseudo-random bit sequence (PRBS15) non-return-to-zero (NRZ) signal from a pulse pattern generator (PPG). The lines are recombined, amplified and transmitted through 10 km of ITU-T G.652 standard single-mode fiber (SMF).

At the transmit antenna a variable optical attenuator (VOA) allows variation of the power incident on the photodiode (PD) between 0 dBm and 8 dBm, thus giving control over the power of the output RF signal at f_{RF} resulting from the beating of the two signal lines on the PD. A pair of parabolic antennas—with a gain of 48 dBi each—allows wireless transmission of the RF signal over distances between 20 m and 70 m.

The received W-band signal is amplified with the help of a low noise amplifier (LNA) providing 40 dB gain before down-conversion takes place in a Schottky diode based envelope detector (ED) with a 3 dB bandwidth of 3 GHz.

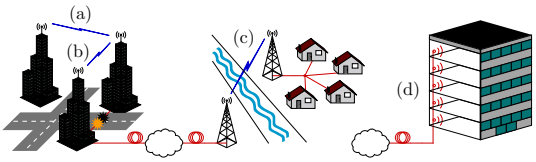

Fig. 1. Network scenarios for the hybrid fiber-wireless link. (a)–(c) outdoor medium distance links: (a) building-to-building communication, (b) recovery and protection of fiber links, (c) spanning obstacles and providing broadband access to rural ares; (d) short-range indoor wireless distribution

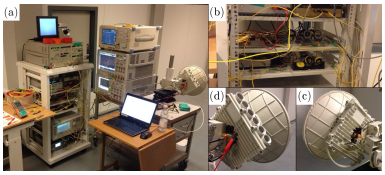

Fig. 2. (a) Portable laboratory setup with photonic upconversion, (b) Rack-mounted optical setup, (c) Transmit antenna with PD, (d) Receive antenna with LNA and ED

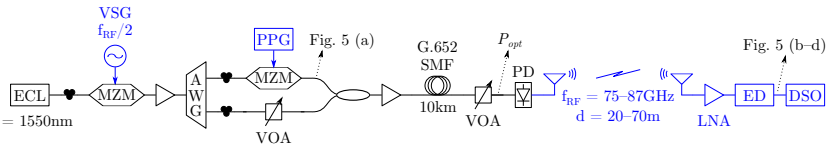

Fig. 3. Experimental setup for radio-over-fiber transmission. ECL: external cavity laser, VSG: vector signal generator, MZM: Mach-Zehnder modulator, AWG: arrayed waveguide grating, PPG: pulse pattern generator, VOA: variable optical attenuator, SMF: single-mode fiber, PD: photodiode, LNA: low noise amplifier, ED: envelope detector, DSO: digital storage oscilloscope

Employing envelope detection rather than down-conversion with an electrical mixer alleviates the need for a local oscillator at the receiver and thus—together with employing a passive wireless transmitter and only a single LNA at the receiver—minimizes complexity of the RF chain at both ends. Finally the received baseband signal is recorded using a digital storage oscilloscope (DSO) and bit-error rate (BER) values are determined through offline processing, consisting of simple thresholding and error counting over four recorded sequences with a combined length >10 Mbit.

With both RF carrier frequency and optical power incident on the photodiode tunable, this setup allows analysis of transmission performance over a parameter space spanning the lower half of the W-band and for transmission distances covering typical indoor environments as well as a number of building-to-building scenarios as shown in Fig. 1.

3. Experimental Results

In this work we analyze the transmission performance of a W-band hybrid photonic-wireless link transmitting over 10 km SMF and wireless distances between 20 m and 70 m, employing RF carrier frequencies between 75 GHz and 87 GHz. Fig. 4 (a) shows BER as a function of power on the PD and its dependency on wireless carrier frequency. While the general trend confirms the prediction of the Friis free-space loss model that required transmit power increases with carrier frequency due to increased path loss, it is clear that performance across the regarded frequency band is dominated by the variation of the involved RF equipment, rather than the frequency dependent loss which amounts to only 1.3 dB extra loss when comparing RF carriers at 75 GHz and 87 GHz.

Fig. 4 (b) shows BER as a function of both power on the PD and distance (the displayed BER of 10^{-7} at the high powers indicates successful and error free transmission for the analyzed sequences with a combined length >10 Mbit), while Fig. 5 gives a comparison of transmitter and receiver eye diagrams and shows the evolution of the latter with wireless distance at a fixed optical power of 5 dBm. The correlation between transmission distance and required optical power is immediately visible and at a BER of 10^{-6} minimum optical powers of 0.7 dBm and 4.4 dBm are found for distances of 40 m and 70 m respectively. The translation of this increase in optical power to resulting transmitted RF power compares well with the increase necessary to overcome the additional loss of 4.9 dB resulting from the increased transmission distance. With as much as 3 dB in additional optical power available at the PD, an increase in wireless distance well beyond the mark of 100 m is expected to be within the power budget of the presented system.

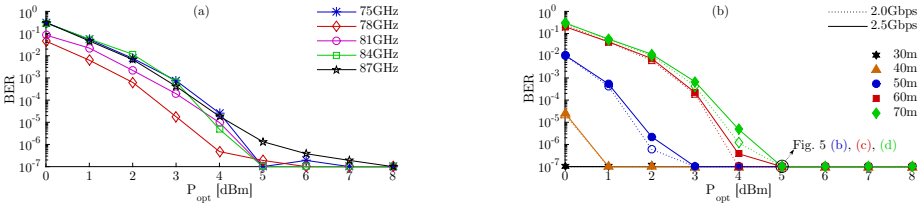

Fig. 4. Evolution of BER vs P_{opt}: (a) for different RF carrier frequencies at 2.5 Gbit/s and after 70 m wireless transmission, (b) for wireless transmission distances between 30 m and 70 m at data rates of 2 Gbit/s and 2.5 Gbit/s and with an RF carrier frequency of 84 GHz

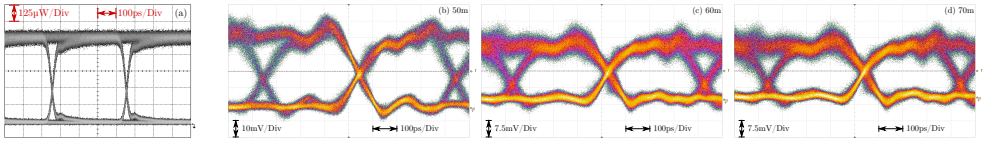

Fig. 5. Eye diagrams: (a) transmitter 2.5 Gbit/s NRZ signal, (b) receiver after envelope detection of the 2.5 Gbit/s NRZ signal on an 84 GHz RF carrier and 10 km SMF and 50 m to 70 m wireless transmission for $P_{opt} = 5$ dBm

4. Conclusions

We have demonstrated W-band wireless transmission with a setup of reduced complexity in the RF domain, avoiding down-mixing by employing envelope detection at the receiver and minimizing the number of RF amplifiers through the use of a passive wireless transmitter. Transmission with a BER $< 10^{-6}$ was achieved over distances between 20 m and 70 m and with RF carriers between 75 GHz and 87 GHz, giving a good indication of the performance achievable in the W-band even with reduced complexity setups and covering typical indoor and building-to-building scenarios.

Acknowledgments

The authors thank Siklu Communication Ltd. for providing the antennas. This work was partly funded by the DFF FTP mmW-SPRAWL and EC IPHOBAC-NG projects. L. Cavalcante thanks the Science without Borders program.

References

[1] J. Wells, "Faster than fiber: The future of multi-G/s wireless," IEEE Microw. Mag. **10**, pp. 104–112 (2009).
[2] K.-i. Kitayama, T. Kuri, J. J. Vegas Olmos, and H. Toda, "Fiber-Wireless Networks and Radio-over-Fibre Technique," in *Proc. CLEO 2008* (OSA, San Jose, 2008), paper CThR4.
[3] H. Yang, A. Ng'oma, B. Shih, A. Gowda, and L. Kazovsky, "Fiber-based Solutions for In-door Multi-Gbit/s Wireless Access," in *Proc. OFC 2015* (OSA, Los Angeles, 2015), paper W3F.1.
[4] S. Rommel, A. Galvis Quintero, L. C. P. Cavalcante, J. J. Vegas Olmos, and I. Tafur Monroy, "Channel Characterization for High-Speed W-Band Wireless Communication Links," in *Proc. OECC 2015* (Shanghai, 2015).
[5] X. Pang, A. Lebedev, J. J. Vegas Olmos, and I. Tafur Monroy, "Multigigabit W-Band (75-110 GHz) Bidirectional Hybrid Fiber-Wireless Systems in Access Networks," J. Lightw. Technol. **32**, pp. 3983–3990 (2014).
[6] A. Stöhr et al., "Robust 71-76GHz Radio-over-Fiber Wireless Link with High-Dynamic Range Photonic Assisted Transmitter and Laser Phase-Noise Insensitive SBD Receiver," in *Proc. OFC 2014* (OSA, San Francisco, 2014), paper M2D.4.
[7] C.-H. Li, M.-F. Wu, C.-H. Lin, and C.-T. Lin, "W-band OFDM RoF System with Simple Envelope Detector Down-Conversion," in *Proc. OFC 2015* (OSA, Los Angeles, 2015), paper W4G.6.

PAPER5: W-band photonic-wireless link with a Schottky diode envelope detector and bend insensitive fiber

S. Rommel, L. C. P. Cavalcante, A. G. Quintero, A. K. Mishra, J. J. Vegas Olmos, and I. Tafur Monroy. "W-band photonic-wireless link with a Schottky diode envelope detector and bend insensitive fiber". In: *Optics Express* 24.11 (May 2016), pp. 11312–11322. DOI: 10.1364/OE.24.011312

W-band photonic-wireless link with a Schottky diode envelope detector and bend insensitive fiber

Simon Rommel,[1,*] **Lucas C. P. Cavalcante,**[1] **Alexander G. Quintero,**[2] **Arvind K. Mishra,**[3] **J. J. Vegas Olmos**[1] **and Idelfonso Tafur Monroy**[1]

[1]*Department of Photonics Engineering, Technical University of Denmark, Ørsteds Plads, 2800 Kgs. Lyngby, Denmark*
[2]*GIDATI, Telecommunications Engineering Faculty, Universidad Pontificia Bolivariana, Campus de Laureles, Medellín, Colombia*
[3]*Centre of Excellence, Sterlite Technologies Limited, E1-E3, MIDC Waluj, Aurangabad 431 136, Maharashtra, India*

[*]*sirem@fotonik.dtu.dk*

Abstract: The performance and potential of a W-band radio-over-fiber link is analyzed, including a characterization of the wireless channel. The presented setup focuses on minimizing complexity in the radio frequency domain, using a passive radio frequency transmitter and a Schottky diode based envelope detector. Performance is experimentally validated with carriers at 75–87GHz over wireless distances of 30–70m. Finally the necessity for and impact of bend insensitive fiber for on-site installation are discussed and experimentally investigated.

OCIS codes: (060.5625) Radio frequency photonics; (060.4510) Optical communications.

References and links

1. X. Pang, A. Lebedev, J. J. Vegas Olmos, and I. Tafur Monroy, "Multigigabit W-band (75-110 GHz) bidirectional hybrid fiber-wireless systems in access networks," J. Lightwave Technol. **32**, 3983–3990 (2014).
2. T. Pfeiffer, "Next generation mobile fronthaul architectures," in *Proc. OFC 2015* (OSA, 2015), pp. 1–3.
3. H. Yang, A. Ng'oma, B. Shih, A. Gowda, and L. Kazovsky, "Fiber-based solutions for in-door multi-Gbit/s wireless access," in *Proc. OFC 2015* (OSA, Los Angeles, 2015), paper W3F.1.
4. J. J. Vegas Olmos, T. Kuri, T. Sono, K. Tamura, H. Toda, and K.-i. Kitayama, "Wireless and optical-integrated access network with peer-to-peer connection capability," IEEE Photonics Technol. Lett. **20**, 1127–1129 (2008).
5. K.-i. Kitayama, T. Kuri, J. J. Vegas Olmos, and H. Toda, "Fiber-wireless networks and radio-over-fibre technique," in *Proc. CLEO/QELS 2008* (OSA, 2008), pp 1–2..
6. J. Wells, "Faster than fiber: The future of multi-G/s wireless," IEEE Microw. Mag. **10**, 104–112 (2009).
7. J. J. Vegas Olmos, T. Kuri, and K.-i. Kitayama, "Reconfigurable radio-over-fiber networks: Multiple-access functionality directly over the optical layer," IEEE Trans. Microw. Theory Tech. **58**, 3001–3010 (2010).
8. W.-J. Jiang, H. Yang, Y.-M. Yang, C.-T. Lin, and A. Ng'oma, "40 Gb/s RoF signal transmission with 10 m wireless distance at 60 GHz," in *OFC/NFOEC 2012* (OSA, 2012), pp. 1–3.
9. A. Lebedev, X. Pang, J. J. Vegas Olmos, S. Forchhammer, and I. Tafur Monroy, "Simultaneous 60-GHz RoF transmission of lightwaves emitted by ECL, DFB, and VCSEL," IEEE Photonics Technol. Lett. **26**, 733–736 (2014).
10. C.-H. Li, M.-F. Wu, C.-H. Lin, and C.-T. Lin, "W-band OFDM RoF system with simple envelope detector down-conversion," in *Proc. OFC 2015* (OSA, 2015), pp. 1–3.
11. S. Rommel, L. C. P. Cavalcante, J. J. Vegas Olmos, and I. Tafur Monroy, "Low RF complexity photonically enabled indoor and building-to-building w-band wireless link," in *Proc. ACP 2015* (OSA, 2015), paper AM1B.7.
12. S. Koenig, F. Boes, D. Lopez-Diaz, J. Antes, R. Henneberger, R. M. Schmogrow, D. Hillerkuss, R. Palmer, T. Zwick, C. Koos, W. Freude, O. Ambacher, I. Kallfass, and J. Leuthold, "100 Gbit/s wireless link with mm-wave photonics," in *Proc. OFC 2013* (OSA, 2013), pp 1–3.

#259469 Received 23 Feb 2016; revised 3 May 2016; accepted 12 May 2016; published 17 May 2016

13. H. Xu, V. Kukshya, and T. S. Rappaport, "Spatial and temporal characteristics of 60-GHz indoor channels," IEEE J. Sel. Areas Commun. **20**, 620–630 (2002).
14. A. P. Garcia, W. Kotterman, R. S. Thoma, U. Trautwein, D. Bruckner, W. Wirnitzer, and J. Kunisch, "60 GHz in-cabin real-time channel sounding," in *Proc. ChinaCOM 2009* (IEEE, 2009), pp 1–5.
15. S. Rommel, A. Galvis Quintero, L. C. P. Cavalcante, J. J. Vegas Olmos, and I. Tafur Monroy, "Channel characterization for high-speed W-band wireless communication links," in *Proc. OECC 2015* (IEEE, 2015), pp. 1–3.
16. A. Stöhr, O. Cojucari, F. van Dijk, G. Carpintero, T. Tekin, S. Formont, I. Flammia, V. Rymanov, B. Khani, and R. Chuenchom, "Robust 71-76 GHz radio-over-fiber wireless link with high-dynamic range photonic assisted transmitter and laser phase-noise insensitive SBD receiver," in *Proc. OFC 2014* (OSA, 2014), paper M2D.4.
17. R. Chuenchom, X. Zou, V. Rymanov, B. Khani, M. Steeg, S. Dülme, S. Babiel, A. Stöhr, J. Honecker, and A. G. Steffan, "Integrated 110 GHz coherent photonic mixer for CRoF mobile backhaul links," in *Proc. MWP 2015* (IEEE, 2015), paper 1–4.
18. S. Rommel, S. Rodriguez, L. Chorchos, E. P. Grakhova, A. K. Sultanov, J. P. Turkiewicz, J. J. Vegas Olmos, and I. Tafur Monroy, "225m outdoor W-band radio-over-fiber link using an optical SFP+ module," in *Proc. OFC 2016* (OSA, 2016), paper Th2A.16.
19. C. Lim, A. Nirmalathas, M. Bakaul, K.-L. Lee, D. Novak, and R. Waterhouse, "Mitigation strategy for transmission impairments in millimeter-wave radio-over-fiber networks," J. Opt. Netw. **8**, 201–214 (2009).
20. A. Lebedev, J. J. Vegas Olmos, X. Pang, S. Forchhammer, and I. Tafur Monroy, "Demonstration and comparison study for V- and W-band real-time high-definition video delivery in diverse fiber-wireless infrastructure," Fiber Integrated Opt. **32**, 93–104 (2013).
21. M. Morant, A. Macho, and R. Llorente, "Optical fronthaul of LTE-advanced MIMO by spatial multiplexing in multicore fiber," in *Proc. OFC 2015* (OSA, 2015), paper W1F.6.
22. D. Z. Chen, W. R. Belben, J. B. Gallup, C. Mazzali, P. Dainese, and T. Rhyne, "Requirements for bend insensitive fibers for Verizon's FiOS and FTTH applications," in *Proc. OFC 2008* (IEEE, 2008), pp. 1–7.
23. S. Rommel, L. C. P. Cavalcante, J. J. Vegas Olmos, I. Tafur Monroy, and A. K. Mishra, "Requirements for bend insensitive fiber in millimeter-wave fronthaul systems," in *Proc. MWP 2015* (IEEE, 2015), pp. 1–4.
24. B. Sklar, "Rayleigh fading channels in mobile digital communication systems - Part I: characterization," IEEE Commun. Mag. **35**, 90–100 (1997).
25. T. S. Rappaport, *Wireless Communications: Principles and Practice*, 2nd ed. (Prentice Hall, 2002).
26. I. Oppermann, M. Hämäläinen, and J. Iinatti, eds., *UWB: Theory and Applications* (John Wiley and Sons, 2004).

1. Introduction

The immense growth in the usage of mobile and wireless data – driven by the use of bandwidth intensive applications on mobile consumer devices – has lead to an increasing demand for high-speed multi-gigabit wireless connections. In order to accommodate this need, new strategies must be employed both in direct wireless access and in wireless point-to-point links leading up to the access point, such as in mobile front- and backhaul, wireless building-to-building links or wireless bridges over obstacles [1–4]. A migration away from the already congested conventional wireless bands and towards higher frequency bands – such as the millimeter-wave (mmW) region – is generally considered a necessity to support the required bandwidths and mmW radio-over-fiber (RoF) links have been identified as a key candidate, combining the advantages of optical and wireless communications [4–7].

Hybrid photonic-wireless links in the IEEE V- (50–75 GHz) [3, 8, 9] and W-bands (75–110 GHz) [1,10,11] and beyond [12] have been demonstrated with a variety of setups, achieving transmission distances ranging from a few to multiple hundred meters. While carriers at 60 GHz have been in focus for Gbit/s indoor wireless [3, 9] this region is affected by a large peak in atmospheric absorption [6], severely limiting it to short-range transmissions. The W-band however does not share this limitation and may thus be a candidate for indoor and building-to-building transmission scenarios as well as mobile front- and backhaul [1–3] as shown in Fig. 1.

To ensure the feasibility of mmW wireless links in all the aforementioned scenarios however, three issues require additional attention and are addressed in this article:

- *characterization of the wireless channel*: most efforts for channel characterization and modelling have regarded frequencies in and below V-band or only estimated path loss

#259469 Received 23 Feb 2016; revised 3 May 2016; accepted 12 May 2016; published 17 May 2016

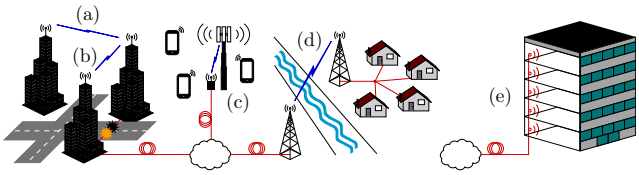

Fig. 1. Network scenarios for the hybrid fiber-wireless link. (a)–(d) outdoor medium distance links: (a) building-to-building communication, (b) recovery and protection of fiber links, (c) mobile front-/backhaul, (d) spanning obstacles and providing broadband access to rural ares; (e) short-range indoor wireless distribution

[13, 14]. A characterization of the W-band wireless channel has been performed [15] and is presented in section 2.

- *complexity of the setup*: Gbit/s class W-band wireless transmissions reaching long distances have been performed with high complexity in both the optical and radio frequency (RF) domains; setups with reduced complexity employing envelope detection for (RF) downconversion were suggested [10, 16], but only recently [11, 17, 18] reached distances beyond 10 m wireless transmission. A setup with a passive RF transmitter and a Schottky diode based envelope detector to minimize complexity in the RF domain has been developed [11] and is presented in section 3. Section 4 presents experimental results, successfully transmitting 2.5 Gbit/s of data over wireless distances of 30 to 70 m with carriers at 75 to 87 GHz as shown in section 4.1.

- *fiber installation*: the requirements for fiber to be installed directly to the transmitting antenna have not been regarded; previous investigations have focussed on the transmission fiber and associated impairments [19, 20] or on capacity enhancements through fiber spatial multiplexing and multiple-input multiple-output (MIMO) RF transmission [21]. The necessity for bend insensitive fiber (BIF) for on-site installation is obvious and similar to the case of fiber-to-the-x [22, 23] and the impact of including it in the transmission line is analyzed and discussed in section 4.2.

Finally section 5 summarizes and concludes the article.

2. W-Band Wireless Channel Characterization

2.1. Wireless Channel Modelling

The characterization of the phenomena affecting communication signals during propagation in wireless systems is fundamental to the definition and development of the digital signal processing required for their compensation or mitigation. The manifestations of fading channels are commonly classified in two groups: large-scale and small-scale fading [24], with the former mainly due to the distance between the transmitting and receiving antennas, the given environment and the resulting attenuation, while the latter is described by a number of characteristics including the time and frequency responses of the channel.

Large-scale fading is characterized statistically by calculating the mean of the observed attenuation in dependence on transmission distance – path loss – and its variations around this mean – shadowing. While a variety of models for path loss estimation is found in the literature [25], two of the most commonly employed have been selected for comparison. The free-space loss model (FSL, referred to as Friis model) defines path loss as in (1), where d is the distance between transmitting and receiving antenna, f the carrier frequency and c the speed of light in

#259469 Received 23 Feb 2016; revised 3 May 2016; accepted 12 May 2016; published 17 May 2016

Fig. 2. Schematic of the experimental setup for W-band channel characterization and photograph of the pair of pyramidal waveguide horns. LO: local oscillator, ESA: electrical spectrum analyzer

vacuum.

$$FSL_{[dB]} = 10\log\left((4\pi df/c)^2\right) = 20\log(4\pi df/c) \tag{1}$$

The generic empirical path loss model (GEPL) in (2) expresses total path loss as the observed loss L_0 at a reference distance d_0 and a term dependent on both distance d and the path loss exponent n, with the latter adapting the model to the studied environment.

$$GEPL_{[dB]} = 10n\log(d/d_0) + L_0 \tag{2}$$

Shadowing is easily calculated from experimental path loss data as a random variable – the shadowing parameter (σ_S) – with log-normal distribution additive to path loss [25].

The small-scale fading behavior of a channel includes its frequency selectivity as well as possible multipath phenomena and is characterized by the respective associated parameters, including coherence bandwidth (B_c), root mean squared delay (τ_{rms}), Doppler shift (f_d) and coherence period (T_c) [24–26].

2.2. *Channel Measurement Setup and Raw Results*

For the characterization of a short distance indoor W-band wireless link a setup as depicted in Fig. 2 is used, in which a vector signal generator (VSG) in combination with a frequency sextupler generates the signal to be transmitted, while at the receiver the signal is down-converted to intermediate frequency (IF) using a harmonic mixer driven by a 4–6 GHz local oscillator (LO). The resulting received spectra and power levels are recorded on an electrical spectrum analyzer (ESA). Wireless transmission is based on a pair of pyramidal waveguide horn antennas with a mid-band gain of 25 dBi each.

In order to ensure reliability and comparability of the measurement results, the involved VSG and ESA were adjusted to give agreeing and consistent power readings and the frequency response of the mixer was accounted for according to manufacturer measurements; it should be noted however that not all uncertainty may be calibrated out of the setup and a certain effect of the equipments' response over frequency may affect the measurement results. For the antennas a flat frequency response is assumed across the entire sounded band.

A single-tone method as described in [26] is used to sweep the complete W-band spectrum with a 1 MHz resolution, recording received power levels at distances between 0.5 m and 4 m. The recorded data allows for both large and small scale analysis, but already in their raw form as shown in Fig. 3 gives a clear indication of the distance dependency of path loss; the reduced performance at the upper frequency edge of the analyzed band is caused by frequency limitations of the employed equipment.

2.3. *Large-Scale Fading Analysis*

The experimentally obtained W-band path loss values are compared to the predictions of the Friis model in Figs. 4(a) and 4(b) for distance and frequency dependency respectively. In both cases good agreement between prediction and experimental data is found although a loss over distance slightly higher than predicted by the Friis model is observed in Fig. 4(a), while in Fig. 4(b) the observed loss is marginally below the prediction of the Friis model especially for

#259469 Received 23 Feb 2016; revised 3 May 2016; accepted 12 May 2016; published 17 May 2016

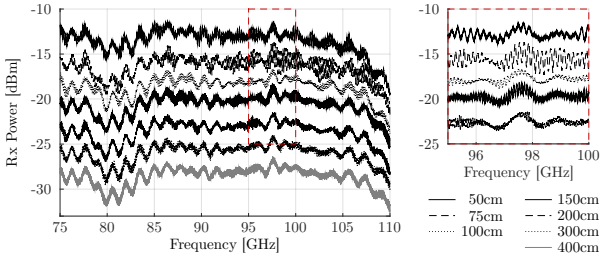

Fig. 3. Received power over frequency at distances of 0.5–4 m; close up: showing the aggregated effects of path loss, shadowing and small-scale fading

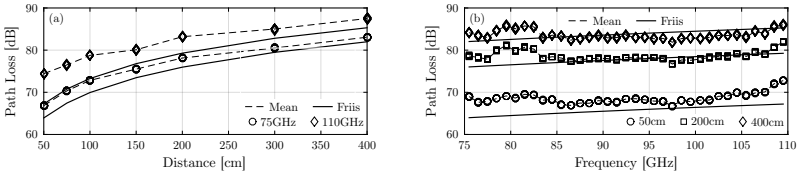

Fig. 4. Path loss over (a) distance and (b) frequency compared to predictions based on the Friis transmission equation (1)

the larger distances. With a mean error of 2.1 dB at 75 GHz and 4.3 dB at 110 GHz this confirms the Friis model to be a good model for the measured point-to-point link.

The path loss exponent (n) and shadowing parameter (σ_S) were calculated from the experimental data as discussed in [25], finding the GEPL to approximate the experimental data well for path loss exponents of $n \approx 2.2$ and $n \approx 2.5$ at 75 GHz and 110 GHz respectively, confirming the expectations for a short directive link in an indoor environment [25]. Due to the short distances and moderate directivity of the link, the observed shadowing is very small at 0.05 dB and 0.12 dB for 75 GHz and 110 GHz respectively.

Overall it is clear that for short distance links under the present conditions the dependency of path loss on distance is by far the dominant effect, with an increase in distance from 0.5 m to 4 m resulting in an additional 13.1 dB to 16.2 dB of path loss depending on frequency. This frequency dependency of path loss seen in Fig. 4(b) implies an increase in path loss of 3.8 dB at 0.5 m, 3.3 dB at 2 m and 1.9 dB at 4 m for an increase of frequency from 75 GHz to 110 GHz. While small in comparison to the impact of varying distance and easily compensated in narrow band systems, such frequency dependent variations in path loss may be detrimental to signal integrity for systems with bandwidths as large as expected for future communication systems in W-band. Large-scale fading analysis of the channel is thus insufficient to describe the encountered channel effects in the required detail and small-scale fading analysis becomes a necessity.

2.4. Small-Scale Fading Analysis

For signals with bandwidths of multiple GHz – as expected in future systems and when using photonic upconversion – the relevant channels are likely to be characterized by a multipath rich profile, resulting in significantly lower power levels for each multipath component. Analysis of the experimentally obtained S_{21} parameters using the inverse fast Fourier transformation (IFFT) and the Hermitian method [26] allows calculation of the frequency response of the channel,

#259469 Received 23 Feb 2016; revised 3 May 2016; accepted 12 May 2016; published 17 May 2016

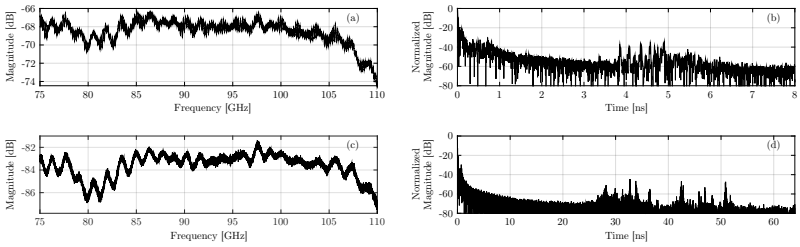

Fig. 5. Wireless channel frequency ((a), (c)) and time ((b), (d)) response at 50 cm ((a), (b)) and 400 cm ((c), (d)) transmission distance

shown in Figs. 5(a) and 5(c) for distances of 0.5 m and 4 m respectively. Except for a dip around 80 GHz – likely due to a dip in efficiency of the frequency generation setup – and a drop near the upper end of the band caused by the operational limits of the involved devices, the channel frequency response is very uniform across the whole band, with its magnitude strongly determined by path loss due to the directivity of the link.

The normalized time response of the channel – shown in Figs. 5(b) and 5(d) for distances of 0.5 m and 4 m respectively – represents good approximation of the power delay profile (PDP) of the channel [26], allowing the calculation of the corresponding root mean square delay τ_{rms} and coherence bandwidth B_c. Assuming a threshold of −60 dBm for the selection of significant multipath components, values of $\tau_{rms} = 0.16$ ns and $B_c = 6.3$ GHz are obtained for $d = 0.5$ m while at $d = 4$ m values of $\tau_{rms} = 0.40$ ns and $B_c = 2.5$ GHz are found. It is clear that with increasing transmission distance the delays grow – as the difference in distance traveled by the multipath components increases – and hence coherence bandwidth reduces. For a modulated signal of 6 GHz bandwidth this would indicate that while at 0.5 m the encountered channel may be quasi flat, at 4 m severe frequency fading will cause a significant degradation of signal quality. The assumed threshold of −60 dBm may appear low when considering observed path loss and typical receiver sensitivities and with a higher threshold all significant components might belong to the first tap of the PDP; when considering links with lower directivity or the introduction of point-to-multipoint transmission however, the limitations posed by multipath propagation will be significant and may result in coherence bandwidths considerably smaller than those found.

2.5. *Discussion*

The results obtained from the channel characterization suggest that the well known models for path loss estimation – i.e. Friis and the GEPL models – retain their validity in predicting large-scale phenomena and received power levels. Multipath propagation effects have been observed to potentially pose limits on the usable signal bandwidths, depending on link directivity, the considered threshold level for the significance of multipath contributions and on whether transmission takes place in a point-to-point or point-to-multipoint scenario. The specific channel analyzed may be considered line-of-sight and – even though only covering short distances – the channel characteristics found may give an indication towards conditions for longer distance transmissions. This is especially the case if an increase in transmission distance is accompanied by an increase in antenna directivity, such as in the following sections where wireless distances of 30–70 m are covered by employing a pair of highly directive parabolic antennas.

While on one hand for short distance transmissions or systems with highly directive antennas the channel may be considered as line-of-sight only, for systems with low directivity on the

#259469 Received 23 Feb 2016; revised 3 May 2016; accepted 12 May 2016; published 17 May 2016

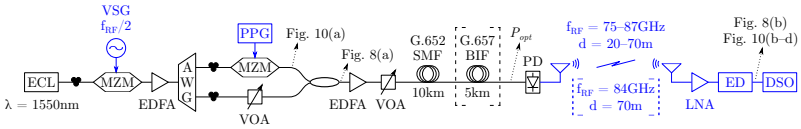

Fig. 6. Experimental setup for radio-over-fiber transmission and bend insensitive fiber analysis. ECL: external cavity laser, VSG: vector signal generator, MZM: Mach-Zehnder modulator, EDFA: erbium doped fiber amplifier, AWG: arrayed waveguide grating, PPG: pulse pattern generator, VOA: variable optical attenuator, SMF: standard single-mode fiber, BIF: bend insensitive fiber, PD: photodiode, LNA: low noise amplifier, ED: envelope detector, DSO: digital storage oscilloscope

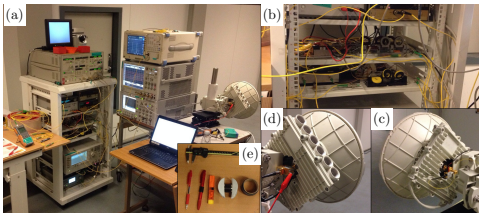

Fig. 7. (a) Portable laboratory setup with photonic upconversion, (b) rack-mounted optical setup, (c) transmit antenna with PD, (d) receive antenna with LNA and ED, (e) mandrels of different radii for bending analysis

other hand it may be necessary to compensate for the signal degradation resulting from path loss and shadowing – potentially through employing a degree of diversity, gaining additional uncorrelated estimates of the signal – and to mitigate the observed frequency selectivity, either through pre-processing or by applying equalization.

3. Low RF Complexity Fiber-Wireless Transmission System Setup

The radio-over-fiber (ROF) transmission system employed for the analysis of transmission performance and the study of mitigating fiber bending impacts through the use of bend insensitive fiber (BIF) is shown in Figs. 6 and 7. The setup consists of three distinct parts which in a deployment case would be geographically separate: (I) optical signal generation and modulation linked by optical fiber transmission to (II) optical to radio-frequency (RF) conversion linked by W-band RF transmission to (III) the receiver.

Signal generation – i.e. the left hand side of Fig. 6 – consists of an external cavity laser (ECL) at $\lambda = 1550\,\text{nm}$, followed by a Mach-Zehnder modulator (MZM) biased at its minimum transmission point and driven with a sinusoidal at $f_{RF}/2$ to generate two spectral lines spaced at f_{RF}. In order to allow performance analysis at different RF carrier frequencies the frequency of the driving signal is varied, generating line spacings of 75–87 GHz. The signal is amplified by 22 dB using an erbium doped fiber amplifier (EDFA) with a noise figure (NF) 5.8 dB and an arrayed waveguide grating (AWG) separates the two spectral lines, allowing to modulate one with data. A $2^{15} - 1$ bit long pseudo-random bit sequence (PRBS15) non-return-to-zero (NRZ) signal at speeds between 1 Gbit/s and 2.5 Gbit/s – generated with a pulse pattern generator (PPG) – directly drives the second MZM, biased in the linear part of its transmission curve for optimum extinction ratio. Two variable optical attenuators (VOAs) ensure equal power of the two arms and allow control over the output optical power. The experimental setup for signal

#259469 Received 23 Feb 2016; revised 3 May 2016; accepted 12 May 2016; published 17 May 2016

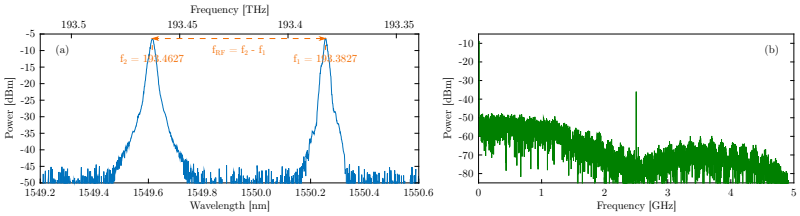

Fig. 8. Signal spectra: (a) Optical signal at the output of the 3 dB coupler before fiber transmission and photonic upconversion, for the generation of a signal with an 80 GHz carrier; (b) Received electrical spectrum after envelope detection of the 2.5 Gbit/s NRZ signal on an 84 GHz carrier and 70 m wireless transmission with $P_{opt} = 5$ dBm

generation is depicted in Fig. 7(b), while Fig. 8(a) shows the spectrum of the generated signal at the output of the coupler.

A second EDFA with a 4.3 dB NF amplifies the signal by 20 dB before it is transmitted through 10 km of ITU-T G.652 standard single-mode fiber (SMF) with one of three spool samples of 5 km Sterlite BIF added to the transmission line for the investigation of performance when subjected to macrobending. After fiber transmission the optical signal is converted to an RF signal by beating the two spectral lines on a photodiode (PD) with a nominal 3 dB bandwidth of 100 GHz and a responsivity of 0.5 A/W. The generated RF signal is transmitted without further amplification through a pair of parabolic antennas – shown in Figs. 7(c) and 7(d) – with a gain of 48 dBi each.

At the receiver site the signal is amplified by a low noise amplifier (LNA) providing 40 dB gain before down-conversion takes place in a Schottky diode based envelope detector (ED) with a 3 dB bandwidth of 3 GHz, yielding a baseband signal as shown in Fig. 8(b) for an exemplary case. Employing envelope detection rather than down-conversion with an electrical mixer alleviates the need for a local oscillator at the receiver and thus – together with the a passive wireless transmitter and only a single LNA at the receiver – minimizes complexity of the RF chain at both ends. Finally the received baseband signal is recorded using a digital storage oscilloscope (DSO) and bit-error rate (BER) values are determined through offline processing, consisting of simple thresholding and error counting over four recorded sequences with a length >2.5 Mbit each.

For the analysis of transmission performance the power incident on the PD is varied between 0–8 dBm through the use of the second VOA while wireless distance and carrier frequency are varied between 30–70 m and 75–87 GHz respectively. During the analysis of the effects of fiber bending and their mitigation through the use of BIF, carrier frequency and wireless distance are fixed to 84 GHz and 70 m respectively. Macrobending is induced by winding the different fiber samples for 1–10 turns around mandrels with radii between 5–15 mm – shown in Fig. 7(e) – and performance is analyzed by monitoring the resulting incident power on the PD with a 1 % tap and by recording BER values.

4. Experimental Results

4.1. W-Band Transmission Performance Analysis

The performance of the reduced RF complexity W-band photonic-wireless link is analyzed for wireless links of 30–70 m and utilizing carrier frequencies between 75–87 GHz, while the optical transmission link consists of 10 km SMF in all cases. Figure 9 shows BER as a function

#259469 Received 23 Feb 2016; revised 3 May 2016; accepted 12 May 2016; published 17 May 2016

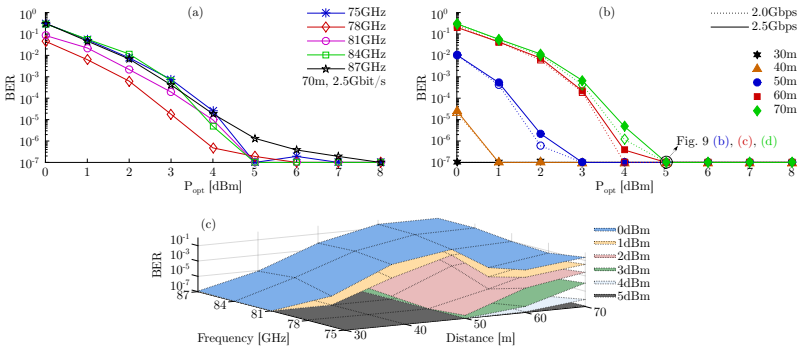

Fig. 9. Evolution of BER: (a) vs P_{opt} for different RF carrier frequencies at 2.5 Gbit/s and after 70 m wireless transmission, (b) vs P_{opt} for wireless transmission distances between 30 m and 70 m at data rates of 2 Gbit/s and 2.5 Gbit/s and with an RF carrier frequency of 84 GHz, (c) vs distance and carrier frequency for $0\,\text{dBm} \leq P_{opt} \leq 5\,\text{dBm}$

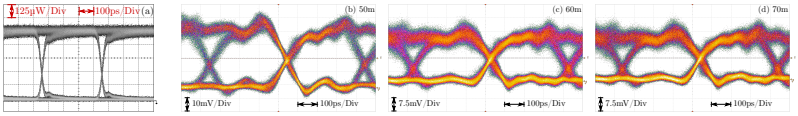

Fig. 10. Eye diagrams: (a) transmitted 2.5 Gbit/s NRZ signal, (b–d) received signal after envelope detection of the 2.5 Gbit/s NRZ signal on an 84 GHz carrier and 50–70 m wireless transmission with $P_{opt} = 5\,\text{dBm}$

of power incident on the PD and compares performance dependency on wireless distance and carrier frequency. Figure 9(a) allows analysis of frequency dependency at a fixed distance and data rate, finding it to be low while following the trend predicted by the Friis model; with the additional free space loss amounting to only 1.3 dB when comparing RF carriers at 75 GHz and 87 GHz performance variations of the involved RF equipment clearly dominate when regarding frequency dependency.

Figure 9(b) details evolution of transmission performance over distance with a fixed carrier frequency of 84 GHz, while Fig. 10 shows corresponding transmitter and receiver eye diagrams for a fixed optical power of 5 dBm; Fig. 8(b) gives the received electrical spectrum after 70 m wireless transmission. It should be noted that in all of Fig. 9 a plotted BER of 10^{-7} indicates successful and error free transmission of four sequences with a length of >2.5 Mbit each. Assuming a BER of 10^{-6} as reference minimum, optical powers on the PD of 0.7 dBm and 4.4 dBm are found for distances of 40 m and 70 m respectively, translating into an increase in available RF power adequate to overcome the additional free space loss of 4.9 dB, while also allowing for a slightly less optimal alignment of the antennas at the larger distances.

Overall the system is found to be power limited, as is also seen in Fig. 9(c) with the surfaces – corresponding to optical powers on the PD – neatly nested and allowing different distance-frequency combinations depending on selected BER limit. With no error observed at 5 dBm and an additional 3 dB in optical power available it is expected that transmission distances beyond the mark of 100 m would be within reach of the system.

#259469 Received 23 Feb 2016; revised 3 May 2016; accepted 12 May 2016; published 17 May 2016

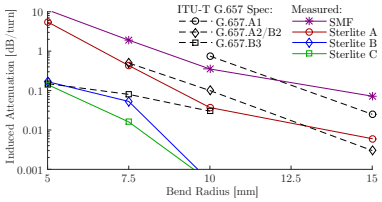

Fig. 11. Comparison of macrobending losses of Sterlite BIF fiber samples at 1550 nm with ITU-T G.657 A1, A/B2 and B3 specifications

4.2. Mitigation of Fiber Bending Impacts – Performance with Bend Insensitive Fiber

The first step in analyzing how BIF can help mitigate the impact of fiber bending is a comparison of macrobending loss of the different fibers under test with the specifications of ITU-T G.657 as shown in Fig. 11. As the number of turns in an installation may easily reach the equivalent of ten turns, the observed bending loss of SMF suggests minimum bending radii of 15 mm or above, depending on system power budget. With losses well below those required by ITU-T G.657.A1 and as much as an order of magnitude lower at radii of 10–15 mm than those of SMF, sample A allows significantly tighter radii. Samples B and C compare favorably to the requirements of G.657.A2/B2 and G.657.B3 respectively with sample C showing a five times lower loss at 7.5 mm radius, suggesting macrobending loss at this radius to be near negligible and radii down to 5 mm to be allowable while maintaining lower loss per turn values than SMF at 15 mm bending radius.

Further analysis of transmission performance is dependent on the system under test, but may give a good indication of the benefit obtained through the used of BIF. At a distance of 70 m and with a carrier of 84 GHz, setting $P_{opt} = 6$ dBm as reference power and assuming a required maximum BER of 10^{-6} suggests a margin for allowable loss through fiber bending of about 2 dB. Figures 12(a) and 12(c) show the dependency of system BER performance on the optical power P_{opt} incident on the PD at 1 Gbit/s and 2.5 Gbit/s respectively. Figures 12(b) and 12(d) visualize the corresponding numbers of turns at different radii that were found to be allowable with the different fiber samples while maintaining system performance with a BER $< 10^{-6}$, while setting a BER limit of 10^{-3} does not significantly alter the picture with only a single data point being changed for each of the data rates, as indicated by the $\triangledown$ and $\triangle$ in Figs. 12(b) and 12(d) respectively. Both clearly show the benefit with respect to bending tolerance that may be obtained with BIF and correspond well to the loss margin of 2 dB. It is clear that at radii of 10 mm G.657.A1 type fiber may sufficiently reduce the encountered macrobending losses, while for even smaller radii A2/B2 and B3 fibers may be required. While in the present case no difference was seen between samples B and C, an extrapolation of their encountered loss per turn values from Fig. 11 up to the loss margin suggests as many as 11 and 14 turns to be allowable at 5 mm, while at 7.5 mm up to 38 and 126 turns respectively are expected be possible without degrading system performance.

While the margin of 2 dB for allowable bending loss is specific to the assessed system and link, the indication of requiring BIF for radii of 10 mm and below is a general one as is the scale of the benefit to be obtained by the different fiber types. This serves to highlight the trade-off to be found between system parameters such as the available power budget and logistical challenges such as the required tolerance to bending and ease of installation on one side and economical considerations such as the additional cost of BIF on the other side.

#259469 Received 23 Feb 2016; revised 3 May 2016; accepted 12 May 2016; published 17 May 2016

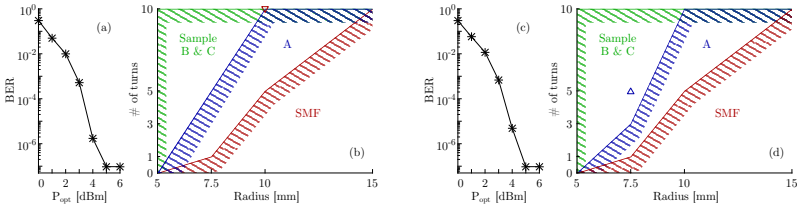

Fig. 12. BER vs P_{opt} without bending (a,b) and allowable numbers of turns at different radii (b,d) for a system performance with BER $< 10^{-6}$; wireless distance: 70 m, carrier frequency: 84 GHz. (a,b) at 1 Gbit/s ($\triangledown$: BER $= 2.0 \times 10^{-4}$ for 10 turns @ 10 mm with SMF fiber), (c,d) at 2.5 Gbit/s ($\triangle$: BER $= 2.5 \times 10^{-6}$ for 5 turns @ 7.5 mm with sample A)

5. Conclusions

The wireless channel in W-band was characterized and a radio-over-fiber transmission link with reduced complexity in the RF domain demonstrated, achieving successful transmission of a 2.5 Gbit/s signal. The wireless channel is found to be affected by multipath propagation and resulting impairments, however in the case of short distances or high link directivity it may be regarded as purely line-of-sight.

The complexity of the RoF link setup was reduced by employing a passive RF transmitter and a Schottky diode based envelope detector for signal downconversion, minimizing the number of required RF amplifiers and alleviating the need for RF mixers and a local oscillator at the receiver. Successful transmission is demonstrated for RF carriers at 75–87 GHz – i.e. the lower half of the W-band – and over wireless distances of 30–70 m, with distances of 100 m and beyond predicted to be achievable. The system is thus shown to be applicable in both indoor and outdoor scenarios, including building-to-building connections and mobile front- and backhaul.

Furthermore the performance impact of including bend insensitive fiber for on-site installation was experimentally analyzed, employing three samples of Sterlite bend insensitive fiber. A clear benefit in terms of tolerance to macrobending is found, with bend radii as small as 5 mm and more than ten turns allowable without significant degradation of system BER performance.

Through the reduction in complexity and the inclusion of bend insensitive fiber, the applicability of W-band hybrid photonic-wireless links as a key enabler for future wireless and mobile networks is highlighted and with the obtained transmission results their performance is experimentally confirmed.

Acknowledgments

This work was partly funded by the DFF FTP mmW-SPRAWL project and the EC FP7-ICT IPHOBAC-NG project under grant No. 619870. L. Cavalcante thanks the Science without Borders program for its support under scholarship agreement No. 11964-13-8.

#259469 Received 23 Feb 2016; revised 3 May 2016; accepted 12 May 2016; published 17 May 2016

PAPER6: 225m Outdoor W-Band Radio-over-Fiber Link Using an Optical SFP+ Module

S. Rommel, S. Rodriguez, L. Chorchos, E. P. Grakhova, A. K. Sultanov, J. P. Turkiewicz, J. J. Vegas Olmos, and I. Tafur Monroy. "225m Outdoor W-Band Radio-over-Fiber Link Using an Optical SFP+ Module". In: *Optical Fiber Communication Conference 2016*. Mar. 2016, paper Th2A.16. DOI: 10.1364/OFC.2016.Th2A.16

225m Outdoor W-Band Radio-over-Fiber Link Using an Optical SFP+ Module

Simon Rommel[1,*], Sebastian Rodriguez[1], Łukasz Chorchos[1,2], Elizaveta P. Grakhova[1,3], Albert Kh. Sultanov[3], Jarosław P. Turkiewicz[2], Juan José Vegas Olmos[1], Idelfonso Tafur Monroy[1]

[1]*Department of Photonics Engineering, Technical University of Denmark, 2800 Kgs. Lyngby, Denmark*
[2]*Institute of Telecommunications, Warsaw University of Technology, 00-665 Warsaw, Poland*
[3]*Department of Telecommunication Systems, Ufa State Aviation Technical University, 450000 Ufa, Russia*

[*]*sirem@fotonik.dtu.dk*

Abstract: A W-band radio-over-fiber link based on a commercial SFP+ module is demonstrated, allowing easy integration into existing PON solutions. Without active laser control good RF frequency stability and 225m wireless distance are achieved.

OCIS codes: (060.5625) Radio frequency photonics, (060.4510) Optical communications.

1. Introduction

The increasing use of bandwidth intensive applications—such as high definition video streaming and holographic video conferencing—on consumer devices has created a large demand for high-speed mobile and wireless connections. Recent advances in mobile access technology enable the latter, resulting in the need for high-speed wireless front- and optical backhaul solutions as radio access units need to be adequately connected to the core infrastructure. Additionally these front- and backhaul links must seamlessly tie in with existing distribution networks such as passive optical networks (PONs) [1]. Mm-wave radio-over-fiber (RoF) solutions stand out as a prime candidate as they combine the relatively large available bandwidth in the mm-wave bands with easy optical distribution over significant fiber distances and may coexist with other services on already deployed distribution networks [1, 2].

Mm-wave wireless transmissions for front- and backhaul have been demonstrated in a number of configurations [3, 4], of which heterodyning of two independent lasers for photonic upconversion is one of the simplest and most promising for integration of RoF links with existing infrastructure. However in oder to truly enable mm-wave backhaul scenarios they need to be based on technology already used in deployed systems, such as SFP+ modules [1].

In this work a W-band hybrid photonic wireless link is demonstrated, based on heterodyne upconversion of the signal of a commercial enhanced small form-factor pluggable (SFP+)—transmitted through 15 km of fiber—with an independent laser as local oscillator. This is, to the best of our knowledge, the first SFP+-based W-band transmission and at 2.5 Gbit/s we achieve an outdoor wireless distance of 225 m, limited only by available radio frequency power.

2. Experimental Setup

The SFP+ based W-band transmission setup with low complexity in the radio-frequency (RF) domain is depicted in Fig. 1 while Fig. 2 shows the corresponding experimental setup. A commercial SFP+ module is fed with a 2.5 Gbit/s $2^{15}-1$ bit long pseudo-random bit sequence (PRBS15) non-return-to-zero (NRZ) signal from a pulse pattern generator (PPG) to generate a modulated optical signal which is amplified and transmitted through a combination of 10 km ITU-T G.652 standard single-mode fiber (SMF) and 5 km ITU-T G.657.B3 bend insensitive fiber (BIF).

An external cavity laser (ECL) acts as a tunable local oscillator (LO) employed for heterodyne photonic upconversion on a photodiode (PD), with the optical input power P_{opt} controlled by two variable optical attenuators (VOA). The resulting RF signal is amplified by 8 dB before being transmitted over distances between 100 m and 225 m using a pair of parabolic antennas with a gain of 48 dBi each. At the receiver side a low noise amplifier (LNA) provides 40 dB gain before the signal is downconverted using a Schottky diode based W-band envelope detector (ED) with a nominal 3 dB bandwidth of 3 GHz. The baseband signal is filtered with a 1.8 GHz Bessel filter to limit noise bandwidth and recorded on a digital storage oscilloscope (DSO).

Using heterodyne photonic upconversion and employing a commercial SFP+ for signal generation the suggested setup minimizes complexity and cost in the optical domain, while maintaining low complexity in the RF domain by using envelope detection.

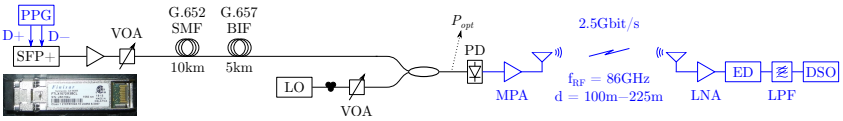

Fig. 1. Experimental setup for radio-over-fiber transmission. SFP+: enhanced small form-factor pluggable, PPG: pulse pattern generator, VOA: variable optical attenuator, LO: local oscillator, PD: photodiode, MPA: medium power amplifier, LNA: low noise amplifier, ED: envelope detector, LPF: Low-pass filter, DSO: digital storage oscilloscope.

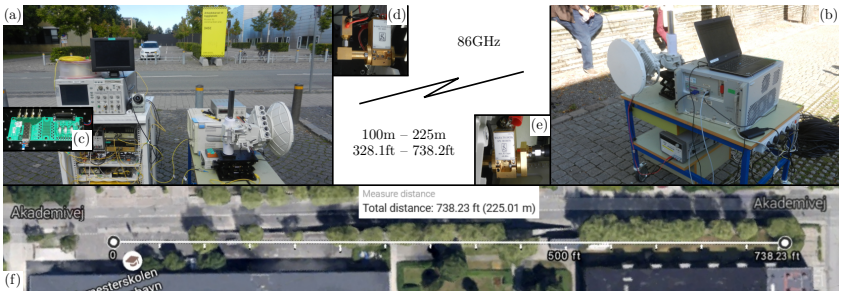

Fig. 2. Outdoor experimental setup: (a) transmitter station, (b) receiver station, (c) evaluation board with SFP+, (d) PD and MPA mounted on transmit antenna, (e) LNA and ED mounted on receive antenna, (f) geographic overview of experiment location and wireless transmission path.

3. Experimental Results

Since heterodyne photonic upconversion is performed with two independent lasers and without actively tracking the wavelength of the signal with the LO any wavelength drift of the two lasers may result in a frequency drift of the generated RF signal. Fig. 3 shows the results of an indoor stability measurement over 12 h, finding power stability of the lasers to be within ± 0.3 dB of the set power while a small wavelength drift is observed on both lasers after power on, stabilizing after ca. 2 h to small variations within ± 0.02 nm. The resulting RF carrier frequency is shown in Fig. 3 (d) and found to vary by less than ± 0.5 GHz across the whole 12 h period, despite the uncontrolled drift of laser wavelength observed after power on. This variation is small in comparison to both the bandwidth available in W-band and that of the signal, confirming no active control of the RF generation to be needed.

Hybrid photonic wireless transmission is performed over a total of 15 km of fiber and wireless distances of 100 m to 225 m while monitoring received signal quality. Error free transmission was achieved at all distances with recorded sequences of a total length >25 Mbit, suggesting a BER on the order of 10^{-7} or lower. Fig. 4 confirms this by plotting experimentally obtained Q factors over distance alongside resulting BER estimates according to (1), finding an estimated BER of 2.6×10^{-8} at 225 m and even lower error rates for shorter distances.

$$BER \approx 3/4 \mathrm{erfc}\left(Q/\sqrt{2}\right) \tag{1}$$

The observed Q factors suggest a linear relation to distance and thus the system to be limited by received power and additive white gaussian noise. They further confirm and adhere to expectations derived from previous experiments in similar conditions [4].

The presented system setup based on a commercial SFP+ module offers seamless integration of W-band radio access units into existing optical distribution schemes such as PONand WDM point-to-point links based on standard SFP+ pluggables. Despite allowing both lasers to freely drift with no tracking of the signal frequency with the LO the system achieves good frequency stability, allowing reliable transmission of a signal of 5 GHz bandwidth within an allocation of only 6 GHz. Allowing for an additional guard band of 1 GHz between channels this suggests an availability of 5 similar channels within the lightly licensed W-band.

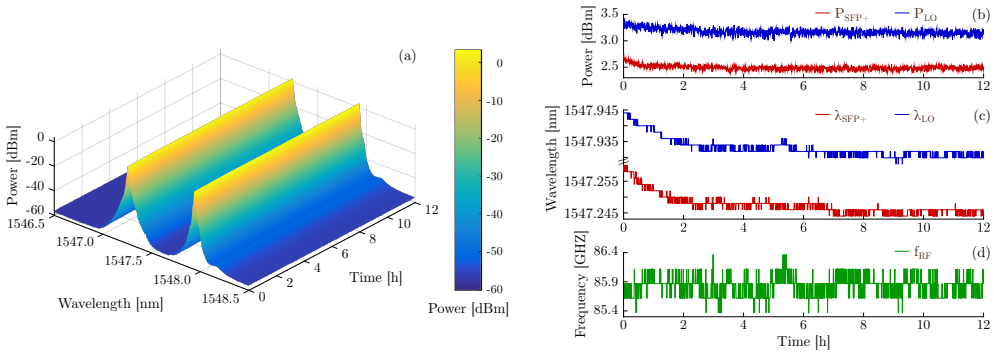

Fig. 3. SFP+ and LO laser power and wavelength and resulting RF carrier frequency stability over 12 h: (a) recorded spectra, (b) laser powers, (c) laser wavelengths, (d) RF carrier frequency.

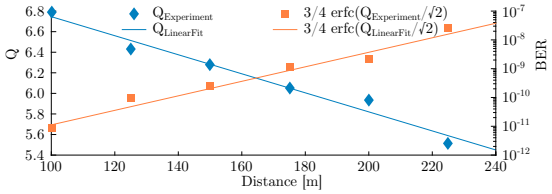

Fig. 4. Observed Q factors and derived BER estimates after 225 m wireless transmission of a 2.5 Gbit/s signal on an 86 GHz carrier.

4. Conclusions

A ROF link based on a commercial SFP+ module and employing heterodyne photonic upconversion has been demonstrated, including analysis of the frequency stability of the generated RF carrier. The observed stability suggests up to five channels of 5 GHz bandwidth to be available in the W-band and with the achieved transmission distance of 225 m only limited by available RF transmission power longer distances should be achievable. This highlights the possibility and demonstrates the feasibility of seamlessly extending existing PON structures to enable front- and backhaul to radio access units, based on commercial SFP+ modules.

Acknowledgments

This work was partly funded by the DFF FTP mmW-SPRAWL and EC IPHOBAC-NG and FiWiN5G projects.

References

1. M. P. Thakur *et al.*, "Cost-Efficient DWDM-PON / Mm-Wave Wireless Integration using Coherent Radio-over-Fiber (CRoF)," in *Proc. MWP 2015* (IEEE, Paphos, 2015), paper P-19.
2. K.-i. Kitayama, T. Kuri, J. J. Vegas Olmos, and H. Toda, "Fiber-Wireless Networks and Radio-over-Fibre Technique," in *Proc. CLEO 2008* (OSA, San Jose, 2008), paper CThR4.
3. A. R. Islam, M. Bakaul, A. Nirmalathas, and G. E. Town, "Simplification of millimeter-wave radio-over-fiber system employing heterodyning of uncorrelated optical carriers and self-homodyning of RF signal at the receiver," Opt. Express **20**, 5707–5724 (2012).
4. S. Rommel, L. C. P. Cavalcante, J. J. Vegas Olmos, and I. Tafur Monroy, "Low RF Complexity Photonically Enabled Indoor and Building-to-Building W-Band Wireless Link," in *Proc. ACP 2015* (OSA, Hong Kong, 2015), paper AM1B.7.

PAPER7: Outdoor W-Band Hybrid Photonic Wireless Link Based on an Optical SFP+ Module

S. Rommel, S. Rodriguez, L. Chorchos, E. P. Grakhova, A. K. Sultanov, J. P. Turkiewicz, J. J. Vegas Olmos, and I. Tafur Monroy. "Outdoor W-Band Hybrid Photonic Wireless Link Based on an Optical SFP+ Module". In: *IEEE Photonics Technology Letters* 28.21 (Nov. 2016), pp. 2303–2306. DOI: 10.1109/LPT.2016.2592326

Outdoor *W*-Band Hybrid Photonic Wireless Link Based on an Optical SFP+ Module

Simon Rommel, *Student Member, IEEE*, Sebastián Rodríguez, *Student Member, IEEE*, Łukasz Chorchos, *Student Member, IEEE*, Elizaveta P. Grakhova, Albert Kh. Sultanov, Jarosław P. Turkiewicz, *Senior Member, IEEE*, Juan José Vegas Olmos, *Senior Member, IEEE*, and Idelfonso Tafur Monroy, *Senior Member, IEEE*

***Abstract*— This letter proposes a *W*-band hybrid photonic wireless link based on a commercial small form-factor pluggable (SFP+) module and experimentally demonstrates its performance. Using a free running laser as local oscillator and heterodyne photonic upconversion, good frequency stability is achieved. Outdoor wireless transmission over 225 m with a bit error rate below 10^{-6} is demonstrated, and the maximum reach of the system with typical RF components is calculated, finding wireless distances above 2 km to be feasible. Being based on a commercial SFP+, the proposed hybrid photonic wireless link offers seamless integration with existing distribution networks and passive optical networks, and thus paves the way for future mobile front- and backhaul architectures.**

***Index Terms*— Radio-over-fiber, millimeter-wave communications, W-band wireless, microwave photonics, small form factor pluggables.**

I. Introduction

THE increasing use of bandwidth intensive applications—such as high definition video streaming and holographic video conferencing—on consumer devices has created a large demand for high-speed mobile and wireless connections. To enable these, a transition away from the already crowded and congested conventional wireless bands is necessary and millimeter wave (mm-wave) frequencies in the IEEE V- and W-bands (40–75 GHz and 75–110 GHz) are seen as prime candidates [1]–[4]. While the region around 60GHz has received major attention with regards to indoor wireless distribution [2], frequencies at 71–76 GHz and 81–86 GHz—commonly referred to as E-band after the corresponding waveguide band—are the prime candidates for medium and long distance mm-wave wireless links, due to the lower atmospheric absorption [2] and the large continuous spectrum allocations for wireless communications [5], [6].

Supporting the density and data rates envisioned for the coming generations of mobile networks will require major changes to front-, mid- and backhaul architectures for radio access units (RAUs) [5] and thus to the way the latter are connected to and integrated with the core infrastructure. Additionally these new front-, mid- and backhaul links must seamlessly tie in with existing optical distribution networks such as passive optical networks (PONs) [1], [7]. Radio-over-fiber (RoF) links in the mm-wave range stand out as prime candidates since they combine the relatively large available bandwidths in the mm-wave bands with the easy optical distribution over significant fiber distances [1], [8].

Mm-wave photonic wireless links have been demonstrated in a number of configurations [6]–[13], of which heterodyning of two independent lasers for photonic upconversion is one of the most promising for integration with existing optical distribution infrastructure [7]. However in order to make these truly feasible they do not only need to easily integrate with already deployed systems, but also need to be based on technology already used therein, such as enhanced small form-factor pluggable modules (SFP+) [7].

In [13] a W-band photonic wireless link based on a commercial SFP+ module was demonstrated, enabling seamless integration with existing optical distribution networks based on SFP+ modules, such as PONs and wavelength division multiplexing (WDM) point-to-point links. The radio frequency (RF) signal is generated through heterodyne photonic upconversion with an independent laser as local oscillator. This was, to the best of our knowledge, the first SFP+ based W-band transmission and at 2.5Gbit/s achieved an outdoor wireless distance of 225m. In this letter we discuss the link and setup in more detail and give a calculation of the maximum achievable distance with increased transmission power, using readily available mm-wave RF equipment and showing wireless distances in excess of 2km to be within reach.

The letter is structured as follows: section II describes the SFP+ based setup and section III discusses the experimental results, including analysis of the frequency stability of the generated RF signal (III-A), transmission performance for wireless distances of 100–225 m (III-B) and evaluation of the maximum wireless range of the presented setup (III-C). Section III-D gives a short discussion of the results, before finally section IV summarizes and concludes the letter.

Manuscript received March 4, 2016; revised June 28, 2016; accepted July 14, 2016. Date of publication July 18, 2016; date of current version September 28, 2016. This work was supported in part by the Det Frie Forskningsråd Technology and Production Sciences through the mmW-SPRAWL Project and in part by Cordis within the European Commission through the Integrated Photonic Broadband Radio Access Units for Next Generation Optical Access Networks Project and through the Fiber-Wireless Integrated Networks for 5th Generation Delivery Project under Grant 619870 and Grant 642355.

S. Rommel, S. Rodríguez, J. J. Vegas Olmos, and I. Tafur Monroy are with the Department of Photonics Engineering, Technical University of Denmark, Kongens Lyngby 2800, Denmark (e-mail: sirem@fotonik.dtu.dk; juse@fotonik.dtu.dk; jjvo@fotonik.dtu.dk; idtm@fotonik.dtu.dk).

Ł. Chorchos and J. P. Turkiewicz are with the Institute of Telecommunications, Warsaw University of Technology, Warsaw 00-665, Poland (e-mail: lukaszchorchos@gmail.com; jturkiew@tele.pw.edu.pl).

E. P. Grakhova and A. Kh. Sultanov are with the Department of Telecommunication Systems, Ufa State Aviation Technical University, Ufa 450008, Russia (e-mail: eorlingsbest@mail.ru; tks@ugatu.ac.ru).

Color versions of one or more of the figures in this letter are available online at http://ieeexplore.ieee.org.

Digital Object Identifier 10.1109/LPT.2016.2592326

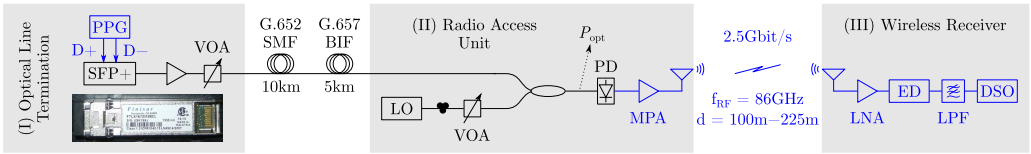

Fig. 1. Experimental setup for hybrid photonic wireless transmission. SFP+: enhanced small form-factor pluggable, PPG: pulse pattern generator, VOA: variable optical attenuator, LO: local oscillator, PD: photodiode, MPA: medium power amplifier, LNA: low noise amplifier, ED: envelope detector, LPF: low-pass filter, DSO: digital storage oscilloscope.

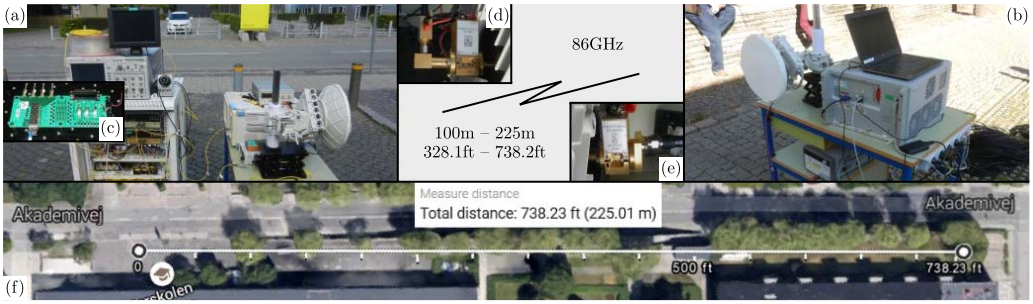

Fig. 2. Outdoor experimental setup: (a) transmitter station, (b) receiver station, (c) evaluation board with SFP+, (d) PD and MPA mounted on transmit antenna, (e) LNA and ED mounted on receive antenna, (f) geographic overview of experiment location and wireless transmission path.

II. SFP+ Based W-Band Transmission Setup

The SFP+ based W-band transmission setup is depicted in Fig. 1 and consists of three sections which in a deployment case would be geographically separate:

(I) *Optical Line Termination*: generates the optical signal, based on a commercial enhanced small form-factor pluggable (SFP+). Linked by optical fiber transmission to
(II) *Radio Access Unit*: performs optical to radio-frequency conversion and allows W-band wireless transmission to
(III) *Wireless Receiver*: receives the W-band signal and down-converts it to baseband.

The outdoor experimental setup is shown in Fig. 2 and consists of a transmitter station—where optical line termination (OLT), fiber transmission and radio access unit (RAU) are co-located—and a receiver station. The optical signal is generated using a SFP+ module (Finisar FTLX1672M3BCL), which includes a limiting driver and is fed a 2.5Gbit/s $2^{15}-1$ bit long pseudo-random bit sequence (PRBS15) non-return-to-zero (NRZ) signal from a pulse pattern generator (PPG). The output of the SFP+ has an extinction ratio of 9dB and 0dBm optical power. The signal is amplified and transmitted through a combination of 10km ITU-T G.652 standard single-mode fiber (SMF) and 5km ITU-T G.657.B3 bend insensitive fiber (BIF), representing a typical optical link and allowing for the inclusion of BIF for on-site installation and antenna feeding.

For optical to RF conversion an external cavity laser (ECL) acts as a tunable local oscillator (LO) for heterodyne photonic upconversion on a photodiode (PD). The optical input power P_{opt} incident on the PD is controlled through two variable optical attenuators (VOAs), allowing separate adjustment of signal and LO powers. The RF signal is amplified by 8dB using a medium power RF amplifier (MPA) before being transmitted over 100–225 m using a pair of parabolic antennas with a gain of 48dBi each.

At the receiver station a low noise amplifier (LNA) provides 40dB gain before the signal is downconverted using a Schottky diode based W-band envelope detector (ED) with a nominal 3dB bandwidth of 3GHz. A low pass Bessel filter with a 3dB cutoff frequency of 1.8GHz limits noise bandwidth before the signal is recorded on a digital storage oscilloscope (DSO) to determine received signal quality and for offline error counting to estimate bit error rates (BER).

The suggested setup minimizes cost and complexity in the optical domain by using heterodyne photonic upconversion and by employing a commercial SFP+ for signal generation, which further allows easy integration with existing deployed infrastructure. The use of envelope detection allows a simple RF setup at the receiver, while the RF transmitter requires only a single MPA.

III. Experimental Results

A. Frequency Stability of the Generated mm-Wave Signal

Frequency stability of the RF signal is a requirement in any wireless transmission and thus the stability of the signal generated with the SFP+ based setup has been analyzed. With a free running laser as LO and no tracking of signal wavelength, any wavelength drift of the two involved lasers may result in a frequency drift of the generated RF signal and thus spectra of the optical signal just before upconversion have been recorded over 12h at intervals of 30s. Fig. 3 (a) shows the recorded spectra over time, while Fig. 3 (b) and (c) show laser powers and frequencies; Fig. 3 (d) finally shows the frequency of the generated RF carrier over time. Power stability of the lasers is found to be within ±0.3dB of the power levels set, while on the laser wavelength a small drift is observed after power on,

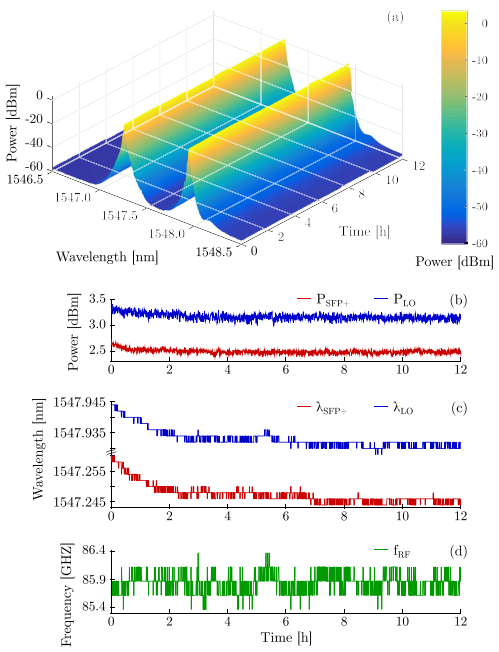

Fig. 3. SFP+ and LO laser power and wavelength and resulting RF carrier frequency stability over 12h: (a) recorded spectra, (b) laser powers, (c) laser wavelengths, (d) RF carrier frequency.

stabilizing to variation within ±0.02nm after ca. 2h. With both lasers only featuring basic in-package cooling, similar or better stability may be achieved with improved temperature control, even if signal generation and upconversion take place under different ambient conditions.

The resulting RF carrier is found to vary by less than ±0.5GHz across the whole 12h period, despite the wavelength drift observed after power on. While clearly above the ±150ppm recommended by the ITU-R [14], such a variation may be acceptable for a highly directive point to point transmission link with a large bandwidth and is found to not affect the presented system. To adhere to ITU-R recommendations, setups based on a single laser are likely to be required [15] and thus a trade-off between complexity, easy integration with PON systems and RF frequency stability needs to be found.

B. Outdoor W-Band Wireless Transmission Results

W-band wireless transmission is performed outdoors on the university campus over distances of 100–225 m. The optical power incident on the photodiode P_{opt} is set to 5dBm and the received signal quality is monitored in distance steps of 25m. Transmission was found to be error free at all distances with recorded sequences of a total length >25 Mbit, suggesting a BER on the order of 10^{-7} or lower. Calculation of the Q factor of the received signals and estimating BER as:

$$Q = \frac{\mu_1 - \mu_0}{\sigma_1 + \sigma_0} \tag{1}$$

$$BER \approx 3/4\text{erfc}\left(Q/\sqrt{2}\right) \tag{2}$$

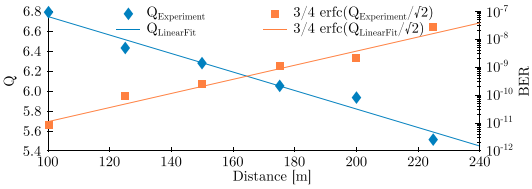

Fig. 4. Observed Q factors and derived BER estimates after 225m wireless transmission of a 2.5Gbit/s signal on an 86GHz carrier.

(where μ_0, μ_1 are the mean values of the signal levels and σ_0, σ_1 their standard deviation) finds an estimated BER of 2.6×10^{-8} at 225m and even lower error rates for shorter distances, confirming the performance estimate derived from observing no errors. This confirms the viability of using a SFP+ in ROF links despite its larger linewidth and lower extinction ratio and suggests higher order amplitude modulation formats to be possible if an SFP+ with linear drivers is used.

Fig. 4 plots the obtained Q factors over distance alongside resulting BER estimates, suggesting a linear relation with distance and thus the system to be limited by available transmitter power and additive white Gaussian noise. They further confirm and adhere to expectations derived from previous experiments in similar conditions [8] and that due to its high directivity the link may be considered practically line-of-sight, even at 225m wireless distance.

C. Maximum Achievable Wireless Distance

Further comparison of transmission performance with that found in [8] where a similar setup—in particular the same receiver—was employed, allows estimation of the maximum achievable distance for a system limited by the available RF transmitter power. From the photocurrents observed at the optical to RF conversion stage the RF signal level P_{PD} generated by the PD at a reference optical power of $P_{opt} =$ 5dBm is easily estimated and found to be −9dBm. Together with the antenna gains and the loss observed in the wireless channel this allows an estimation of the receiver sensitivity.

Assuming line of sight transmission, the loss in the wireless channel L can be estimated as the sum of free space propagation loss L_{FS} following the Friis' model and the atmospheric absorption L_A [2], [4]:

$$L_{FS} = 10\log\left((4\pi df/c)^2\right) = 20\log(4\pi df/c) \tag{3}$$

$$L = L_{FS} + L_A d = 20\log(4\pi df/c) + L_A d \tag{4}$$

where c is the speed of light in vacuum, f the carrier frequency and d the transmission distance; an atmospheric absorption L_A of 0.2dB/km for transmission at 86GHz [2] is used for receiver sensitivity and maximum distance estimations. The received power P_{Rx} at the output of the receiver antenna is then easily estimated from the generated RF power P_{PD}, the amplifier gains at the transmitter G_{Amp}, the antenna gains G_{Tx} and G_{Rx} and the attenuation during transmission L:

$$P_{Rx} = P_{PD} + G_{Amp} + G_{Tx} - L + G_{Rx} \tag{5}$$

With Eq. (5) the values from this letter and those of [8] independently yield a receiver sensitivity of −23dBm.

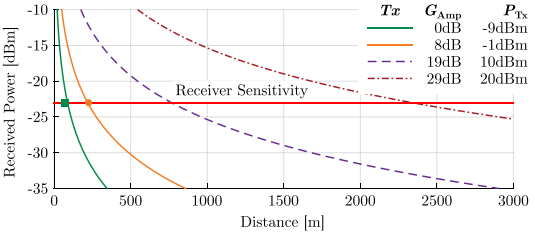

Fig. 5. Received powers over distance for different RF transmitter configurations; ■: experimental data from [8], ●: experimental data in this letter.

TABLE I
MAXIMUM ACHIEVABLE WIRELESS DISTANCE

Amplifiers	P_{PD} [dBm]	G_{Amp} [dB]	P_{Tx} [dBm]	d_{Max} [m]
none	−9	0	−9	85
MPA1	−9	8	−1	220
LNA	−9	19	10	770
LNA+MPA2	−9	29	20	2340

With the receiver sensitivity known, the maximum wireless reach of the system can be estimated, depending on the received optical power and the RF amplifier configuration at the wireless transmitter. Fig. 5 shows received power over distance for a number of amplifier configurations and Table I compares the corresponding radiated powers and maximum achievable distances. The calculated distances of 85–2340 m fit the experimentally demonstrated distances of this letter and [8] and suggest distances in excess of 2km to be reachable with only two amplifiers required at the transmitter and while maintaining the same low complexity Schottky diode based wireless receiver. It should be noted however that for links of such distances, multipath propagation and associated fading may come in to effect [4], making the link no longer line-of-sight as considered in [8] and this letter.

D. Discussion

Using the signal from a standard commercial SFP+, the presented system is designed to use equipment already deployed in distribution networks such as PONs. With a free running laser as local oscillator it enables hybrid RAUs for mobile front-, mid- and backhaul, while demonstrating seamless integration beyond that of [7]. The system combines a commercial SFP+, a free running LO for up- and envelope detection for downconversion to offer a radio-over-fiber link with high capacity, large wavelength drift tolerance and seamless integration with existing optical distribution networks.

Analysis of transmission performance shows bit error rates below 10^{-6} at a wireless distance of 225m and evaluation of the maximum wireless reach of the proposed system shows wireless links of up to 2340m to be possible. The system achieves sufficient frequency stability to allow reliable transmission of a 2.5Gbit/s signal, despite allowing both lasers to drift freely. Allowing a guard band of 1.5GHz between channels, this suggests an availability of 5 channels in the lightly licensed W-band. With 15km of fiber transmission included in the experiment this demonstrates that the reach necessary for future front-, mid- or backhaul links can be achieved with readily available technology.

IV. CONCLUSIONS

In this letter a hybrid photonic wireless link based on a commercial SFP+ module and employing heterodyne photonic upconversion has been demonstrated. Experimental analysis includes frequency stability measurement of the generated RF signal and wireless transmission over distances up to 225m at data rates of 2.5Gbit/s with BER $< 10^{-6}$. Wireless distance is found to be limited only by the available transmitter RF power and calculation of the maximum achievable distance with typical RF amplifiers at the transmitter yields a wireless reach of well above 2km, confirming the potential of long distance mm-wave links.

The presented system setup based on a commercial SFP+ module offers seamless integration of hybrid W-band radio access units into existing optical distribution schemes, such as PON and WDM point-to-point links based on standard commercial SFP+ modules.

REFERENCES

[1] K.-I. Kitayama, T. Kuri, J. J. Vegas Olmos, and H. Toda, "Fiber-wireless networks and radio-over-fibre technique," in *Proc. CLEO*, 2008, pp. 1–2, paper CThR4.
[2] J. Wells, "Faster than fiber: The future of multi-G/s wireless," *IEEE Microw. Mag.*, vol. 10, no. 3, pp. 104–112, May 2009.
[3] P. T. Dat, A. Kanno, and T. Kawanishi, "Bidirectional transmission of LTE-A carrier aggregation signal over a seamless fiber-wireless system in W-band," in *Proc. OFC*, 2015, pp. 1–3, paper W1F.5.
[4] S. Rommel, L. C. P. Cavalcante, A. G. Quintero, A. K. Mishra, J. J. Vegas Olmos, and I. Tafur Monroy, "W-band photonic-wireless link with a Schottky diode envelope detector and bend insensitive fiber," *Opt. Exp.*, vol. 24, no. 11, pp. 11312–11322, 2016.
[5] T. Pfeiffer, "Next generation mobile fronthaul and midhaul architectures," *J. Opt. Commun. Netw.*, vol. 7, no. 11, pp. B38–B45, 2015.
[6] S. Rommel, L. C. P. Cavalcante, J. J. Vegas Olmos, I. Tafur Monroy, and A. K. Mishra, "Requirements for bend insensitive fiber in millimeter-wave fronthaul systems," in *Proc. IEEE MWP*, Oct. 2015, pp. 1–4.
[7] M. P. Thakur, S. Mikroulis, C. C. Renaud, J. J. Vegas Olmos, M. C. R. Medeiros, and J. E. Mitchell, "Cost-efficient DWDM-PON/mm-wave wireless integration using coherent radio-over-fiber (CRoF)," in *Proc. IEEE MWP*, Oct. 2015, pp. 1–4.
[8] S. Rommel, L. C. P. Cavalcante, J. J. Vegas Olmos, and I. Tafur Monroy, "Low RF complexity photonically enabled indoor and building-to-building W-band wireless link," in *Proc. ACP*, 2015, pp. 1–3, paper AM1B.7.
[9] A. Hirata *et al.*, "Transmission characteristics of 120-GHz-band wireless link using radio-on-fiber technologies," *J. Lightw. Technol.*, vol. 26, no. 15, pp. 2338–2344, Aug. 1, 2008.
[10] A. H. M. Razibul Islam, M. Bakaul, A. Nirmalathas, and G. E. Town, "Simplification of millimeter-wave radio-over-fiber system employing heterodyning of uncorrelated optical carriers and self-homodyning of RF signal at the receiver," *Opt. Exp.*, vol. 20, no. 5, pp. 5707–5724, 2012.
[11] A. Kanno *et al.*, "Coherent radio-over-fiber and millimeter-wave radio seamless transmission system for resilient access networks," *IEEE Photon. J.*, vol. 4, no. 6, pp. 2196–2204, Dec. 2012.
[12] J. Xiao, J. Yu, X. Li, Y. Xu, Z. Zhang, and L. Chen, "20-Gb/s PDM-QPSK signal delivery over 1.7-km wireless distance at W-band," in *Proc. OFC*, 2015, pp. 1–3, paper W4G.4.
[13] S. Rommel *et al.*, "225 m outdoor W-band radio-over-fiber link using an optical SFP+ module," in *Proc. OFC*, 2016, pp. 1–3, paper Th2A.16.
[14] *Frequency Tolerance of Transmitters*, document Rec. ITU-R SM.1045-1, 1997.
[15] A. Kanno *et al.*, "Evaluation of frequency fluctuation in fiber-wireless link with direct IQ down-converter," in *Proc. IEEE ECOC*, Sep. 2014, pp. 1–3.

PAPER8: Demonstration of 4Gbit/s Duobinary Ka-Band Hybrid Photonic-Wireless Transmission

S. Rommel, L. Yi, M. Shi, I. Tafur Monroy, and J. J. Vegas Olmos. "Demonstration of 4Gbit/s Duobinary Ka-Band Hybrid Photonic-Wireless Transmission". In: *Asia Communications and Photonics Conference 2015*. Nov. 2015, paper ASu1J.2. DOI: 10.1364/ACPC.2015.ASu1J.2

Demonstration of 4Gbit/s Duobinary Ka-Band Hybrid Photonic-Wireless Transmission

Simon Rommel[1], Lilin Yi[2], Mengyue Shi[2], Idelfonso Tafur Monroy[1], J. J. Vegas Olmos[1]

[1]*Department of Photonics Engineering, Technical University of Denmark, 2800 Kgs. Lyngby, Denmark*
[2]*State Key Laboratory of Advanced Optical Communication Systems and Networks, Shanghai Jiao Tong University, Shanghai 200240, China*
sirem@fotonik.dtu.dk

Abstract: We demonstrate transmission of a 4Gbit/s duobinary signal over a Ka-band hybrid photonic-wireless link consisting of 12.5km SMF and 2m wireless distance, using RF carrier frequencies aligned with the Ka-band spectrum allocations for mobile communications.
OCIS codes: (060.5625) Radio frequency photonics; (060.4510) Optical communications.

1. Introduction

The ever increasing demand for high-speed mobile data services and resulting need for larger bandwidth channels have brought millimeter wave (mmW) carrier frequencies into the focus for future wireless communications [1–3]. In the IEEE Ka-band, i.e. the frequency range between 26.5 GHz and 40 GHz and thus the lower edge of the mmW range, two bands around 28 GHz and 36 GHz have been allocated for possible use in mobile communication networks with an additional allocation in the adjacent K-band at 24 GHz. These bands have attracted considerable interest [1, 2] and channel characterizations have found them suitable for both indoor and outdoor communications [1].

Although these bands allow for larger channel bandwidths the efficient use thereof remains an important issue and a trade-off between spectral efficiency and the complexity of transmitting and receiving equipment must be found. Duobinary signaling has been shown to allow doubling the spectral efficiency compared to on-off keying [4–6] while maintaining receiver simplicity.

In this paper we demonstrate transmission of a 4 Gbit/s duobinary signal over a Ka-band hybrid photonic-wireless link, including fiber transmission over 12.5 km and wireless distances up to 2 m.

2. Duobinary Signaling

Polybinary or partial response signaling has been proposed to reduce the spectral occupation of a signal by introducing correlation between adjacent transmission symbols [4–6]. In the case where a polybinary sequence is generated digitally rather than through strong filtering of an NRZ signal [7] this correlation is introduced by transmitting an M-level sequence $\{c_k\}$ where each symbol is the algebraic sum of the current and $M-2$ preceding bits of the sequence $\{b_k\}$:

$$c_k = \sum_{i=0}^{M-2} b_{k-i} \tag{1}$$

If the elements of the latter are obtained from an input bit sequence $\{a_k\}$ and $M-2$ of its own previous elements according to the precoding relationship

$$b_k = a_k \oplus b_{k-1} \oplus b_{k-2} \oplus \ldots \oplus b_{k-M+2} \tag{2}$$

(where $\oplus$ represents the exclusive-or binary logic), then at the receiver an estimate $\{\hat{a}_k\}$ of the sequence $\{a_k\}$ can be recovered element-wise by a simple symbol-by-symbol detector performing the modulo 2 operation on the value of the elements of the received sequence $\{\hat{c}_k\}$

$$\hat{a}_k = \hat{c}_k \bmod 2 \tag{3}$$

preventing error propagation which would affect uncoded polybinary signaling [5].

For duobinary signaling—the simplest case of polybinary signaling with $M = 3$—this allows a reduction of spectral occupation by a factor of two as shown in Fig. 1, comparing the bandwidth of 4 Gbit/s NRZ and duobinary signals generated with an arbitrary waveform generator. The observed 3 dB bandwidths of 1.5 GHz and 0.75 GHz and 10 dB bandwidths of 2.8 GHz and 1.4 GHz respectively further show the 10 dB bandwidth of the duobinary signal to be below the 3 dB bandwidth of the NRZ signal of the same data rate.

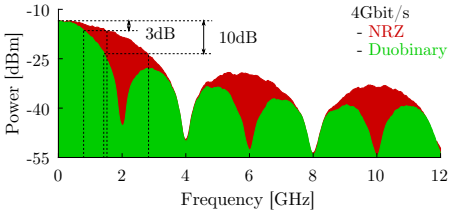

Fig. 1. Comparison of the bandwidth requirements for 4 Gbit/s NRZ and duobinary signals obtained from an arbitrary waveform generator

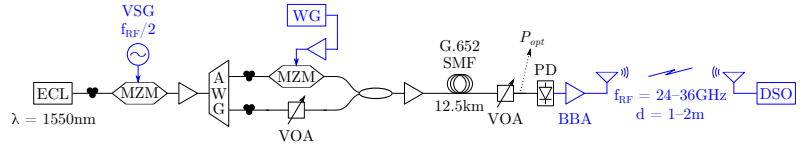

Fig. 2. Experimental setup for Ka-band hybrid photonic-wireless transmission. ECL: external cavity laser, VSG: vector signal generator, MZM: Mach-Zehnder modulator, AWG: arrayed waveguide grating, WG: arbitrary waveform generator, VOA: variable optical attenuator, SMF: single-mode fiber, PD: photodiode, BBA: RF broadband amplifier, DSO: digital storage oscilloscope

3. Experimental Setup

The Ka-band transmission setup is depicted in Fig. 2. Photonic up-conversion is employed at the transmitter, consisting of an external cavity laser (ECL) at $\lambda = 1550\,\text{nm}$, followed by a Mach-Zehnder modulator (MZM) driven with a sinusoidal at $f_{RF}/2$ to generate two spectral lines spaced at f_{RF}. While the wavelength of the ECL is constant, the driving frequency for the MZM is varied in order to generate line spacings between 24 GHz and 36 GHz.

The signal is amplified and an arrayed waveguide grating (AWG) separates the two lines while suppressing the residual carrier, allowing one line to be modulated with a 4 Gbit/s duobinary signal in a second MZM driven by the amplified output of an arbitrary waveform generator (WG). The duobinary signal is generated offline by precoding a $2^{15}-1$ bit long pseudo-random bit sequence (PRBS15) according to (2) and duobinary signal generation as in (1); it is upsampled to 12 GSa/s and uploaded to the output memory of the WG. The two signal lines are recombined, amplified and transmitted through 12.5 km of ITU-T G.652 standard single-mode fiber (SMF).

At the transmit antenna a variable optical attenuator (VOA) allows variation of the optical power P_{opt} incident on the photodiode (PD) between 0 dBm and 8 dBm, thus affording control over the power of the output RF signal at f_{RF} resulting from the beating of the two signal lines on the PD. The RF signal is amplified with a broadband RF amplifier (BBA) with a nominal gain and 3 dB bandwidth of 29 dB and 38 GHz respectively. A pair of Ka-band pyramidal horn antennas—with a gain of 20 dBi each—allows wireless transmission of the RF signal.

The received signal is directly recorded using a digital storage oscilloscope (DSO) and digitally bandfiltered, down-converted and low-pass filtered in offline signal processing. Finally bit-error rate (BER) values are determined through symbol-by-symbol detection as per (3) and error counting over multiple recorded sequences with a combined length >1 Mbit.

4. Experimental Results

We demonstrate transmission of a 4 Gbit/s duobinary signal over a hybrid photonic-wireless link using RF carrier frequencies in the Ka-band. Transmission performance is analyzed as a function of optical power P_{opt} incident on the PD and for carrier frequencies representative of the frequency bands allocated to mobile transmissions in the Ka-band.

Fig. 3 shows obtained BER values for transmission over 12.5 km of SMF and wireless distances of 1 m and 2 m, using RF carriers at 24 GHz, 28 GHz and 36 GHz. In all cases transmission performance increases with increasing power on the PD—and thus increasing RF power—up to an optimum of about $P_{opt} = 5\,\text{dBm}$, beyond which performance begins

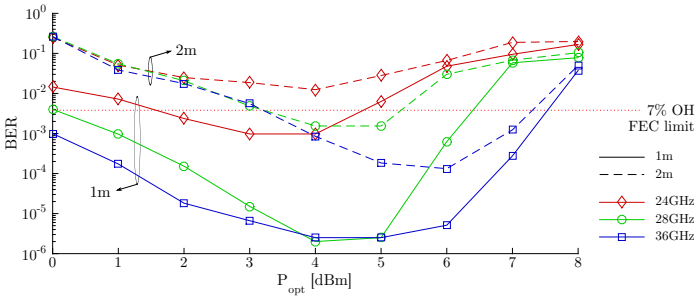

Fig. 3. Evolution of BER vs P_{opt} for a 4 Gbit/s duobinary signal on different RF carrier frequencies after transmission over 12.5 km SMF and wireless distances of 1 m and 2 m

to degrade due to the PD becoming saturated.

While the performance with Ka-band carriers at 28 GHz and 36 GHz is very similar—with slight improvements from higher antenna gain and directivity for the higher frequency carrier—the performance of the K-band carrier at 24 GHz is severely degraded by being at the very edge of the antenna transmission region. Consequently while at 1 m wireless distance and optimum incident power the performance of all carriers remains below the $3.8 \cdot 10^{-3}$ BER limit of a 7 % overhead (OH) commercial forward error correction (FEC), at 2 m this is only case for the Ka-band carriers. The limitation of transmission distance is due to low received RF powers and the consequent impact of quantization noise; an extension of transmission distance is expected to be possible through introducing additional RF amplification.

5. Conclusions

In this work we demonstrated transmission of a 4 Gbit/s duobinary signal over a Ka-band hybrid photonic-wireless link employing a set of RF carriers in the frequency bands allocated for possible use in mobile communications. Transmission with BER below the limit of a commercial FEC with 7 % overhead is achieved over 12.5 km SMF and 2 m wireless distance.

Acknowledgments

This work was partly funded by the DFF FTP mmW-SPRAWL, EC IPHOBAC-NG and Villum Kann Rasmusen SEES projects.

References

[1] H. Zhao, R. Mayzus, S. Sun, M. Samimi, J. K. Schulz, Y. Azar, K. Wang, G. N. Wong, F. Gutierrez, and T. S. Rappaport, "28 GHz millimeter wave cellular communication measurements for reflection and penetration loss in and around buildings in new york city," in *Proc. ICC 2013* (IEEE, Budapest, 2013), pp. 5163–5167.

[2] T. Hirasawa, K. Minoguchi, M. Oishi, S. Akiba, J. Hirokawa, and M. Ando, "Amplitude modulated digital signal transmission in RoF system for MMW-RF antenna beam steering," in *Proc. OECC 2015* (Shanghai, 2015).

[3] S. Rommel, A. Galvis Quintero, L. C. P. Cavalcante, J. J. Vegas Olmos, and I. Tafur Monroy, "Channel characterization for high-speed W-band wireless communication links," in *Proc. OECC 2015* (Shanghai, 2015).

[4] A. Lender, "Correlative digital communication techniques," IEEE Trans. Commun. Technol. **12**, pp. 128–135 (1964).

[5] R. D. Howson, "An analysis of the capabilities of polybinary data transmission," IEEE Trans. Commun. Technol. **13**, p. 312–319 (1965).

[6] A. Sekey, "An analysis of the duobinary technique," IEEE Trans. Commun. Technol. **14**, pp. 126–130 (1966).

[7] J. J. Vegas Olmos, L. F. Suhr, B. Li, and I. Tafur Monroy, "Five-level polybinary signaling for 10Gbps data transmission systems," Opt. Express **21**, pp. 20417–20422 (2013).

PAPER9: 15Gbit/s Duobinary Transmission Over a W-Band Radio-over-Fiber Link

S. Rommel, J. J. Vegas Olmos, and I. Tafur Monroy. "15Gbit/s Duobinary Transmission Over a W-Band Radio-over-Fiber Link". In: *Advances in Wireless and Optical Communications 2016*. Nov. 2016, pp. 197–200. DOI: 10.1109/RTUWO.2016.7821883

15Gbit/s Duobinary Transmission Over a W-Band Radio-over-Fiber Link

Simon Rommel, Juan José Vegas Olmos, Idelfonso Tafur Monroy
Department of Photonics Engineering
Technical University of Denmark
2800 Kgs. Lyngby, Denmark
sirem@fotonik.dtu.dk

***Abstract*—In this paper the transmission of a 15Gbit/s duobinary signal over a W-band hybrid photonic wireless link is demonstrated experimentally. The radio-over-fiber link consists of 10km SMF and a wireless distance of 50m, utilizing RF carriers at 83–87GHz. Transmission of a 15Gbit/s duobinary signal is achieved with a BER of 2.9×10^{-3}, i.e. below the limit for a 7% overhead FEC.**

***Index Terms*—Radio-over-fiber, millimeter-wave communications, W-band wireless, duobinary transmission.**

I. Introduction

Mobile and wireless connections have evolved to become the most common data connection, providing access to the internet anywhere and at any time for billions of users around the globe [1]. With their abundance and the increased wireless use of bandwidth intensive applications—such as video conferencing, online gaming and cloud storage—however, come challenges to the availability of link capacity and radio spectrum. The use of wireless frequencies in the millimeter-wave (mm-wave) range has been suggested for mobile access, mobile front-, mid- and backhaul as well as for direct point-to-point wireless access [2]–[4]. While for indoor, short-distance wireless distribution the region around 60 GHz is the major focus [2], the IEEE W-band—i.e. frequencies in the range 75–110 GHz—is seen as the prime candidate for medium and long distance mm-wave wireless links, but to its lower atmospheric absorption [2] and the large continuous spectrum allocations for wireless communications under light licensing conditions [5]–[7].

The use of polybinary—or partial response—signaling, where a correlation between adjacent symbols is introduced to reduce a signal's spectral width, was suggested and discussed in the 1960s [8]–[10] and has more recently attracted significant interest as a possible candidate to increase the capacity available from severely band-limited channels [11]–[18].

In this paper duobinary signaling is employed for high data rate transmission over a mm-wave radio-over-fiber (RoF) link consisting of 10 km ITU-T G.652 [19] standard single mode fiber (SMF) and a wireless distance of 50 m. Photonic upconversion allows direct generation of radio frequency (RF) signals in the IEEE W-band, carrying the duobinary signal, while a balanced mixer is employed at the receiver for signal downconversion. Transmission of a 15 Gbit/s duobinary signal is achieved with a bit error rate (BER) below the limit of a commercial 7 % overhead forward error correction (FEC), demonstrating the viability of duobinary signaling to increase the capacity achievable in mm-wave RoF links without significantly increasing complexity. Demonstrating transmission at data rates of 11.6 Gbit/s, 12.5 Gbit/s and 15 Gbit/s the system lends itself ideally as a wireless bridge, allowing the transport of ITU-T G.709 OTU2, OTU2e and OTU2f signals [20] while allowing for a sufficient overhead.

The remainder of this paper is structured as follows: section II discusses duobinary signal generation and the signals employed in the experiment, section III discusses the transmission setup, while section IV presents and discusses the achieved results. Section V finally summarizes and concludes the paper.

II. Duobinary Signaling

In polybinary signaling, a correlation between adjacent symbols is introduced to reduce a signal's spectral width, while maintaining the symbol and data rate. The correlation between the adjacent symbols may be introduced digitally by transmitting a sequence $\{c_k\}$ with M signal levels, where each symbol is the algebraic sum of the current and $M-2$ previous bits of the bit sequence $\{b_k\}$

$$c_k = \sum_{i=0}^{M-2} b_{k-i} \tag{1}$$

or through strong filtering of the signal—in digital signal processing or with the help of analog filters. The bit sequence $\{b_k\}$ is obtained from the input bit sequence $\{a_k\}$ through a pre-coding, applied in order to prevent error propagation and to facilitate easy symbol by symbol detection at the receiver [9]:

$$b_k = a_k \oplus b_{k-1} \oplus b_{k-2} \oplus \ldots \oplus b_{k-M+2} \tag{2}$$

(where $\oplus$ represents the exclusive-or binary logic). A simple symbol-by-symbol detector performing the modulo 2 operation on the value of the elements of the received sequence $\{\hat{c}_k\}$ then allows the receiver to gain an estimate $\{\hat{a}_k\}$ of the original bit sequence $\{a_k\}$:

$$\hat{a}_k = \hat{c}_k \bmod 2 \tag{3}$$

Obviously a combination of the digital pre-coding and multilevel signal generation with a digital or analog filter may

978-1-5090-1535-1/16/$31.00 ©2016 IEEE

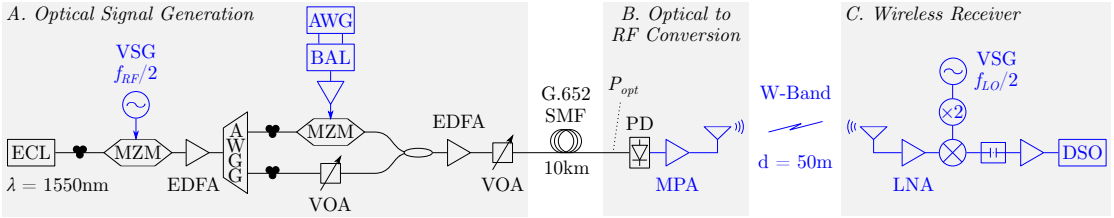

Fig. 2. Schematic of the experimental setup; ECL: external cavity laser, MZM: Mach-Zehnder modulator, VSG: vector signal generator, RF: radio frequency, EDFA: erbium doped fiber amplifier, AWGG: arrayed waveguide grating, AWG: arbitrary waveform generator, BAL: balun, VOA: variable optical attenuator, SMF: standard single mode fiber, PD: photodiode, MPA: medium power amplifier, LNA: low noise amplifier, LO: local oscillator, DSO: digital storage oscilloscope.

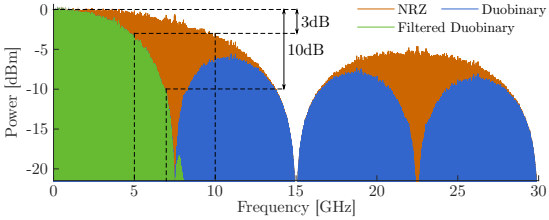

Fig. 1. Normalized spectrum of the generated filtered duobinary signal at a speed of 15 Gbit/s, compared to the normalized specra of an unfiltered duobinary signal and an NRZ signal of the same data rate.

combine the advantage of preventing error propagation with that of achieving a stronger suppression of the signal components outside the desired range.

In the presented work a number of duobinary signals—i.e. the simplest case of polybinary signaling with $M = 3$—is generated according to Eqs. (2) and (1) and digitally filtered to half the signal baud rate. The thus generated signals have half the 3 dB bandwidth of non-return to zero (NRZ) of the same bit- and baudrate, but further feature a much increased suppression at higher frequencies, as observed in Fig. 1.

In the presented case of a 15 Gbit/s signal, 3 dB bandwidths of 10 GHz and 5 GHz are observed for the NRZ and duobinary signals respectively, while the filtered duobinary signal additionally features a 10 dB bandwidth of only 7 GHz.

III. Experimental Setup

The experimental setup used to demonstrate high-capacity duobinary transmission over a hybrid photonic-wireless link is schematically shown in Fig. 2 and consists of three sections that are linked by fiber and wireless transmission respectively. An optical signal with two spectral lines spaced at the desired frequency of the radio carrier f_{RF} and carrying the duobinary signal is generated at the transmitter station—the equivalent to an optical line terminal (OLT) in a passive optical network (PON). The signal is transmitted through 10 km of ITU-T G.652 standard single mode fiber (SMF) to the optical to radio frequency (RF) conversion station, converting the signal to a mm-wave RF signal and constituting the equivalent of a radio access unit (RAU). The RF signal is transmitted wirelessly over a distance of 50 m to the wireless receiver which downconverts the signal and analyzes transmission quality in terms of bit error rate (BER). The setup of the different stations is described in detail in the following sections.

A. Optical Signal Generation

The optical signal is generated by an external cavity laser (ECL) at $\lambda = 1550$ nm, followed by a Mach-Zehnder modulator (MZM) biased at its minimum transmission point and driven from a vector signal generator (VSG) with a sinusoid at a frequency of $f_{RF}/2$, generating the second harmonic and thus resulting in two spectral lines spaced at f_{RF}. After amplification in an erbium doped fiber amplifier (EDFA) the spectral lines are separated with the help of an arrayed waveguide grating (AWGG), allowing one to be modulated in a second MZM driven with the duobinary data signal.

The latter was digitally produced—as discussed section II—from a pseudorandom bit sequence (PRBS) with a length of $2^{15}-1$ bits and generated with an arbitrary waveform generator (AWG), converted to an unbalanced signal with a balun (BAL) and amplified to achieve a voltage swing sufficient to drive the MZM. On the second arm a variable optical attenuator (VOA) allows adjustment of the optical power to achieve a balance between the two sides before they are coupled and amplified by another EDFA for transmission. A second VOA allows control of the launched power and thus the power at the optical-to-RF conversion stage after transmission through 10 km of ITU-T G.652 SMF.

For laboratory convenience the optical signal generation station is housed in a half-size rack, shown in Fig. 3(a).

B. Optical to Radio Frequency Conversion

The optical to RF conversion station is designed for minimum complexity and consists of a high-speed photodiode (PD) with a 3 dB bandwidth of 90 GHz and a responsivity of 0.5 A/W on which the RF signal is generated through beating of the two optical lines, followed by a medium power amplifier (MPA), boosting the RF signal by 10 dB; both PD and MPA are shown in Fig. 3(e). Wireless transmission over a distance of 50 m with a pair of parabolic antennas—providing an antenna gain of 48 dBi each—links the wireless transmitter to the receiver station. The wireless path, transmitter and receiver antennas are shown in Figs. 3(b)–(d) respectively.

Fig. 3. Laboratory setup for duobinary transmittion in W-band; (a) optical signal generation, (b) optical to RF conversion station and transmission path, (c)–(d) transmitter and receiver parabolic antennas, (e) PD and MPA at optical to RF conversion, (f) LNA mixer and frequency doubler at the wireless receiver.

TABLE I
EMPLOYED DATA RATES, CORRESPONDING RF, LO AND IF FREQUENCIES AND RESULTING BER AFTER TRANSMISSION

Data Rate [Gbit/s]	f_{RF} [GHz]	f_{LO} [GHz]	f_{IF} [GHz]	min. BER
11.6	83	75	8	2.3×10^{-4}
12.5	83	75	8	3.9×10^{-4}
15.0	84	75	9	2.9×10^{-3}
16.0	85	75	10	7.2×10^{-3}
20.0	87	75	12	1.3×10^{-1}

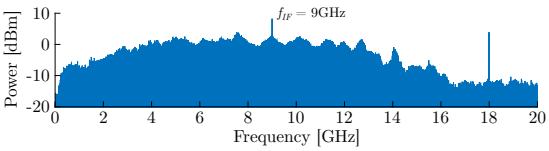

Fig. 4. Spectrum of the 15 Gbit/s duobinary signal at an IF of 9 GHz.

C. Wireless Receiver and Signal Processing

The received RF signal is amplified by 20 dB using a low noise amplifier (LNA) before it is downconverted to an intermediate frequency (IF) at $f_{IF} = f_{RF} - f_{LO}$ in a balanced mixer. The local oscillator (LO) for the mixer is obtained from a passive frequency doubler, driven with a sinusoid at $f_{LO}/2$ from a second VSG; the combination of LNA, mixer and frequency doubler is shown in Fig. 3(f). A blocking capacitor blocks any direct-current, before the resulting IF signal undergoes a final amplification and is recorded on a digital storage oscilloscope (DSO) for offline processing.

The signal processing consists of a Costas loop [21] for carrier frequency recovery to allow conversion of the IF signal to baseband, after it was band-filtered for noise bandwith reduction. The baseband signal is further low-pass filtered and downsampled, before being equalized in a decision feedback equalizer (DFE) with 32 feed forward and feedback taps. Duobinary decoding is performed with a modulo two operation as discussed in Eq. (3) and finally the BER is determined through error counting over four recorded sequences with a length of more than 0.1 MSymbol each.

IV. Performance Measurements and Discussion

To evaluate the performance of duobinary transmission over a W-band hybrid photonic wireless link with the presented setup, a number of signals are generated with data rates between 11.6 GHbit/s and 20 GHbit/s. The RF carrier frequency f_{RF} and LO frequency f_{LO} are adjusted to allow an IF large enough to support the data signal; an overview of the signal speed and frequency configurations tests is given in Table I.

Fig. 4 shows the spectrum of the 15 Gbit/s duobinary spectrum on its 9 GHz IF carrier, showing a heavily distorted upper sideband and a significant mixing component at the harmonic of the IF. The latter is removed by bandpass filtering around the signal before donconversion, while the equalizer may reduce the impairments from the non-flat frequency response of the employed RF components—especially the balanced mixer.

Despite the heavy distortions transmission of duobinary signals of 11.6 Gbit/s, 12.5 Gbit/s and 15 Gbit/s with BERs below the limit for a commercial 7 % overhead forward error correction of 3.8×10^{-3} is achieved as shown in Fig. 5. For a 16 Gbit/s duobinary signal the observed BER of 7.2×10^{-3} would require a FEC with a larger overhead, e.g. a 25 % overhead FEC; the minimum BER observed for all employed configurations is further shown in Table I. The rapid decline in transmission performance for a comparably small increase in data rate is due to a strong dip in the mixer frequency response, which with the increased IF and signal bandwidth falls in the required signal band; further causing any signal of even wider bandwidths to be completely irrecoverable—as seen for the 20 Gbit/s signal in Fig. 5.

Fig. 5 further shows only small improvements to be gained from an increase in optical power on the PD—and thus an increased RF transmitter power,—suggesting the link to be limited by frequency distortions, rather than the available power. As these frequency distortions stem from the mixer and amplifiers at the receiver, an increase in transmission distance well beyond the mark of 100 m is expected to be within the capabilities of the presented setup as a further 3 dB in optical power were available [22].

With transmission rates of 11.6 Gbit/s and 12.5 Gbit/s the system would be able to directly transport streams at the data rates for ITU-T G.709 OTU2, OTU2e and OTU2f signals [20] while allowing a sufficient overhead for encapsulation and a 7 % overhead FEC. The system would thus directly enable a wireless bridge for any optical system carrying signals such

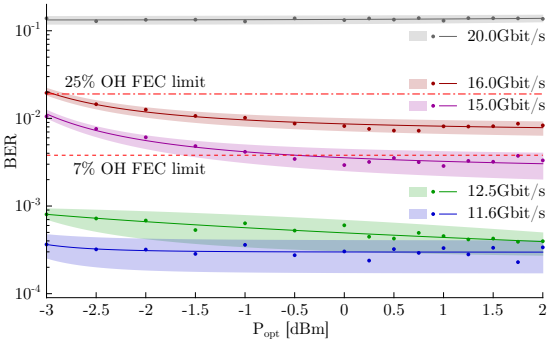

Fig. 5. BER against optical power on the PD. •: measured BER, ▭: 95 % confidence intervals calculated from spread of experimental measurements.

as SONET/SDH OC-192, STM-64 [23], 10G Ethernet [24] or 10G Fibre Channel [25].

V. Conclusions

This paper demonstrates the use of duobinary signaling to extend the capacity available from a bandwidth limited hybrid phtonic wireless link the W-band. Transmission with a BER below the limit for a commercial forward error correction with 7 % overhead is experimentally demonstrated for duobinary signals with speeds of up to 15 Gbit/s on a radio-over-fiber link consisting of 10 km standard single mode fiber and a wireless distance of 50 m. The transmission link is found to be limited by frequency distortions from the receiving RF equipment and an increase in wireless distance to 100 m and beyond is expected to be within reach of the system.

Demonstrating transmission at data rates of 11.6 Gbit/s, 12.5 Gbit/s and 15 Gbit/s the system lends itself ideally as a wireless bridge, allowing the transport of ITU-T G.709 OTU2, OTU2e and OTU2f signals while allowing for a sufficient overhead.

Acknowledgments

This work was partly funded by the DFF FTP mmW-SPRAWL project as well as the EC IPHOBAC-NG project under grant No. 619870. The authors thank Keysight Technologies for providing access to the AWG.

References

[1] E. Dahlman *et al.*, "5G wireless access: Requirements and realization," *IEEE Commun. Mag.*, vol. 52, no. 12, pp. 42–47, 2014.

[2] J. Wells, "Faster than fiber: The future of multi-G/s wireless," *IEEE Microw. Mag.*, vol. 10, no. 3, pp. 104–112, 2009.

[3] J. J. Vegas Olmos, T. Kuri, T. Sono, K. Tamura, H. Toda, and K.-i. Kitayama, "Wireless and optical-integrated access network with peer-to-peer connection capability," *IEEE Photon. Technol. Lett.*, vol. 20, no. 13, pp. 1127–1129, 2008.

[4] J. E. Mitchell, "Integrated wireless backhaul over optical access networks," *J. Lightw. Technol.*, vol. 32, no. 20, pp. 3373–3382, 2014.

[5] T. Pfeiffer, "Next generation mobile fronthaul and midhaul architectures," *J. Opt. Commun. Netw.*, vol. 7, no. 11, pp. B38–B45, 2015.

[6] S. Rommel *et al.*, "225m outdoor W-band radio-over-fiber link using an optical SFP+ module," in *Proc. OFC 2016*. Anaheim: OSA, 2016, paper Th2A.16.

[7] S. Rommel, L. C. P. Cavalcante, A. G. Quintero, A. K. Mishra, J. J. Vegas Olmos, and I. Tafur Monroy, "W-band photonic-wireless link with a Schottky diode envelope detector and bend insensitive fiber," *Opt. Express*, vol. 24, no. 11, pp. 11 312–11 322, 2016.

[8] A. Lender, "Correlative digital communication techniques," *IEEE Trans. Commun. Technol.*, vol. 12, no. 4, pp. 128–135, 1964.

[9] R. D. Howson, "An analysis of the capabilities of polybinary data transmission," *IEEE Trans. Commun. Technol.*, vol. 13, no. 3, pp. 312–319, 1965.

[10] A. Sekey, "An analysis of the duobinary techniques," *IEEE Trans. Commun. Technol.*, vol. 14, no. 2, pp. 126–130, 1966.

[11] S. Straullu, S. Abrate, A. Nespola, P. Savio, and R. Gaudino, "Different modulation formats for gigabit-over-POF," in *Proc. ANIC 2012*. Colorado Springs: OSA, 2012, paper AW3A.5.

[12] N. Fujimoto and H. Mochizuki, "614 Mbit/s OOK-based transmission by the duobinary technique using a single commercially available visible LED for high-speed visible light communications," in *Proc. ECOC 2012*. Amsterdam: OSA, 2012, paper P4.03.

[13] J. J. Vegas Olmos, L. F. Suhr, B. Li, and I. Tafur Monroy, "Five-level polybinary signaling for 10 Gbps data transmission systems," *Opt. Express*, vol. 21, no. 17, pp. 20 417–20 422, 2013.

[14] L. F. Suhr, J. J. Vegas Olmos, B. Mao, X. Xu, G. N. Liu, and I. Tafur Monroy, "112-Gbit/s × 4-lane duobinary-4-PAM for 400GBase," in *Proc. ECOC 2014*. Cannes: IEEE, 2014, paper Tu.4.3.2.

[15] S. Rommel, L. Yi, M. Shi, I. Tafur Monroy, and J. J. Vegas Olmos, "Demonstration of 4Gbit/s duobinary Ka-band hybrid photonic-wireless transmission," in *Proc. ACPC 2015*. Hong Kong: OSA, 2015, paper ASu1J.2.

[16] L. F. Suhr, P. Madsen, I. Tafur Monroy, and J. J. Vegas Olmos, "Analog-based duobinary-4-PAM for electrical bandwidth limited optical fiber links," *Opt. Appl.*, vol. XLVI, no. 1, 2016.

[17] J. J. Vegas Olmos *et al.*, "Challenges in polybinary modulation for bandwidth limited optical links," *J. Laser Opt. Photonics*, vol. 3, no. 1, 2016.

[18] J. Wei, K. Grobe, C. Wagner, E. Giacoumidis, and H. Griesser, "40 Gb/s lane rate NG-PON using electrical/optical duobinary, PAM-4 and low complex equalizations," in *Proc. OFC 2016*. Anaheim: OSA, 2016, paper Tu3C.5.

[19] *Characteristics of a single-mode optical fibre and cable*, ITU, ITU-T G.652, 2009.

[20] *Interfaces for the optical transport network*, ITU, ITU-T G.709, 2012.

[21] J. P. Costas, "Synchronous communications," *Proc. IRE*, vol. 44, no. 12, pp. 1713–1718, 1956.

[22] S. Rommel *et al.*, "Outdoor W-band hybrid photonic wireless link based on an optical SFP+ module," *IEEE Photon. Technol. Lett.*, vol. 28, no. 21, pp. 2303–2306, 2016.

[23] *Network node interface for the synchronous digital hierarchy (SDH)*, ITU, ITU-T G.707, 2007.

[24] *IEEE Standard for Ethernet*, IEEE, IEEE 802.3, 2012.

[25] *Fibre Channel–Physical and Signaling Interface (FC-PH),*, ANSI, ANSI X3.230-1994, 1994.

PAPER10: Capacity Enhancement for Hybrid Fiber-Wireless Channels with 46.8Gbit/s Wireless Multi-CAP Transmission over 50m at W-Band

S. Rommel, R. Puerta, J. J. Vegas Olmos, and I. Tafur Monroy. "Capacity Enhancement for Hybrid Fiber-Wireless Channels with 46.8Gbit/s Wireless Multi-CAP Transmission over 50m at W-Band". In: *Optical Fiber Communication Conference 2017*. Mar. 2017, paper M3E.5. DOI: 10.1364/OFC.2017.M3E.5

Capacity Enhancement for Hybrid Fiber-Wireless Channels with 46.8Gbit/s Wireless Multi-CAP Transmission over 50m at W-Band

Simon Rommel[1*], Rafael Puerta[1], Juan José Vegas Olmos[1], Idelfonso Tafur Monroy[1,2]

[1]*Department of Photonics Engineering, Technical University of Denmark, 2800 Kgs. Lyngby, Denmark*
[2]*ITMO University, 197101 St. Petersburg, Russia*

[*]*sirem@fotonik.dtu.dk*

Abstract: Transmission of a 46.8 Gbit/s multi-band CAP signal is experimentally demonstrated over a 50 m W-band radio-over-fiber link. Bit error rates below 3.8×10^{-3} are achieved, employing nine CAP bands with bit and power loading.

OCIS codes: (060.5625) Radio frequency photonics, (060.4510) Optical communications.

1. Introduction

Ever increasing capacity demands driven by the drastic growth of mobile and wireless traffic have prompted a move to higher carrier frequencies in the millimeter-wave (mm-wave) range [1]. Radio-over-fiber (RoF) transmission is a key candidate for next generation mm-wave mobile front- and backhaul as well as wireless access, as it effectively combines fiber optic and wireless transmission to provide large capacity and high flexibility combined with low latency while further allowing significant fiber distances between central office and antenna site [1–3].

Despite the large spectrum allocations to mm-wave wireless networks however, a move to modulation formats with a higher spectral efficiency than that of simple on-off keying is required [3, 4]. A promising candidate technique combining low complexity with good system performance has been identified in carrierless amplitude phase (CAP) modulation, showing promising performance in both radio frequency (RF) and optical wireless transmissions [3–5] and breaking records in other severely bandwidth limited systems [6].

In this paper the transmission of a 46.8 Gbit/s multi-band CAP (multi-CAP) signal over a RoF link consisting of 10 km standard single mode fiber (SMF) and 50 m W-band wireless transmission at 87.5 GHz is experimentally demonstrated. With a multi-CAP signal with nine bands of different constellations and an overall width of 12 GHz, bit error rates (BER) below the limit for a commercial forward error correction (FEC) with 7 % overhead (OH) of 3.8×10^{-3} are achieved.

2. Experimental Setup

The experimental setup used to demonstrate high-capacity multi-CAP transmission over a hybrid photonic-wireless link is shown in Fig. 1. The optical signal is generated by an external cavity laser (ECL) at $\lambda = 1550$ nm, followed by a Mach-Zehnder modulator (MZM) driven from a vector signal generator (VSG) with a sinusoid at $f_{RF}/2 = 43.75$ GHz, generating the second harmonic and thus resulting in two spectral lines spaced at $f_{RF} = 87.5$ GHz. After amplification in an erbium doped fiber amplifier (EDFA) the spectral lines are separated with the help of an arrayed waveguide grating (AWGG), allowing one to be modulated in a second MZM driven with the multi-CAP signal.

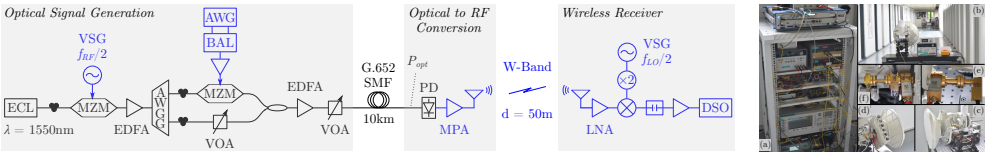

Fig. 1. Schematic of the experimental setup and photograph of the laboratory setup; (a) optical signal generation, (b) transmission path, (c)-(d) transmitter and receiver antennas, (e) PD and MPA, (f) LNA, mixer and frequency doubler.

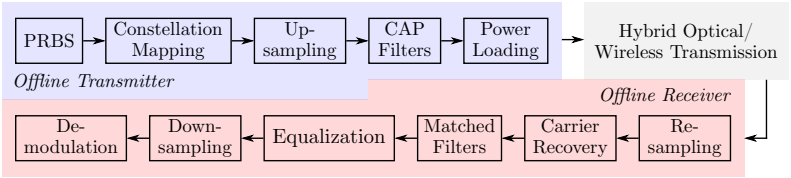

Fig. 2. Schematic of the multi-CAP signal generation, transmission and demodulation.

The latter was generated with an arbitrary waveform generator (AWG) followed by a balun (BAL) and amplified to achieve a voltage swing sufficient to drive the MZM. A variable optical attenuator (VOA) allows adjustment of second arm to achieve equal power, before they are coupled and amplified by another EDFA for transmission. A second VOA allows control of power launched into the 10 km of ITU-T G.652 SMF and thus the power on the high-speed photodiode (PD) used for optical-to-RF conversion by beating of the two optical lines.

The RF signal is boosted by 10 dB with a medium power amplifier (MPA) and wirelessly transmitted over a distance of 50 m with a pair of parabolic antennas providing an antenna gain of 48 dBi each. The received RF signal is amplified by 20 dB with a low noise amplifier (LNA) before being downconverted to an intermediate frequency (IF) at $f_{IF} = f_{RF} - f_{LO} = 12.5$ GHz in a balanced mixer. The local oscillator (LO) for the latter is obtained from a passive frequency doubler, driven with a sinusoid at $f_{LO}/2 = 37.5$ GHz from a second VSG. The resulting IF signal undergoes a final amplification and is recorded on a digital storage oscilloscope (DSO) for offline processing.

3. Multi-CAP Signal Generation and Processing

A multi-band CAP (multi-CAP) signal with nine bands was designed and generated for high-speed transmission in W-band. As observed transmission quality varies between bands, bit loading is performed—with constellations ranging from 8-PSK to 32-QAM—and for each band a pseudo random bit sequence (PRBS) of 2^{11}-1 bits is mapped in to the respective symbol constellation. Symbol sequences are upsampled and each band is formed with a pair of orthogonal CAP filters, followed by power loading to optimize transmission performance. The overall offline transmitter is shown in Fig. 2 alongside the corresponding offline receiver, while Table 1 gives the multi-CAP parameters.

At the receiver the signal that was recovered from the DSO is band-filtered for noise bandwidth reduction and resampled, before the IF carrier is recovered with the help of a Costas loop, allowing conversion to baseband. Orthogonal CAP matched filters retrieve the symbol sequences of each band and a decision feedback equalizer (DFE) mitigates impairments from the transmission channel and device imperfections. The signal is demodulated, the error vector magnitude (EVM) estimated and BER for each band separately by error counting across a number of stored traces from the DSO with at least 0.18 Mbit analyzed per band.

4. Transmission Results and Discussion

To evaluate the performance of multi-CAP W-band transmission the generated signal is transmitted over the RoF link, downconverted to IF and recorded for offline processing. The resulting IF spectrum is shown in Fig. 3, showing a relatively flat lower sideband with the upper sideband seriously degraded due to bandwidth limitations of the mixer used for downconversion. Despite the heavy distortions of the upper sideband, all bands were successfully recovered clearly highlighting the advantage obtained from multi-CAP allowing different constallations in its bands.

Transmission BER was determined after 50 m wireless transmission for optical powers on the PD between −2 dBm and 3 dBm and is shown in Fig. 4, achieving transmission with a BER below the limit of 3.8×10^{-3} for a commercial 7 % OH FEC. The observed behaviour suggests the system to be power limited at the lower powers, while no improvement

Table 1. Multi-CAP signal parameters for transmission of 46.8 Gbit/s in nine bands.

Band	1	2	3	4	5	6	7	8	9
Symbol rate [GBd]	1.3	1.3	1.3	1.3	1.3	1.3	1.3	1.3	1.3
Constellation	32-QAM	32-QAM	16-QAM	16-QAM	8-PSK	16-QAM	16-QAM	16-QAM	8-PSK
Bit rate [Gbit/s]	6.5	6.5	5.2	5.2	3.9	5.2	5.2	5.2	3.9
Power loading [dB]	1.0	0.0	0.0	0.5	2.5	0.0	0.0	0.5	1.5

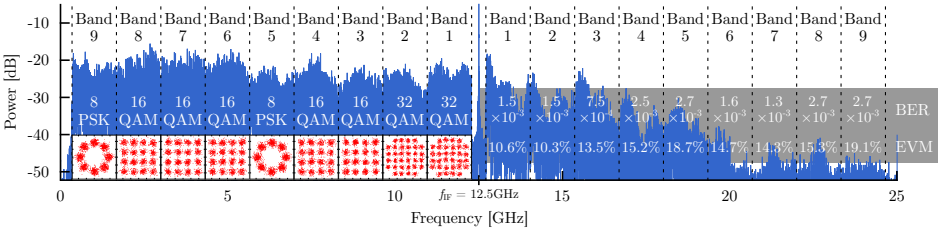

Fig. 3. Signal spectrum after downconversion to the intermediate frequency f_{IF} and received constellation diagrams after equalization for $P_{\mathrm{opt}} = 3\,\mathrm{dBm}$.

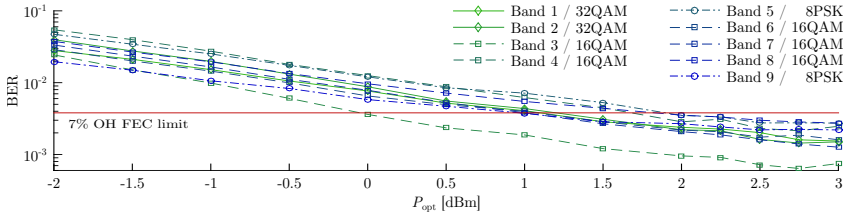

Fig. 4. BER over optical power on the PD after 50 m W-band transmission of 46.8 Gbit/s multi-CAP.

in performance was observed at higher optical powers, due to saturation of the amplifier at the receiver. With as much as 3.5 dB additional power available from the system, this suggest the wireless reach of the system to be significantly larger and distances of 100 m and more to be achievable [7].

5. Conclusions

Successful transmission of a 46.8 Gbit/s multi-CAP signal over a 10 km fiber and 50 m W-band RoF link was demonstrated with a BER below the limit of $3.8{\times}10^{-3}$ for a commercial 7 % OH FEC. The demonstrated capacity is sufficient to accommodate four 10G ethernet streams plus an additional FEC overhead, clearly highlighting how multi-CAP with its inherent flexibility can help increase link capacity. It further underlines the potential of mm-wave RoF transmission for high capacity links with antenna remoting by fiber optics.

Acknowledgments

This work was partly funded by the DFF FTP mmW-SPRAWL project. The authors thank Keysight Technologies for providing access to the AWG. R. Puerta thanks the Colombian Administrative Department of Science, Technology and Innovation (COLCIENCIAS).

References

[1] J. Wells, "Faster than fiber: The future of multi-G/s wireless," IEEE Microw. Mag. **10**, pp. 104–112 (2009).
[2] S. Rommel *et al.*, "W-band photonic-wireless link with a Schottky diode envelope detector and bend insensitive fiber," Opt. Express **24**, pp. 11312–11322 (2016).
[3] J. Zhang *et al.*, "Experimental demonstration of 24-Gb/s CAP-64QAM radio-over-fiber system over 40-GHz mm-wave fiber-wireless transmission," Opt. Express **21**, pp. 26888–26895 (2013).
[4] M. Xu *et al.*, "Multiband OQAM CAP modulation in MMW RoF systems with enhanced spectral and computational efficiency," in *Proc. OFC 2016*, paper Tu3B.3 (2016).
[5] K. Wange *et al.*, "Full-Duplex Gigabit Indoor Optical Wireless Communication System With CAP Modulation," IEEE Photon. Technol. Lett. **28**, pp. 790–793 (2016).
[6] R. Puerta *et al.*, "107.5 Gb/s 850 nm multi- and single-mode VCSEL transmission over 10 and 100 m of multimode fiber," in *Proc. OFC 2016*, paper Th5B.5 (2016).
[7] S. Rommel *et al.*, "Outdoor W-Band Hybrid Photonic Wireless Link Based on an Optical SFP+ Module," IEEE Photon. Technol. Lett. **28**, pp. 2303–2306 (2016).

PAPER11: Optically Generated Single Side-Band Radio-over-Fiber Transmission of 60Gbit/s over 50m at W-Band

R. Puerta, **S. Rommel**, J. J. Vegas Olmos, and I. Tafur Monroy. "Optically Generated Single Side-Band Radio-over-Fiber Transmission of 60Gbit/s over 50m at W-Band". In: *Optical Fiber Communication Conference 2017*. Mar. 2017, paper M3E.4. DOI: 10.1364/OFC.2017.M3E.4

Optically Generated Single Side-Band Radio-over-Fiber Transmission of 60Gbit/s over 50m at W-Band

Rafael Puerta[1*], Simon Rommel[1], Juan José Vegas Olmos[1], Idelfonso Tafur Monroy[1,2]

[1]*Department of Photonics Engineering, Technical University of Denmark, 2800 Kgs. Lyngby, Denmark*
[2]*ITMO University, St. Petersburg 197101, Russia*

[*]*rapur@fotonik.dtu.dk*

Abstract: 60 Gbit/s single side-band multi-band CAP radio-over-fiber transmission at W-band is demonstrated. A spectral efficiency of 3.8 bit/s/Hz and bit error rates below 3.8×10^{-3} are achieved after 50 m wireless transmission.

OCIS codes: (060.5625) Radio frequency photonics, (060.4080) Modulation, (060.4510) Optical communications.

1. Introduction

High-speed wide-band wireless communication systems have become a requirement in order to support the higher data rates required in wireless access and mobile front- and backhaul. This is driven by the rapid increase of data demands from cloud computing, multimedia applications on portable devices, and the internet of things (IoT). To cope with these demands, millimeter-wave (mm-wave) frequencies (30–300 GHz) offer the bandwidth available for appealing new broadband solutions [1]. Additionally, through mm-wave technology, wireless transmission can match speeds and bandwidths of fiber optic links, enabling integration with current optical networks [2–4].

In order to efficiently exploit the bandwidth available of mm-wave photonics-enabled links, advanced modulation schemes and digital signal processing (DSP) are required. Recently, carrierless amplitude phase modulation (CAP) and its multi-band approach (multi-CAP), have shown high spectral efficiency and flexibility to adjust to impairments from fiber optic and wireless links [4–6]. Further, by means of DSP, single side-band (SSB) modulation can be enabled, considerably increasing spectral efficiency. SSB W-band wireless links have been demonstrated up to 2 m [7, 8], relaxing hardware requirements compared to double side-band (DSB) transmissions of comparable spectral efficiency [9, 10].

In this paper we propose and experimentally demonstrate a 60 Gbit/s W-band wireless transmission employing multi-CAP modulation and the Hilbert transform to achieve SSB operation and effectively doubling spectral efficiency. Transmission was performed over 10 km standard single mode fiber (SMF) and 50 m wireless distance. With a multi-CAP signal of three bands and an overall width of 15.7 GHz, a spectral efficiency of 3.8 Bit/Hz and bit error rates (BER) below the limit for a commercial forward error correction (FEC) with 7 % overhead (OH) of 3.8×10^{-3} are achieved.

2. Experimental Setup

Figure 1 shows the experimental setup used for optical SSB signal generation, wireless transmission, and signal recovery. The output of a free running external cavity laser (ECL) at 1550 nm is used as input to a Mach-Zehnder modulator (MZM). By driving the modulator with a pure sinusoidal tone at 44 GHz, generated by a vector signal generator (VSG), the second harmonic of this tone is obtained at the output of the MZM. Thus, the generation of two optical signals with a separation of 88 GHz is achieved. An erbium doped fiber amplifier (EDFA) is used to amplify the signal, and an arrayed waveguide grating (AWGG) separates the two optical lines to enable the modulation of one thereof.

The data signal is generated by an arbitrary waveform generator (AWG) at a sampling rate of 60 GSa/s. Optical SSB modulation is achieved by means of a single optical I/Q modulator. By applying the Hilbert transform to the original multi-CAP signal, the in-phase (I) and quadrature (Q) components to drive the modulator are generated, removing the upper side-band (USB) as shown in the inset of Fig. 1. The I and Q components are amplified with driver amplifiers to obtain suitable voltage magnitudes to drive the I/Q modulator. A variable optical attenuator (VOA) is used to set equal power in both the unmodulated and modulated optical signals and an optical coupler combines the two. A second EDFA and a second VOA are employed to set the launch power into the 10 km SMF. After fiber transmission, a high speed photodiode (PD) converts the optical signal to the electrical domain, where the signal is boosted by a 10 dB medium power amplifier (MPA) before wireless transmission over 50 m.

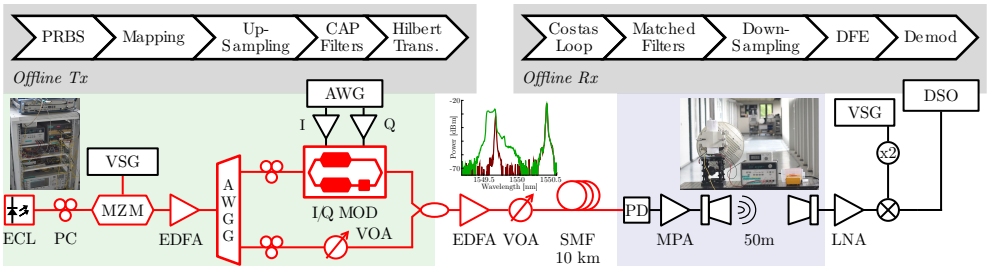

Fig. 1. Schematic of the experimental setup and offline DSP at the transmitter and receiver; photographs of optical signal generation and radio transmission setups; inset: SSB optical spectrum.

Table 1. Multi-CAP signal parameters for transmission of 60 Gbit/s in three bands.

Band	1	2	3
Symbol rate [GBd]	5	5	5
Constellation	16-QAM	16-QAM	16-QAM
Bit rate [Gbit/s]	20	20	20
Power loading [dB]	0	1	3

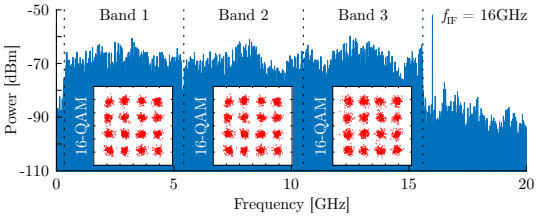

Fig. 2. Signal spectrum after downconversion to f_{IF} and received constellations after equalization for $P_{opt} = 3$ dBm.

A pair of parabolic antennas, with 48 dBi gain each, is used for wireless transmission. At the receiver, the transmitted signal is amplified by a 20 dB low noise amplifier (LNA). Heterodyne downconversion is performed by a balanced mixer to an intermediate frequency (IF) of 16 GHz. The mixer is driven by a 72 GHz local oscillator (LO) generated by a passive frequency doubler with a pure sinusoid of 36 GHz from a second VSG. The IF signal was recorded on a digital storage oscilloscope (DSO) at a sampling rate of 80 GSa/s for offline DSP.

3. Single-Sideband Multi-CAP Signal Generation and Processing

In order to mitigate channel unevenness and maximize data rate, a multi-CAP signal with three bands, each with a baudrate of 5 Gbaud, is generated offline. For each band, pseudo-random bit sequences (PRBSs) of length 2^{11}-1 are mapped into 16-QAM symbol sequences, which are up-sampled and filtered by the corresponding orthogonal CAP filters. By means of power loading a BER below FEC threshold is ensured for each band. The Hilbert transform is applied to the generated multi-CAP signal for SSB operation, doubling transmission spectral efficiency. The offline transmitter is shown in Fig. 1 alongside the corresponding offline receiver, while Table 1 gives the multi-CAP parameters.

The IF signal that was recovered from the DSO is resampled, before carrier recovery and donconversion with a Costas loop. Orthogonal CAP matched filters retrieve the symbol sequences of each band and a decision feedback equalizer (DFE) with 11 feed forward and 21 feed back tap mitigates impairments from the transmission channel and device imperfections. After demodulation, error vector magnitude (EVM) and BER are estimated separately for each band by error counting with at least 0.23 Mbit analyzed per band.

4. Transmission Results and Discussion

Performance evaluation of the optically generated 60 Gbit/s SSB multi-CAP RoF transmission is performed after 50 m W-band wireless and downconversion to IF. The received spectrum is shown in Fig. 2, clearly confirming successful SSB transmission and showing the IF carrier at 16 GHz; insets show recovered constellations after equalization.

Observed BER after transmission is shown in Fig. 3 for optical powers on the PD of −0.5–6.5 dBm, showing a minimum around 3 dBm; Table 2 gives corresponding BER and EVM. Despite the use of power loading, significant differences in BER are observed between the bands, with the second band showing worst performance. Nevertheless, all bands achieve a BER below the limit of 3.8×10^{-3} for a standard commercial FEC with only 7 % overhead.

The BER performance of the system clearly suggests a power limited regime at the lower powers, while at higher

Table 2. BER and EVM for the 60 Gbit/s SSB multi-CAP signal after 50 m wireless transmission with $P_{opt} = 3$ dBm.

Band	1	2	3
BER	8.9×10^{-4}	3.5×10^{-3}	1.9×10^{-3}
EVM	13.6 %	14.9 %	14.9 %

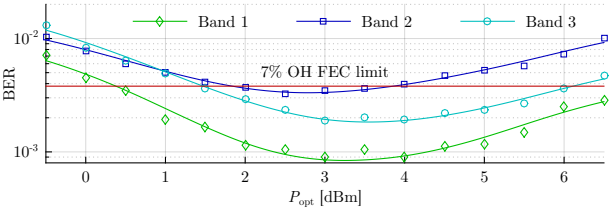

Fig. 3. BER over optical power on the PD after 50 m W-band transmission of 60 Gbit/s SSB multi-CAP.

powers BER performance is degraded due to saturation of the receiving LNA. The availability of an additional 3.5 dB optical power beyond the optimum observed, together with receiver amplifier saturation, suggests a significant extension of transmission distance to as much as 100 m to be possible [2]; this could however not be tested due to laboratory space restrictions.

From the IF spectrum in Fig. 2 the spectral efficiency of the system is easily calculated. With a symbol rate of 5 GBd in each multi-CAP band and guard bands of only 2 %, the signal occupies only 15.3 GHz of spectrum and thus—with an additional gap of 400 MHz to the carrier—the overall system requires only 15.7 GHz of RF bandwidth. This results in a spectral efficiency of 3.8 bit/Hz for a single polarization, single carrier and single input single output system. To the best of the authors' knowledge this is the first time SSB transmission at W-band has been demonstrated over distances beyond 2 m, outperforming previous demonstrations in both data rate and wireless distance [7, 8].

5. Conclusions

Transmission of a 60 Gbit/s SSB multi-CAP signal over 10 km SMF and a wireless distance of 50 m is successfully demonstrated with a BER below the limit for a FEC with 7 % overhead. Optical SSB generation by means of the Hilbert transform and a single I/Q modulator is exploited to achieve a spectral efficiency of 3.8 Bit/Hz in both the optical and wireless transmission. To the best of the authors' knowledge, this the first demonstration of SSB transmission in W-band over significant wireless distances.

Acknowledgments

R. Puerta thanks the Colombian Administrative Department of Science, Technology and Innovation (COLCIENCIAS) for partly funding his research. This work was partly funded by the DFF FTP mmW-SPRAWL project. The authors thank Keysight Technologies for providing access to the AWG.

References

[1] C. Dehos *et al.*, "Millimeter-Wave Access and Backhauling: The Solution to the Exponential Data Traffic Increase in 5G Mobile Communications Systems?," IEEE Commun. Mag. **52**, pp. 88–95 (2014).
[2] S. Rommel *et al.*, "Outdoor W-Band Hybrid Photonic Wireless Link Based on an Optical SFP+ Module," IEEE Photon. Technol. Lett. **28**, pp. 2303–2306 (2016).
[3] L. Cavalcante *et al.*, "On the capacity of radio-over-fiber links at the W-band," Opt. Quant. Electron. **48** (2016).
[4] J. Zhang *et al.*, "Experimental demonstration of 24-Gb/s CAP-64QAM radio-over-fiber system over 40-GHz mm-wave fiber-wireless transmission," Opt. Express **21**, pp. 26888–26895 (2013).
[5] R. Puerta *et al.*, "Up to 35 Gbps Ultra-Wideband Wireless Data Transmission Links," in *Proc. PIMRC 2016*, paper WeD7.2 (2016).
[6] R. Puerta *et al.*, "107.5 Gb/s 850 nm multi- and single-mode VCSEL transmission over 10 and 100 m of multimode fiber," in *Proc. OFC 2016*, paper Th5B.5 (2016).
[7] X. Li, Y. Xu and J. Yu, "Single-sideband W-band photonic vector millimeter-wave signal generation by one single I/Q modulator," Opt. Lett. **41**, pp. 4165–4165 (2016).
[8] C. Ho *et al.*, "High spectral efficient W-band optical/wireless system employing Single-Sideband Single-Carrier Modulation," Opt. Express **22**, pp. 3911–3917 (2016).
[9] A. Stöhr *et al.*, "High Spectral-Efficient 512-QAM-OFDM 60 GHz CRoF System using a Coherent Photonic Mixer (CPX) and an RF Envelope Detector," in *Proc. OFC 2016*, paper Tu3B.4 (2016).
[10] M. Xu *et al.*, "Multiband OQAM CAP modulation in MMW RoF systems with enhanced spectral and computational efficiency," in *Proc. OFC 2016*, paper Tu3B.3 (2016).

PAPER12: Performance Evaluation of Wavelet-Coded OFDM on a 4.9 Gbps W-Band Radio-over-Fiber Link

L. C. P. Cavalcante, **S. Rommel**, R. Dinis, L. G. Q. Silveira, L. F. Q. Silveira, and I. Tafur Monroy. "Performance Evaluation of Wavelet-Coded OFDM on a 4.9 Gbps W-Band Radio-over-Fiber Link". In: *Journal of Lightwave Technology* 35.14 (July 2017), pp. 2803–2809. DOI: 10.1109/JLT.2017.2701358

Performance Evaluation of Wavelet-Coded OFDM on a 4.9 Gb/s W-Band Radio-Over-Fiber Link

Lucas C. P. Cavalcante, Simon Rommel, *Student Member, IEEE*, Rui Dinis, *Senior Member, IEEE*, L. G. Q. Silveira Junior, *Member, IEEE*, L. F. Q. Silveira, *Member, IEEE*, and Idelfonso Tafur Monroy, *Senior Member, IEEE*

***Abstract*—Future generation mobile communications running on mm-wave frequencies will require great robustness against frequency selective channels. In this paper, we evaluate the transmission performance of 4.9 Gb/s wavelet-coded orthogonal frequency division multiplexing (OFDM) signals on a 10 km fiber plus 58 m wireless radio-over-fiber link using a mm-wave radio frequency carrier. The results show that a 2 × 128 wavelet-coded OFDM system achieves a bit-error rate of 1e-4 with nearly 2.5 dB less signal-to-noise ratio than a convolutional coded OFDM system with equivalent spectral efficiency for 8 GHz-wide signals with 512 subcarriers on a carrier frequency of 86 GHz. Our findings confirm the Tzannes' theory that wavelet coding enables high diversity gains with a low complexity receiver and, most notably, without compromising the system's spectral efficiency.**

***Index Terms*—Frequency selectivity, mm-Wave, OFDM, radio-over-fiber, W-band, wavelet-coding.**

I. Introduction

AS THE fifth generation (5G) of mobile communications technology is developed and implemented, worldwide solutions propose the use of much greater spectrum allocations in both licensed and unlicensed spectrum, including the mm-wave frequency band [1]–[5]. Radio-over-fiber links allow straight forward integration of the mobile front- and backhaul with deployed optical distribution networks, while readily offering the use of large modulation bandwidths [1], [2], [5]. Such a requirement imposes a critical demand for broadband wireless links, implying in high-bit-rate transmissions that are loudly subjected to channel-induced inter-symbol interference (ISI) incurred by frequency selectivity [6].

Adding frequency diversity in an Orthogonal Frequency Division Multiplexing (OFDM) design is an effective way of mitigating the effect of frequency-selective fading, which is generally achieved by sub-carrier redundancy, or channel coding [7]. Therefore, most of the practical OFDM systems are associated with forward error correction (FEC) codes [8] such as Reed-Solomon (RS) code [9], [10], convolutional code [11], [12], trellis-coded modulation (TCM) [13], turbo code [14], and low-density parity-check (LDPC) code [15].

The Wavelet-Coding scheme has been proposed in [16] as a new diversity strategy that: i) does not add redundancy to the original bit stream, which makes it a very competitive solution in comparison to other coding schemes such as convolutional or LDPC codes [7]; that ii) has a considerable simplified receptor, beating trellis or turbo based decoders in terms of computational costs [7]; and that iii) shows enormous performance gains on fading channels, as demonstrated over the past years [17], [18].

Recently, in [19], the Wavelet-Coding was used to enable high time-diversity gains in Doppler-rich channels with no cost to system spectral efficiency and yet with very simple decoding. Those findings were extended in [20], where it has been found that the Wavelet-Code can substantially compensate for the combined effects of deep frequency fading and error bursts that disrupt orthogonality among OFDM sub-carriers.

In this work, we experimentally demonstrate the transmission of 4.9 Gbps Wavelet-Coded (WC) OFDM signals as proposed in [20] on a 10 km fiber plus 58 m wireless Radio-over-Fiber link using a mm-wave carrier frequency of 86 GHz. We evaluate the performance of 2 × 128 and 2 × 8 WC-OFDM schemes in terms of bit-error rate (BER) for several OFDM resolutions. The results are contrasted with an uncoded scheme and a state-of-the-art coded scheme, all of them with equivalent spectral efficiency of 1 bit/s/Hz.

Our findings show that the proposed system substantially compensates for the effects of frequency distortion caused by electronic and optical components with non-flat frequency response. The results confirm the theory of Tzannes [16] that WC enables high diversity gains with a low complexity receiver, and, most notably, without compromising the system's spectral efficiency. The results also validate the solution proposed in [17] on modulation schemes that support the integration of WC with

Manuscript received August 2, 2016; revised October 24, 2016, December 25, 2016, and March 12, 2017; accepted May 2, 2017. Date of publication May 3, 2017; date of current version May 31, 2017. This work was supported in part by the DFF FTP mmW-SPRAWL project and the EC FP7-ICT IPHOBAC-NG project under Grant 619870. The work of L. C. P. Cavalcante was supported by CAPES under scholarship 11964-13-8. The work of R. Dinis was supported by FCT-MCES and IT under project UID/EEA/50008/2013. *(Corresponding author: Lucas C. P. Cavalcante.)*

L. C. P. Cavalcante, S. Rommel, and I. T. Monroy are with the Department of Photonics Engineering, Technical University of Denmark, DK-2800 Kgs. Lyngby, Denmark (e-mail: luca@fotonik.dtu.dk; sirem@fotonik.dtu.dk; idtm@fotonik.dtu.dk).

R. Dinis is with the Instituto de Telecomunicações and DEE-FCT, Universidade Nova de Lisboa, 2829-516 Lisboa, Portugal (e-mail: rdinis@fct.unl.pt).

L. G. Q. Silveira Junior and L. F. Q. Silveira are with the Departamento de Engenharia de Computação, Universidade Federal do Rio Grande do Norte, Mirassol, 59072-970 Natal, Brazil (e-mail: junior@ct.ufrn.br; lfelipe@dca.ufrn.br; idtm@fotonik.dtu.dk).

Color versions of one or more of the figures in this paper are available online at http://ieeexplore.ieee.org.

Digital Object Identifier 10.1109/JLT.2017.2701358

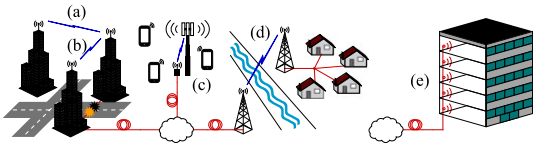

Fig. 1. Network scenarios for the hybrid fiber-wireless link.

power-limited systems. To the best of the authors' knowledge, the transmission of WC signals has never been experimentally demonstrated.

The proposed system fits as a key enabler for the use of mm-wave frequencies in future generation mobile communications for outdoor medium distance links such as (a) building-to-building communication, (b) recovery and protection of fiber links, (c) mobile front-/backhaul, (d) spanning obstacles for providing broadband access to rural ares, and (e) short-range indoor wireless distribution. The network scenario for the hybrid fiber-wireless link proposed in this work is represented in Fig. 1.

This paper is organized as follows: Section II explains the wavelet coding/decoding algorithm; Section III describes the proposed system in detail, including transmission and reception schemes, and the experimental setup. Section IV explains the applied methodology and discusses the results. Finally, Section V draws the conclusions.

II. Wavelet-Coding Scheme

Wavelet-Coding enables diversity gains without necessarily diminishing the system's efficiency [16] through the use of Wavelet-Coefficient Matrices (WCMs). WCMs have arbitrarily long rows, which are orthogonal to each other, even when moved and/or added. This work focuses on the use of integer flat WCMs. The matrix $A = (a_k^j)$ with dimensions $m \times mg$, whose coefficients a_k^j take value in the integer set $\{+1, -1\}$ is said to be a wavelet matrix with rank m and genus g if it satisfies the *modified wavelet scaling conditions* [16], [21]. Those conditions ensure that:

i) the sum of the elements in the first row of A is equal to the matrix rank m; that
ii) the sum of the elements from all remaining rows of A is equal to zero; and that
iii) the WCM's rows are mutually orthogonal, even when shifted by m-multiple positions, and orthogonal to copies of themselves shifted by m-multiple positions.

The diversity gains from WC can be continuously enhanced by employing WCM with larger dimensions [17].

A. Coding Algorithm

In this approach, the wavelet encoder multiplies successive source bits by distinct rows of a WCM, called wavelet codewords, to encode the information bits. Let a discrete source generate statistically independent and identically distributed (i.i.d.) bits $\{x_n\} \in \{+1, -1\}$. The wavelet symbol produced at time

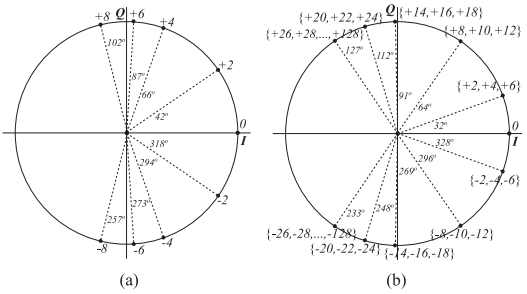

Fig. 2. PSK constellations after mapping of wavelet symbols. (a) 9-PSK constellation for 2×8 wavelet coding; (b) 11-PSK constellation for 2×129 wavelet coding.

$n = pm + q$ is expressed by

$$y_{pm+q} = \sum_{j=0}^{m-1} \sum_{l=0}^{g-1} a_{lm+g}^{j} x_{(p-l)m+j}. \quad (1)$$

The produced wavelet symbols take values in the set $\{-mg, -mg+2, \ldots, 0, \ldots, mg-2, mg\}$ with probability

$$Pr(y_n = 2k - mg) = \binom{mg}{k} 0.5^{mg}, 0 \le k \le mg. \quad (2)$$

Within this process, the information represented by an information bit is spread along the transmitted sequence, causing a small part of the signal to contain information about an entire block of data. This way, it is expected that the coded signal can withstand nullifying of closely-spaced symbols. This process can be used for improving robustness against the combined effects of varying fading and noise bursts [18], [19]. The longer the matrices employed, the larger the bit-blocks that will be coded by each row, and therefore more frequent deep fading of the channel may occur without disrupting the transmission. It can be verified that m information bits are encoded in m wavelet symbols sent during m signaling intervals, thus allowing a spectral efficiency of 1 bit/s/Hz.

In this work, wavelet matrices with parameters $m_1 = 2$, $g_1 = 4$, and $m_2 = 2$, $g_2 = 64$ are employed, therefore with dimensions $\mathcal{D}_1 = 2 \times 8$ and $\mathcal{D}_2 = 2 \times 128$, meaning that the wavelet decoder at the receiver must decide between 9 levels for the case $\mathcal{D}_1$ and 129 levels for the case $\mathcal{D}_2$.

In [17], a solution has been proposed for integrating wavelet-coding with power-limited systems, resulting in probabilistically shaped, non-uniform constellation diagrams that take into account the facts that:

i) for an i.i.d. source, successive wavelet symbols have similar levels;
ii) the generated wavelet levels are not equiprobable, according to (2), and consequently the performance gains of these systems are significantly influenced by their modulation scheme;
iii) decision errors between two close wavelet levels do not necessarily result in any bit errors, whereas decision errors between wavelet levels far from each other may considerably degrade correct bit estimation.

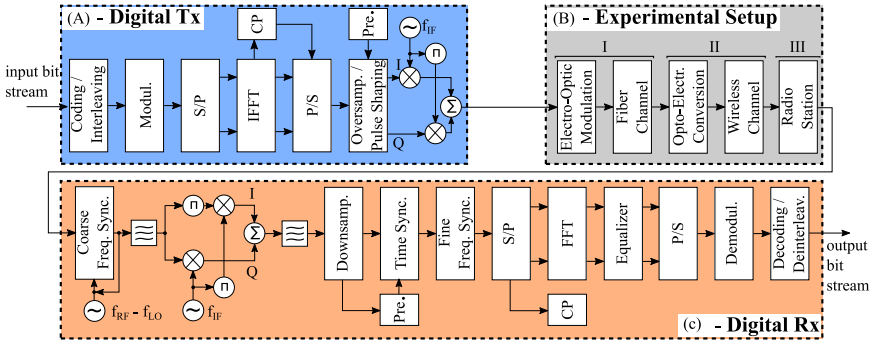

Fig. 3. Block diagram of the proposed system, including digital transmitter (A–top-left), experimental setup (B–top-right), and digital receiver (C–bottom).

Based on that solution, the transmitted data symbols for the case $\mathcal{D}_1$ will belong to a 9-PSK (i.e. phase shift keying) signal space according to Fig. 2(a). In order to avoid performance degradation due to constellation crowding on the case $\mathcal{D}_2$, a many-to-one mapping $\mathcal{P}(\cdot)$ of the wavelet symbols generated by (1) is performed onto an 11-PSK signal space, according to Fig. 2(b). The effect of such a quantization mapping on the BER floor is reported in [17].

B. Decoding Algorithm

At the receptor, the transmitted information bit sequence $\{x_n\}$ at the moment $i = m(g+p)-1$ can be estimated from the wavelet symbol sequence y_n by using a bank of m correlators of length mg matched with the m rows of the WCM as

$$z_i^j = \sum_{k=0}^{mg-1} a^j_{(mg-1)-k}(y_{i-k} + e_{i-k}), \tag{3}$$

where e_{i-k} is an integer random variable that denotes the *demodulation noise* [18]. Due to the orthogonally of the MCWs' rows, the original transmitted bits can be estimated as $\hat{x}_{j+1-(mg-1)} = sgn(z_i^j)$. The decoding process' computational simplicity is one of the main features of wavelet coding [16], [21].

III. System Description

Fig. 3 shows the block diagram of the proposed transmission system together with the actual laboratory setup in terms of three main parts: A) Digital transmitter (top-left); B) experimental setup (top-right); and C) digital receiver (bottom), as described in the following subsections.

A. Digital Transmitter

A pseudo-random sequence of bits x with length l is generated and coded according to Section II-A. The wavelet symbols resulting from (1) are randomly interleaved and delivered to an inverse fast Fourier transform (IFFT) after serial-to-parallel conversion in order to form OFDM symbols, expressed in time domain as [22]:

$$s[n] = \mathcal{F}^{-1}(S[k]), \quad k = 0, 1, \ldots, N-1, \tag{4}$$

where $\mathcal{F}(\cdot)^{-1}$ denotes the inverse Fourier transform operation with size N, and $S[k]$ is the frequency-domain symbol for the k-th sub-carrier.

OFDM symbols with $N = 512$, $N = 1024$, and $N = 2048$ sub-carriers are considered in this work. For each OFDM symbol, the transmitted symbols are denoted as $\mathbf{S} = [S[0], S[1], \ldots, S[N-1]]^T$, where the first N_{null} tones and the last N_{null} tones are designated as null sub-carriers to be used as guard bands. The number of required sub-carriers is a composite of the $l + m * g - 2$ coded output symbols plus null sub-carriers. The IFFT sizes are chosen to be fixed, always equal to such a number of required sub-carriers.

Every OFDM symbol has pilot tones $\mathbf{P}$ at periodically-located sub-carriers, which are used for a frequency-domain interpolation to estimate the channel response along the frequency axis at the receptor. Let S_f be the period of the pilot tones in frequency domain to be allocated along the N_U used sub-carriers, then the pilot tones $\mathbf{P}$ are allocated in $\mathbf{S}$ according to $\mathbf{S} = [P[N_{null} + S_f], P[N_{null} + 2S_f], \ldots, P[N - 1 - N_{null}]]$. A period of $S_f = 6$ data tones per pilot tone is considered in this work.

Each OFDM symbol is extended with a cyclic prefix (CP) before parallel-to-serial conversion. CP lengths of 0%, 6.25%, and 12.5% of the OFDM sizes are considered in this work. When an OFDM frame (a set of serial OFDM symbols) is mounted, a preamble of 2.5 times the length of the OFDM symbol is appended to its beginning for time-domain synchronization and fine frequency synchronization at the receiver. After eight times oversampling and pulse shaping by a raised cosine (RC) filter, the resultant digital signal is pre-modulated by an intermediate frequency (IF) of 6.5 GHz and clipped to 40% of its maximum for peak-to-average power reduction (PAPR), before being delivered for digital-to-analog conversion (DAC).

B. Experimental Setup

The setup consists of three stations, as shown in Fig. 3(b) and further expanded into Fig. 4, which in a deployment case would be geographically separated: *Station I)* optical signal generation and modulation followed by optical fiber transmission; *Station*

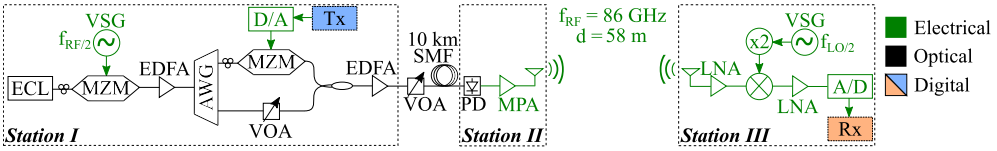

Fig. 4. Schematic of the proposed experimental setup for radio-over-fiber transmission, including optical (black) and electronic components (green). ECL: external cavity laser, VSG: vector signal generator, MZM: Mach-Zehnder modulator, EDFA: erbium doped fiber amplifier, AWG: arrayed waveguide grating, D/A: digital-to-analog conversion (performed by an arbitrary waveform generator - AWG), VOA: variable optical attenuator, SMF: standard single-mode fiber, PD: photodiode, MPA: medium power amplifier, LNA: low noise amplifier, A/D: analog-to-digital conversion (performed by a digital storage oscilloscope - DSO).

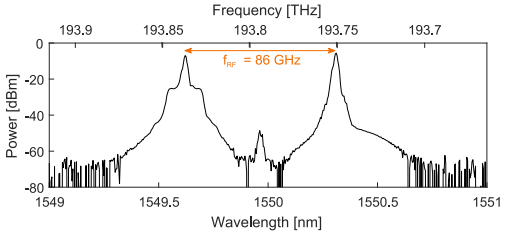

Fig. 5. Signal spectra of the optical signal at the output of the 3 dB coupler, before fiber transmission and photonic upconversion, for the generation of a signal with an 86 GHz carrier.

Fig. 6. Experimental Setup. Top-left: *Station I* and *Station III*. Top-right: *Station II*. Bottom-left: fiber span. Bottom-right: transmitting antenna. Bottom-center: receiving antenna.

II) optical to radio-frequency (RF) conversion followed by W-band RF transmission; and *Station III)* the receiver station.

1) Station I): Signal generation consists of an external cavity laser (ECL) at $\lambda = 1550$ nm, followed by a Mach-Zehnder modulator (MZM) biased at its minimum transmission point and driven with a sinusoidal at $f_{RF}/2 = 43$ GHz to generate two spectral lines spaced at $f_{RF} = 86$ GHz. The signal is amplified by 22 dB using an erbium doped fiber amplifier (EDFA) with a noise figure (NF) < 6 dB and an arrayed waveguide grating (AWG) separates the two spectral lines, allowing to modulate one with data.

A 64 GSa/s arbitrary waveform generator (AWG) serves as a DAC for the signal produced by the digital transmitter layer, as described in Section III-A. After a driving amplifier, the signal at a speed of 8 Gbps drives the second MZM with ca. 90% modulation depth. The digital clipping before DAC ensures the majority of the signal will be in the linear range of the MZM transmission curve for optimum extinction ratio.

Two variable optical attenuators (VOAs) ensure equal power of the two arms and allow control over the output optical power. Fig. 5 shows the spectrum of the generated signal at the output of the coupler. A second EDFA with a 4.3 dB NF amplifies the signal by 20 dB before it is transmitted through 10 km of ITU-T G.652 standard single-mode fiber (SMF).

2) Station II): After fiber transmission the optical signal is converted to an RF signal by beating the two spectral lines on a photodiode (PD) with a nominal 3 dB bandwidth of 100 GHz and a responsivity of 0.5 A/W. The power incident on the PD is varied between -5.5 dBm and 2.5 dBm through the use of the second VOA for analysis of transmission performance. The generated RF signal is amplified by 10 dB and thus mm-wave signals with powers from -20 dBm to -4 dBm are transmitted over a wireless distance of 58 m through a pair of parabolic antennas with a gain of 48 dBi each.

3) Station III): At the receiver station the signal is amplified by a low noise amplifier (LNA) providing 25 dB gain before down-conversion to an intermediary frequency with a double balanced electrical mixer. The local oscillator for the mixer is obtained by feeding a passive frequency doubler with a sinusoidal at $f_{LO/2} = 37.5$ GHz. Downmixing yields the 8 GHz-wide signal centered at a frequency of $f_{RF-LO} = 11$ GHz. The received signal is amplified by 16 dB and recorded for bit-error rate (BER) measurements using a digital storage oscilloscope (DSO) that serves as an analog-to-digital converter for further offline digital processing.

A photograph of the laboratory setup is depicted in Fig. 6.

C. Digital Receiver

At the receptor, coarse frequency synchronization and coherent downconversion by $f_{RF} - f_{LO} = 11$ GHz is achieved by a Costas loop. Fig. 7(a) shows the spectrum of the received signal before downconversion. A band pass filter isolates the 8 GHz-wide signal now centred at the intermediate frequency $f_{IF} = 6.5$ GHz, as shown in Fig. 7(b). The resultant digital signal is then demodulated with a 6.5 GHz carrier frequency, as shown in Fig. 7(c), and finally low-pass filtered before being downsampled by a factor of eight, as shown in Fig. 7(d). Fig. 7(d) also shows the baseband original signal spectrum before transmission.

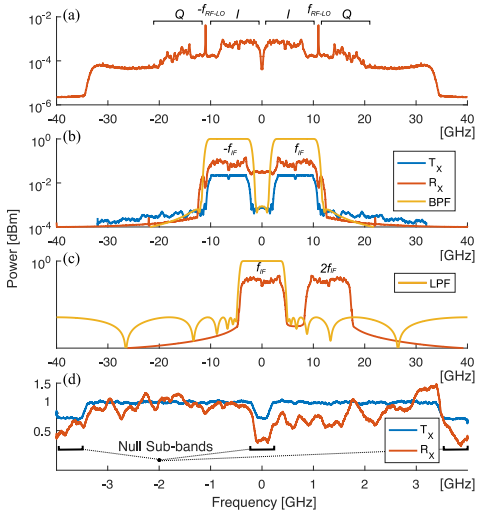

Fig. 7. Signal spectra of the signal and the digital filters: (a) after analog-to-digital conversion, and before RF-LO carrier recovery, (b) T_X signal before IF modulation (in blue), and R_X signal before IF post-demodulation (in red), (c) R_X signal before downsampling, (d) baseband T_X and R_X signals.

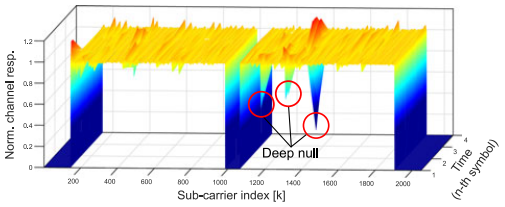

Fig. 8. Estimated baseband channel response, obtained as described in (5), for a 2048-sized OFDM symbol.

In baseband domain, the appended preamble is used for time synchronization and fine frequency offset correction [23]. After proper CP removal, the process of Fast Fourier Transform (FFT) with size N on the received signal produces the frequency domain symbols as $\tilde{\mathbf{S}} = \mathcal{F}(\mathbf{R})$. The received pilot tones $\tilde{\mathbf{P}}$ are extracted from $\tilde{\mathbf{S}}$ at their positions in the sub-carrier domain. Then, the least-square (LS) algorithm estimates the channel effects $\hat{H}[k]'_{LS}$ as:

$$\hat{H}'_{LS}[m] = \frac{\tilde{P}[m]}{P[m]}, \quad m = 0, 1, \ldots, \left\lceil \frac{N_U}{S_f} \right\rceil - 1, \qquad (5)$$

where N_U is the number of used sub-carriers and S_f stands for the period of pilot tones in the sub-carrier domain, as explained in Section III-A. Subsequently, $\hat{\mathbf{H}}'_{LS}$ is interpolated by *zero-padding* and *low pass filtering* to generate $\hat{\mathbf{H}}_{LS}$, which can be written for each subcarrier as $\hat{H}_{LS}[k]$, $k = 0, 1, \ldots, N-1$. The channel estimate $\hat{\mathbf{H}}_{LS}$ (as illustrated in Fig. 8) is utilized to generate an estimation of the transmitted data symbols as $\hat{\mathbf{S}} = \tilde{\mathbf{S}}/\hat{\mathbf{H}}_{LS}$.

Although the LS channel estimation does not consider the loss of orthogonality between sub-carriers, it has been widely used for channel estimation due to its simplicity. However, its mean-square error (MSE) is inversely proportional to the signal-to-noise ratio (SNR), which implies that it may be subject to noise enhancement, especially when the channel is in a deep null [8]. The wavelet symbols are then extracted from their positions, deinterleaved and finally decoded according to (3) for BER evaluation.

TABLE I
MODULATION SCHEMES FOR COMPARISON

			FFT Size		
			512	1024	2048
		N_U	420	840	1680
		ΔB (MHz)	15.62	7.81	3.90
		N_{symb}	22	10	4
		τ_{pre} (ns)	160	320	640
GI Size	0 %	τ_{symb} (ns)	64	128	256
GI Size	6.25 %	τ_{symb} (ns)	68	136	272
GI Size	12.5 %	τ_{symb} (ns)	72	144	288
GI Size	0 %	τ_{total} (μs)	1.568	1.600	1.664
GI Size	6.25 %	τ_{total} (μs)	1.656	1.680	1.728
GI Size	12.5 %	τ_{total} (μs)	1.744	1.760	1.792
GI Size	0 %	R (Gbps)	4.910	4.375	3.365
GI Size	6.25 %	R (Gbps)	4.649	4.166	3.240
GI Size	12.5 %	R (Gbps)	4.415	3.977	3.125
GI Size	0 %	SE (bit/s/Hz)	0.6138	0.5469	0.4206
GI Size	6.25 %	SE (bit/s/Hz)	0.5811	0.5208	0.4050
GI Size	12.5 %	SE (bit/s/Hz)	0.5519	0.4971	0.3906

IV. RESULTS AND DISCUSSION

A. Experimental Results

Recent simulation based studies [20] for the performance of WC-OFDM systems on slow-varying frequency selective channels indicated that coding gains of nearly 4 dB to 6 dB are achieved in relation to convolution-coded OFDM systems for a BER of 1e-3. In this work, the performance of WC-OFDM communication systems is experimentally evaluated on a composite radio-over-fiber link with 10 km optical transmission through standard SMF plus 58 m wireless transmission in the W-Band. Results were obtained for transmitted signals with a fixed rate of 1 pilot tone for every 6 data tones, within a bandwidth of 8 GHz on a radio frequency of 86 GHz, where each transmission is recorded 25 times, resulting in a total of 924.000 analyzed bits. Three OFDM resolutions, three CP lengths and two pilot levels were considered. Table I summarizes how these values affect the the number of used sub-bands per OFDM symbol (N_U), the sub-band spacing (ΔB), the number of OFDM symbols per OFDM frame (N_{symb}), the preamble transmission time (τ_{pre}), the transmission time of each OFDM symbol (τ_{symb}), the total frame transmission time (τ_{total}), the net bitrate (R), and the spectral efficiency (SE) on the use of the channel.

Fig. 9 shows the results obtained in terms of BER vs. optical power for 2×128 WC-OFDM signals with different FFT sizes and CP lengths. As can be seen, better BER is observed insofar

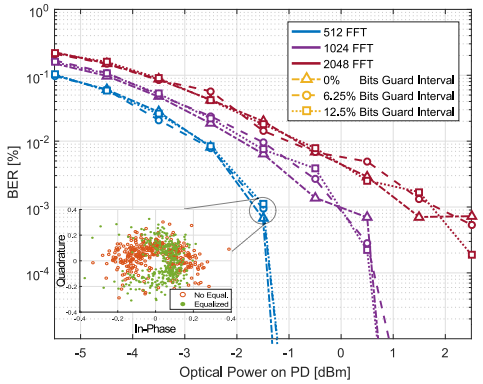

Fig. 9. BER vs. Optical Power on PD for WC-OFDM signals with different FFT sizes and CP lengths. Dark-blue curves represent the performance of 512-sized OFDM. Purple curves represent the performance of 1024-sized OFDM. Dark-red curves represent the performance of 2048-sized OFDM. Triangle marks (△) represent the situation in which 0 bits is used as CP, circle marks (◯) represent the situation in which 6.25% bits of the FFT size are used as CP, Square marks (□) represent the situation in which 12.5% bits of the FFT size are used as CP. The bottom-left constellation represents space of 11-PSK signals for 2 × 128 WC-symbols before and after equalization.

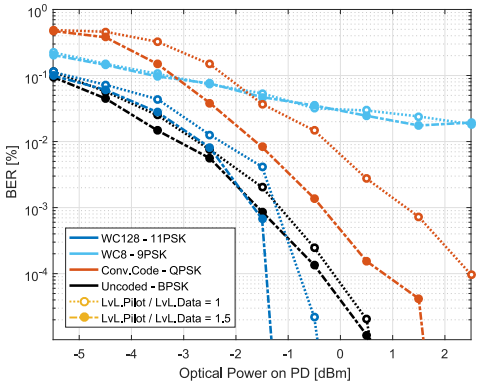

Fig. 10. BER vs. Optical Power on PD for different transmission schemes of equivalent spectral efficiency of 1 bit/s/Hz. Dark-blue curves represent the performance of WC-OFDM transmission with 2 × 128 Coding Wavelet Matrix and 11-PSK modulation. Light-blue curves represent the performance of WC-OFDM transmission with 2 × 8 Coding Wavelet Matrix and 9-PSK modulation. Red curves represent the performance of Convolution Code with rate 1/2 and QPSK modulation. Black curves represent the performance of uncoded BPSK scheme. Pointed lines with unfilled circles (· ○ ·) represent the situation in which pilot tones have the same level as data tones, whereas dashed lines with filled circles (-●-) represent the situation in which pilot tones have 1.5 times more power than data tones.

as the OFDM resolution (FFT size) decreases. This effect is explained by the fact that the larger the OFDM resolution is, the longer the OFDM symbols duration (τ_{symb}) gets – as shown in Table I – implying a larger phase walk off between the RF signal after the PD and the LO at the receiver, thus strongly affecting the transmission coherence due to degradation of sub-band orthogonality. Moreover, it can be seen that, regardless of the OFDM resolution, an increase of the CP length does not yield any performance improvement. This is striking evidence that the propagated signal was not subjected to any significant multipath propagation, as was expected since greatly directive antennas were used for a single-input-single-output (SISO) line-of-sight (LoS) wireless transmission, and because no multipath phenomena are expected from transmission within SMF.

Fig. 10 shows the results obtained in terms of BER vs. optical power incident on the PD for four transmission schemes with equivalent spectral efficiency of 1 bit/s/Hz, two ratios of pilot-tone level over data-tone level, and a fixed OFDM resolution of 512 sub-bands per symbol. The first thing to notice is that a greater pilot/data level ratio resulted in better performance, regardless of the coding scheme—with the exception of the 2× 8 WC case. This effect is a consequence of improved equalization although at the price of decreased SNR, showing a trade-off where finding an optimum configuration yields large performance gains. It should be stressed however, that due to power limitations imposed by some of the utilized electronic components—such as A/D and D/A converters, mixers etc.—it was expected that a further increase in the pilot/data level ratio would not lead to any greater performance improvement.

For a fixed BER of 1e-4, Fig. 10 shows the 2 × 128 WC scheme with a pilot/data level ratio of 1.5 to outperform the uncoded BPSK scheme by 1 dB. Furthermore, the 2 × 128 WC outperforms the convolutional QPSK scheme by nearly 2.5 dB.

B. Discussion

From prior studies on WC [17], it is expected that, in purely additive white Gaussian noise (AWGN) channels, both the 2× 8 and the 2× 128 WC schemes have the same performance as the uncoded BPSK scheme. It is moreover expected, still assuming a purely AWGN channel, that the convolutional coded scheme should outperform the uncoded scheme, even considering a twice higher-dimension signal constellation – which does not occur. These evidences point to the conclusion that the observed propagation channel is indeed subject to some frequency selectivity, as observed in Fig. 8, even in such a purely LoS SISO link with the 1st Fresnel zone within a radius of 22 cm.[1] A detailed investigation on the frequency response of the wireless W-Band channel and previous findings [4], [5] corroborate this conclusion.

Moreover, as chromatic dispersion (CD) will not significantly affect an 8 GHz signal within an optical link of 10 km of SMF, nor is the channel affected by multipath (as concluded from Fig. 9), there is a substantial indication that such a frequency selectivity is caused by the composite non-flat frequency response of electronic and optical components within the setup. While component bandwidths at all stages were larger than that of the signal – the MZM and driver amplifier have a BW of 40 GHz, the RF amplifiers are full band W-Band and the IF amplifier has a BW of ca. 25 GHz – their frequency response within the their bandwidth may vary and especially for the RF amplifiers will not be flat. Combined with non-flat frequency response of the antennae and most significantly that of the mixer employed for down-conversion these may cause the distortions observed in Figs. 7 and 8.

[1] $r = 17.32 \times \sqrt{0.058[\mathrm{Km}]/(4 \times 86[\mathrm{GHz}])} = 0.22$ m

The observed results suggest that the diversity gains provided by WC do compensate for fading effects in digital transmission, corroborating results from previous studies [18]–[20]. The reduced performance of the 2×8 WC scheme indicates that, due to the trade-off between diversity gain and SNR reduction resulting from the more complex signal constellation, the use of this particular coding-modulation dimension is not recommended for the proposed scenario. However, the performance improvements observed from the use of a larger-dimension WCM are very consistent with results obtained in prior studies [17] inasmuch as greater diversity gains can compensate for more frequent deep fading caused by the channel. The potential gains enabled by WC thus make it a strong candidate for additional coding in future mobile communications.

V. Conclusion

Several methods have been presented to compensate unsolved frequency selectivity in OFDM systems, including the application of channel coding over the sub-carrier domain. These solutions usually require either an expensive computational complexity or some decrease in system spectral efficiency. Confirming the findings of [19] and [20], that WC can substantially compensate for the combined effects of deep frequency fading and error bursts disrupting orthogonality among OFDM sub-carriers, we experimentally demonstrate transmission of 4.9 Gbps 2×8 and 2×128 WC-OFDM signals over a radio-over-fiber link of 10 km fiber plus 58 m wireless distance (with distances of 100 m and beyond predicted to be achievable analog to [5]), using a radio carrier frequency of 86 GHz. We find that, for a fixed BER of 1e-4, the $2\times$ 128 WC scheme outperforms an uncoded BPSK by 1 dB while outperforming a convolutional coded QPSK by nearly 2.5 dB.

Considering a SISO LoS setup, the results indicate that the proposed system is able to compensate for the combined effects of noise bursts and frequency distortions caused by electronic components. It is important to stress that these results confirm the theory of Tzannes [16] that the WC enables high diversity gains with a low complexity receiver, without compromising the system's spectral efficiency. Moreover, the results also validate the solution proposed in [18] on modulation schemes that support the integration of WC with power-limited systems. To the best of the authors' knowledge, this is the first time that the transmission of WC signals has been experimentally demonstrated.

The current study indicates that the proposed system fits as a key enabler for the use of mm-wave frequencies in future generation mobile communications, due to its robustness to the harsh effects of frequency selective channels caused either by unsolved multipath or, as in the case of this work, by the highly non-flat frequency response of the employed RF and optical components. It is worth noting though that the Wavelet-Coding algorithm presented in this work is still tied up to 1 bit/s/Hz modulation schemes. Future work should therefore consider strategies to allow higher order modulation formats. Moreover, further investigation must be done on the effects of frequency offset, time offset, and phase distortions on the performance of the proposed system. Signal fading between the antennas should also be considered.

References

[1] L. Kazovsky, S. W. Wong, T. Ayhan, K. M. Albeyoglu, M. R. Ribeiro, and A. Shastri, "Hybrid optical-wireless access networks," *Proc. IEEE*, vol. 100, no. 5, pp. 1197–1225, May 2012.

[2] T. S. Rappaport *et al.*, "Millimeter wave mobile communications for 5G Cellular: It will work!," *IEEE Access*, vol. 1, pp. 335–349, May 2013.

[3] L. Cavalcante, S. Rommel, J. J. Vegas Olmos, and I. T. Monroy, "On the capacity of radio-over-fiber links at the W-band," *Springer Opt. Quantum Electron.*, vol. 48, no. 5, pp. 1–10, Apr. 2016.

[4] S. Rommel, L. Cavalcante, A. G. Quintero, A. K. Mishra, J. J. Vegas Olmos, and I. T. Monroy, "W-band photonic-wireless link with a Schottky diode envelope detector and bend insensitive fiber," *OSA Opt. Express*, vol. 24, no. 11, pp. 11312–11322, May 2016.

[5] S. Rommel *et al.*, "Outdoor W-Band hybrid photonic wireless link based on an optical SFP+ Module," *IEEE Photon. Technol. Lett.*, vol. 28, no. 21, pp. 2303–2306, Nov. 2016.

[6] B. Sklar, "Rayleigh fading channels in mobile digital communication systems Part I: Characterization," *IEEE Commun. Mag.*, vol. 35, no. 7, pp. 90–100, Jul. 1997.

[7] W. Gao, C. Duan, and J. Zhang, "Subcarrier spreading for ICI mitigation in OFDM/OFDMA systems," in *Proc. IEEE Conf. Commun.*, May 2010, pp. 1–6.

[8] Y. S. Cho, J. Kim, W. Y. Yang, and C. G. Kang, *MIMO-OFDM Wireless Communications With MATLAB*, Chichester, U.K.: Wiley, 2010.

[9] T. Masakawa and H. Ochiai, "Design of reed-solomon codes for OFDM systems with clipping and filtering," in *Proc. IEEE Wireless Commun. Netw. Conf.*, Mar. 2007, pp. 1361–1366.

[10] M. Chen, X. Xiao, J. Yu, F. Li, Z. R. Huang, and H. Zhou, "Demonstration of software-reconfigurable real-time FEC-Enabled 4/16/64-QAM-OFDM signal transmission in an X-band RoF system," *IEEE Photon. J.*, vol. 8, no. 2, Apr. 2016, Art. no. 7902908.

[11] W. Jian, C. Liu, H.-C. Chien, and S.-H. Fan, "Link performance improved 16QAM-OFDM 60-GHz radio-over-Fiber system employing convolutional codes," in *Proc. IEEE Opt. Fiber Commun., Collocated National Fiber Opt. Eng. Conf.*, Mar. 2010, Paper OThO4.

[12] A. Vallavaraj, G. S. Brian, K. H. David, and G. M. Francis, "Optimizing the rate 1/2 convolutional code for OFDM applications in terms of bit-error-rate and peak-to-average power ratio," in *Proc. IEEE GCC Conf.*, Mar. 2006, pp. 1–6.

[13] B. Lu and X. Wang, "A space-time trellis code design method for OFDM systems," *Springer Wireless Personal Commun.*, vol. 24, no. 3, pp. 403–418, Feb. 2003.

[14] Z. Cao, J. Yu, Q. Tang, G. Zeng, and L. Chen, "Long-reach 60-GHz radio-over-fiber system based on turbo-coded OFDM," *OSA Chinese Opt. Lett.*, vol. 8, no. 11, pp. 1024–1027, Nov. 2010.

[15] I. B. Djordjevic, L. Xu, and T. Wang, "Adaptive LDPC-coded OFDM for radio-over-fiber technologies," in *Proc. IEEE LEOS Annu. Meeting Conf. Proc.*, Oct. 2009, pp. 448–449.

[16] M. A. Tzannes, "Bit-by-bit channel coding using wavelets," in *Proc. IEEE GLOBECOM*, Dec. 1992, vol. 2, pp. 684–688.

[17] L. F. Silveira, "Análise da Codificação Wavelet em Sistemas Sujeitos ao Desvanecimento Rayleigh Plano," Ph.D. dissertation, Dept. Electr. Eng., Universidade Federal do Rio Grande do Norte, Natal, RN, Brazil, 2006.

[18] L. F. Silveira, L. G. Silveira, F. M. Assis, and E. L. Pinto, "Analysis and optimization of wavlet-coded communication systems," *IEEE Trans. Wireless Commun.*, vol. 8, no. 2, pp. 563–567, Feb. 2009.

[19] L. Cavalcante, L. F. Silveira, S. Rommel, J. J. Vegas Olmos, and I. T. Monroy, "Performance analysis of wavelet channel coding in COST207-based channel models on simulated radio-over-fiber systems at the W-band," *Springer Opt. Quantum Electron.*, vol. 48, no. 1, pp. 1–9, Jan. 2016.

[20] L. Cavalcante, R. Dinis, L. G. Silveira, L. F. Silveira, J. J. Vegas Olmos, and I. T. Monroy, "Wavelet-Coded OFDM for next generation mobile communications," in *Proc. IEEE Veh. Technol. Conf.*, Sep. 2016.

[21] H. Resnikoff and R. Wells, *Wavelet Analysis: The Scalable Structure of Information*, New York, NY, USA: Springer-verlag, 1998.

[22] A. Gorokhov and J. P. Linnartz, "Robust OFDM receivers for dispersive time–varying Channels: Equalization and channel acquisition," *IEEE Trans. Commun.*, vol. 52, no. 4, pp. 572–583, Apr. 2004.

[23] H. Minn, V. K. Bhargava, and K. B. Letaief, "A robust timing and frequency synchronization for OFDM systems," *IEEE Trans. Wireless Commun.*, vol. 2, no. 4, pp. 822–839, Jul. 2003.

Authors' biographies not available at the time of publication.

PAPER13: Non-Orthogonal Multiple Access and Carrierless Amplitude Phase Modulation for 5G Mobile Networks

J. A. Altabas, **S. Rommel**, R. Puerta, D. Izquierdo, I. Garcés, J. A. Lazaro, J. J. Vegas Olmos, and I. Tafur Monroy. "Non-Orthogonal Multiple Access and Carrierless Amplitude Phase Modulation for 5G Mobile Networks". In: *43rd European Conference on Optical Communication*. Sept. 2017, paper Tu.1.B.2. *(inpress)*

Non-Orthogonal Multiple Access and Carrierless Amplitude Phase Modulation for 5G Mobile Networks

Jose A. Altabas[(1)], Simon Rommel[(2)], Rafael Puerta[(2)], David Izquierdo[(1,3)], Ignacio Garces[(1)], Jose A. Lazaro[(4)], Juan Jose Vegas Olmos[(5)], Idelfonso Tafur Monroy[(2)]

[(1)] Aragon Institute of Engineering Research (I3A), Universidad de Zaragoza, Zaragoza, Spain; email: jaltabas@unizar.es
[(2)] Department of Photonics Engineering, Technical University of Denmark (DTU), Kgs. Lyngby, Denmark, email: sirem@fotonik.dtu.dk
[(3)] Centro Universitario de la Defensa (CUD), Zaragoza, Spain
[(4)] Universitat Politecnica de Catalunya (UPC-BarcelonaTech), Barcelona, Spain
[(5)] Mellanox Technologies, Ledreborg Alle 130B, 4000, Roskilde, Denmark

Abstract *A combined NOMA and multiCAP scheme is proposed for capacity enhancement of 5G mobile networks and experimentally tested over a W-band millimeter-wave radio-over-fiber system. The evaluated NOMA-CAP system provides an aggregated transmission rate of 30Gbps.*

Introduction

Traffic demand over wireless networks is growing exponentially due to new multimedia streaming services, the Internet of Things (IoT) and machine-to-machine communications[1]. This growing traffic on 5G networks requires the use of non-congested wireless bands such as millimeter-wave (mm-wave), and so it will require a re-design of front- and backhaul architectures for radio access networks (RANs). The use of centralized radio access networks (C-RANs) is suggested as a key enabler[1,2] and its combination with radio-over-fiber (RoF) on passive optical networks (PON) is a promising candidate to flexibly support 5G mobile networks[2].

In RANs, the design of the access to the medium is a key technology in order to improve system capacity and to dynamically allocate the available resources. Non-orthogonal multiple access (NOMA) is a promising candidate for addressing these requirements and to enhance both capacity and flexibility of the network[3].

The NOMA technique multiplexes the data of several users in the power domain by adding the contributing signals and allows combination with time- or frequency multiplexing. Successive interference cancellation (SIC) is employed in the terminal units in order to recover the contributing signals and thus demultiplex the NOMA users[3].

High data rate demands require a migration from inefficient modulation formats, such as impulse radio or on-off keying, to advanced modulation schemes as multi-band carrierless amplitude phase (multiCAP) modulation[4].

In this paper, NOMA and multiCAP techniques are combined in order to allow flexible resource provisioning that addresses the dynamic nature of user density and capacity demands. Fig. 1 shows a possible application scenario where two users are located at different distances to the base station (BS) and share the medium by NOMA multiplexing.

The NOMA-CAP is experimentally validated on a W-band RoF link. NOMA-CAP using six 1.25GHz multiCAP bands and two quadrature phase shift keying (QPSK) NOMA levels has been tested achieving aggregated transmission rate of 30Gbps.

Experimental Setup

Figs. 2 and Fig. 3 shows the transmitter and receiver digital signal processing (DSP) respectively, while Fig. 4 shows the experimental setup used to validate the proposed NOMA-CAP transmission over a hybrid photonic-wireless link.

The transmitter DSP for NOMA-CAP, shown in Fig. 2, distributes the data of each user or NOMA level among all the multiCAP bands and maps them to QPSK symbols. The NOMA levels are power weighted and added for each multiCAP band. The band signals are up-sampled and filtered with a pair of band specific multiCAP orthogonal filters. Finally, the multiCAP bands are aggregated. In the test case, two NOMA levels and six 1.25GHz multiCAP bands are used.

The optical signal generation, depicted in Fig. 4a), is based on the modulation of a narrow linewidth external cavity laser (ECL) at λ=1550nm by a Mach-Zehnder modulator (MZM) biased at its minimum transmission point with a sinusoidal signal at $f_{RF}/2$ from a vector signal generator (VSG). This configuration generates two

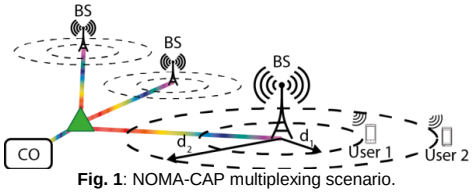

Fig. 1: NOMA-CAP multiplexing scenario.

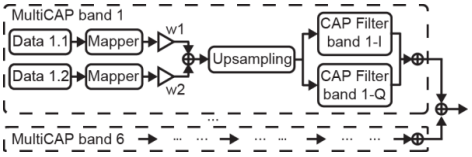

Fig. 2: Transmitter DSP block diagram.

spectral lines spaced at f_{RF}=84GHz, which later serve for the photonic generation of the RF signal. After amplification in an erbium doped fiber amplifier (EDFA), the lines are separated in an arrayed waveguide grating (AWGG). Finally, one of the spectral lines is modulated with the NOMA-CAP signal using a second MZM. The power of both lines are adjusted to be equal employing a variable optical amplifier (VOA) before they are added and amplified by a second EDFA. The launch power is adjusted with a second VOA before transmission through 10km of ITU-T G.652 standard single mode fiber (SMF).

Optical to RF conversion, shown in Fig. 4b), is performed by a RAU designed for minimum complexity. The high-speed photodiode (PD) receives the optical signal and the generated RF signal is the beating of the two optical lines. The PD bandwidth is 90GHz and its responsivity is 0.5A/W. RF power is amplified by a 10dB medium power amplifier (MPA) up to a saturation output power of 12dBm. A parabolic antenna with a gain of 48dBi is used to transmit the signal.

The wireless receiver, depicted in Fig. 4c), consists of an identical antenna after which the RF signal is amplified by a 20dB low noise amplifier (LNA) before down-conversion to an intermediate frequency (IF) at $f_{IF} = f_{RF} - f_{LO}$ is performed in a balanced mixer. The local oscillator (LO) for the mixer is obtained from a passive frequency doubler, driven with a sinusoid at $f_{LO}/2$ from a second VSG. The resulting IF signal is DC blocked and amplified before it is recorded on an oscilloscope (DSO) for offline processing.

The receiver DSP block diagram, which is the same for all users, is shown in Fig. 3a) and consists of a Costas loop for carrier frequency and -phase recovery for IF to baseband conversion, after the signal was band-filtered for noise bandwidth reduction. The baseband signal is low-pass filtered and each multiCAP band is extracted, employing the pair of orthogonal filters for

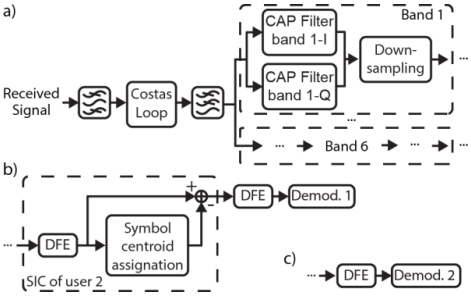

Fig. 3: Receiver DSP block diagram: (a) multiCAP band recovery (common to all receivers), (b) user 1 receiver with SIC processing, (c) user 2 receiver without SIC processing.

the band of interest. The close users have to implement SIC as is shown in Fig. 3b), consisting of a decision feedback equalizer (DFE) with 30 forward and 20 backward taps, calculation of the symbol centroid of the far user and subtraction from the equalized signal. After SIC, the DFE is applied again to the new signal and finally the signal is de-mapped. In the case of far users, shown in Fig. 3c), SIC is not required and the DFE and de-mapping are performed directly.

Results

The wireless transmission analysis for both user types with an available data rate of 15Gbps for each user, in terms of wireless distance and NOMA power ratio between users is shown in Fig. 5 (far user) and Fig. 6 (close user).

The received optical power on the PD is varied between -3dB and +2.5dB from a reference level of 0dBm using the second VOA, while wireless distance remains constant (50m). This optical power is directly related to the transmitted RF power, so its variation can be used to emulate the wireless distance without moving the antennas[2]. The total power of the NOMA-CAP signal is kept constant and the power ratio between users (r_{power}) is defined as

$$r_{power} = 10 \log\left(\frac{w_2}{w_1}\right) \quad (1)$$

where w_1 is the weight of the close user, while w_2 is the weight of the far user.

The distance analysis has been performed employing the respective BER limits of 3.8×10^{-3} and 1.32×10^{-2} for forward error corrections (FEC) with 7% and 25% overhead (OH)[5].

For user 2, i.e. the user located far, the NOMA

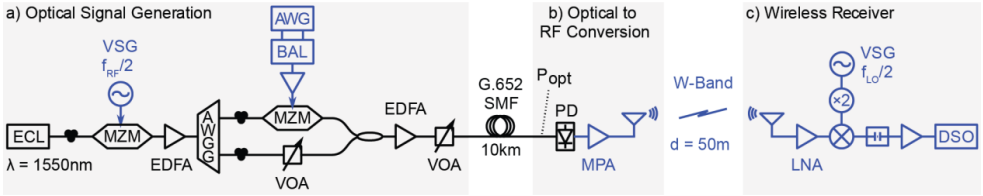

Fig. 4: Schematic of the experimental setup.

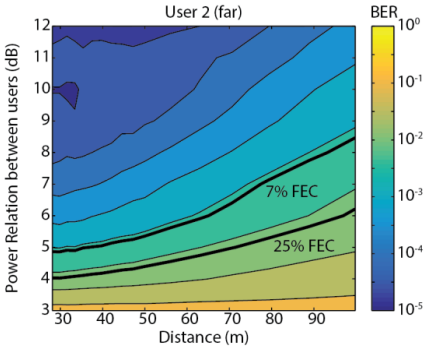

Fig. 5: BER map in terms of distance and power ratio between users for the user located far to the antenna.

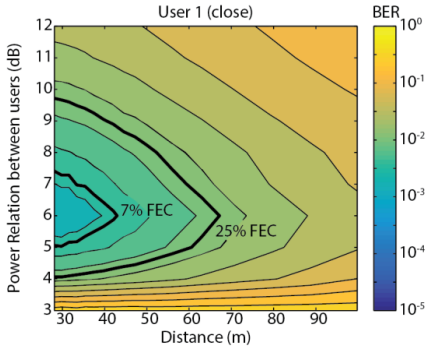

Fig. 6: BER map in terms of distance and power ratio between users for the user located close to the antenna.

multiplexing with the signal of user 1 will be regarded as an increment of the received noise and thus a reduction of the power ratio between users will increase the user BER and reduce the achievable distance for user 2 as seen Fig. 5.

In the same scenario, user 1, i.e. the user close by, will apply SIC cancellation before demodulation in order to remove the signal of user 2. Any errors in the calculation of the centroid of user 2 will propagate to the decoding of user 1 in the SIC process and thus they will cause a high BER for the user 1, as can be seen in Fig. 6 The use of a low power ratio between users, i.e. when the powers of user 1 and user 2 are comparable, will have a similar effect as placing user 1 at a long distance, resulting in errors in the calculation of the user 2 centroid and consequent error propagation to user 1 decoding. On the other hand, the BER of user 1 will increase with high power ratios as the signal will be too weak after SIC, even if the SIC process perfectly calculates the user 2 centroids. Thus, user 1 will only be successfully demodulated for intermediate power relations and for close distances, as seen in Fig. 6.

Tab. 1 summarizes the maximum reachable distances for both users under different power ratios. User 2 would thus prefer a scenario with high power ratio (r_{power}>8dB), and user 1 will prefer scenarios with medium power ratios (r_{powe}=6-7dB). The increment of the operational range of one user will decrease the range of the other user. If the effective data rate can be reduced, a 25% OH FEC can be implemented and both users can be placed farther.

Tab. 1: Summary of maximum achievable distances for both users and different power ratios. x denotes no transmission distance possible below BER limit. Ø denotes a distance greater than those experimentally tested.

	User 1 (close)		User 2 (far)	
Power ratio	7% FEC	25% FEC	7% FEC	25% FEC
5dB	x	61m	36m	70m
6dB	43m	67m	65m	96m
7dB	33m	59m	77m	Ø
8dB	x	52m	Ø	Ø
9dB	x	40m	Ø	Ø

Conclusions

A combination of multiCAP and NOMA is proposed for application in future 5G mobile RANs, allowing optimization of capacity. An experimental demonstration was given for a NOMA-CAP RoF system in W-band.

The experimental demonstration achieved an aggregate system capacity of 30Gbps using a NOMA-CAP signal consisting of six 1.25GHz multiCAP and two NOMA levels. BER measurements are shown for different power ratios between the contributing NOMA signals and for different optical powers, relating to wireless distances between 30m and 100m.

Acknowledgements

This work was supported in part by the DFF FTP mmW-SPRAWL project, Spanish MINECO projects muCORE (TEC2013-46917-C2-2-R) and SUNSET (TEC2014-59583-C2-1-R) co-funded by FEDER, Diputación General de Aragón (T25); Centro Universitario de la Defensa project BIO-DIVING (CUD2016-18) and MECD grant FPU-13/00620.

References

[1] T. Pfeiffer, "Next generation mobile fronthaul and midhaul architectures," IEEE J. Opt. Commun. Netw., Vol. **7**, no. 11, pp. B38-B45, (2015).

[2] S. Rommel et al. "Outdoor W-band hybrid photonic wireless link based on an optical SFP+ module," Photon. Technol. Lett, Vol. 28, no. 21, pp. 2303-2306, (2016).

[3] K. Higuchi et al. "Non-orthogonal multiple access (NOMA) with successive interference cancellation for future radio access," IEICE Trans. Commun., Vol**. E98-B**, no. 3, pp. 403-414, (2015).

[4] M. I. Olmedo et al., "Multiband carrierless amplitude phase modulation for high capacity optical data links," J. Lightwave Technol., Vol. **32**, no. 4, pp. 798-804, (2014).

[5] [21] ITU-T Recommendation G.975.1 (2004)

PAPER14: Non-Orthogonal Multiple Access and Carrierless Amplitude Phase Modulation for Flexible Multi-User Provisioning in 5G Mobile Networks

J. A. Altabas, **S. Rommel**, R. Puerta, D. Izquierdo, I. Garcés, J. A. Lazaro, J. J. Vegas Olmos, and I. Tafur Monroy. "Non-Orthogonal Multiple Access and Carrierless Amplitude Phase Modulation for Flexible Multi-User Provisioning in 5G Mobile Networks". In: *Journal of Lightwave Technology* (2017). DOI: 10.1109/JLT.2017.2761541. *(inpress)*

Non-Orthogonal Multiple Access and Carrierless Amplitude Phase Modulation for Flexible Multi-User Provisioning in 5G Mobile Networks

Jose Antonio Altabas, Simon Rommel, *Student Member, IEEE*, Rafael Puerta, *Student Member, IEEE*, David Izquierdo, Juan Ignacio Garces, *Member, IEEE*, Jose Antonio Lazaro, *Member, IEEE*, Juan José Vegas Olmos, *Senior Member, IEEE*, and Idelfonso Tafur Monroy, *Senior Member, IEEE*

***Abstract*—In this paper, a combined non-orthogonal multiple access (NOMA) and multiband carrierless amplitude phase modulation (multiCAP) scheme is proposed for capacity enhancement of and flexible resource provisioning in 5G mobile networks. The proposed scheme is experimentally evaluated over a W-band millimeter wave radio-over fiber system. The evaluated NOMA-CAP system consists of six 1.25 GHz multiCAP bands and two NOMA levels with quadrature phase shift keying and can provide an aggregated transmission rate of 30 Gbit/s. The proposed system can dynamically adapt to different user densities and data rate requirements. Bit error rate performance is evaluated in two scenarios: a low user density scenario where the system capacity is evenly split between two users and a high user density scenario where NOMA and multiCAP are combined to serve up to twelve users with an assigned data rate of 2.5 Gbit/s each. The proposed system demonstrates how NOMA-CAP allows flexible resource provisioning and can adapt data rates depending on user density and requirements.**

***Index Terms*—Non-orthogonal multiple access, multi-band carrierless amplitude phase modulation, radio-over-fiber, millimeter-wave communications, W-band wireless.**

I. Introduction

TRAFFIC demand over wireless networks is growing exponentially due to new multimedia streaming services, the Internet of Things (IoT) and machine-to-machine communications [1]–[4]. These high bandwidth multi-gigabit wireless connections require 5G access networks that not only use the current and congested wireless bands but also the millimeter wave (mm-wave) bands such as IEEE V- (40–75 GHz) and W-bands (75–110 GHz) [3]–[8]. The V-band has been proposed for indoor communications and next generation Wi-Fi due to the atmospheric oxygen absorption peak [7], [9] while the W-band presents a lower atmospheric absorption [7] and is thus favored for both indoor and outdoor wireless communications.

The introduction of mm-wave frequencies to 5th generation mobile communications requires a re-design of front- and backhaul radio access network (RAN) architectures, to enable them support high data rates, heterogeneous user density scenarios and flexible resource provisioning [2]. The use of centralized radio access networks (C-RANs) is suggested as a key enabler [3], [4], [8], which, combined with radio-over-fiber (RoF) on passive optical networks (PONs), is a promising candidate to flexibly support 5G mobile networks [8], [10].

In RANs, the design of the access to the medium is essential to improve the system capacity and to dynamically allocate the available resources. Non-orthogonal multiple access (NOMA) is a promising candidate for addressing these requirements and to enhance both capacity and flexibility of the network [11]–[16]. NOMA uses power multiplexing as a multiple access approach, allowing a direct sharing of time and frequency resources between users. NOMA can also improve the spectral efficiency of the RAN, allowing massive connectivity, low transmission latency and low cost [11], [14], [15].

In addition, high data rate demands require a migration from inefficient modulation formats, such as impulse radio or on-off keying, to advanced and flexible modulation schemes such as multi-band orthogonal frequency division multiplexing (MB-OFDM) [17] or multi-band carrierless amplitude phase (multiCAP) modulation [18]. Although MB-OFDM has shown flexible adaptation to a dynamically changing wireless medium, multiCAP allows less complex transceivers [19] and has shown promising results [20]–[23], achieving large capacities even under difficult channel conditions.

In this paper, both NOMA and multiCAP techniques are combined in order to allow flexible resource provisioning, able to address the dynamic nature of user density and capacity demands. This proposed NOMA-CAP combination can be a feasible technique for the standardization of the future 5G networks.

Fig. 1(a) shows a scenario of only two users at different distances to the base station (BS). A high capacity link will be

Manuscript received August 25, 2017; revised ??; accepted ??. This work was partly funded by the DFF FTP mmW-SPRAWL project, Diputación General de Aragón (T25), Spanish MINECO (muCORE TEC2013-46917-C2-2-R, SUNSET TEC2014-59583-C2-1-R within FEDER) and MECD (FPU-13/00620). R. Puerta would like to express his gratitude to the Colombian Administrative Department of Science, Technology and Innovation (COLCIENCIAS).

J. A. Altabas, D. Izquierdo and J. I. Garces are with the Department of Electrical Engineering and Communications, Aragon Institute of Engineering Research, University of Zaragoza, 50018 Zaragoza, Spain, e-mail: jaltabas@unizar.es.

S. Rommel and R. Puerta are with the Department of Photonics Engineering, Technical University of Denmark, 2800 Kgs. Lyngby, Denmark, e-mail: sirem@fotonik.dtu.dk.

D. Izquierdo is also with the Centro Universitario de la Defensa, 50090 Zaragoza, Spain.

J. A. Lazaro is with the School of Telecommunications Engineering, Polytechnic University of Catalonia, 08034 Barcelona, Spain.

J. J. Vegas Olmos is with Mellanox Technologies, 4000 Roskilde, Denmark.

I. Tafur Monroy is with the Institute for Photonics Integration, Eindhoven University of Technology, 5600 MB Eindhoven, Netherlands.

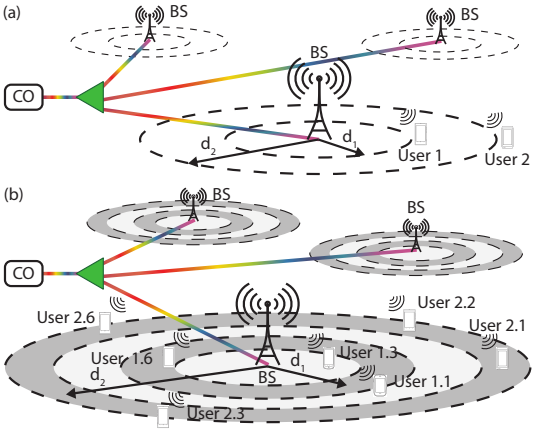

Fig. 1. NOMA-CAP multiplexing scenarios with different user densities.

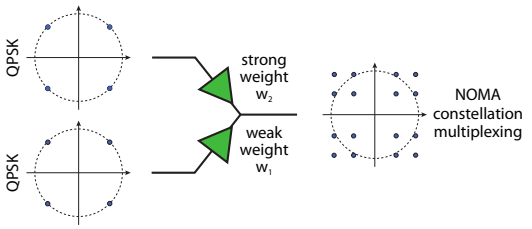

Fig. 2. NOMA constellation multiplexing for two users with QPSK signals.

assigned to each by means of sharing all multiCAP bands using NOMA multiplexing. When new users try to access the RAN, the resources can be flexibly allocated, assigning different multiCAP bands to different users, as shown in Fig. 1(b). In this high density scenario, NOMA power multiplexing and multiCAP are employed in combination, reducing the assigned capacity to each user, but increasing the user density of the RAN and optimizing overall system throughput. In addition, the overall system throughput can be raised even more by employing power loading and narrower band guards [22] or employing single side-band transmissions [21].

The proposed NOMA-CAP technique [20] is experimentally validated on a W-band RoF downlink using six 1.25 GHz wide multiCAP bands and two NOMA levels with quadrature phase shift keying (QPSK) achieving an aggregated transmission rate of 30 Gbit/s. The two scenarios shown in Fig. 1 have been evaluated, where either two users use all the multiCAP bands and evenly share the capacity of the RAN or twelve users are multiplexed employing NOMA and multiCAP. The transition between scenarios—or any intermediate scenario—is dynamic depending on user demands and showcases the flexible resource provisioning that NOMA-CAP can provide to the RAN. This proof of concept shows two possible operation cases of NOMA-CAP, showing the trade-off between the number of users and the per-user capacity. These scenarios have been tested on a W-band RoF link as a demonstration of the high throughput employing the future 5G frequency ranges, although the NOMA-CAP technique is carrier independent and it could be operated in the traditional frequency ranges used for mobile communications.

The remainder of this paper is structured as follows: section II discusses NOMA and CAP as well as their combination to NOMA-CAP, while section III describes the experimental setup used for validation of NOMA-CAP in W-band; section IV shows experimentally obtained transmission results and their relation to 5G networks; finally, section V summarizes and concludes the paper.

II. Multi-Band Carrierless Amplitude Phase Modulation with Non-Orthogonal Multiple Access

This section provides a short discussion of the concepts of non-orthogonal multiple access (NOMA) and carrierless amplitude phase modulation (CAP) before discussing their combination into NOMA-CAP as proposed in this paper.

A. Non-Orthogonal Multiple Access

The NOMA power multiplexing technique multiplexes the data of several users in the power domain by combining the contributing signals and it is fully compatible with time- or frequency multiplexing. Successive interference cancellation (SIC) is employed in the terminal units in order to recover the contributing signals and thus demultiplex the different NOMA users data [13]. In wireless communications this technique may exploit the near-far effect, causing asymmetrical channel gains between the users [11].

NOMA power multiplexing is applied at the symbol level and a NOMA constellation for two users—as shown in Fig. 2—is obtained by assigning different weights to the user symbols before directly adding them:

$$x_{\mathrm{NOMA}} = w_1 x_1 + w_2 x_2 \tag{1}$$

where x_{NOMA} is the multiplexed signal for two NOMA users, w_1 and x_1 are the weight and symbol of the close user, while w_2 and x_2 are the weight and symbol of the far user. The weights are calculated in order to obtain the desired power ratio r_{Power} between users in the multiplexed signal.

$$r_{\mathrm{Power}} = 20 \log \left(\frac{w_2}{w_1} \right) \tag{2}$$

The user located closer to the base station (BS), i.e., receiving a higher multiplexed signal quality, will be assigned a weak weight in the multiplexed symbol and will implement SIC to remove the higher power signal for the far user, as depicted in Fig. 3. During SIC the user first decodes the undesired, stronger signal intended for the far user and subtracts it from the received signal, after which the desired weaker signal may be decoded. The user located far from the BS, i.e., with a lower received signal quality, will be assigned a stronger weight and thus the high power signal within the multiplexed symbol and will only decode their own signal [12], [15].

In the case of more than two users, SIC is implemented iteratively, decoding the largest power within the received

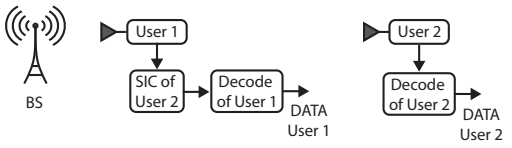

Fig. 3. NOMA receivers for two users with SIC employed by user 1 to remove the signal of user 2 before decoding its own signal.

multiplexed signal and subtracting it from the received signal until the signal of interest is the strongest in the remaining signal so it is possible to finally decode the data.

B. Multi-Band Carrierless Amplitude Phase Modulation

CAP is a scheme that, like quadrature amplitude modulation (QAM), transmits two streams of data separately by means of two orthogonal signals, namely the in-phase (I) and quadrature (Q) components. Additionally, a special feature of CAP modulation is the use of a pulse shaping function to significantly improve the spectral efficiency of the system. Unlike QAM, the generation of the CAP signal is not achieved by modulating two orthogonal carriers with the same frequency (i.e., sine and cosine). Instead two orthogonal filters are used to generate the two components of the signal. These filters are the result of the time-domain multiplication of the pulse shaping function and two orthogonal carriers. In this paper, the root raised cosine (RRC) pulse shaping function is employed to generate the filters, allowing the receiver to use a pair of matched filters with the same shape to retrieve the signal. Therefore, by combining the transmitter and the receiver, the complete response of the filters has the characteristics of a raised cosine (RC) function, which minimizes intersymbol interference (ISI).

CAP modulation, as many other modulation schemes, requires a flat frequency response of the transmission link to ensure good performance. In order to mitigate this impairment, the multi-band CAP (multiCAP) has been proposed for wireless and optical links, achieving high spectral efficiency over large bandwidths [23], [24]. By splitting the spectrum into sub-bands, multiCAP modulation enables the use of bit- and power-loading techniques for each band independently [18], according to its signal to noise ratio (SNR). Thus, with an adequate number of sub-bands, non-flat frequency responses (e.g. uneven antenna gain or non-flat frequency response of devices) can be alleviated to maximize spectral efficiency.

C. Non-Orthogonal Multiple Access with Multi-Band Carrierless Amplitude Phase Modulation

In this article, NOMA power multiplexing is combined with multiCAP modulation to enhance the capacity and flexibility of the RAN. System capacity is increased by reaping the benefits of multiCAP, optimizing the signal to channel conditions, while both multiCAP and NOMA lend themselves ideally to flexible and adaptive user provisioning.

At the transmitter NOMA power multiplexing is applied at the constellation level for each multiCAP band independently and before generation of the multiCAP signal. NOMA-CAP

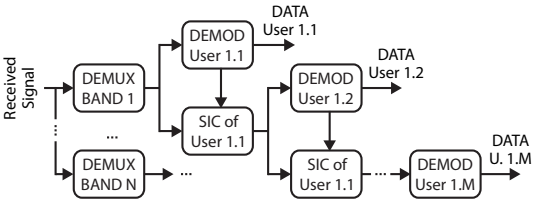

Fig. 4. NOMA-CAP with multiCAP band separation and SIC receiver.

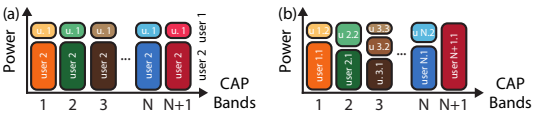

Fig. 5. Power multiplexing using NOMA and multiCAP: (a) NOMA multiplexing of two users employing all multiCAP bands, (b) multiple users are multiplexed employing NOMA and multiCAP.

reception will require the extraction of each multiCAP band—employing its matched filters—and then the SIC process to extract the signal of interest. If several NOMA users have been multiplexed, the SIC process will be applied iteratively after multiCAP demultiplexing until the user signal of interest is demodulated, as is shown in Fig. 4.

The combination of NOMA and multiCAP allows a dynamic assignment of the resources to fulfill the user demands. For example, in a low density user distribution scenario, such as shown in Fig. 5(a), the users can use all multiCAP bands simultaneously while their data is multiplexed by NOMA. In this scenario, the users equally share the maximum available capacity of the RAN. If the number of users increases, NOMA multiplexing can be applied independently to each multiCAP band (with potentially different numbers of users per band) and bands can be assigned to different groups of users, as shown in Fig. 5(b). This enables a flexible distribution of the RAN capacity over many users and avoids blocking new users to a large degree.

In the next section, a NOMA-CAP system employing two levels of NOMA with QPSK signals and six 1.25 GHz multiCAP bands is proposed and demonstrated. The proposed NOMA-CAP system may provide an aggregated transmission rate of 30 Gbit/s and has been evaluated in two different scenarios. In the fist scenario—a low user density scenario—the capacity of the RAN is distributed between two users employing NOMA-CAP, as in Fig. 5(a), to obtain 15 Gbit/s per user. In the second scenario, twelve users are multiplexed using NOMA-CAP, similar to Fig. 5(b), where the different multiCAP bands carry different users, and the RAN capacity is divided evenly among all users to obtain 2.5 Gbit/s per user.

III. SETUP

The experimental setup used to evaluate the proposed NOMA-CAP transmission over a hybrid photonic-wireless downlink follows the concepts of a C-RAN with analog ROF fronthaul [3], [4] and mm-wave radio access units (RAUs) of reduced complexity [8]. The setup—schematically shown in

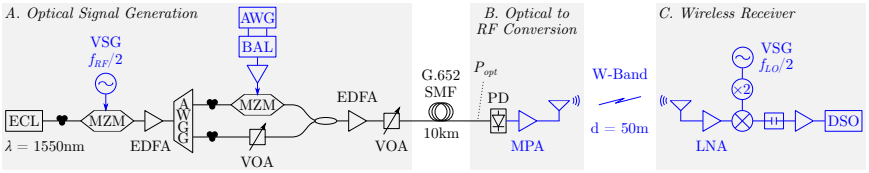

Fig. 6. Schematic of the experimental setup; ECL: external cavity laser, MZM: Mach-Zehnder modulator, VSG: vector signal generator, RF: radio frequency, EDFA: erbium doped fiber amplifier, AWGG: arrayed waveguide grating, AWG: arbitrary waveform generator, BAL: balun, VOA: variable optical attenuator, SMF: standard single mode fiber, PD: photodiode, MPA: medium power amplifier, LNA: low noise amplifier, LO: local oscillator, DSO: digital storage oscilloscope.

Fig. 6 and previously tested on [21], [22], [25]—consists of three stations, linked by optical fiber and wireless transmission respectively: Optical Signal Generation, Optical to RF Conversion and Wireless Receiver. The *A. Optical Signal Generation* is the equivalent of the central office (CO) and generates an optical signal with two spectral lines spaced at the frequency of the radio carrier $f_{RF} = 84\,\text{GHz}$. The signal carries the NOMA-CAP signal and links via an analog RoF system over 10 km of standard single mode fiber (SMF) to *B. Optical to Radio Frequency Conversion* in the RAU, from where the signal is wirelessly delivered to *C. the Wireless Receiver*. The latter recovers the RF signal, translates it to baseband and performs the DSP required to decode the NOMA-CAP signal. The different stations are described in detail in the following sections.

A. Optical Signal Generation

The optical output of a narrow linewidth external cavity laser (ECL) at $\lambda = 1550\,\text{nm}$ is modulated by a Mach-Zehnder modulator (MZM) biased at its minimum transmission point with a sinusoidal signal at $f_{\text{RF}}/2$ obtained from a vector signal generator (VSG). This configuration generates the basic optical signal for photonic generation of the RF signal with two spectral lines spaced at f_{RF}. After amplification in an erbium doped fiber amplifier (EDFA), the lines are separated in an arrayed waveguide grating (AWGG) demultiplexer before modulating of one of them with the NOMA-CAP signal.

The block diagram for the digital signal processing (DSP) to generate the NOMA-CAP signal is shown in Fig. 7. First, the user data—pseudo random bit sequences (PRBSs) of length $2^{11} - 1$—are distributed among all the assigned multiCAP bands (varying between one and all available bands) and are QPSK mapped for each NOMA level. The two NOMA levels are power weighted and added for each multiCAP band before the band signals are upsampled and filtered using a pair of band specific multiCAP orthogonal filters. In all scenarios a total of six multiCAP bands of 1.25 GHz width are used. Finally, these signals are aggregated into the full transmitted NOMA-CAP signal.

The latter is generated with an arbitrary waveform generator (AWG), converted to single-ended with a balun (BAL) and amplified to achieve a voltage swing able to modulate one of the spectral lines in a second MZM. The power of the other spectral line is adjusted with a variable optical attenuator (VOA) to ensure equal power of both spectral lines. A second EDFA amplifies the signal for transmission, while a second

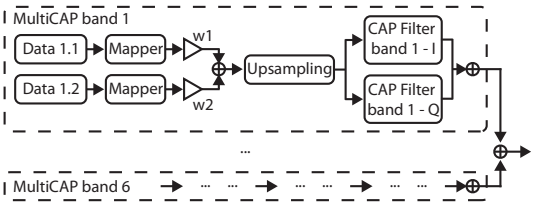

Fig. 7. Transmitter DSP block diagram for NOMA-CAP signal generation.

Fig. 8. Laboratory setup for NOMA-CAP transmission in W-band; (a) optical signal generation, (b) optical to RF conversion station and transmission path, (c)–(d) transmitter and receiver parabolic antennas, (e) PD and MPA at optical to RF conversion, (f) LNA, mixer and frequency doubler at the wireless receiver.

VOA controls the launched power and thus the power at the optical to RF conversion stage after transmission through 10 km of ITU-T G.652 SMF.

For laboratory convenience the optical signal generation is housed in a half-size rack, shown in Fig. 8(a).

B. Optical to Radio Frequency Conversion

Optical to RF conversion is performed by a RAU designed for minimum complexity, consisting only of a high-speed photodiode (PD), a single medium power amplifier (MPA) and the transmitter antenna. The RF signal is generated through the beating of the two optical lines on a PD that features a 3 dB bandwidth of 90 GHz and a responsivity of 0.5 A/W.

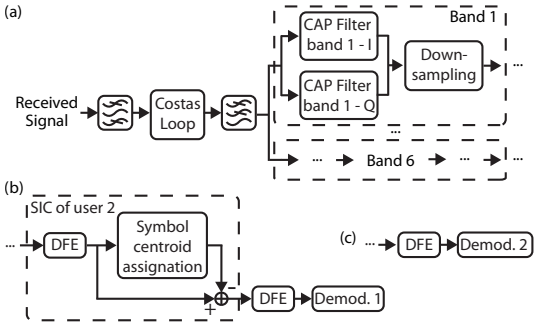

Fig. 9. Receiver DSP block diagram: (a) multiCAP band recovery (common to all receivers), (b) user type 1 receiver with SIC processing, (c) user type 2 receiver without SIC processing.

The variable incoming optical power allows for generation of different RF powers which are amplified by 10 dB by the MPA up to a saturation output power of 12 dBm; PD and MPA, are shown in Fig. 8(e). A parabolic antenna with a gain of 48 dBi is used to transmit the signal to the wireless receiver as shown in Figs. 8(b) and (c) respectively.

C. Wireless Receiver and Signal Processing

At the receiver an identical antenna—shown in Fig. 8(d)—recovers the RF signal which is amplified by 20 dB using a low noise amplifier (LNA) before its downconversion in a balanced mixer to an intermediate frequency (IF) at $f_{IF} = f_{RF} - f_{LO} = 10\,\text{GHz}$. The local oscillator (LO) for the mixer is obtained from a passive frequency doubler, driven with a sinusoid at $f_{LO}/2$ from a second VSG; the combination of LNA, mixer and frequency doubler is shown in Fig. 8(f). The resulting IF signal is DC blocked and amplified before it is recorded on a digital storage oscilloscope (DSO) for offline processing.

The receiver signal processing block diagram is shown in Fig. 9 and consists of a band-pass filter for noise bandwidth reduction and a Costas loop [26] for carrier frequency and phase recovery for IF to baseband conversion. The baseband signal is low-pass filtered and each multiCAP band is extracted, employing the pair of orthogonal filters for the band of interest, as described in section II-B; this part is common to all the receivers and is shown in Fig. 9(a). The close users further implement SIC as is shown in Fig. 9(b), in order to remove the far users' data. The first step of the SIC consists of a decision feedback equalizer (DFE) with 30 forward and 20 backward taps, after which the symbol centroid of the interfering user's signal is calculated employing the k-means algorithm [18]. Finally, the symbol centroid of the far user is subtracted from the equalized signal. After SIC, the DFE is applied again to the new signal and finally the signal is demapped. In the case of farther users, SIC is not required and the DFE and demapping are performed directly, as shown in Fig. 9(c).

IV. Experimental Results

This section discusses the results of applying NOMA-CAP in a W-band RoF link, proving the functionality and applicability of NOMA-CAP for 5G networks. First, optical and electrical spectra at different stages of the experimental system are shown and discussed. Then the system transmission performance is evaluated through bit error rate measurements in two scenarios with different numbers of users and for varying NOMA-CAP parameters. Finally, the results and their applicability are discussed.

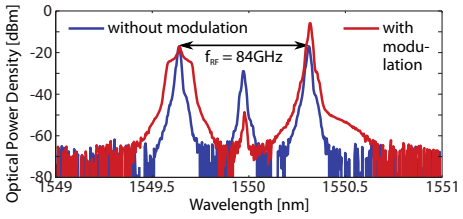

Fig. 10. Optical spectra of the two spectral lines generated with the first MZM before and after modulation.

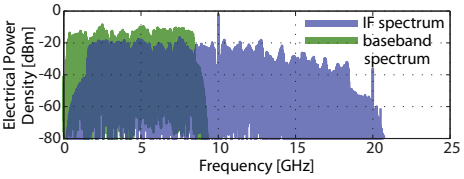

Fig. 11. Electrical spectra of the received IF signal (top) and the received baseband signal after Costas loop (bottom).

A. Signal Generation and Reception

Fig. 10 depicts the optical spectrum after the first MZM, clearly showing the two spectral lines separated by $f_{RF} = 84\,\text{GHz}$. The optical spectrum after modulating one of these two spectral lines previous to their transmission along the fiber is also shown. In Fig. 11, the electrical spectrum of the received signal after the analog downconversion to IF and digital downconversion to baseband is shown. The electrical spectra allow recognition of the multiCAP bands, but show severe and non-uniform impairments from the wireless channel, receiver electrical response and the downconversion process itself. This effect can be partly corrected by a passband filter before the Costas loop, removing the upper side band of the signal that is the most distorted.

B. System Transmission Performance

For the analysis of transmission performance, the received optical power on the PD is varied between −3 dBm and 2.5 dBm using the second VOA while the wireless distance remains constant (50 m). This optical power is directly related with the transmitted RF power, so its variation can be used to emulate the wireless distance without moving the antennas [27]. The power ratio between users is defined as in Eq. (2) and the total power of the digitally generated NOMA-CAP signal is kept constant. The analysis of distance has been performed employing the respective BER limits of 3.8×10^{-3}

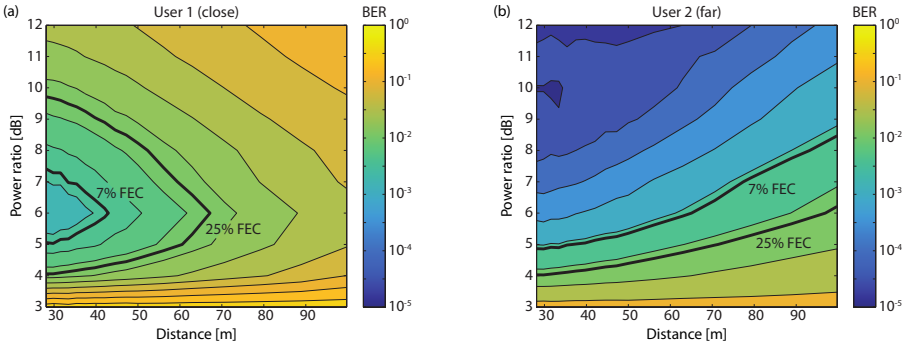

Fig. 12. BER maps in terms of distance and power ratio for (a) the close by user and (b) the user located far from the transmitting antenna.

TABLE I
SUMMARY OF MAXIMUM ACHIEVABLE DISTANCES FOR BOTH USERS AND DIFFERENT POWER RATIOS.

Power-ratio	*User 1 (close)* Distance* (7% FEC)	*User 1 (close)* Distance (25% FEC)	*User 2 (far)* Distance† (7% FEC)	*User 2 (far)* Distance† (25% FEC)
5dB	×	61m	36m	70m
6dB	43m	67m	65m	96m
7dB	33m	59m	77m	○
8dB	×	52m	○	○
9dB	×	40m	○	○

*× denotes cases where no transmission below BER limit for the respective FEC could be achieved.

†○ denotes cases where distance greater than those experimentally tested is expected to be achievable.

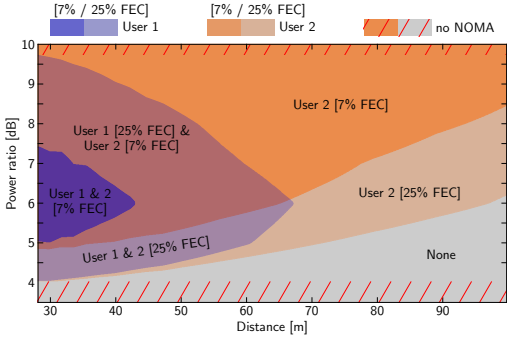

Fig. 13. Achievable distances and required FEC overhead for the two users at different power ratios

and 1.32×10^{-2} for standard forward error corrections (FEC) with 7 % and 25 % overhead (OH) [28].

System transmission BER performance in the first scenario with only two users present—similar to the low density user distribution scenario in Fig.1(a)—is shown in Fig. 12, where BER is plotted in terms of wireless distance and power ratio r_{Power} between the close and the far user. Both users employ all six bands available and share the full system capacity—i.e., 15 Gbit/s each. For user 2—i.e., the user located far from the transmitting antenna—the NOMA multiplexing with the signal of user 1 will be regarded as an increment of the received noise and thus a reduction of the power ratio between users will increase the user BER and reduce the achievable distance for user 2 as is seen in Fig. 12(b). The user 2 would thus prefer a scenario with high power ratio since with power ratios above 8 dB a BER below the limit for a 7% OH FEC is achieved for all analyzed distances.

In the same scenario, user 1—i.e., the user close to the transmitting antenna—will apply SIC cancellation before demodulation in order to remove the signal of user 2. Any errors in the calculation of the centroid of user 2 will affect the decoding of user 1 in the SIC process and thus they will cause a higher BER. An increase in the transmission distance for user 1 will result in an increase in the number of errors in the centroid calculation, causing an increase in BER of user 1, as can be seen in Fig. 12(a). The use of a low power ratio between users—i.e., the power of user 1 and user 2 are comparable—will have a similar effect as placing user 1 at a long distance, resulting in errors in the calculation of the user 2 centroid and consequently transmitting the error to user 1 decoding. On the other hand, the BER of user 1 will also increase with high power ratios as the signal will be too weak after SIC, even if the SIC process perfectly calculates the user 2 centroids. In consequence, user 1 will only be successfully demodulated for intermediate power relations and for close distances, as seen in Fig. 12(a).

Table I summarizes the maximum reachable distances for both users under different power ratios. When the power ratio is 6 dB and a 7% OH FEC is assumed, user 1 can be placed as far as 43 m and the user 2 at up to 65 m. If the user 2 needs to be placed further, the power ratio can be changed to 7 dB and the user 2 could be placed as far as 77 m, but the distance of user 1 will have to be reduced and cannot be greater than 33 m. Therefore, the increment of the operational range of one user will decrease the range of the other user. If the effective data rate can be reduced, a 25% OH FEC can be implemented and both users can be placed farther. In this case, user 1 can be placed at 67 m and user 2 at 96 m with a power ratio of 6 dB

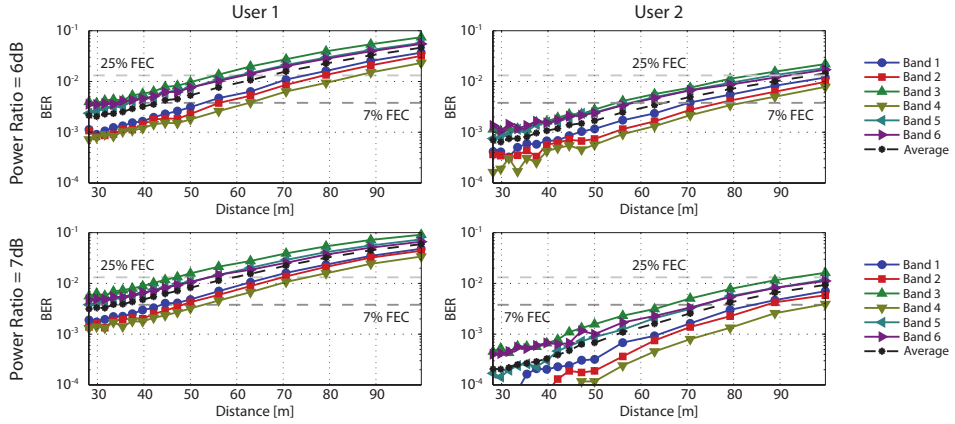

Fig. 14. BER over wireless distance for different multiCAP bands, each carrying a close and a far user multiplexed with NOMA.

TABLE II
SUMMARY OF MAXIMUM ACHIEVABLE DISTANCES FOR EACH MULTICAP BAND AND BOTH USER TYPES WITH POWER RATIOS OF 6 DB AND 7 DB.

Power-ratio [dB]	User Type	FEC OH [%]	MultiCAP Band*† #1 [m]	#2 [m]	#3 [m]	#4 [m]	#5 [m]	#6 [m]
6	close	7	53	47	30	63	36	34
		25	75	79	55	86	61	61
	far	7	70	78	56	82	59	59
		25	○	○	84	○	89	91
7	close	7	44	49	×	53	30	×
		25	67	70	47	75	54	54
	far	7	84	87	66	99	73	73
		25	○	○	93	○	○	○

*× denotes cases where no transmission below BER limit for the respective FEC could be achieved.

†○ denotes cases where distance greater than those experimentally tested is expected to be achievable.

while for 7 dB the far user achieves distances beyond those measured. The power ratio between the user signals will thus allow adapting the system to the required range as is seen in Fig. 13 which illustrates the achievable distances (and required FEC overhead) for the two users for different power ratios.

The BER of each multiCAP band and the average BER are shown in Fig. 14 in terms of distance of near and far users with power ratios of 6 dB and 7 dB. Fig. 14 is used to study a second scenario with twelve users, six users of type 1 and six users of type 2, with a capacity of 2.5 Gbit/s per user. These users are multiplexed employing NOMA and all the multiCAP bands, similar to the scenario described in Fig. 1(b).

The BER of each multiCAP band in terms of user distance and power ratio shows a similar behavior to that previously described for a NOMA-CAP system where all bands are employed by the same users. The maximum distances for both types of users and for each multiCAP band are summarized in Table II for both FEC types and for power ratios of 6 dB and 7 dB. The BER of each band is different due to the differing channel and system impairments and thus in this scenario some of the bands (1, 2 and 4) allow longer distances while other bands (3, 5 and 6) are limited to shorter distances.

If the user capacity is kept stable—i.e., only the 7% OH FEC is used—band 3 and 6 will not allow the use of a power ratio of 7 dB since users of type 1 in these bands cannot obtain a BER below the respective FEC limit. The remaining bands may be used with both power ratios, depending on the necessities and position of the different users. Therefore, an optimal accommodation of the users in different multiCAP bands is possible by adjusting the NOMA power ratio in each band independently.

Finally, Fig. 15 shows the constellation diagrams for all multiCAP bands and for both types of NOMA users, given a power relation of 6 dB and a distance of 30 m. The constellation multiplexing can be observed with the symbols of user 1 visibly superimposed on the symbols of user 2. For user 1 the symbols of user 2 have been removed with the SIC process and only the desired symbols are observed.

V. CONCLUSIONS

A combination of multiCAP modulation and NOMA multiplexing was suggested for application in future 5th generation mobile RANs, allowing the optimization of the available capacity as well as flexible user provisioning. An experimental demonstration was given for a NOMA-CAP RoF system in the W-band, analyzing BER in two different scenarios with different user density.

The experimental demonstration achieved an aggregate system capacity of 30 Gbit/s using a NOMA-CAP signal consisting of six bands with a width of 1.25 GHz each. BER measurements are shown for different power ratios between the contributing NOMA signals and for different optical power, relating to wireless distances between 30 m and 100 m. Power ratios close to 6 dB are found to be optimum and in a two user scenario allow distances of 43 m and 65 m respectively, with BER values below the limit for a standard FEC with 7% OH.

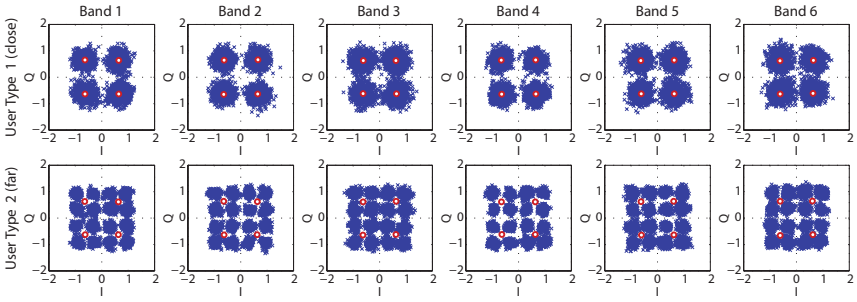

Fig. 15. Received constellations for both types of NOMA users and the six multiCAP bands for a power ratio of 6 dB and a distance of 30 m.

The introduction of NOMA-CAP over W-band RoF allows the RAN to dynamically adapt itself to varying user data rate demands and user densities. This flexible multi-user provisioning will also permit to change the data rate provided to the current users to grant access to new users in the RAN. In a low user density scenario, a high data rate can be provided to the users. If new users need to be served by the RAN, the delivered data rate can be reduced, independently assigning the multiCAP bands to these new users and avoiding blocking to a maximum degree. The experimental demonstration of these situations proves the operation with two users with 15 Gbit/s data rate each or twelve users with 2.5 Gbit/s each, showing the trade-off between the number of users and per-user capacity. The number of users could be raised with an increment of the number of multiCAP bands and NOMA levels, but causing a reduction of the per-user capacity.

REFERENCES

[1] M. Fiorani *et al.*, "Challenges for 5G transport networks," in *Proc. ANTS 2014*, 2014.

[2] T. Pfeiffer, "Next generation mobile fronthaul and midhaul architectures," *IEEE J. Opt. Commun. Netw.*, vol. 7, no. 11, pp. B38–B45, 2015.

[3] P. Rost *et al.*, "Cloud technologies for flexible 5G radio access networks," *IEEE Commun. Mag.*, vol. 52, no. 5, pp. 68–76, 2014.

[4] C. Liu *et al.*, "A novel multi-service small-cell cloud radio access network for mobile backhaul and computing based on radio-over-fiber technologies," *J. Lightw. Technol.*, vol. 31, no. 17, pp. 2869–2875, 2013.

[5] K. Kitayama, T. Kuri, J. Vegas Olmos, and H. Toda, "Fiber-wireless networks and radio-over-fibre technique," in *Proc. CLEO 2008*, 2008, paper CThR4.

[6] S. Rommel *et al.*, "W-band photonic-wireless link with a Schottky diode envelope detector and bend insensitive fiber," *Opt. Express*, vol. 24, no. 11, pp. 11 312–11 322, 2016.

[7] J. Wells, "Faster than fiber: The future of multi-G/s wireless," *IEEE Microw. Mag.*, vol. 10, no. 3, pp. 104–112, 2009.

[8] S. Rodríguez, S. Rommel, J. J. Vegas Olmos, and I. Tafur Monroy, "Reconfigurable radio access unit to dynamically distribute W-band signals in 5G wireless access networks," *Opt. Switch. Netw.*, vol. 24, pp. 21–24, 2017.

[9] F. Lu *et al.*, "Non-orthogonal multiple access with successive interference cancellation in millimeter-wave radio-over-fiber systems," *J. Lightw. Technol.*, vol. 34, no. 17, pp. 4179–4186, 2016.

[10] Ł. Chorchos *et al.*, "Reconfigurable radio access unit for DWDM to W-band wireless conversion," *IEEE Photonics Technol. Lett.*, vol. 29, no. 6, pp. 489–492, 2017.

[11] L. Dai *et al.*, "Non-orthogonal multiple access for 5G: solutions, challenges, opportunities, and future research trends," *IEEE Commun. Mag.*, vol. 53, no. 9, pp. 74–81, 2015.

[12] A. Benjebbour *et al.*, "Concept and practical considerations of non-orthogonal multiple access (NOMA) for future radio access," in *Proc. ISPACS 2013*, 2013, pp. 770–774.

[13] K. Higuchi and A. Benjebbour, "Non-orthogonal multiple access (NOMA) with successive interference cancellation for future radio access," *IEICE Trans. Commun.*, vol. E98-B, no. 3, pp. 403–414, 2015.

[14] Z. Ding, Z. Zhao, M. Peng, and H. V. Poor, "On the spectral efficiency and security enhancements of NOMA assisted multicast-unicast streaming," *IEEE Trans. Commun.*, vol. 65, no. 7, pp. 3151–3163, 2017.

[15] T. Manglayev, R. C. Kizilirmak, and Y. H. Kho, "Optimum power allocation for non-orthogonal multiple access (NOMA)," in *Proc. AICT 2016*, 2016.

[16] Z. Chen, Z. Ding, X. Dai, and R. Zhang, "An optimization perspective of the superiority of NOMA compared to conventional OMA," *IEEE Trans. Sig. Process.*, vol. 65, no. 19, pp. 5191–5202, 2017.

[17] V. Sipal *et al.*, "Adaptive OFDM for wireless interconnect in confined enclosures," *IEEE Wireless Commun. Lett.*, vol. 2, no. 5, pp. 507–510, 2013.

[18] M. I. Olmedo *et al.*, "Multiband carrierless amplitude phase modulation for high capacity optical data links," *J. Lightw. Technol.*, vol. 32, no. 4, pp. 798–804, 2014.

[19] J. L. Wei *et al.*, "Performance and power dissipation comparisons between 28 Gb/s NRZ, PAM, CAP and optical OFDM systems for data communication applications," *J. Lightw. Technol.*, vol. 30, no. 20, pp. 3273–3280, 2012.

[20] J. A. Altabas *et al.*, "Non-orthogonal multiple access and carrierless amplitude phase modulation for 5G mobile networks," in *Proc. ECOC 2017*, 2017, paper Tu.1.B.2.

[21] R. Puerta, S. Rommel, J. J. Vegas Olmos, and I. Tafur Monroy, "Optically generated single side-band radio-over-fiber transmission of 60Gbit/s over 50m at W-band," in *Proc. OFC 2017*, 2017, paper M3E.4.

[22] S. Rommel, R. Puerta, J. J. Vegas Olmos, and I. Tafur Monroy, "Capacity enhancement for hybrid fiber-wireless channels with 46.8Gbit/s wireless multi-CAP transmission over 50m at W-band," in *Proc. OFC 2017*, 2017, paper M3E.5.

[23] R. Puerta, S. Rommel, J. J. Vegas Olmos, and I. Tafur Monroy, "Up to 35Gbps ultra-wideband wireless data transmission links," in *Proc. PIMRC 2016*, 2016.

[24] R. Puerta *et al.*, "Effective 100Gb/s IM/DD 850nm multi- and single-mode VCSEL transmission through OM4 MMF," *J. Lightw. Technol.*, 2016.

[25] L. C. P. Cavalcante *et al.*, "Performance evaluation of wavelet-coded OFDM on a 4.9 Gb/s W-band radio-over-fiber link," *J. Lightwave Technol.*, vol. 35, no. 14, pp. 2803–2809, 2017.

[26] J. P. Costas, "Synchronous communications," *Proc. IRE*, vol. 44, no. 12, pp. 1713–1718, 1956.

[27] S. Rommel *et al.*, "Outdoor W-band hybrid photonic wireless link based on an optical SFP+ module," *IEEE Photonics Technol. Lett.*, vol. 28, no. 21, pp. 2303–2306, 2016.

[28] ITU-T G.975.1, "Forward error correction for high bit-rate DWDM submarine systems," 2004.

PAPER15: W-Band Real-Time Transmission Utilizing a Reconfigurable RAU for NG-PON Networks

L. Chorchos, **S. Rommel**, S. Spolitis, J. P. Turkiewicz, I. Tafur Monroy, and J. J. Vegas Olmos. "W-Band Real-Time Transmission Utilizing a Reconfigurable RAU for NG-PON Networks". In: *Advances in Wireless and Optical Communications 2016*. Nov. 2016, pp. 66–69. DOI: 10.1109/RTUWO.2016.7821857

W-Band Real-Time Transmission Utilizing a Reconfigurable RAU for NG-PON Networks

Łukasz Chorchos,
Jarosław P. Turkiewicz
Institute of Telecommunications
Warsaw University of Technology
lukaszchorchos@gmail.com

Simon Rommel, Idelfonso Tafur Monroy, Juan José Vegas Olmos
Department of Photonics Engineering
Technical University of Denmark
{sirem,idtm,jjvo}@fotonik.dtu.dk

Sandis Spolitis
Institute of Telecommunications
Riga Technical University

***Abstract*—In this article, we propose and test a reconfigurable Remote Access Unit (RAU) to interface optical and W-band wireless communication links (75–110 GHz), utilizing optical heterodyne signal upconversion. The RAU is composed of a tunable local oscillator, narrow optical filter and a control unit. The RAU can be software-reconfigured to select a specific dense wavelength division multiplexed (DWDM) channel. Real-time tests with 100 GHz spaced DWDM signals have been performed. Real-time 2.5 Gbit/s error free radio transmission in the 75 GHz to 95 GHz range of the W-band was achieved after 15 km of standard single mode fiber and 50 m of wireless link.**

Keywords—Radio-over-fiber, millimeter-wave communications, W-band wireless, microwave photonics, real-time systems

I. INTRODUCTION

Growing demand for high speed wireless data transmission increases year to year, mostly due to the emerging end users need for wireless services like audio and videostreaming, videoconferencing, cloud storage and online gaming [1]. The new mobile standard called 5G is going to meet those requirements partially by use of higher radio frequencies from the mm-wave range [2], [3]. Operation in this frequency range (from 30 GHz up to 300 GHz) allows the use of wider transmission channels. This clearly opens a possibility for higher bit rates. Furthermore, regulations in mm-waves allow lightly licensed link establishment. Nevertheless, signal generation in the mm-wave frequency range with traditional oscillators is complex.

To overcome this problem the use of optical heterodyne signal upconversion was proposed [4] and in recent years this technique of signal generation has attracted the interest of many researchers [5]–[8] and even joint projects were established in this field. Those projects are aimed to provide feasible solutions integrating present and future optical networks with wireless communication by utilizing photonic techniques. One of the projects focused on this problem is Integrated Photonic Broadband Radio Access Units for Next Generation Optical Access Networks (IPHOBAC-NG). The aim of the project is to provide seamlessly integrable photonic solutions for wireless communication and adapt them into currently existing wavelength division multiplexed passive optical networks (WDM-PON) and even ultra dense wavelength division multiplexed PONs (UDWDM-PON). Under those solutions, the project assumes to provide a complementary broadband access with speeds between 1–10 Gbit/s and a mobile backhaul with the speed of 3 Gbit/s. To fulfill those requirements the IPHOBAC-NG project plans to develop a new photonic RAU that will support reconfiguration of the optical channel allocation, will not have an impact on the digital signal processing in the optical network unit (ONU) and optical network terminal (ONT), and will be energy efficient, fully integrated and compact. The projected IPHOBAC-NG heterogeneous network architecture is presented in Fig. 1.

In this article, we propose and test a reconfigurable deployable RAU interfacing optical DWDM transmission with wireless transmission for the IPHOBAC-NG network architecture. The proposed RAU utilizes the principles of optical heterodyne signal upconversion for wireless data transmission in millimeter-wave range. The comprehensive study devoted to the heterodyne technique used in the RAU was presented e.g. in [9]. In general, the proposed RAU is composed of a reconfigurable optical filter for DWDM channel selection, a reconfigurable optical reference signal source, photodiode and control unit. In section II an extensive description of the proposed RAU is given, section III describes the measurement setup and procedure. In section IV we show results for 2.5 Gbit/s real-time wireless data transmission over 15 km of fiber and a wireless distance of 50 m.

II. REMOTE ACCESS UNIT DESIGN

The reconfigurable RAU proposed in this article and presented in Fig. 1 is in line with IPHOBAC-NG's assumptions on the RAU: the input signal is a 100 GHz spaced DWDM signal in the C-band, operating at 2.5 Gbit/s. The WDM pipe signal goes into a tunable, voltage controlled optical fiber Fabry-Perot filter, where the desired channel designated for a wireless data transmission is selected. The used filter has 2.5 dB insertion loss, a 3 dB bandwidth of 15 GHz and a 20 dB bandwidth of 125 GHz. This value of suppression outside the filter transmission allows device operation in 100 GHz spaced DWDM systems. The control voltage required to cover the

978-1-5090-1535-1/16/$31.00 ©2016 IEEE

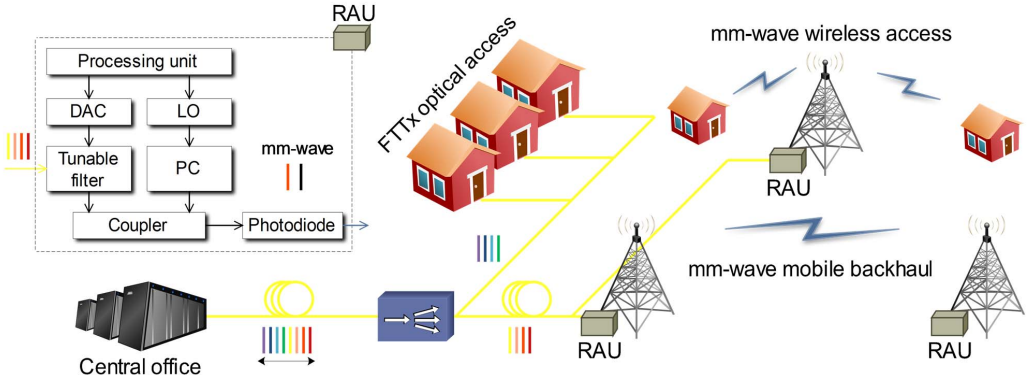

Fig. 1. The IPHOBAC-NG architecture and a block diagram of the proposed RAU. The scope of the RAU is to interface any DWDM optical signal to the wireless W-Band

whole C-band for the selected filter is 16 V. The filter is controlled through a digital-to-analog converter (DAC). The DAC provides adjustable output voltage range from minimum −18 V to maximum 18 V with 16 bit resolution, ensuring finesse to select any DWDM channel.

The selected channel from the DWDM signal is fed into a 3 dB coupler where it is combined with the reference signal from a local oscillator (LO, a tunable laser covering the C-band with 100 kHz linewidth and fine frequency tuning). The LO signal is connected to the coupler through a manual polarization controller to adjust the state of polarization and maximize beating on the photodiode. In the next revision of the RAU an electrically driven polarization controller can be implemented and, through a feedback loop from the second output of the optical coupler, the polarization controller can be adjusted to find the optimal LO signal polarization. The LO and the DAC are controlled by a processing unit. The device used as a processing unit is low-cost Raspberry Pi 2 with 40 general purpose input/output pins, 4 USB ports, an Ethernet socket and UNIX based operating system can control various devices. Moreover, this single-board controller can be loaded with software-defined networking (SDN) extensions, effectively softwareizing the RAU.

The coupled data and reference signal, spaced according to the desired radio frequency, is connected to a photodiode (Finisar XPDV4120R) with 90 GHz 3 dB bandwidth and responsivity of 0.5 A/W. As a result of the heterodyning process at the photodiode, a radio signal in the frequency range of the W-Band is generated. The total RAU optical insertion losses are 5.5 dB: 2.5 dB from the optical filter and 3 dB from the coupler.

III. SYSTEM DESCRIPTION

In this section, the experimental set-up and the measurement procedure to test the proposed RAU are described.

A. Experimental Set-Up

Fig. 2 depicts a block diagram of the experimental setup. Eight 100 GHz spaced lasers were multiplexed in two 4x1 couplers with distinction for even and odd channels. Next, the two streams (4 signals each) were fed into two Mach Zehnder modulators (MZMs). The MZMs were preceded by two polarization controllers (PC). Both MZM were biased at the center of their linear region and driven with two 2.5 Gbit/s non-return-to-zero (NRZ) pseudo random bit sequences (PRBSs) with a length of $2^{11}-1$ bits from a pulse pattern generator. The sequence modulating the odd channels was negated and shifted with a delay line to decorrelate the signals.

The signals from the MZMs were combined in a 3 dB coupler and transmitted through a combination of 10 km standard single mode fiber (SSMF) and 5 km of bend insensitive fiber (BIF, ITU-T G.657.B3). This combination secures compatibility with deployment scenarios where BIF is used to overcome strong bending losses, while having little impact on the performance of the W-band signal [10].

After the fiber, the DWDM signal was amplified with an erbium doped fiber amplifier (EDFA) to provide sufficient power for radio signal generation and transmission. The reason why the EDFA was placed just before the RAU, not right after the coupler in the transmitter part, is because of not sufficient output power per channel of the available EDFA. By applying different EDFA with the output power like 22 dBm and moving it to the central office (OLT) the maximum distance possible to achieve in the considered system configuration exceeds 20 km (assuming received data signal power before the photodiode equals to 1 dBm, 13 dBm per channel after the EDFA in the OLT, 5.5 dBm insertion losses of the RAU and 0.3 dB/km fiber attenuation for the SSMF). The other possible solution excluding need for the EDFA is to use semiconductor optical amplifiers right after the optical filter in the RAU.

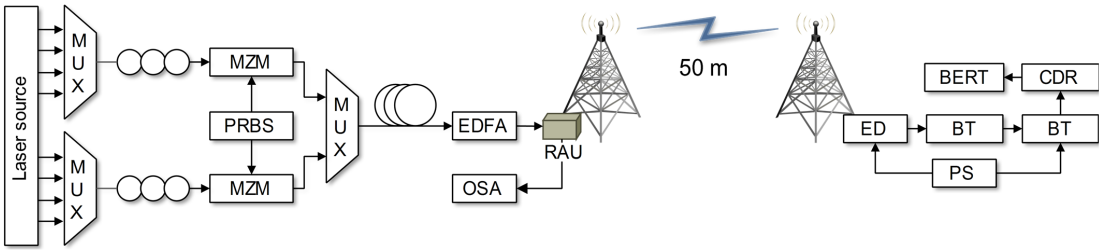

Fig. 2. Experimental setup for hybrid photonic wireless transmission.

After the EDFA, the amplified signal is fed to the RAU. For each of the measured channels, polarization of the LO signal was adjusted to provide the maximum beating on the photodiode. Part of the signal from the RAU's coupler went to an optical spectrum analyzer (OSA) to monitor the signal in the optical domain. The output RF signal from the RAU was transmitted over a distance of 50 m using a pair of parabolic W-band antennas with 48 dBi gain each. After 50 m of wireless transmission, the output of the receiver antenna was downconverted with a W-band envelope detector (ED) based on Schottky diode with a 3 dB bandwidth of 3 GHz. Next, two bias tees (BT) were cascaded: the first, inverted to remove unwanted DC components from the ED and the second to provide a 3.3 V DC required by the used clock and data recovery module (CDR). The output of the CDR was connected to the bit error rate tester (BERT) where bit error rate measurements were conducted.

B. *Measurement Procedure*

All experiments were performed for W-band frequencies starting from 75 GHz up to 95 GHz with 2 GHz steps. The 95 GHz frequency upper bound was caused by the operational bandwidth of the photodiode and the additional beating caused by adjacent channels. The impact of those two phenomena is discussed in section IV. Decision about using W-band was made mainly due to lower attenuation in comparison with 60 GHz V-band, which is also strongly considered for 5G networks.

The signal transmission tests with the proposed RAU were conducted for the 1st, 5th and 8th DWDM channels from the transmission system described in the previous section. The measurements were set through the control unit of the RAU, to which channel number and frequency target in the W-band were indicated. The control unit, through a look-up table, would set up the filter and the LO. The measurement procedure therefore follows the next sequence: first, the DWDM signal was filtered in the RAU; next the reference signal from the LO was added at the frequency of 75 GHz. According to the previously performed analysis and experiments [11], [12] the optimal power ratio between a local oscillator and a data signal providing maximized RF signal is equal to 1. It means the best operation is achieved when two lasers work with equal power levels. In the presented system the power of the lasers was 1 dBm each. The power the photodiode was fed with thus equals to 4 dBm. Fig. 3 presents the optical spectrum before the transmission for the 5th DWDM channel and the LO set at

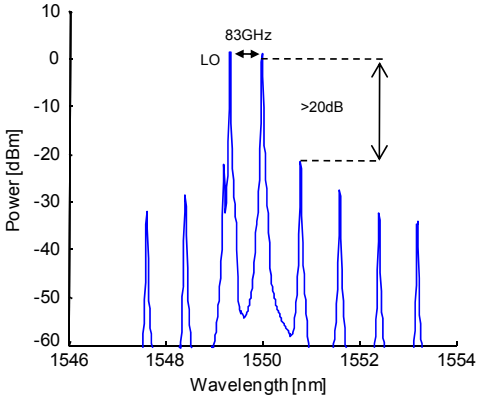

Fig. 3. Optical signal spectrum inside the RAU (after the coupler).

83 GHz apart from the data channel. It can be clearly observed that adjacent DWDM channels are suppressed by over 20 dB

After verification of proper system operation, bit error tests were performed. The time of BER measurements was equal to 20 s. With the speed of 2.5 Gbit/s the total number of sent bits was 50Gbit. This number of transmitted bits guarantees BER measurement accuracy up to 10^{-10}. After the BER measurement, the LO spacing was set to a higher frequency, with a step of 2 GHz, through the control unit and the procedure was repeated. Measurements were conducted for every mentioned W-band frequency and afterwards the DWDM channel was changed and the whole procedure was repeated. It has to be said that the optical spectrum analyzer used to monitor signal before transmission had 2 GHz accuracy. This might impose small inaccuracy in the reference signal tuning as the LO signal was monitored over mentioned optical spectrum analyzer.

IV. RESULTS AND DISCUSSION

Fig. 4 presents results of the measurements described in the previous section. Independently from the selected DWDM channel, similar BER characteristics were obtained. In the frequency range from 75 GHz to 87 GHz transmission below 7 % forward error correction (FEC) level (BER = 3.8×10^{-3}) is possible for all tested channels. For the frequencies located closely to 80 GHz even transmission considered as error free

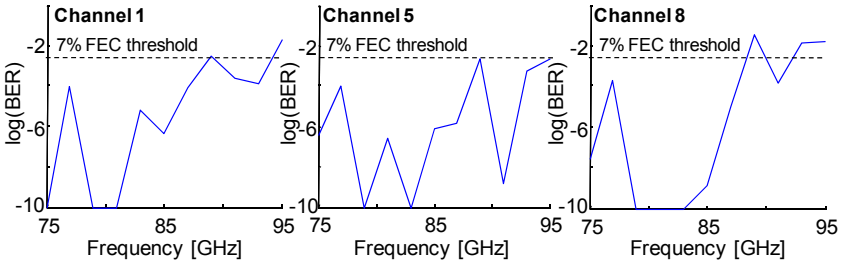

Fig. 4. BER measurement results obtained for real-time data transmission at frequencies ranging from 75 to 95 GHz: 1st, 5th and 8th DWDM channel

can be performed (BER below the level of 10^{-9}). It is worth to mention that this frequency range was designated by US Federal Communication Commission (FCC) for high-density fixed wireless services with 5 GHz wide spectrum and the RAU proposed in this article can be easily utilized for this application.

For the frequencies above 87 GHz impact of two factors causing an increase in the BER are visible and should be discussed. First is the limited bandwidth of the photodiode and its frequency response. After 90 GHz we observe a steady decrease (2 dB per 10 GHz) in the frequency response of the photodiode. This directly decreases the power of the transmitted radio signal. The second limiting factor that may play an even bigger role is a beating from adjacent channels. As a higher radio frequency is generated the LO is moved closer to the adjacent channels (see Fig. 3). It can produce additional spectral components within the antenna transmission region on the transmitted signal frequency or close to it. To reduce their impact the electrical filter selecting desired channel may be used. In the worst case when the data signal is spaced 100 GHz from the LO we have mixing products from: a) the LO with the selected data channel, b) the LO and another data channel, c) products from any two data channels spaced 100 GHz apart. What is more, when the LO signal is moved closer to the adjacent channel impact of this channel on the LO signal may also have an impact on the LO stability. The mentioned beating products may also explain the increase in the BER visible on the frequency of 81 GHz for the 5th channel.

V. CONCLUSIONS

In this article, we proposed and verified operation of a RAU utilizing optical heterodyne signal upconversion for generation and transmission of radio signals in the millimeter-wave range. The proposed RAU is widely reconfigurable in terms of DWDM channel selection and location of the LO signal and thus radio carrier frequency, implying numerous configuration options in both DWDM channel selection and W-band RF frequency allocation. Furthermore, the device meets the requirements of the IPHOBAC-NG project, effective and smoothly interfacing the optical and the wireless media, and showed excellent operation for FCC frequency allocation for fixed wireless services.

The performed tests demonstrated that error free (bit error rate below the level of 10^{-9}) transmission with a bitrate of 2.5 Gbit/s can be achieved after 15 km of fiber and 50 m of wireless links. Our previous work showed that the wireless transmission distances can be extended [13] by increasing the RF power, and therefore, the wireless length demonstrated in this experiment is not limited by any fundamental impairment.

ACKNOWLEDGEMENTS

This work was partly funded by the DFF FTP mmW-SPRAWL and EC IPHOBAC-NG projects.

REFERENCES

[1] P. Rost *et al.*, "Cloud technologies for flexible 5G radio access networks," *IEEE Commun. Mag.*, vol. 52, no. 5, pp. 68–76, 2014.

[2] T. S. Rappaport *et al.*, "Millimeter wave mobile communications for 5G cellular: It will work!" *IEEE Access*, vol. 1, pp. 335–349, 2013.

[3] J. G. Andrews *et al.*, "What will 5G be?" *IEEE J. Sel. Areas Commun.*, vol. 32, no. 6, pp. 1065–1082, 2014.

[4] D. Wake *et al.*, "Optical generation of millimeter-wave signals for fiber-radio systems using a dual-mode DFB semiconductor laser," *IEEE Trans. Microw. Theory Tech.*, vol. 43, no. 9, pp. 2270–2276, 1995.

[5] S. Rommel *et al.*, "W-band photonic-wireless link with a Schottky diode envelope detector and bend insensitive fiber," *Opt. Express*, vol. 24, no. 11, pp. 11312–11322, 2016.

[6] W.-J. Jiang *et al.*, "40 Gb/s RoF signal transmission with 10 m wireless distance at 60 GHz," in *Proc. OFC 2012*. OSA, 2012, paper OTu2H.1.

[7] A. Hirata *et al.*, "Transmission characteristics of 120-ghz-band wireless link using radio-on-fiber technologies," *J. Lightw. Technol.*, vol. 26, no. 15, pp. 2338–2344, Aug 2008.

[8] S. Rommel *et al.*, "225m outdoor W-band radio-over-fiber link using an optical SFP+ module," in *Proc OFC 2016*. OSA, 2016, paper Th2A.16.

[9] L. Deng *et al.*, "42.13 Gbit/s 16QAM-OFDM photonics-wireless transmission in 75-110 GHz band," *Prog. Electromagn. Res.*, vol. 126, pp. 449–461, 2012.

[10] S. Rommel, L. C. Pereira, J. J. Vegas Olmos, I. Tafur Monroy, and A. K. Mishra, "Requirements for bend insensitive fiber in millimeterwave fronthaul systems," in *Proc. MWP 2015*. IEEE, 2015, paper P-30.

[11] A. Lebedev *et al.*, "Feasibility study and experimental verification of simplified fiber-supported 60-GHz picocell mobile backhaul links," *IEEE Photon. J.*, vol. 5, no. 4, paper 7200913, 2013.

[12] X. Pang *et al.*, "DWDM fiber-wireless access system with centralized optical frequency comb-based RF carrier generation," in *Proc. OFC 2013*. OSA, 2013, paper JTh2A.56

[13] S. Rommel *et al.*, "Outdoor W-band hybrid photonic wireless link based on an optical SFP+ module," *IEEE Photon. Technol. Lett.*, vol. 28, no. 21, pp. 2303–2306, 2016.

PAPER16: Reconfigurable Radio Access Unit for DWDM to W-Band Wireless Conversion

L. Chorchos, **S. Rommel**, J. P. Turkiewicz, I. Tafur Monroy, and J. J. Vegas Olmos. "Reconfigurable Radio Access Unit for DWDM to W-Band Wireless Conversion". In: *IEEE Photonics Technology Letters* 29.6 (Mar. 2017), pp. 489–492. DOI: 10.1109/LPT.2017.2656894

Reconfigurable Radio Access Unit for DWDM to W-Band Wireless Conversion

Łukasz Chorchos, *Student Member, IEEE*, Simon Rommel, *Student Member, IEEE*, Jarosław P. Turkiewicz, *Senior Member, IEEE*, Idelfonso Tafur Monroy, *Senior Member, IEEE*, and Juan José Vegas Olmos, *Senior Member, IEEE*

***Abstract*— In this letter a reconfigurable remote access unit (RAU) is proposed and demonstrated, interfacing dense wavelength division multiplexed (DWDM) optical and W-band wireless links. The RAU is composed of a tunable local oscillator, a narrow optical filter, and a control unit, making it reconfigurable via software. The RAU allows selection of a DWDM channel and tuning of the radio carrier frequency. Real-time transmission results at 2.5 Gbit/s and performance measurements with offline data processing at 4 and 5 Gbit/s are presented. Error free real-time transmission was achieved after 15 km of standard single mode fiber and 50 m of wireless transmission with carriers between 75 and 95 GHz.**

***Index Terms*— Radio-over-fiber, millimeter-wave communications, W-band wireless, real-time systems.**

I. Introduction

GROWING demand for high speed wireless data transmission increases year to year mostly due to the emerging end user demand for wireless services like 4K/Ultra High Definition TV or mobile gaming [1]. The new 5G mobile standard will meet those requirements partially by the use of higher radio frequencies from the millimeter wave (mm-wave) range [2], [3]. Operation at these frequencies– from 30 GHz to 300 GHz – allows the use of wider transmission channels and clearly opens a possibility for significantly higher bit rates. Furthermore, regulations for the use of mm-waves allow lightly licensed or unlicensed link establishment. Nevertheless, signal generation in the mm-wave frequency range with traditional oscillators is complex.

To overcome this problem, the use of optical heterodyne signal upconversion was proposed [4] and in recent years has attracted interest of many researchers [5]–[8] and even joint projects were established in this field. Those projects aim to provide feasible solutions, integrating present and future optical networks with wireless communications by utilizing photonic techniques. The Integrated Photonic Broadband Radio Access Units for Next Generation Optical Access Networks (IPHOBAC-NG) project is one thereof and aims to provide seamlessly integrable photonic solutions for wireless communications and to adapt them into currently existing wavelength division multiplexed passive optical networks (WDM-PONs) and even ultra dense wavelength division multiplexed PONs. The project targets to provide a complementary broadband access with speeds between 1–10 Gbit/s and a mobile backhaul with the speed of 3 Gbit/s. To fulfill these requirements the IPHOBAC-NG project assumes the development of a new photonic RAU which will support reconfiguration of the optical channel allocation, which will not have an impact on the digital signal processing in the optical network unit (ONU) and optical network terminal (ONT), and will be energy efficient, fully integrated and compact. The proposed IPHOBAC-NG heterogeneous network architecture is presented in Fig. 1.

In this letter a reconfigurable Remote Access Unit (RAU) is proposed and demonstrated, interfacing DWDM optical and W-band wireless links to enable the IPHOBAC-NG network architecture. The proposed RAU utilizes optical heterodyne signal upconversion [9] for mm-wave wireless signal generation. The proposed RAU is composed of a reconfigurable optical filter for DWDM channel selection, a reconfigurable optical reference signal source, a photodiode and a control unit; section II provides a full description. Section III describes measurement setup and procedure. In section IV bit error rate measurements after transmission over 15 km of fiber and a wireless distance of 50 m are shown for 2.5 Gbit/s real-time transmission and 4 and 5 Gbit/s transmission with offline data processing.

II. Remote Access Unit Design

The reconfigurable RAU proposed in this letter and presented in Fig. 1 assumes a 100 GHz spaced, C-band DWDM input signal which is fed into a tunable, voltage-controlled, optical fiber Fabry-Perot filter, selecting the desired channel. The filter employed has 2.5 dB insertion losses, a 3 dB bandwidth of 15 GHz and a 20 dB bandwidth of 125 GHz, allowing operation in 100 GHz spaced DWDM systems. The filter is controlled through a digital analog converter (DAC), providing an adjustable output voltage range between -18 V and +18 V with 16 bit resolution, ensuring finesse to select any DWDM channel and easily reaching the required 16 V range for filter tuning across the whole C-band.

The selected channel from the DWDM signal is fed into a 3 dB coupler where it is combined with the reference signal from a local oscillator (LO, a tunable laser with 100 kHz

Manuscript received September 17, 2016; revised January 11, 2017; accepted January 19, 2017. Date of publication January 23, 2017; date of current version February 22, 2017. This work was supported by the DFF FTP mmW-SPRAWL and EC IPHOBACNG Projects under Grant 619870.

Ł. Chorchos and J. P. Turkiewicz are with the Institute of Telecommunications, Warsaw University of Technology, 00-665 Warsaw, Poland (e-mail: lukaszchorchos@gmail.com).

S. Rommel, I. Tafur Monroy, and J. J. Vegas Olmos are with the Department of Photonics Engineering, Technical University of Denmark, 2800 Kongens Lyngby, Denmark (e-mail: sirem@fotonik.dtu.dk).

Color versions of one or more of the figures in this letter are available online at http://ieeexplore.ieee.org.

Digital Object Identifier 10.1109/LPT.2017.2656894

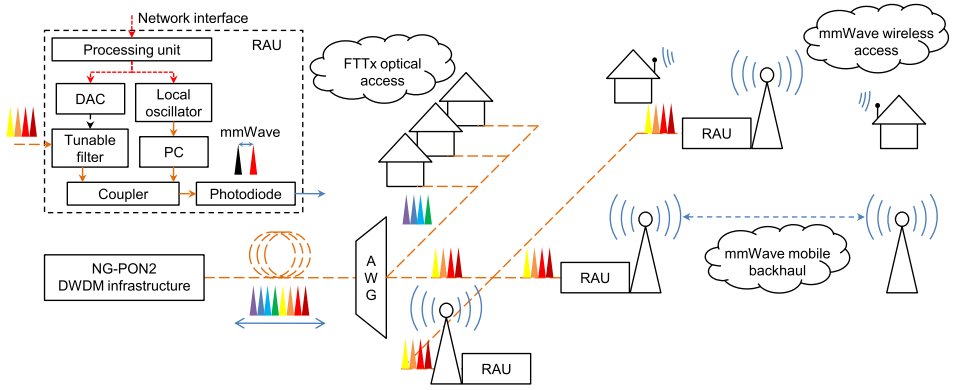

Fig. 1. IPHOBAC-NG architecture and block diagram of the proposed RAU, converting a DWDM optical signal to a W-band wireless signal.

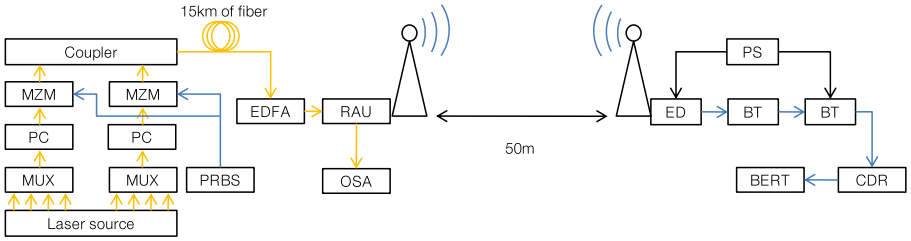

Fig. 2. Experimental setup for hybrid photonic 2.5 Gbit/s real time wireless transmission.

linewidth and fine frequency tuning). The polarization of the LO it is controlled with a manual polarization controller, to align signal and LO polarization and thus maximize beating efficiency on the photodiode. The addition of automatic LO polarization control – similar to eg. [10] – would alleviate the need for manual intervention and allow a fully remote controlled RAU. The LO wavelength and DAC output are controlled by the processing unit, in the present case a low-cost Raspberry Pi 2 which can control a number of devices. Moreover, this single-board controller can be loaded with software-defined networking (SDN) extensions, effectively softwarizing the RAU.

The coupled data and reference signal, spaced according to the desired radio frequency, are sent to a photodiode (Finisar XPDV4120R) with 90 GHz 3 dB bandwidth and a responsivity of 0.5 A/W. As a result of the heterodyning process at the photodiode, a radio signal with a carrier frequency in the W-band range is generated. The total RAU optical insertion losses are 5.5 dB: 2.5 dB from the optical filter and 3 dB from the coupler.

III. Transmission Performance Measurements

A. Experimental Setup

Fig. 2 depicts a block diagram of the experimental setup. Eight 100 GHz spaced lasers were multiplexed in two 4×1 couplers with distinction for even and odd channels. Next, the two streams of four wavelengths each were fed into two

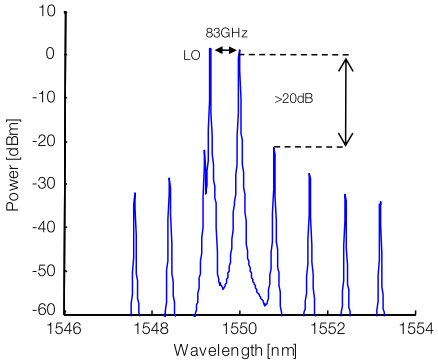

Fig. 3. Optical signal spectrum inside the RAU (after the coupler).

Mach-Zehnder modulators (MZM), preceded by two polarization controllers (PC). Both MZMs were biased at the center of their linear region and driven with two 2.5 Gbit/s (4 and 5 Gbit/s for offline data processing) non-return-to-zero (NRZ) pseudo random bit sequences (PRBS) with a length of $2^{11} - 1$ bits from a pulse pattern generator. The sequence modulating the odd channels was negated and shifted with a delay line to impose signal decorrelation. The signals from MZMs were combined in a 3 dB coupler and transmitted through a combination of 10 km standard single mode fiber (SSMF) and

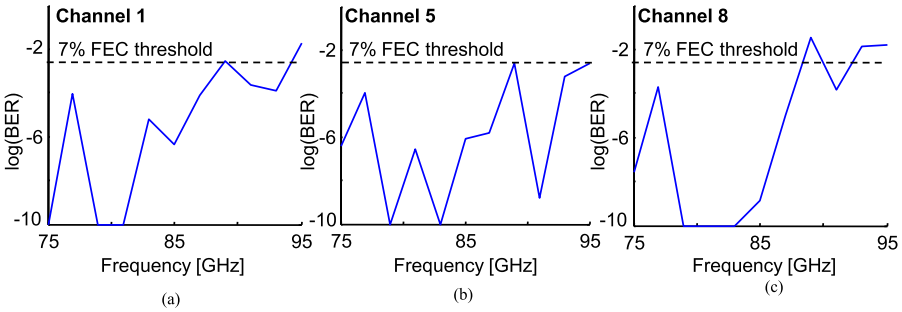

Fig. 4. BER measurement results obtained for 2.5 Gbit/s real time data transmission at frequencies ranging from 75 to 95GHz: a) 1^{st} b) 5^{th} and c) 8^{th} DWDM channel

5 km of bend insensitive fiber (ITU-T G.657.B3) (BIF). This combination secures compatibility with deployment scenarios where BIF fiber is required to avoid large bending losses, while having little impact on the performance of the hybrid optical wireless system [11].

After the fiber, the DWDM signal was amplified with an erbium doped fiber amplifier (EDFA) to provide sufficient power for radio frequency (RF) signal generation and transmission. The EDFA was placed at the RAU rather than before fiber transmission, due to a limited output power of the available EDFA and thus insufficient power per channel if placed before fiber transmission. The use of an EDFA with an exemplary output power of 22 dBm would allow EDFA placement in the central office (OLT) and yields a maximum fiber distance in the considered system configuration exceeding 20 km (assuming 13 dBm per channel after the EDFA, 0.3 dB/km fiber attenuation, 5.5 dBm insertion losses of the RAU and a required power of 1 dBm on the photodiode). The use of any EDFA might be avoided through the use of a semiconductor optical amplifier after the optical filter in the RAU.

After the EDFA the amplified signal is fed to the RAU. For each of the measured channels, polarization of the LO signal was adjusted to provide the maximum beating on the photodiode. The unused output of the coupler was used for signal monitoring with an optical spectrum analyzer (OSA). The output RF signal was transmitted over a distance of 50 m using a pair of parabolic W-band antennas with 48 dBi gain each.

After 50 m of wireless transmission, the output of the receiver antenna was amplified and downconverted with a W-band Schottky diode envelope detector (ED) with a 3 dB bandwidth of 3 GHz. For the 2.5 Gbit/s real-time measurement two bias tees (BT) were cascaded, the first removing unwanted DC components from the envelope detector and the second providing the required 3.3 V DC for the clock and data recovery module (CDR). The output of the CDR was connected to a bit error rate tester (BERT) allowing direct bit error rate (BER) measurements. The receiver configuration for 4 Gbit/s and 5 Gbit/s transmission is analog to that described in [8].

B. Measurement Procedure

The 2.5 Gbit/s real time and 4 Gbit/s with offline processing experiments were conducted for RF carrier frequencies between 75 GHz and 95 GHz with 2 GHz steps. Those measurements were performed for 1^{st}, 5^{th} and 8^{th} DWDM channel. The 95 GHz frequency upper bound was due to the operational bandwidth limit of the photodiode. The 5 Gbit/s experiment was performed for all DWDM channels at a frequency of 83 GHz. The decision to use W-band frequencies was made mainly due to lower attenuation in comparison to the 60 GHz V-band which is also considered for 5G networks.

The measurement conditions were set through the control unit of the RAU, to which channel number and mm-wave frequency target were indicated. The control unit, through a look-up table, automatically set up the filter and LO. The LO was manually co-polarized with the signal and its power set level to the data channel to provide maximum generated RF signal power [7], [12]; the actual power was 1 dBm each. Fig. 3 presents the optical spectrum for the 5^{th} DWDM channel inside the RAU after the filter and with the LO set 83 GHz apart from the data channel. It can be clearly observed that adjacent DWDM channels are suppressed by over 20 dB. For the real-time 2.5 Gbit/s transmission 5×10^{10} bits were evaluated per measurement point. For the 4 Gbit/s and 5 Gbit/s measurements the number of analyzed bits was >20 Mbit.

IV. Results and Discussion

Fig. 4 presents results for the 2.5 Gbit/s real-time measurement. Independent of the selected DWDM channel, similar BER characteristics were obtained. In the frequency range from 75 GHz to 87 GHz transmission with a BER below the limit of 3.8×10^{-3} for a commercial forward error correction (FEC) with an overhead of 7% is possible for all tested channels. For carrier frequencies located close to 80 GHz transmission considered as error free (BER $< 10^{-9}$) can be achieved. It is worth to mention that this frequency range was designated for high-density fixed wireless services by the US Federal Communication Commission (FCC) and the RAU proposed in this letter can be easily utilized for this application.

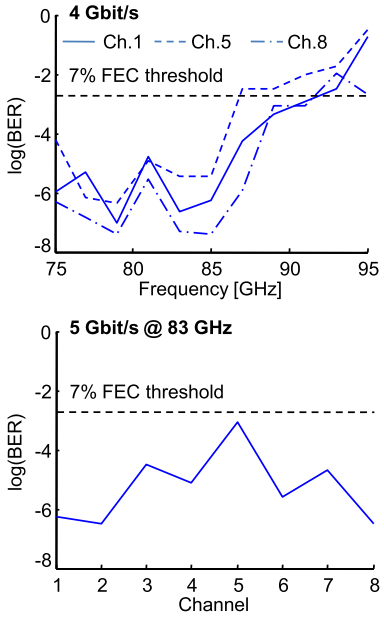

Fig. 5. Results of 4 and 5 Gbit/s tests with offline data processing.

For carriers above 87 GHz an increase in the BER is visible, caused partially by the limited bandwidth of the photodiode and thus a lower conversion efficiency and second by interference from adjacent channels. Although adjacent channels are suppressed by more than 20 dB, their remainders may beat with the selected channel, causing an RF component at 100 GHz, i.e. within W-band and thus within the transmission bandwidth of the antennas and the bandwidth of the receiver. Further impact may be taken from a loss of LO power due to beating with the closest adjacent channel. These are especially significant for the higher carrier frequencies and further explain the small advantage in BER observed for the outer channels where only one adjacent channel exists.

Fig. 5 shows the results obtained for the 4 and 5 Gbit/s transmission with offline data processing. At 4 Gbit/s transmission below FEC limit was achieved for frequencies up to 85 GHz. Above this frequency strong impact of the effects described above occur, especially for 5th channel where the difference in BER at 87 GHz between this channel and the 1st is two orders of magnitude and compared to 8th exceeds three orders of magnitude. Consequently the 5th channel shows the worst performance among all channels. This relationship was further confirmed by the measurement at 5 Gbit/s and 83 GHz where the 5th channel also showed worst performance, close to the FEC limit. These results demonstrate that the middle channels are most affected by unwanted mixing products and loss of LO power even though the adjacent channels are attenuated more than 20 dB. Never the less transmission of a 5 Gbit/s signal was successful for all channels on a 83 GHz carrier.

It should be noted that the achieved maximum wireless distance of 50 m is limited only by the available RF power and significantly longer distance should be achievable as demonstrated in [8].

V. Conclusions

In this letter, a RAU utilizing optical heterodyne signal upconversion for generation and transmission of radio signals in millimeter-waves range was proposed and experimentally validated. The proposed RAU is widely reconfigurable allowing direct selection of the desired DWDM channel and gapless tuning of the local oscillator signal, allowing free selection of the radio carrier frequency in the W-band. Furthermore, the proposed RAU meets the requirements of the IPHOBAC-NG project, effectively and smoothly interfacing the optical and the wireless media. By allowing easy integration with existing PONs and by allowing extension of the control unit to support SDN it thus enables heterogeneous network architectures as envisioned in IPHOBAC-NG.

The performed measurements demonstrate error free (BER $< 10^{-9}$) real-time transmission with a bitrate of 2.5 Gbit/s after 15 km of fiber and 50 m of wireless links. Transmission at data rates up to 5 Gbit/s is achieved with offline processing and a BER below the FEC limit. An increase in wireless distance analog to [8] by increasing the RF power is possible, and therefore the wireless distance demonstrated in these experiments is not limited by any fundamental impairment.

References

[1] P. Rost *et al.*, "Cloud technologies for flexible 5G radio access networks," *IEEE Commun. Mag.*, vol. 52, no. 5, pp. 68–76, May 2014.
[2] T. S. Rappaport *et al.*, "Millimeter wave mobile communications for 5G cellular: It will work!" *IEEE Access*, vol. 1, pp. 335–349, May 2013.
[3] J. G. Andrews *et al.*, "What will 5G be?" *IEEE J. Sel. Areas Commun.*, vol. 32, no. 6, pp. 1065–1082, Jun. 2014.
[4] D. Wake, C. R. Lima, and P. A. Davies, "Optical generation of millimeter-wave signals for fiber-radio systems using a dual-mode DFB semiconductor laser," *IEEE Trans. Microw. Theory Techn.*, vol. 43, no. 9, pp. 2270–2276, Sep. 1995.
[5] A. Hirata *et al.*, "Transmission characteristics of 120-GHz-band wireless link using radio-on-fiber technologies," *J. Lightw. Technol.*, vol. 26, no. 15, pp. 2338–2344, Aug. 1, 2008.
[6] W.-J. Jiang, H. Yang, Y.-M. Yang, C.-T. Lin, and A. Ng'oma, "40 Gb/s RoF signal transmission with 10 m wireless distance at 60 GHz," in *Proc. OFC*, 2012, pp. 1–3, paper OTu2H.1.
[7] X. Pang *et al.*, "25 Gbit/s QPSK hybrid fiber-wireless transmission in the W-band (75–110 GHz) with remote antenna unit for in-building wireless networks," *IEEE Photon. J.*, vol. 4, no. 3, pp. 691–698, Jun. 2012.
[8] S. Rommel *et al.*, "Outdoor *W*-band hybrid photonic wireless link based on an optical SFP+ module," *IEEE Photon. Technol. Lett.*, vol. 28, no. 21, pp. 2303–2306, Nov. 1, 2016.
[9] L. Deng *et al.*, "42.13 Gbit/s 16QAM-OFDM photonics-wireless transmission in 75-110 GHz band," *Prog. Electromagn. Res.*, vol. 126, pp. 449–461, Mar. 2012, doi: 10.2528/PIER12013006.
[10] M. Yagi, S. Satomi, and S. Ryu, "Field trial of 160-Gbit/s, polarization-division multiplexed RZ-DQPSK transmission system using automatic polarization control," in *Proc. OFC*, 2008, pp. 1–3, paper OThT7.
[11] S. Rommel, L. C. P. Cavalcante, A. G. Quintero, A. K. Mishra, J. J. V. Olmos, and I. T. Monroy, "W-band photonic-wireless link with a Schottky diode envelope detector and bend insensitive fiber," *Opt. Exp.*, vol. 24, no. 11, pp. 11312–11322, 2016.
[12] X. Pang *et al.*, "Centralized optical-frequency-comb-based RF carrier generator for DWDM fiber-wireless access systems," *J. Opt. Commun. Netw.*, vol. 6, no. 1, pp. 1–7, 2014.

PAPER17: Reconfigurable radio access unit to dynamically distribute W-band signals in 5G wireless access networks

S. Rodriguez, **S. Rommel**, J. J. Vegas Olmos, and I. Tafur Monroy. "Reconfigurable radio access unit to dynamically distribute W-band signals in 5G wireless access networks". In: *Optical Switching and Networking* 24 (Apr. 2017), pp. 21–24. DOI: 10.1016/j.osn.2016.10.002

Optical Switching and Networking 24 (2017) 21–24

Contents lists available at ScienceDirect

Optical Switching and Networking

journal homepage: www.elsevier.com/locate/osn

Reconfigurable radio access unit to dynamically distribute W-band signals in 5G wireless access networks

Sebastián Rodríguez[a,*], Simon Rommel[a], Juan José Vegas Olmos[a], Idelfonso Tafur Monroy[a,b]

[a] Department of Photonics Engineering, Technical University of Denmark, Ørsteds Plads, 2800 Kgs. Lyngby, Denmark
[b] ITMO University, St Petersburg, Russia

ARTICLE INFO

Keywords:
Optical switching
Millimeter-wave communications
Radio access networks
W-band wireless

ABSTRACT

In this paper a new type of radio access unit is proposed and demonstrated. This unit is composed only of the reduced amount of components (compared to conventional unit designs) to optically generate wireless signals on the W-band (75–110 GHz) in combination with a switching system. The proposed system not only achieves BER values below the FEC limit, but gives an extra level of flexibility to the network by easing the redirection of the signal to different antennas.

1. Introduction

Today's mobile networks are designed as distributed access networks (D-RANs), composed of a number of base stations, connected via backhaul links to different service and support nodes in the core network which are in charge of the different operations and processing functions. In this approach, the growth in the number of users and applications brings a necessity to increase the capacity of the core, resulting in the implementation of more nodes, introducing more complexity in the network and translating to bigger costs for both deployment and maintenance.

As an alternative, the concept of a centralized access network (C-RAN) has been recently proposed and discussed [1,2]. In this architecture, the most important hardware of the network is moved to a central office that will be connected to various radio access units (RAUs) to transmit the signal in the wireless channel. With this change, the central office will take care of the complex processing of the network, allowing the implementation of simpler RAUs that only need the hardware necessary for signal conversion to the wireless channel [1]. With this approach, the expansion of the network would only require an upgrade in the central office and the densification of various RAUs that take care of the wireless access of smaller areas of the network, reducing the total costs for both deployment and operation.

This scenario can be further expanded with the inclusion of radio-over-fiber (RoF) technologies on the front- and backhaul networks [3]. The central office will then be able to generate the wireless signal directly in the optical domain, and distribute it to the various RAUs [4,5]. Here, the signal is converted to the electrical domain and transmitted wirelessly at millimeter-wave (mm-wave) frequencies [6–11]. Thus a new type of access network can be achieved in order to fulfill the requirements of future networks [12,13].

Current works on the design of dynamically reconfigurable access networks have been reported using technologies like dense wavelength division multiplexing (DWDM), optical cross-connections and multi-core fiber to exploit the available resources, while giving flexibility to the network [4,12–14]. Furthermore, architectures based on reconfigurable optical switches have been shown [15,16] and their implementation in centralized scenarios has been proposed [17], enabling the implementation of fully flexible software defined networks for future front- and backhaul.

In this paper, a reconfigurable RAU (R-RAU), composed of an arrayed waveguide grating (AWG) an optical switch and a local oscillator, is proposed and demonstrated in a scenario that combines DWDM and mm-wave RoF. This R-RAU enables flexibility of the infrastructure, active delivery and smooth integration with software defined optic network approaches.

The remainder of the paper is structured as follows: Section 2 describes the proposed architecture, Section 3 describes the experimental setup and Section 4 discusses the experimental results before Section 5 summarizes and concludes the paper.

2. Proposed mobile front- and backhaul architecture

The proposed architecture is shown in Fig. 1. As previously stated, it is based on the idea of the C-RAN, where a large number of distributed R-RAUs, connected to the same central office (CO), is assumed. With this kind of implementation, all the processing of higher layers is performed by the CO and the signals are distributed to the R-

* Corresponding author.
E-mail addresses: juse@fotonik.dtu.dk (S. Rodríguez), sirem@fotonik.dtu.dk (S. Rommel), jjvo@fotonik.dtu.dk (J.J. Vegas Olmos), idtm@fotonik.dtu.dk (I.T. Monroy).

http://dx.doi.org/10.1016/j.osn.2016.10.002
Received 15 March 2016; Received in revised form 20 September 2016; Accepted 25 October 2016
Available online 11 November 2016

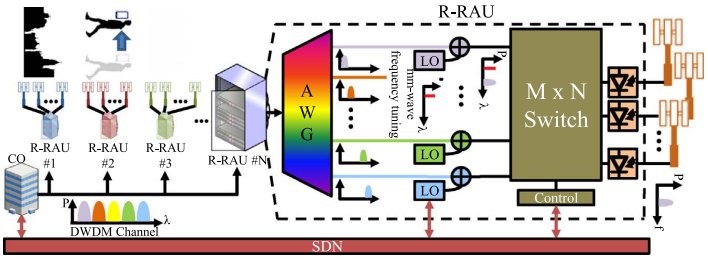

Fig. 1. Proposed radio access unit and network architecture. CO: central office; R-RAU: reconfigurable radio access unit; AWG: arrayed waveguide grating.

RAU using DWDM.

The multiplexed signals arrive at the R-RAU through an AWG which separates them into *M* different channels. Each of these outputs will be combined with a tunable local oscillator—spaced from the signal at the desired mm-wave signal frequency—and will then serve as inputs to an *M*×*N* controllable switch. The function of this switch is to distribute the signals among its *N* outputs in order to be up-converted. The up-conversion takes place on a broadband photodiode, using the heterodyne photonic up-conversion technique as described in [17,18]. The output of this process will be a modulated signal in the mm-wave bands, which will be delivered to an antenna in order to be transmitted wirelessly. These approaches enable the RAU to have different antennas distributed over a large area (indoor or outdoor), or have several small nodes of communication for scenarios related to the internet of things (IoT).

This architecture allows the RAU to be simplified, since its design only needs the elements to select one of the channels of a DWDM signal and the necessary hardware to transmit the RF signal. This implementation also agrees with previous works on architectures for the access networks [5,4,18], taking part of the RF front end to the central office, and leaving in the RAU only the O/E interface, RF amplification and antenna. With the optical switch, the R-RAU has more flexibility to redirect the signal according to the necessities of the network. Moreover, since it can be remotely controlled, this allows its implementation as part of a SDN in the front- and backhaul networks.

3. Experimental setup

The experimental setup is presented in Fig. 2 and its implementation is shown in Fig. 3. The central office is emulated using a DWDM generator with eight light sources spaced according to the ITU-T G.694.1 50 GHz grid. All the light sources are modulated using a Mach–Zehnder modulator (MZM) with a 2.5 Gbps NRZ signal from a pulse pattern generator (PPG). The DWDM signal is transmitted through 10 km of standard single mode fiber to the R-RAU. With the AWG, one of the wavelengths is selected. The signal is then boosted using an erbium doped fiber amplifier (EDFA) and divided into two: one branch for transmission and one for switching reference.

The first part is combined with the LO and a variable optical attenuator (VOA1) is used to ensure equal powers of signal and LO to achieve optimum optical to RF conversion [19]. Then the two signals enter the switching system composed of an optical MEMS switch

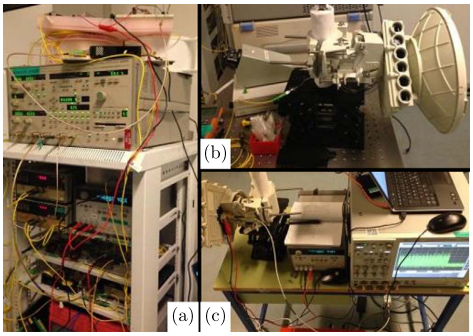

Fig. 3. Experimental setup: (a) optical setup for signal generation and R-RAU, (b) transmitting antenna, (c) receiver station with a packet shown on the DSO.

controlled with a microcontroller (μC). The two signals go through 5 km of bend insensitive fiber (BiF) to a second variable optical attenuator (VOA2), controlling power incident on the photodiode and thus transmitted radio-frequency power, allowing for bit-error-rate (BER) measurements in dependency on power.

Upconversion is performed by direct heterodyning on a large bandwidth photodiode (Finisar XPDV4120R) with a 3 dB bandwidth of 90 GHz. The result is a double sideband modulated NRZ signal with a central carrier at 85 GHz, achieving transmission in the W-band. The signal is fed to a parabolic antenna with an antenna gain of 48 dBi and transmitted over a wireless distance of 50 m. At the receiver, a similar 48 dBi parabolic antenna recovers the signal. A 40 dB gain low noise amplifier (LNA) is used before the signal is downconverted using a Schottky diode based W-band envelope detector (ED) with a nominal 3 dB bandwidth of 3 GHz. A low pass Bessel filter with a 3 dB cutoff frequency of 1.8 GHz limits noise bandwidth before the signal is recorded on a digital storage oscilloscope (DSO) for offline post-processing.

On the switching branch of the system, the reference signal passes through a variable optical attenuator (VOA3) that controls the power delivered to a low speed PD and the resulting signal is further band limited with a low pass filter. This signal is used as reference on the μC to change the output state of the switch.

For the experiment, a packet composed of a number of $2^7 - 1$

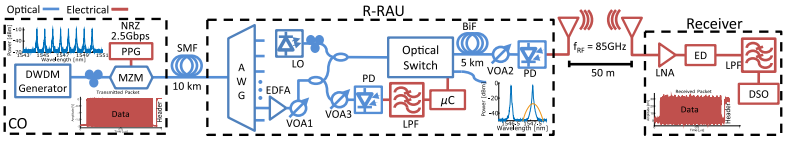

Fig. 2. Experimental setup for switching demonstration of W-band signals. PPG: pulse pattern generator; MZM: Mach–Zehnder modulator; LO: local oscillator; EDFA: erbium doped fiber amplifier; VOA: variable optical attenuator; BiF: bend insensitive fiber; AWG: arrayed waveguide grating; PD: photodiode; LPF: low pass filter; μC: microcontroller; ED: envelope detector; LNA: low noise amplifier; DSO: digital storage oscilloscope.

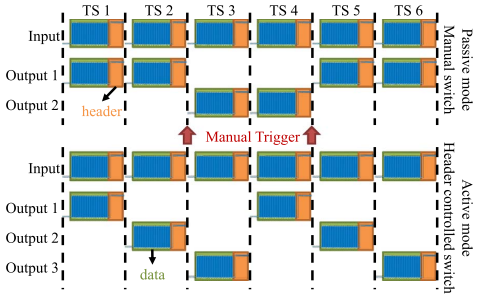

Fig. 4. Timing considerations for the different switching modes. TS: time slot.

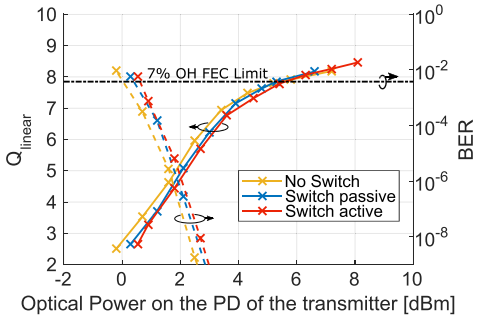

Fig. 5. Observed Q factors and estimated BER for the three cases: without optical switch and when including the switch in both passive and active.

pseudorandom bit sequences (PRBS7) and a header of ones—in order to give the switching command to the μC—is transmitted. On the switching system two modes of operation were programed:

(a) *Passive mode*: In this mode the switch will change status only after the μC receives a manually triggered command and will stay in the same position until the next command is given.
(b) *Active mode*: In this mode the part of the signal taken as switching reference is used to trigger the command to the switch automatically, looping between a set of outputs previously defined.Fig. 4 exemplifies the two modes of operation for different time slots. In the experiment, individual packets are received and analyzed for bit error rate and to determine the Q factor of the received signal. Packet error rates are estimated assuming a typical commercial 7% overhead forward error correction.

4. Experimental results

The results show case performance for three cases: the system without the switch, the system in passive switching mode and the system with active switching. The PPG is set to generate the packets previously described and at the receiver 500 packets are individually received and analyzed via offline processing. The transmission presented error free for various values of optical power, so the Q factor was used to give a better description of the system performance. The calculation of Q factor and estimation of BER is as follows:

$$Q = \frac{\mu_1 - \mu_0}{\sigma_1 + \sigma_0} \tag{1}$$

$$BER \approx 3/4\,\mathrm{erfc}(Q/\sqrt{2}) \tag{2}$$

with μ_0, μ_1 corresponding to the mean values of the signal levels and σ_0, σ_1 their standard deviation.

The Q factor and estimated BER versus optical power incident on the PD are plotted in Fig. 5. It can be observed that the estimated sensitivities of the system are 0 dBm, 0.4 dBm and 0.6 dBm, for the case without switch, the passive mode and the active mode respectively. The scenarios with and without the switch have similar results, the main difference being in the power levels in each curve, which is due to the fact of extra attenuation in the signal path, i.e. the inclusion of the insertion loss of the switch. It can further be noticed that in active switching mode the system has an insignificant difference in the results when compared to passive switching mode. In the three cases, the value of the Q reaches a maximum point, mainly due to the fact that as the optical power on the PD increases, the PD starts to saturate.

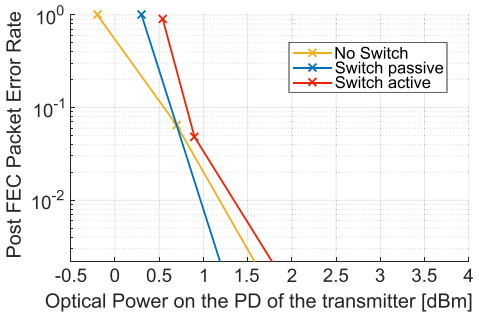

Fig. 6. Packet error rates after applying forward error correction with 7% overhead for the three cases: without optical switch and when including the switch in both passive and active.

In order to evaluate performance in terms of packet error rate, packets were analyzed for their BER. Packets with a BER above the limit of 3.8×10^{-3}, for a typical forward error correction (FEC) with 7% overhead (OH), are considered erroneous packets. The measured packet error rates after applying the FEC are shown in Fig. 6 for the three analyzed cases. As the optical power in the PD starts to drop, the systems start to approach to the sensitivity values. Once the power is below 2 dBm the system starts to present erroneous packets until the point where the sensitivity is reached and all packets are considered erroneous.

These results compare well with BER measurements from [9,19] where similar implementations were evaluated in both BER and Q performance, achieving similar results. The transmission reach of the proposed system can further be expanded with RF setups similar to that presented in [9]. Moreover, the stability of these kinds of systems is measured, showing the potential of the W-band RAU.

5. Conclusions

A reconfigurable radio access unit for W-band transmission, based on an AWG and a programmable optical switching system, has been proposed and experimentally demonstrated. The inclusion of the switch causes no signal impairments beyond the addition of extra insertion losses, and thus the switching does not have a significant impact on system performance, moreover it enables more flexibility and reconfigurability in the network.

Because of its simplistic approach, the proposed R-RAU appears to be a good candidate for the implementation of the next generation of centralized networks, where the dense deployment of these units at a low cost is desired, while fulfilling the requirements of the 5th generation of mobile front- and backhaul networks.

Acknowledgments

This work was partly funded by the Marie Curie FiWiN5G (grant No. 642355), DFF FTP mmW-SPRAWL and EC IPHOBAC-NG (grant No. 619870) projects.

References

[1] P. Rost, C. Bernardos, A. Domenico, M. Girolamo, M. Lalam, A. Maeder, D. Sabella, D. Wübben, Cloud technologies for flexible 5G radio access networks, IEEE Commun. Mag. 52 (5) (2014) 68–. http://dx.doi.org/10.1109/MCOM.2014.6898939.

[2] T. Pfeiffer, Next generation mobile fronthaul architectures, in: Proceedings of OFC 2015, OSA, Los Angeles, 2015, p. M2J.7. http://dx.doi.org/10.1364/OFC.2015.M2J.7.

[3] A. Kanno, P.T. Dat, T. Kuri, I. Hosako, T. Kawanishi, Y. Yoshida, Y. Yasumura, K. Kitayama, Coherent radio-over-fiber and millimeter-wave radio seamless transmission system for resilient access networks, IEEE Photon. J. 4 (6) (2012) 2196–. http://dx.doi.org/10.1109/JPHOT.2012.2228182.

[4] J.M. Galve, I. Gasulla, S. Sales, J. Capmany, Reconfigurable radio access networks using multicore fibers, IEEE J. Quantum Electron. 52 (1) (2016) 1–. http://dx.doi.org/10.1109/JQE.2015.2497244.

[5] C. Liu, L. Zhang, M. Zhu, J. Wang, L. Cheng, G.-K. Chang, A novel multi-service small-cell cloud radio access network for mobile backhaul and computing based on radio-over-fiber technologies, J. Lightw. Technol. 31 (17) (2013) 2869–. http://dx.doi.org/10.1109/JLT.2013.2274193.

[6] X. Pang, A. Caballero, A. Dogadaev, V. Arlunno, R. Borkowski, J.S. Pedersen, L. Deng, F. Karinou, F. Roubeau, D. Zibar, X. Yu, I. Tafur Monroy, 100 Gbit/s hybrid optical fiber-wireless link in the W-band (75–110GHz), Opt. Express 19 (25) (2011) 24944–. http://dx.doi.org/10.1364/OE.19.024944.

[7] M. Beltran, J.B. Jensen, X. Yu, R. Llorente, R. Rodes, M. Ortsiefer, C. Neumeyr, I. Tafur Monroy, Performance of a 60-GHzDCM-OFDM and BPSK-impulse ultra-wideband system with radio-over-fiber and wireless transmission employing a directly-modulated VCSEL, IEEE J. Sel. Areas Commun. 29 (6) (2011) 1295–. http://dx.doi.org/10.1109/JSAC.2011.110616.

[8] J.A. Nanzer, P.T. Callahan, M.L. Dennis, T.R. Clark, D. Novak, R.B. Waterhouse, Millimeter-wave wireless communication using dual-wavelength photonic signal generation and photonic upconversion, IEEE Trans. Microw. Theory Techn. 59 (12) (2011) 3522–. http://dx.doi.org/10.1109/TMTT.2011.2171710.

[9] S. Rommel, S. Rodriguez, L. Chorchos, E.P. Grakhova, A.K. Sultanov, J.P. Turkiewicz, J.J. Vegas Olmos, I. Tafur Monroy, Outdoor W-band hybrid photonic wireless link based on an optical SFP+ module, IEEE Photon. Technol. Lett. (2016). http://dx.doi.org/10.1109/LPT.2016.2592326.

[10] S. Rommel, L. Yi, M. Shi, I. Tafur Monroy, J.J. Vegas Olmos, Demonstration of 4 Gbit/s duobinary Ka-band hybrid photonic-wireless transmission, in: Proceedings of ACP 2015, OSA, 2015, p. ASu1J.2. http://dx.doi.org/10.1364/ACPC.2015.ASu1J.2.

[11] S. Rodriguez, R. Puerta, H. Kim, J.J. Vegas Olmos, I. Tafur Monroy, Photonic up-conversion of carrierless amplitude phase signals for wireless communications on the KA-band, Microw. Opt. Technol. Lett. 58 (9) (2016) 2068–. http://dx.doi.org/10.1002/mop.29975.

[12] Nan Chi, J.J. Vegas Olmos, K. Thakulsukanant, Zhuoran Wang, O. Ansell, Siyuan Yu, D. Huang, Experimental characteristics of optical crosspoint switch matrix and its applications in optical packet switching, J. Lightw. Technol. 24 (10) (2006) 3646–. http://dx.doi.org/10.1109/JLT.2006.881853.

[13] J.J. Vegas Olmos, T. Kuri, T. Sono, K. Tamura, H. Toda, K.-i. Kitayama, Wireless and optical-integrated access network with peer-to-peer connection capability, IEEE Photon. Technol. Lett. 20 (13) (2008) 1127–. http://dx.doi.org/10.1109/LPT.2008.924657.

[14] J.J. Vegas Olmos, T. Kuri, K.-i. Kitayama, Dynamic reconfigurable WDM 60-GHz millimeter-waveband radio-over-fiber access network: architectural considerations and experiment, J. Lightw. Technol. 25 (11) (2007) 3374–. http://dx.doi.org/10.1109/JLT.2007.906806.

[15] K. Vyrsokinos, A. Maziotis, C. Kouloumentas, C. Stamatiadis, N. Pleros, An optical MEMS-based dynamic capacity allocation scheme for handoff using moving extended cells in radio-over-fiber networks, Opt. Commun. 284 (19) (2011) 4390–. http://dx.doi.org/10.1016/j.optcom.2011.05.058.

[16] N. Pleros, K. Vyrsokinos, K. Tsagkaris, N.D. Tselikas, A 60GHz radio-over-fiber network architecture for seamless communication with high mobility, J. Lightw. Technol. 27 (12) (2009) 1957–. http://dx.doi.org/10.1109/JLT.2009.2022505.

[17] J.J. Vegas Olmos, I. Tafur Monroy, Reconfigurable radio-over-fiber networks, in: Proceedings of OFC 2015, OSA, Los Angeles, 2015, p. W1F.3. http://dx.doi.org/10.1364/OFC.2015.W1F.3.

[18] S. Rommel, S. Rodrıguez, L. Chorchos, E.P. Grakhova, A.K. Sultanov, J.P. Turkiewicz, J.J. Vegas Olmos, I. Tafur Monroy, 225m outdoor W-band radio-over-fiber link using an optical SFP+ module, in: Proceedings of OFC 2016, OSA, Anaheim, 2016, p. Th2A.16. http://dx.doi.org/10.1364/OFC.2016.Th2A.16.

[19] S. Rommel, L.C.P. Cavalcante, A.G. Quintero, A.K. Mishra, J.J. Vegas Olmos, I. Tafur Monroy, W-band photonic-wireless link with a Schottky diode envelope detector and bend insensitive fiber, Opt. Express 24 (11) (2016) 11312–. http://dx.doi.org/10.1364/OE.24.011312.

PAPER18: Real-time Measurements of an Optical Reconfigurable Radio Access Unit for 5G Wireless Access

S. Rodriguez, A. Morales, **S. Rommel**, J. J. Vegas Olmos, and I. Tafur Monroy. "Real-time Measurements of an Optical Reconfigurable Radio Access Unit for 5G Wireless Access". In: *Optical Fiber Communication Conference 2017*. Mar. 2017, paper W1C.3. DOI: 10.1364/OFC.2017.W1C.3

Real-time Measurements of an Optical Reconfigurable Radio Access Unit for 5G Wireless Access Networks

Sebastián Rodríguez[1*], Alvaro Morales[1], Simon Rommel[1], J. J. Vegas Olmos[1], and I. Tafur Monroy[1,2]

[1]*Department of Photonics Engineering, Technical University of Denmark, 2800 Kgs. Lyngby, Denmark*
[2]*ITMO University, St. Petersburg 197101, Russia.*

[*]*juse@fotonik.dtu.dk*

Abstract: A reconfigurable radio access unit able to switch wavelength, RF carrier frequency and optical path is experimentally demonstrated. The system is able to do the switching processes correctly, while achieving BER values below FEC limit.

OCIS codes: (250.6715) Switching (Optoelectronics), (060.5625) Radio frequency photonics.

1. Introduction

The architecture of 5G wireless radio access network (RAN) has evolved from a distributed approach (D-RAN) to a network with its resources centralized (C-RAN). This architecture, takes the complex processes from the radio access unit (RAU) and gives them to the central office (CO) as a set of shared virtualized resources. The RAU will only act as an interface between the fronthaul network and the wireless transmission, simplifying its design and reducing the costs of installation (CAPEX) and operation (OPEX). The CO will handle all the processes directly, reducing the total latency of the network, enabling it to support different standards and smooth their evolution [1]. In order to fully implement the C-RAN, Radio-over-Fiber (RoF) has been proposed as a high capacity backbone technology to transport millimeter wave signals between CO and the various RAUs of the network [2, 3], reusing the already implemented fiber networks. To expand the application of RoF, previous works have shown the viability of added flexibility through the use of multicore fibers and optical switches and labels [2, 4–6].

In this paper we present a full reconfigurable RAU (FRRAU), based on four different subsystems: wavelength selector, RF frequency selector, sector selector and a controller. This FRRAU aims to give an extra layer of reconfigurability and flexibility to the next generation of access networks.

2. Proposed Architecture

The CO generates and modulates the optical channels of a dense wavelength division multiplexed (DWDM) signal. These channels are delivered to all the RAUs in the network. Each RAU is composed by three systems controlled by a microcontroller (μC). First, in a wavelength selection system, the μC receives the remote order to change the voltage of a digital-to-analog converter (DAC). The DAC gives the voltage to a Fabry-Perot tunable band pass filter, selecting one of the channels of the DWDM signal. Second, as a frequency selection system, a tunable laser controlled by the μC is used as LO, to allow the network to change the wireless carrier frequency. Finally, a sector selection system uses an optical switch, based on microelectromechanical systems (MEMS), to redirect the received optical signal to different PDs and perform the optical up-conversion, generating the wireless signal for different antennas. The switch can be set to stay statically in one output or to dynamically change between its different outputs. The μC is connected to a network via an ethernet connection allowing the proposed FRRAU to be implemented as part of a software defined network (SDN).

3. Experimental setup

Figure 1 shows the setup used in the experiment. In the CO, four lasers are combined to create the DWDM signal. The lasers are modulated using a Mach-Zehnder Modulator (MZM) with a 2.5 Gbit/s $2^{15}-1$ bit long pseudo-random bit sequence (PRBS15) non-return-to-zero (NRZ) signal. The optical signals are launched into 10 km of standard

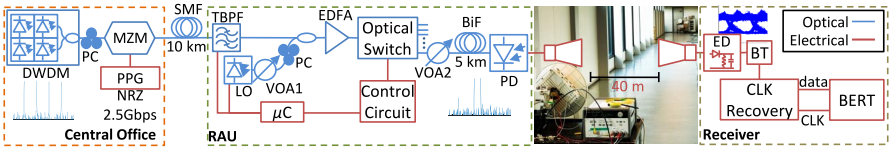

Fig. 1: Implemented setup of the experiment. DWDM: Dense wavelength multiplexion; PPG: Pulse pattern generator; NRZ: Non-return-to-zero; PC: Polarization controller; MZM: Mach-Zehnder modulator; SMF: Single mode fiber; RAU: Radio access network; TBPF: Tunable band pass filter; LO: Local Oscillator; μC: Microcontroller; VOA: Variable optical attenuator; EDFA: Erbium-doped fiber amplifier; BiF: Bend-insensitive fiber; PD: Photodiode; ED: Envelope detector; BT: Bias tee; CLK: Clock; BERT: Bit-error-rate tester.

single-mode fiber (SSMF) to reach the RAU. Here the tunable band-pass filter is used to select one of the channels. The filter is electrically configured with the μC. The selected optical signal is then combined with an external cavity laser (ECL), which serves as a local oscillator (LO) with the optical input power adjusted with a variable optical attenuator (VOA). The two signals are boosted with an erbium-doped fiber amplifier (EDFA). The signals are taken by an optical switching system and distributed to one of its outputs. A second VOA is placed for bit-error-rate (BER) measurements. Afterwards, the signal travels through 5 km of bend insensitive fiber (BiF). Here a high bandwidth PD is used to perform the up-conversion process by direct heterodyning [3]. The result is a double side band modulated signal with a central carrier of 81 GHz, producing the transmission on the W-band. The signal is fed to a horn antenna with a gain of 48 dBi and wirelessly transmitted over 40 m of distance. At the receiver, a second 48 dBi horn antenna recovers the signal and delivers it to a 40 dB gain LNA, before a Schottky diode based W-band envelope detector (ED) down-converts the data signal. Then, a clock recovery stage is used to provide both data and timing information to a bit-error-rate tester (BERT), allowing the real-time measurements of the BER.

4. Experimental results

Figure 2 presents the real-time measurement of the BER and Fig. 3 show the corresponding optical spectrums for each channel. The BER traces are compared to the BER limit for a FEC with 7% of overhead, presenting values below FEC limit with a sensitivity between -3.2 dBm and -5.6 dBm. The optical spectra show some components of the non selected channels, that will act interference in the communication, that will explain the different slopes in the different channels. Channels 1 and 4 presents similar tendency, being the both on the extremes, and the ones to have a better performance. Channel 2 and 3 present some similarities in their performance, but is channel 2 the one that appears more affected by the inter-channel interference.

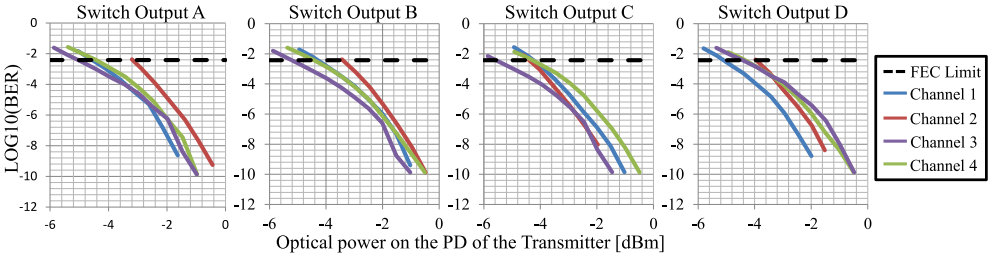

Fig. 2: Real time measurements of the BER vs the optical power on the PD of the transmitter.

Figure 4(a) shows the performance of the sector selection system during the dynamic switching operation, both the BER curve and the switching time signal. As observed, the dynamic operation has a minor effect on the general performance of the system, having an insignificant impact on sensitivity compared to the static system. The performance of the frequency selection system is presented in Fig. 4(b) alongside the optical spectrum of the data signal with the LOs to wirelessly transmit at 81 GHz and 87 GHz. As expected, the higher frequencies present greater attenuation during

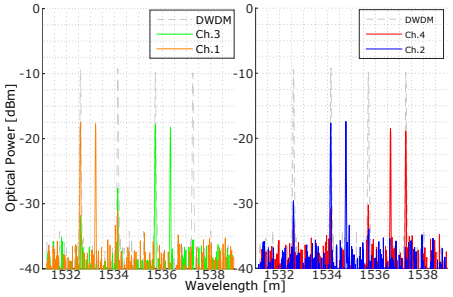

Fig. 3: Optical spectra of the four transmitted channels with their respective local oscillator, in the background the full DWDM signal is shown as reference.

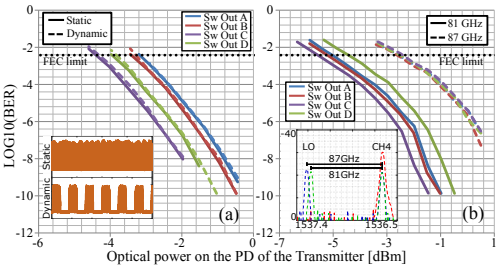

Fig. 4: Real time measurements of the BER vs the optical power on the PD of the transmitter: (a) static and dynamic operation in channel 2. (b) Transmission of 81 GHz and 87 GHz in channel 4.

the transmission, having an extra penalty of around 2.8 dB. Since the slope of the traces are different for 87 GHz, the transmission in not only affected by extra attenuation, but there will be differences because of the wireless channel, the inter-channel interferences and the bandwidth limit of the PD. Although only channels 2 and 4 were tested in for the two last tests respectively, these results can be extended to the other channels.

5. Conclusion

A full reconfigurable radio access network able to transmit signals in the W-band (75 GHz to 110 GHz) over a distance of 40 m has been experimentally demonstrated. The FRRAU is composed by a wavelength, a RF frequency and a sector selection systems and a controller. The wavelength selection system is used to choose a channel of a DWDM signal with a tunable filter. Although some interferences from the adjacent channels are still present after the filter, the system still presents a sensitivity of -3.2 dBm in the worst case. The frequency selection system allows the allocation of resources in different RF frequencies, having as main penalty the extra losses of higher frequencies. The sector selection system allows to select between different outputs of a switch, either statically or dynamically, with minor effects in the performance of the system. The implemented FRRAU is a perfect candidate for the 5G of mobile networks, able to work under the concept of the C-RAN and adding an extra layer of control and reconfigurability to the system, by allowing its implementation in a software defined access network.

References

1. China Mobile Research Institute, "C-RAN The Road Towards Green RAN," *On-line white paper v. 3*, http://labs.chinamobile.com/.
2. J. M. Galve, I. Gasulla, S. Sales, and J. Campany, "Reconfigurable Radio Access Networks Using Multicore-Fibers," *IEEE Journal of Quantum Electronics*, **52**, 1–7 (2016).
3. S. Rommel, S. Rodriguez, L. Chorchos, E. Grakhova, A. Sultanov, J. Turkiewicz, J. J. Vegas Olmos, and I. Tafur Monroy, "Outdoor W-Band Hybrid Photonic Wireless Link Based on an Optical SFP+ Module," *IEEE Photonics Technology Letters*, **28**, 2303–2306 (2016).
4. N. Chi, J. J. Vegas Olmos, K. Thakulsukanant, Zhuoran Wang, O. Ansell, Siyuan Yu, and D. Hua, "Experimental characteristics of optical crosspoint switch matrix and its applications in optical packet switching," *Journal of Lightwave Technology*, **24**, 3646–3653 (2006).
5. J. J. Vegas Olmos, T. Kuri, T. Sono, K. Tamura, H. Toda, and K.-i. Kitayama, "Wireless and Optical-IntegratedAccess Network With Peer-To-Peer Connection Capability," *IEEE Photonics Technology Letters*, **20**, 1127–1129 (2008).
6. J. J. Vegas Olmos and I. Tafur Monroy, "Reconfigurable Radio-Over-Fiber Networks," in *Proc. OFC 2015*, (OSA, Los Angeles, 2015), paper W1F.3.

PAPER19: Characterization of a Fiber-Coupled 36-Core 3-Mode Photonic Lantern Spatial Multiplexer

S. Rommel, J. M. Delgado Mendinueta, W. Klaus, J. Sakaguchi, J. J. Vegas Olmos, Y. Awaji, I. Tafur Monroy, and N. Wada. "Characterization of a Fiber-Coupled 36-Core 3-Mode Photonic Lantern Spatial Multiplexer". In: *OSA Advanced Photonics Congress (Photonic Networks and Devices)*. July 2017, paper NeW3B.2. DOI: 10.1364/NETWORKS.2017.NeW3B.2

Characterization of a Fiber-Coupled 36-Core 3-Mode Photonic Lantern Spatial Multiplexer

Simon Rommel[1,2,*], José Manuel Delgado Mendinueta[1], Werner Klaus[1], Jun Sakaguchi[1], Juan José Vegas Olmos[3], Yoshinari Awaji[1], Idelfonso Tafur Monroy[2] and Naoya Wada[1]

[1] *Photonic Network System Laboratory, National Institute of Communication and Information Technology (NICT), 4-2-1 Nukui-Kitamachi, Koganei, Tokyo 184-8795, Japan*
[2] *Department of Photonics Engineering, Technical University of Denmark, 2800 Kgs. Lyngby, Denmark*
[3] *Mellanox Technologies, Ledreborg Allé 130B, 4000 Roskilde, Denmark*

[*] *sirem@fotonik.dtu.dk*

Abstract: A fiber-coupled 108-port photonic lantern spatial-MUX is characterized with a spatially-diverse optical vector network analyzer. Insertion loss, mode-dependent losses, and time response are measured, showing significant mode mixing at a fiber splice.

OCIS codes: 060.4230 Multiplexing, 120.3180 Interferometry, 060.4510 Optical communications.

1. Introduction

Space division multiplexing (SDM) using fibers with multiple cores and/or supporting multiple modes has enabled increasing the capacity of optical communication networks beyond that of conventional single mode fibers [1,2]. Few-mode fibers (FMFs) supporting multiple spatial modes allow transmission of a number of channels on an orthogonal combination of modes of the FMF, at the cost of requiring multiple-input multiple-output (MIMO) equalization to remove the mode mixing and scrambling occurring in the fiber and during mode (de-)multiplexing [2–4]. Multi-core fibers (MCFs) reduce the footprint and increase capacity at the cost of introducing inter-core crosstalk [1].

Spatial multiplexers (SMUX) are an essential component in SDM systems and their properties directly impact system performance. For the MIMO equalizer to recover the original signals despite significant mode-mixing and resulting signal scrambling across modes in FMFs, mode-dependent loss (MDL) must be small [3]. Furthermore, mode scrambling at the transmitter improves tolerance to MDL and system capacity is maximized if all modes supported by the fiber are used to transmit information [3]. Thus, an SMUX should have low insertion loss (IL) to preserve optical power and low MDL to maintain MIMO processing capability, and should excite all the available orthogonal modes.

In this paper, a 36-core few-mode spatial multiplexer SMUX similar to [5], consisting of 36 photonic lanterns supporting three modes each, is characterized by measuring the full impulse response of all 36 photonic lanterns pertaining to the 36 different cores using a spatially-diverse optical vector network analyzer (SDM-OVNA). The measurement is performed in a reflective manner, with the SMUX coupled to 2.9 m of a 36-core 3-mode MCF, including one splice and cleaved at the fiber end. IL and MDL for each photonic lantern are calculated and their impulse response is analyzed. The MCF cores were designed with high differential mode delay (DMD) [2] and as a result allows identification of the different mode groups within the time domain response, showing significant coupling between mode groups at the 3-mode MCF splice.

2. Spatially-Diverse Optical Vector Network Analyzer

Swept-wavelength interferometry allows measurement of the complex transfer function $H(\omega)$ of an optical device under test (DUT) [6]. To measure the full complex matrix of a multiport SDM component, the scheme is extended to an SDM-OVNA by introducing different delays to separate the transfer matrix components of different spatial paths [4,7]. The SDM-OVNA setup, shown in Fig. 1, measures the full 6×6 transfer matrix of one of the photonic lanterns in the 36-core few-mode SMUX and consisted of a continuously swept laser, followed by an interferometer where one arm serves as a reference while the other arm includes the DUT. To simultaneously measure the impulse response of the DUT in both polarizations and on all three spatial modes of the photonic lantern, first the swept signal is split and one arm delayed before combining them with orthogonal polarizations; second, the resulting signal was split and different delays induced before applying the signal to the input ports of the DUT. As the measurement was performed in a

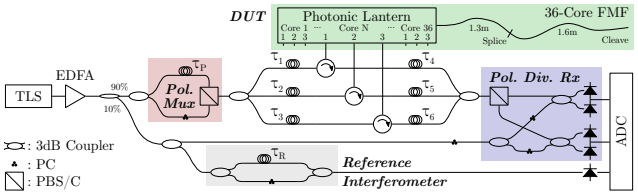

Fig. 1. Spatially-diverse optical vector network analyzer setup for characterization of the 36-core three-mode photonic lantern; TLS: continuously swept tunable laser, EDFA: erbium doped fiber amplifier, PC: polarization controller, PBS/C: polarization beam splitter/combiner, ADC: analog to digital conversion.

reflective manner, optical circulators were used to separate the reflected light and another set of delays was applied before combining the reflections into a single fiber. The resulting signal, together with the output of the reference arm, was detected by a polarization diversity receiver and the interference fringes stored on a digital sampling oscilloscope. An additional reference interferometer allowed compensation of sweep frequency non-linearity [4, 6].

The inclusion of the delay τ_P between the two input polarizations and the delays τ_1 to τ_6 before and after the DUT ensures the components $h_{ij}(t)$ of the time-domain transfer matrix appear well separated in the inverse Fourier transform $h(t)$ of the received interferogram and can be extracted by simple temporal windowing. The Fourier transform of each $h_{ij}(t)$ yields $H_{ij}(\omega)$ and thus allows reconstruction of $H(\omega)$. Finally, IL and MDL can be calculated from the singular values of $H(\omega)$.

3. Characterization of 36-Core Few-Mode Photonic Lantern

The measurement of the 36 photonic lanterns of the SMUX yields a 6×6 time domain impulse response for each core as shown in Fig. 2(a). Each 2×2 sub-matrix corresponds to the four possible polarization paths between an input-output pair and summation over the latter gives a 3×3 matrix as shown in Figs. 2(c) and (d). In the latter, significantly different behavior is observed, with either five or three temporal peaks visible in each $h_{ij}(t)$. Similar behavior was found for cores located in opposite halves of the fiber as indicated on the camera image of the cleaved fiber facet in Fig. 2(b), with cores in the upper-right half predominantly showing all five peaks present, while cores in the lower-left show only three peaks; cores between the highlighted regions, including the central core, show five peaks for some input-output combinations while for others only three peaks are present. In both cases, the presence of multiple peaks suggests the photonic lantern excites both mode groups, although with different efficiency, resulting in varying peak amplitudes.

The fiber attached to the SMUX supports two mode groups with two modes in the LP_{01} group and four modes in the LP_{11} group [2] and by design has high DMD on the order of 7 ps/m. Assuming negligible DMD within each mode group and taking the mode-mixing occurring at discrete points (i.e. the photonic lantern, the splice and the fiber facet) to be dominant over mode-mixing along the fiber—as is evident by the presence of well separated peaks—the possible mode-mixing paths are as shown in Fig. 2(e); the lower half of the tree is symmetric to the upper, with the resulting $\Sigma\Delta\tau$ reduced by $\Delta\tau_1$. With a DMD of 7 ps/m and fiber lengths of approximately 1.3 m and 1.6 m before and after the splice, this yields a total of nine different expected relative delays as shown below the curves in Fig. 2(f), forming five distinct delay groups with uniform spacing.

The outer peaks in the impulse response correspond to the case where a mode excited by the photonic lantern undergoes no mode mixing and thus their delays allow direct estimation of the DMD of the fiber, with DMDs between 6.5 ps/m and 7.5 ps/m found for the different cores, corresponding well with previous measurements [2]. The locations of the three inner peaks match the calculated delay groups, as is shown for two cores in Fig. 2(f). The different delays within each group are not resolved, due to insufficient measurement resolution resulting from laser phase noise. The presence of more than two peaks suggests significant mode-mixing to always be present at the splice, although with mixing characteristics differing between cores, resulting in different numbers of peaks; mode-mixing at the fiber facet cannot be further analyzed as the delays within each delay group are collapsed.

Finally, IL and MDL are calculated from the reconstructed transfer matrix, with IL normalized using a reference trace to exclude losses in the measurement system and the loss arising from the reflection at the cleaved facet. Fig. 3(a) shows IL averaged over the wavelength range of the sweep, finding a mean IL of 8.8 dB. The calculated wavelength-averaged MDL values range between 12.6 dB and 17.4 dB, with a mean of 14.9 dB as shown in Fig. 3(b).

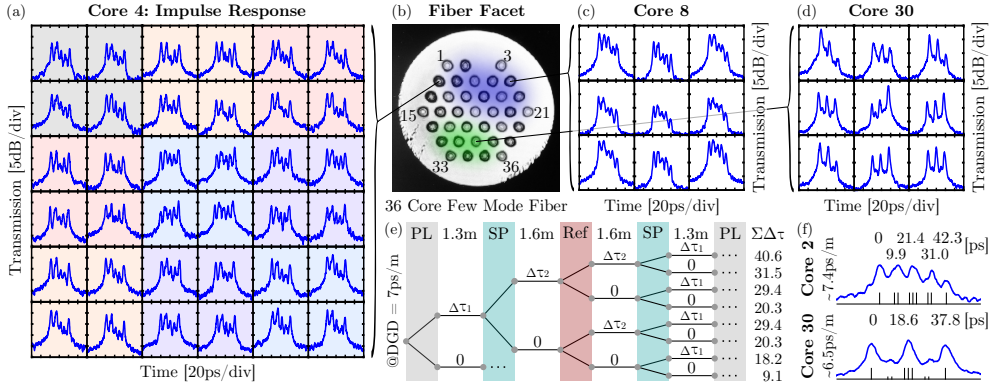

Fig. 2. Characterization results for 36-core few-mode photonic lantern. (a) Full 6×6 impulse response of the photonic lantern for core 4; (b) camera image of cleaved fiber facet, colored areas correspond to different behavior illustrated by: (c)-(d) reduced transfer matrices for cores 3 and 8. (e) Calculation of expected differential group delays between the two present mode groups; (f) example peak timings from cores 2 and 30.

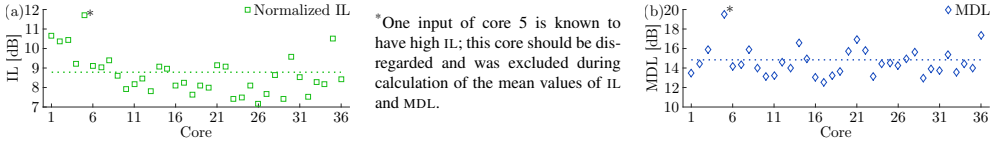

Fig. 3. Total system IL and MDL of all photonic lanterns, averaged from 1530 nm to 1570 nm.

4. Conclusions

A fiber-coupled 36-core photonic lantern few-mode SMUX was characterized using an SDM-OVNA by measuring the complete impulse response of all 36 photonic lanterns, analyzing them in time domain and calculating IL and MDL. Further, analysis of mode-mixing within 2.9 m few-mode multi-core fiber coupled to the SMUX was performed, finding significant and core-dependent mode mixing at a splice present in the fiber.

Acknowledgment This work was partly funded by the DFF FTP mmW-SPRAWL project.

References

[1] W. Klaus *et al.*, "Advanced space division multiplexing technologies for optical networks," J. Opt. Commun. Netw. **9**, C1–C11 (2017).

[2] J. Sakaguchi *et al.*, "Large spatial channel (36-core × 3 mode) heterogeneous few-mode multicore fiber," J. Lightw. Technol. **34**, 93–103 (2016).

[3] P. J. Winzer and G. J. Foschini, "MIMO capacities and outage probabilities in spatially multiplexed optical transport systems," Opt. Express **19**, 16,680–16,696 (2011).

[4] N. K. Fontaine *et al.*, "Characterization of space-division multiplexing systems using a swept-wavelength interferometer," in "Proc. OFC 2013," (2013), p. OW1K.2.

[5] P. Mitchell *et al.*, "57 channel (19x3) spatial multiplexer fabricated using direct laser inscription," in "Proc. OFC 2014," (2014), p. M3K.5.

[6] D. K. Gifford, B. J. Soller, M. S. Wolfe, and M. E. Froggatt, "Optical vector network analyzer for single-scan measurements of loss, group delay, and polarization mode dispersion," Appl. Opt. **44**, 7282–7286 (2005).

[7] G. VanWiggeren and D. Baney, "Swept-wavelength interferometric analysis of multiport components," IEEE Photon. Technol. Lett. **15**, 1267–1269 (2003).

PAPER20: Analysis of Few-Mode Multi-Core Fiber Splice Behavior Using an Optical Vector Network Analyzer

S. Rommel, J. M. Delgado Mendinueta, W. Klaus, J. Sakaguchi, J. J. Vegas Olmos, Y. Awaji, I. Tafur Monroy, and N. Wada. "Analysis of Few-Mode Multi-Core Fiber Splice Behavior Using an Optical Vector Network Analyzer". In: *43rd European Conference on Optical Communication*. Sept. 2017, paper W.3.B.5. *(inpress)*

Analysis of Few-Mode Multi-Core Fiber Splice Behavior Using an Optical Vector Network Analyzer

Simon Rommel[(1),(2),*], José Manuel Delgado Mendinueta[(1)], Werner Klaus[(1)], Jun Sakaguchi[(1)], Juan José Vegas Olmos[(3)], Yoshinari Awaji[(1)], Idelfonso Tafur Monroy[(2)] and Naoya Wada[(1)]

[(1)] Photonic Network System Laboratory, National Institute of Information and Communications Technology (NICT), 4-2-1 Nukui-Kitamachi, Koganei, Tokyo 184-8795, Japan, [*]simon.rommel@ieee.org
[(2)] Department of Photonics Engineering, Technical University of Denmark, 2800 Kgs. Lyngby, Denmark
[(3)] Mellanox Technologies, Ledreborg Allé 130B, 4000 Roskilde, Denmark

Abstract *The behavior of splices in a 3-mode 36-core fiber is analyzed using optical vector network analysis. Time-domain response analysis confirms splices may cause significant mode-mixing, while frequency-domain analysis shows splices may affect system level mode-dependent loss both positively and negatively.*

Introduction

The introduction of space division multiplexing (SDM) using fibers with multiple cores and/or supporting multiple modes has allowed the capacity of optical communication systems to overcome the limit of conventional single mode fibers of around 100 Tbit/s and reach capacities in the Pbit/s range[1,2]. Few-mode multi-core fibers (FM-MCF), combining the use of multiple cores and modes, have driven the number of spatial channels above 100[2], at the cost of requiring multiple-input multiple-output (MIMO) equalization to reverse the mode-mixing taking place at (de-)multiplexers, at fiber splice points[2–4] and along the fiber.

The performance of the MIMO equalization—and hence the achievable system capacity—is, among other impairments, limited by mode-dependent loss (MDL) in the system[3]. Fiber splices between FMFs (and in particular for FM-MCFs) not only introduce insertion loss (IL), but also mode mixing and potentially MDL[5,6]. While splices may severely degrade system performance due to their IL and additional MDL[5], their mode mixing behavior may potentially reduce overall system MDL[5], to the point where artificial introduction of splices was considered for reach increase in FMF transmission systems[6]. As a practical system will feature a splice every 1–2 km, careful characterization of such splices is required to successfully model SDM systems based on FMFs and FM-MCFs.

In this paper, we experimentally investigate the impact of splices in a 36-core 3-mode FM-MCF using a spatially-diverse optical vector network analyzer (SDM-OVNA). The measurement is performed in a reflective manner, using a 3D waveguide spatial multiplexer with 36 photonic lanterns coupling to the 36 MCF fiber cores of a short FM-MCF pigtail which is further spliced to pieces of FM-MCF. The splices are found to significantly alter the complex transfer function of the system, introducing additional IL ranging from 0.01 dB to 1.99 dB for the different cores, changing the wavelength averaged sytem MDL by –1.2 dB to 2.8 dB and significantly altering its wavelength dependent profile. The presented results help to improve the modeling of SDM transmission systems based on FM-MCF, by including the effects of FMF splices.

Splice Characterization Using a Spatially-Diverse Optical Vector Network Analyzer

The analysis of splices between FM-MCFs was performed with an SDM-OVNA based on swept-wavelength interferometry[7], allowing measurement of the full complex transfer function $H(\omega)$ of a multiport SDM system. The SDM-OVNA setup, shown in Fig. 1, uses a continuously swept tunable laser source (TLS), followed by an interferometer including the device under test (DUT) in one of its arms, to iteratively measure the full 6×6 transfer matrix for each of the 36 cores. The TLS signal was split and recombined in a polarization beam combiner to ensure polarization diversity and split onto the different ports of the DUT. The reflections from the cleaved end of the FM-MCF were separated by optical circulators, combined and together with the reference arm of the interferometer fed to a polarization diverse receiver; the resulting interference fringes were stored on a digital sampling oscilloscope. An additional reference interferometer allowed for compensation of sweep frequency non-linearities[4,7].

The fiber delays at the polarization multiplexer (τ_{P}) and before and after the ports of the DUT (τ_1 to τ_6) separate the M^2 different components $h_{ij}(t)$ of the time-domain transfer matrix in the

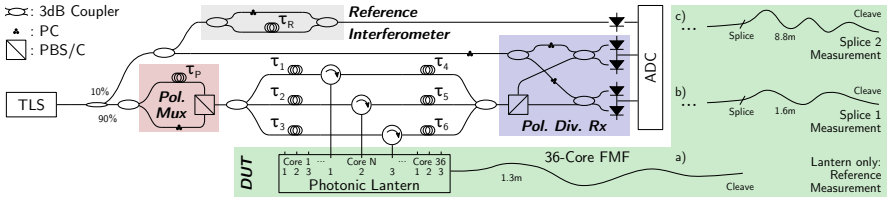

Fig. 1: SDM-OVNA setup and different measurement scenarios: a) photonic lantern and 1.3 m 3-mode MCF, b) photonic lantern and 1.3+1.6 m fiber with splice, c) photonic lantern and 1.3+8.8 m fiber with splice. TLS: continuously swept tunable laser, PC: polarization controller, PBS/C: polarization beam splitter/combiner, ADC: analog to digital converter.

inverse Fourier transform of the recorded interferograms, allowing easy extraction by temporal windowing. The separate Fourier transforms of the $h_{ij}(t)$ are the components $H_{ij}(\omega)$ of the $M \times M$ complex transfer function $H(\omega)$. Singular value decomposition of $H(\omega)$ gives the M singular values $\lambda_i(\omega)$ of the complex transfer function, from which IL and MDL are derived as: $IL(\omega) = \sum_{i=1}^{M} \lambda_i^2(\omega)/M$ and $MDL(\omega) = \max_{0<i\leq M}(\lambda_i^2(\omega))/\min_{0<i\leq M}(\lambda_i^2(\omega))$.

Two splices were introduced between the PL pigtail and two pieces of FM-MCF of 1.6 m and 8.8 m length respectively, to analyze the complex transfer function of the resulting reflective systems and to compare them to the transfer function of the pigtailed photonic lantern (PL). This comparison allows deriving characteristics of the splice, using the difference in wavelength-averaged IL and MDL as well as the ratio of the variance of MDL over wavelength as indicators of splice quality and impact.

Measured FM-MCF Splice Characteristics

Measurement of the system transfer characteristics gives a 6×6 time-domain response matrix for each core, from which by means of Fourier transformation and singular value decomposition the IL and MDL over wavelength can be derived as previously discussed. Two exemplary time-domain response matrices and corresponding IL and MDL are shown in Fig. 2. Detailed analysis of the time-domain responses allows drawing conclusions about mode coupling at different points along the system, including at the splice. Comparison of IL and MDL for the system in presence and absence of a splice allows determining splice quality and splice behavior.

Cores 6 and 33 of splice two were chosen for display in Fig. 2 a) and b) as they show significantly different behavior both in their time-domain response and their IL and MDL profiles. The time domain response of core 6 in Fig. 2 a) shows three clearly separated single peaks, where the approximately 145 ps separation between the outer peaks correspond to the accumulated differential mode delay (DMD) of passing through the 1.3+8.8 m of FM-MCF—which is known to have a DMD of around 7 ps/m[2]—in forward and backward direction. The presence of the central peak thus indicates strong mode-mixing to occur at the cleaved fiber end.

Core 33 on the opposite shows three groups of three closely spaced peaks, indicating that additional mode-coupling must take place. This is found to be mode coupling at the splice, causing peaks located close to the main peaks as the difference in accumulated DMD is equivalent to the DMD of a single pass through the 1.6 m FM-MCF between splice and PL, i.e. about 9.1 ps—which is in good correspondence with the observed peak spacing. While the shown cores represent the extremes, i.e. either practically zero mode-mixing or very strong mode mixing, the remaining cores show varying levels of mode mixing with no overall tendency to either extreme.

The behavior of cores 6 and 33 is further different in IL and MDL, as further shown in Fig. 2, with core 6 showing a nearly flat IL across wavelength and only small variations in MDL, while core 33 shows significant variations of MDL; the observed ringing, especially obvious on the IL of core 33, is due to the temporal windowing process. It should be noted that the presented IL and MDL values have been divided by two to account for the double-pass nature of the reflective measurement and thus represent the actual IL and MDL of the system.

Comparison of the IL and MDL between the system with and without the splice allows deriving the IL of the splice and its impact on MDL. To this end the differences in wavelength averaged IL are shown across a schematic plot of the fiber cross section on the left hand side of Fig. 3 for two different splices, where splice 1 is between the 1.3 m FM-MCF pigtail of the PL and a 1.6 m long piece of FM-MCF, while for the second splice the first splice is removed and a piece of 8.8 m of FM-MCF spliced to the pigtail.

Comparison of $\Delta\overline{IL}$ of the splices shows splice 2 to be of significantly better quality, with $<$0.5 dB IL, except for four isolated cores with IL up to 1.8 dB, potentially due to cleave imperfections,

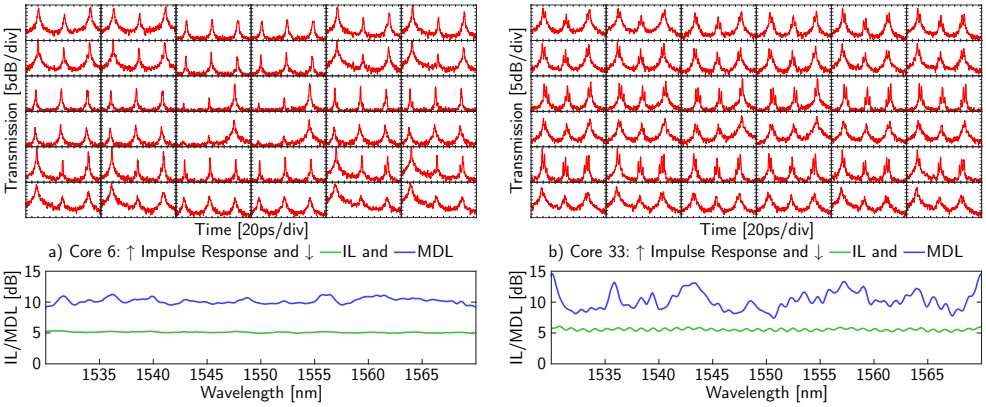

Fig. 2: Impulse responses and IL and MDL over wavelength for cores 6 and 33 for the system with PL and 1.3+8.8 m FM-MCF.

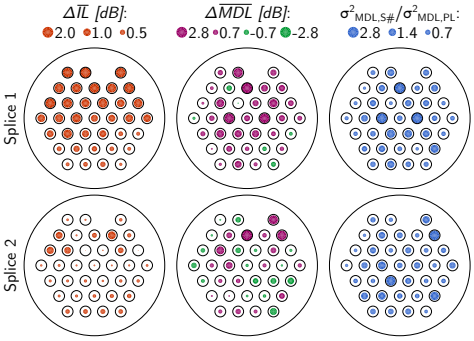

Fig. 3: Indicators for splice quality and impact for two splices of 36-core FM-MCF plotted over the fiber cross-section. $\Delta\overline{IL}$ and $\Delta\overline{MDL}$: difference in wavelength averaged IL and MDL, $\sigma^2_{\mathrm{MDL,S\#}}/\sigma^2_{\mathrm{MDL,PL}}$: ratio of MDL variance over wavelength between system with and without splice.

core displacements or micro-bubbles enclosed in the splice. Splice 1 on the other hand shows overall much higher IL with only the bottom right section of the fiber staying below 0.5 dB IL.

The middle and right parts of Fig. 3 show the difference in mean system MDL and the ratio between variances of MDL caused by the two splices respectively. While these confirm that both system MDL and its variance over wavelength can be reduced by a splice, for the majority of cores MDL increases, with an average increase of 0.8 dB across all cores in splice 1 and 0.2 dB in splice 2. The average impact on MDL variance however is found to be small, with average ratios of 1.0 for splice 1 and 0.9 for splice 2. It should be noted that a decrease in system MDL is connected to mode mixing in the splice and does not indicate gain in the splice.

Overall, these results confirm that splices in FMFs have significant impact on MDL behavior, especially in the case of FM-MCFs, where larger core offsets are unavoidable and thus differences in behavior across cores may be significant.

Conclusions

In this paper the behavior of splices between FM-MCFs has been investigated using optical vector analysis, analyzing splice impact both based on the system time-domain response and the changes in IL and MDL caused by the inclusion of a splice. The results show significant mode-mixing may occur at a splice and splices can significantly alter MDL behavior both positively and negatively. These results allow improved modeling of FM-MCF based SDM systems, by including the impact of fiber splices, and thus more accurately estimating system capacity.

Acknowledgements

This work was partly funded by the DFF FTP mmW-SPRAWL project.

References

[1] T. Mizuno, et al., "Dense space division multiplexed transmission over multicore and multimode fiber for long-haul transport systems," J. Lightw. Technol., Vol. **34**, no. 6, pp. 1484–1493 (2016).

[2] J. Sakaguchi, et al., "Large spatial channel (36-core × 3 mode) heterogeneous few-mode multicore fiber," J. Lightw. Technol., Vol. **34**, no. 1, pp. 93–103 (2016).

[3] P. J. Winzer and G. J. Foschini, "MIMO capacities and outage probabilities in spatially multiplexed optical transport systems," Opt. Express, Vol. **19**, no. 17, pp. 16680–16696 (2011).

[4] N. K. Fontaine, et al, "Characterization of space-division multiplexing systems using a swept-wavelength interferometer," Proc. OFC, OW1K.2, Anaheim (2013).

[5] S. Warm and K. Petermann, "Splice loss requirements in multi-mode fiber mode-division-multiplex transmission links," Opt. Express, Vol. **21**, no. 1, pp. 519–532 (2013).

[6] F. Ferreira, et al, "Reach improvement of mode division multiplexed systems using fiber splices," IEEE Photon. Technol. Lett., Vol. **25**, no. 12, pp. 1091–1094 (2013).

[7] D. K. Gifford, et al, "Optical vector network analyzer for single-scan measurements of loss, group delay, and polarization mode dispersion," Appl. Opt., Vol. **44**, no. 34, pp. 7282–7286 (2005).

PAPER21: Few-mode fiber, splice and SDM component characterization by spatially-diverse optical vector network analysis

S. Rommel, J. M. Delgado Mendinueta, W. Klaus, J. Sakaguchi, J. J. Vegas Olmos, Y. Awaji, I. Tafur Monroy, and N. Wada. "Few-mode fiber, splice and SDM component characterization by spatially-diverse optical vector network analysis". In: *Optics Express* 25.19 (Sept. 2017), pp. 22347–22361. DOI: 10.1364/OE.25.022347

Research Article | Vol. 25, No. 19 | 18 Sep 2017 | OPTICS EXPRESS 22347

Optics EXPRESS

Few-mode fiber, splice and SDM component characterization by spatially-diverse optical vector network analysis

SIMON ROMMEL,[1,2,*] JOSÉ MANUEL DELGADO MENDINUETA,[1] WERNER KLAUS,[1] JUN SAKAGUCHI,[1] JUAN JOSÉ VEGAS OLMOS,[3] YOSHINARI AWAJI,[1] IDELFONSO TAFUR MONROY,[2] AND NAOYA WADA[1]

[1]*Photonic Network System Laboratory, National Institute of Information and Communications Technology (NICT), 4-2-1 Nukui-Kitamachi, Koganei, Tokyo 184-8795, Japan*
[2]*Department of Photonics Engineering, Technical University of Denmark, 2800 Kgs. Lyngby, Denmark*
[3]*Mellanox Technologies, Ledreborg Allé 130B, 4000 Roskilde, Denmark*
[*]*sirem@fotonik.dtu.dk*

Abstract: This paper discusses spatially diverse optical vector network analysis for space division multiplexing (SDM) component and system characterization, which is becoming essential as SDM is widely considered to increase the capacity of optical communication systems. Characterization of a 108-channel photonic lantern spatial multiplexer, coupled to a 36-core 3-mode fiber, is experimentally demonstrated, extracting the full impulse response and complex transfer function matrices as well as insertion loss (IL) and mode-dependent loss (MDL) data. Moreover, the mode-mixing behavior of fiber splices in the few-mode multi-core fiber and their impact on system IL and MDL are analyzed, finding splices to cause significant mode-mixing and to be non-negligible in system capacity analysis.

OCIS codes: (120.3180) Interferometry; (060.4230) Multiplexing; (060.4510) Optical communications.

References and links

1. D. J. Richardson, J. M. Fini, and L. E. Nelson, "Space-division multiplexing in optical fibres," Nat. Photonics **7**, 354–362 (2013).
2. X. Liu, S. Chandrasekhar, X. Chen, P. Winzer, Y. Pan, B. Zhu, T. Taunay, M. Fishteyn, M. Yan, J. M. Fini, E. Monberg, and F. Dimarcello, "1.12-Tb/s 32-QAM-OFDM superchannel with 8.6-b/s/Hz intrachannel spectral efficiency and space-division multiplexing with 60-b/s/Hz aggregate spectral efficiency," in *Proceedings of the European Conference on Optical Communications* (OSA, 2011), Th.13.B.1.
3. S. Randel, R. Ryf, A. Gnauck, M. A. Mestre, C. Schmidt, R. Essiambre, P. Winzer, R. Delbue, P. Pupalaikis, A. Sureka, Y. Sun, X. Jiang, and R. Lingle, "Mode-multiplexed 620-GBd QPSK transmission over 1200-km DGD-compensated few-mode fiber," in *Proceedings of the Optical Fiber Communication Conference* (OSA, 2012), PDP5C.5.
4. T. Mizuno, H. Takara, K. Shibahara, A. Sano, and Y. Miyamoto, "Dense space division multiplexed transmission over multicore and multimode fiber for long-haul transport systems," J. Lightw. Technol. **34**, 1484–1493 (2016).
5. W. Klaus, B. J. Puttnam, R. S. Luís, J. Sakaguchi, J.-M. D. Mendinueta, Y. Awaji, and N. Wada, "Advanced space division multiplexing technologies for optical networks," J. Opt. Commun. Netw. **9**, C1–C11 (2017).
6. J. Sakaguchi, W. Klaus, J. M. Delgado Mendinueta, B. J. Puttnam, R. S. Luis, Y. Awaji, N. Wada, T. Hayashi, T. Nakanishi, T. Watanabe, Y. Kokubun, T. Takahata, and T. Kobayashi, "Large spatial channel (36-core 3 mode) heterogeneous few-mode multicore fiber," J. Lightw. Technol. **34**, 93–103 (2016).
7. P. J. Winzer and G. J. Foschini, "MIMO capacities and outage probabilities in spatially multiplexed optical transport systems," Opt. Express **19**, 16680–16696 (2011).
8. K.-P. Ho and J. M. Kahn, "Linear propagation effects in mode-division multiplexing systems," J. Lightw. Technol. **32**, 614–628 (2014).
9. T. Sakamoto, T. Matsui, K. Saitoh, S. Saitoh, K. Takenaga, T. Mizuno, Y. Abe, K. Shibahara, Y. Tobita, S. Matsuo, K. Aikawa, S. Aozasa, K. Nakajima, and Y. Miyamoto, "Low-loss and Low-DMD 6-mode 19-core fiber with cladding diameter of less than 250 μm," J. Lightw. Technol. **35**, 443–449 (2017).
10. T. Hayashi, T. Nagashima, K. Yonezawa, Y. Wakayama, D. Soma, K. Igarashi, T. Tsuritani, T. Taru, and T. Sasaki, "Six-mode 19-core fiber with 114 spatial modes for weakly-coupled mode-division-multiplexed transmission," J. Lightw. Technol. **35**, 748–754 (2017).

#297941 https://doi.org/10.1364/OE.25.022347
Journal © 2017 Received 15 Jun 2017; revised 28 Aug 2017; accepted 31 Aug 2017; published 6 Sep 2017

Optics EXPRESS

11. N. K. Fontaine, "Characterization of space-division multiplexing fibers using swept-wavelength interferometry," in *Proceedings of the Optical Fiber Communication Conference* (OSA, 2015), W4I.7.
12. E. Awwad, G. R.-B. Othman, and Y. Jaouën, "Space-time coding schemes for MDL-impaired mode-multiplexed fiber transmission systems," J. Lightw. Technol. **33**, 5084–5094 (2015).
13. C. Okonkwo, R. van Uden, H. Chen, H. de Waardt, and T. Koonen, "Advanced coding techniques for few mode transmission systems," Opt. Express **23**, 1411–1420 (2015).
14. N. K. Fontaine and R. Ryf, "Characterization of mode-dependent loss of laser inscribed photonic lanterns for space division multiplexing systems," in *Proceedings of the OptoElectronics and Communications Conference and Photonics in Switching* (IEICE, 2013), MR2–2.
15. J. M. Delgado Mendinueta, W. Klaus, J. Sakaguchi, Y. Awaji, and N. Wada, "Numerical investigation of equalization enhanced phase noise penalties for MQAM modulations in few-mode fiber transmission with time domain equalization," in *Proceedings of Photonic Networks and Devices* (OSA, 2017), NeTu2B.1.
16. S. Warm and K. Petermann, "Splice loss requirements in multi-mode fiber mode-division-multiplex transmission links," Opt. Express **21**, 519–532 (2013).
17. S. Rommel, J. M. Delgado Mendinueta, W. Klaus, J. Sakaguchi, J. J. Vegas Olmos, Y. Awaji, I. Tafur Monroy, and N. Wada, "Analysis of few-mode multi-core fiber splice behavior using an optical vector network analyzer," in *Proceedings of the European Conference on Optical Communications* (IEEE, 2017), W.3.B.5.
18. W. Klaus, S. Rommel, J. M. Delgado Mendinueta, J. Sakaguchi, P. Mitchell, N. Psaila, J. J. Vegas Olmos, I. Tafur Monroy, Y. Awaji, and N. Wada, "Numerical analysis of misalignment effects in few-mode multi-core fiber systems," in *Proceedings of the IEEE Photonics Conference* (IEEE, 2017), TuD2.3.
19. F. Ferreira, D. Fonseca, A. Lobato, B. Inan, and H. Silva, "Reach improvement of mode division multiplexed systems using fiber splices," IEEE Photonics Technol. Lett. **25**, 1091–1094 (2013).
20. G. VanWiggeren, A. Motamedi, and D. Baney, "Single-scan interferometric component analyzer," IEEE Photonics Technol. Lett. **15**, 263–265 (2003).
21. D. K. Gifford, B. J. Soller, M. S. Wolfe, and M. E. Froggatt, "Optical vector network analyzer for single-scan measurements of loss, group delay, and polarization mode dispersion," Appl. Opt. **44**, 7282–7286 (2005).
22. N. K. Fontaine, R. Ryf, M. A. Mestre, B. Guan, X. Palou, S. Randel, Y. Sun, L. Gruner-Nielsen, R. V. Jensen, and R. Lingle, "Characterization of space-division multiplexing systems using a swept-wavelength interferometer," in *Proceedings of the Optical Fiber Communication Conference* (OSA, 2013), OW1K.2.
23. J. Bohn, J. Carpenter, S. Gross, M. J. Withford, and J. Schröder, "Characterization of laser inscribed on-chip photonic lanterns with different core distances," in *Proceedings of the European Conference on Optical Communications* (IEEE, 2015).
24. S. Rommel, J. M. Delgado Mendinueta, W. Klaus, J. Sakaguchi, J. J. Vegas Olmos, Y. Awaji, I. Tafur Monroy, and N. Wada, "Impulse response of a 36-core few-mode photonic lantern hybrid spatial-multiplexer," in *Proceedings of Extremely Advanced Transmission Technologies* (IEICE, 2017), P–4.
25. S. Rommel, J. M. Delgado Mendinueta, W. Klaus, J. Sakaguchi, J. J. Vegas Olmos, Y. Awaji, I. Tafur Monroy, and N. Wada, "Characterization of a fiber-coupled 36-core 3-mode photonic lantern spatial multiplexer," in *Proceedings of Photonic Networks and Devices* (OSA, 2017), NeW3B.2.
26. B. J. Soller, D. K. Gifford, M. S. Wolfe, and M. E. Froggatt, "High resolution optical frequency domain reflectometry for characterization of components and assemblies," Opt. Express **13**, 666–674 (2005).
27. G. VanWiggeren and D. Baney, "Swept-wavelength interferometric analysis of multiport components," IEEE Photonics Technol. Lett. **15**, 1267–1269 (2003).
28. G. H. Golub and C. Reinsch, "Singular value decomposition and least squares solutions," Numer. Math. **14**, 403–420 (1970).
29. B. L. Heffner, "Accurate, automated measurement of differential group delay dispersion and principal state variation using Jones matrix eigenanalysis," IEEE Photonics Technol. Lett. **5**, 814–817 (1993).
30. R. Maruyama, N. Kuwaki, S. Matsuo, and M. Ohashi, "Relationship between mode coupling and fiber characteristics in few-mode fibers analyzed using impulse response measurements technique," J. Lightw. Technol. **35**, 650–657 (2017).
31. P. Mitchell, G. Brown, R. R. Thomson, N. Psaila, and A. Kar, "57 channel (19x3) spatial multiplexer fabricated using direct laser inscription," in *Proceedings of the Optical Fiber Communication Conference* (OSA, 2014), M3K.5.

1. Introduction

As fiber optic communication links rapidly approach the limit of conventional single mode fibers (SMF) of around 100 Tbit/s, space division multiplexing (SDM) has recently been introduced to increase the available transmission capacity [1–6]. Few-mode fibers (FMFS) supporting multiple spatial modes allow transmission of a number of channels on an orthogonal set of modes of the FMF, at the cost of requiring multiple-input multiple-output (MIMO) equalization to invert the mode-mixing that takes place at (de-)multiplexers, at fiber splice points and during propagation through the fiber [6–8]. Multi-core fibers (MCFS) reduce the footprint and increase capacity at the

Optics EXPRESS

cost of introducing inter-core crosstalk [5] and combined with mode-multiplexing form few-mode multi-core fibers (FM-MCF) which make spatial channel counts above 100 feasible [6, 9, 10].

An SDM system using single- or multi-core FMFs consists of a bank of transmitters, connected to a spatial multiplexer (SMUX), followed by an SDM fiber transmission span, a de-multiplexer and finally a bank of coherent receivers. The transmission span may be a simple fiber link, but may also include more complex subsystems such as switches, and amplifiers [11]. Additionally, a fusion splice every few km will be unavoidable in practical SDM systems. To model such systems and estimate their performance in terms of capacity, MIMO complexity and energy consumption, accurate knowledge of the characteristics such as insertion loss (IL), mode-dependent loss (MDL) and differential modal group delay (DMD), of the involved components is essential [7, 8].

For the MIMO equalizer to recover the original signals despite significant mode-mixing in FM-MCFS, mode-dependent loss (MDL) must be small, while mode scrambling at the transmitter improves tolerance to system MDL [7] without requiring additional coding which may also improve tolerance to MDL [12, 13]. System capacity is maximized if all modes supported by the fiber are used to transmit information [7, 14]. Thus, an SMUX should excite all the available orthogonal modes and should have low insertion loss (IL) to preserve optical power and low MDL to maintain MIMO processing performance by avoiding eigenmode signal-to-noise ratio (SNR) degradation. The fiber DMD determines the spread between signal components and thus sets a lower limit to MIMO equalizer complexity. It may further degrade system performance due to equalization enhanced phase noise [15]. Fusion splices within FMFS—and in particular FM-MCFS—not only introduce IL, but may also introduce significant amounts of mode-mixing and MDL [16–18]. While splices may severely degrade system performance due to their IL and additional MDL, their mode mixing behavior may potentially reduce overall system MDL, to the point where artificial introduction of splices has been considered for reach increase in FMF transmission systems [16, 19].

Optical vector network analysis, based on swept wavelength interferometry—where light from a wavelength swept source is sent through an interferometric structure containing the device under test (DUT) and as a result at the receiver creates interference fringes according to the device response—allows direct measurement of the impulse response and the complex transfer function of an optical device or system [20, 21]. More recently, spatially diverse optical vector network analyzer (SDM-OVNA) setups have been introduced, allowing measurement of the temporal and spectral response of FMFS [11, 22], as well as characterization of SDM system components [14, 23, 24]. The mode-mixing at fiber splices and their impact on system IL and MDL was investigated by the authors in [17, 25], based on analysis of the impulse response and comparison of measurements with different splices. A complete description of the SDM-OVNA setup and especially the required digital signal processing (DSP) is however not found in the literature.

In this article, the authors provide a comprehensive discussion of the operating principle of spatially diverse optical vector network analysis and the DSP required to extract the impulse response and complex transfer function matrices as well as the linear parameters (such as IL, MDL and DMD) of the device or system under test. The authors present extended characterization results for the characterization of a 3D waveguide photonic lantern SMUX for a 36-core 3-mode fiber, as well as for the behavior of fusion splices in FM-MCFS [17, 24, 25]. Full characterization of the photonic lantern SMUX is performed using a reflective SDM-OVNA setup, measuring its impulse response and complex transfer function matrices as well as IL and MDL for all cores. Using the SMUX as a basis, the mode-mixing behavior and impact on system IL and MDL is analyzed for different fusion splices and cleaves. Through the extended analysis, separating the impact of fiber splice and cleave, the accuracy of characterization is significantly improved and both are found to have significant impact on IL and MDL. These results confirm spatially diverse optical vector network analysis to be a potent tool for accurate characterization of SDM systems and

Optics EXPRESS

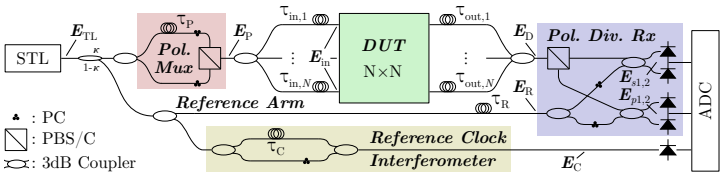

Fig. 1. General SDM-OVNA setup, including reference clock interferometer. STL: wavelength swept tunable laser, PC: polarization controller, PBS/C: polarization beam splitter/combiner, DUT: device under test, ADC: analog to digital converter.

components and by characterizing the impact of splices in FM-MCF allow improved modeling and capacity estimation of SDM systems with a large channel count.

The remainder of this article is organized as follows: section 2 discusses spatially diverse optical vector network analysis, providing a comprehensive discussion of the SDM-OVNA setup, the principle of operation and the required DSP for complete characterization of the device under test. Section 3 discusses the measurements performed and the results obtained, first characterizing the photonic lantern SMUX, then showing how fiber DMD and mode-mixing behavior at discrete mode-mixing points in the fiber can be derived from the measured impulse response and finally analyzing the impact of fiber splices and the cleaved fiber facet used in reflective OVNA measurements on system IL and MDL. Section 4 summarizes and concludes the article.

2. Spatially-diverse optical vector network analysis – principle of operation and digital signal processing

Swept wavelength interferometry allows measurement of the polarization resolved complex transfer function $\boldsymbol{H}(\omega)$ and impulse response $\boldsymbol{h}(t)$ of an optical device under test [20, 26]. To measure the full transfer function matrix of a multiport, space division multiplexing (SDM) system or component, the scheme may be extended to form a spatially diverse optical vector network analyzer (SDM-OVNA) [22, 25, 27]. This section presents the setup and principle of operation of an SDM-OVNA for the analysis of an SDM system or component with $N \times N$ ports in section 2.1 and discusses the digital signal processing (DSP) for measurement of the impulse response, complex transfer function and linear parameters (such as insertion loss (IL), mode-dependent loss (MDL), differential modal group delay (DMD) and mode coupling) of the system or component in section 2.2. Finally, section 2.3 presents a reflective SDM-OVNA setup allowing isolated characterization of single SDM devices or components.

2.1. Spatially-diverse optical vector network analysis setup

The basic setup for a spatially diverse OVNA for transmissive characterization of a device with $N \times N$ ports is shown in Fig. 1. It consists of a wavelength swept tunable laser (STL), followed by an interferometric structure with one arm containing the device under test (DUT) and the other arm serving as reference. While the setup in Fig. 1 is designed to measure the transmission characteristics of the DUT, the use of circulators at the input to the DUT allows measuring its reflective characteristics or, using the reflection from a cleaved fiber facet, to measure transmission characteristics in a reflective manner as discussed in section 2.3.

For polarization resolved measurement, a polarization multiplexing unit generates a signal of two orthogonal polarizations with a relative delay τ_p. The signal is split into N copies, to which differential delays $\tau_{\mathrm{in},1}$ to $\tau_{\mathrm{in},N}$ are applied before input to the DUT. Another set of differential delays $\tau_{\mathrm{out},1}$ to $\tau_{\mathrm{out},N}$ are applied to the output of the DUT before combining the N outputs, beating them with the signal from the reference arm on a polarization diverse receiver and

Optics EXPRESS

recording the resulting interference signals. An additional interferometer with delay τ_C generates a reference signal used to correct for deviations in sweep speed and convert the linear sweep in wavelength performed by the STL into a linear sweep in frequency as required for extraction of the DUT response.

Assuming the optical field $\boldsymbol{E}_{\mathrm{STL}}$ generated by the STL is

$$\boldsymbol{E}_{\mathrm{STL}} = A\,\mathrm{e}^{-j\omega(t)t}\,\boldsymbol{p}_{\mathrm{STL}}, \tag{1}$$

where $\boldsymbol{p}_{\mathrm{STL}}$ is a unit vector representing input polarization orientation, A is the complex field amplitude and $\omega(t) = 2\pi c/\left(\lambda_0 + v_{\mathrm{sweep}}t\right)$ is the angular optical frequency resulting from a linear sweep of laser wavelength, starting at λ_0 and with speed v_{sweep}; c being the speed of light in vacuum. The signal after the polarization multiplexer may then be expressed as

$$\boldsymbol{E}_{\mathrm{P}} = \sqrt{\frac{\kappa}{2}}A\,\mathrm{e}^{-j\omega(t)t}\left[\boldsymbol{R}_{\mathrm{P},s}\,\boldsymbol{p}_{\mathrm{STL}} + \mathrm{e}^{j\omega(t)\tau_{\mathrm{P}}}\,\boldsymbol{R}_{\mathrm{P},p}\,\boldsymbol{p}_{\mathrm{STL}}\right], \tag{2}$$

where $\boldsymbol{R}_{\mathrm{P},s}$ and $\boldsymbol{R}_{\mathrm{P},p}$ are 2×2 polarization rotation matrices, that align $\boldsymbol{E}_{\mathrm{STL}}$ to the polarization axes of the polarization beam combiner (PBC) and the factor $\sqrt{\kappa/2}$ results from the two splitters. Without loss of generality and to simplify notation in the following, we assume the polarization axes of the PBC to be the standard basis, simplifying Eq. (2) to

$$\boldsymbol{E}_{\mathrm{P}} = \sqrt{\frac{\kappa}{2}}A\,\mathrm{e}^{-j\omega(t)t}\left[\begin{pmatrix}1\\0\end{pmatrix} + \mathrm{e}^{j\omega(t)\tau_{\mathrm{P}}}\begin{pmatrix}0\\1\end{pmatrix}\right] = \sqrt{\frac{\kappa}{2}}A\begin{pmatrix}\mathrm{e}^{-j\omega(t)t}\\ \mathrm{e}^{-j\omega(t)(t-\tau_{\mathrm{P}})}\end{pmatrix} = \sqrt{\frac{\kappa}{2}}A\boldsymbol{E}_{2\mathrm{P}}. \tag{3}$$

The N copies of the polarization multiplexed signal at the input to the DUT may then be expressed in a combined notation as the product of a $2N\times 1$ vector $\boldsymbol{E}_{2\mathrm{NP}}$ with elements $(\boldsymbol{E}_{2\mathrm{P}}^T,\ldots,\boldsymbol{E}_{2\mathrm{P}}^T)^T$, a $2N\times 2N$ block diagonal matrix $\boldsymbol{R}_{\mathrm{in}}$ consisting of a set of complex, unitary, independent 2×2 polarization rotation matrices $\boldsymbol{R}_{\mathrm{in},1}$ to $\boldsymbol{R}_{\mathrm{in},N}$ (as highlighted in Eq. (4)) and a $2N\times 2N$ diagonal matrix $\boldsymbol{D}_{\mathrm{in}}$ with the delays $d_{\mathrm{in},i} = \mathrm{e}^{j\omega(t)\tau_{\mathrm{in},i}}$:

$$\boldsymbol{E}_{\mathrm{in}} = \sqrt{\frac{\kappa}{2N}}A\begin{bmatrix}\boldsymbol{R}_{\mathrm{in},1} & & 0\\ & \ddots & \\ 0 & & \boldsymbol{R}_{\mathrm{in},N}\end{bmatrix}\begin{bmatrix}d_{\mathrm{in},1} & 0 & & & 0\\ 0 & d_{\mathrm{in},1} & & & \\ & & \ddots & & \\ & & & d_{\mathrm{in},N} & 0\\ 0 & & & 0 & d_{\mathrm{in},N}\end{bmatrix}\begin{pmatrix}\mathrm{e}^{-j\omega(t)t}\\ \mathrm{e}^{-j\omega(t)(t-\tau_{\mathrm{P}})}\\ \vdots\\ \mathrm{e}^{-j\omega(t)t}\\ \mathrm{e}^{-j\omega(t)(t-\tau_{\mathrm{P}})}\end{pmatrix}$$

$$= \sqrt{\frac{\kappa}{2N}}A\boldsymbol{R}_{\mathrm{in}}\boldsymbol{D}_{\mathrm{in}}\boldsymbol{E}_{2\mathrm{NP}}. \tag{4}$$

E_{in} thus effectively contains $2N$ scaled and shifted copies of the original swept optical signal and the N pairs with differential delay τ_{P} are applied to the N inputs of the DUT. Expressing the $(2N)^2$ complex transfer functions $H_{k,l}(\omega)$ (with $k,l\in[1,2N]$) relating the polarizations of each of the N input ports to the polarizations of each of the N output ports of the DUT in a $2N\times 2N$ matrix $\boldsymbol{H}(\omega)$, allows writing the output signal of the upper arm of the main interferometer as

$$\boldsymbol{E}_{\mathrm{D}} = \frac{\sqrt{\kappa}}{\sqrt{2N}}A\sum_{2\times 1}\boldsymbol{D}_{\mathrm{out}}\boldsymbol{R}_{\mathrm{out}}\boldsymbol{H}(\omega)\boldsymbol{R}_{\mathrm{in}}\boldsymbol{D}_{\mathrm{in}}\boldsymbol{E}_{2\mathrm{NP}}, \tag{5}$$

where $\boldsymbol{D}_{\mathrm{out}}$ and $\boldsymbol{R}_{\mathrm{out}}$ are the delays and polarization rotations after the different outputs of the DUT, defined in the same way as $\boldsymbol{D}_{\mathrm{in}}$ and $\boldsymbol{R}_{\mathrm{in}}$ in Eq. (4). Further, $\sum_{2\times 1}$ is a summation over pairs of rows of the $2N\times 1$ vector resulting from the matrix multiplication in Eq. (5), such that

$$\boldsymbol{E}_{\mathrm{D}} = \frac{\sqrt{\kappa}}{\sqrt{2N}}A\begin{pmatrix}\sum_{k,l=1}^{N}\left[\hat{H}_{2k-1,2l-1}\,\mathrm{e}^{-j\omega(t)(t-\tau_{\mathrm{out},k}-\tau_{\mathrm{in},l})} + \hat{H}_{2k-1,2l}\,\mathrm{e}^{-j\omega(t)(t-\tau_{\mathrm{out},k}-\tau_{\mathrm{in},l}-\tau_{\mathrm{P}})}\right]\\ \sum_{k,l=1}^{N}\left[\hat{H}_{2k,2l-1}\,\mathrm{e}^{-j\omega(t)(t-\tau_{\mathrm{out},k}-\tau_{\mathrm{in},l})} + \hat{H}_{2k,2l}\,\mathrm{e}^{-j\omega(t)(t-\tau_{\mathrm{out},k}-\tau_{\mathrm{in},l}-\tau_{\mathrm{P}})}\right]\end{pmatrix}, \tag{6}$$

Optics EXPRESS

where the unitary polarization rotations $\boldsymbol{R}_{\text{in}}$ and $\boldsymbol{R}_{\text{out}}$ have been combined with $\boldsymbol{H}(\omega)$ into $\hat{\boldsymbol{H}}(\omega) = \boldsymbol{R}_{\text{out}}\boldsymbol{H}(\omega)\boldsymbol{R}_{\text{in}}$ with the $(2N)^2$ complex elements $\hat{H}_{k,l}(\omega)$, where $k, l \in [1, 2N]$.

The signal in the reference arm undergoes delay τ_{R} and at the input of the polarization diverse receiver is

$$\boldsymbol{E}_{\text{R}} = \sqrt{\frac{1-\kappa}{2}} A\, \mathrm{e}^{-j\omega(t)(t-\tau_{\text{R}})}\, \boldsymbol{R}_{\text{R}}\boldsymbol{p}_{\text{STL}}, \tag{7}$$

where $\boldsymbol{R}_{\text{R}}$ represents a random polarization rotation along the fiber.

Splitting $\boldsymbol{E}_{\text{D}}$ from Eq. (6) into orthogonal polarizations represented by unit vectors $\boldsymbol{s}$ and $\boldsymbol{p}$ using a polarization beam splitter (PBS) as

$$\boldsymbol{E}_{\text{D},s} = (\boldsymbol{E}_{\text{D}} \cdot \boldsymbol{s})\, \boldsymbol{s} \qquad \text{and} \qquad \boldsymbol{E}_{\text{D},p} = (\boldsymbol{E}_{\text{D}} \cdot \boldsymbol{p})\, \boldsymbol{p} \tag{8}$$

and combining each with a polarization-aligned half of the reference signal $\boldsymbol{E}_{\text{R}}$ gives the incident fields on the two balanced photodetectors:

$$\boldsymbol{E}_{s1,2} = \frac{1}{\sqrt{2}}\boldsymbol{E}_{\text{D},s} + \frac{1}{2}\boldsymbol{E}_{\text{R}}\boldsymbol{R}_{\text{R},s} = \frac{1}{2}\left[\sqrt{2}\boldsymbol{E}_{\text{D}} \cdot \boldsymbol{s} + \sqrt{\frac{1-\kappa}{2}} A\, \mathrm{e}^{-j\omega(t)(t-\tau_{\text{R}})}\right]\boldsymbol{s} \tag{9}$$

$$\boldsymbol{E}_{p1,2} = \frac{1}{\sqrt{2}}\boldsymbol{E}_{\text{D},p} + \frac{1}{2}\boldsymbol{E}_{\text{R}}\boldsymbol{R}_{\text{R},p} = \frac{1}{2}\left[\sqrt{2}\boldsymbol{E}_{\text{D}} \cdot \boldsymbol{p} + \sqrt{\frac{1-\kappa}{2}} A\, \mathrm{e}^{-j\omega(t)(t-\tau_{\text{R}})}\right]\boldsymbol{p}, \tag{10}$$

where $\boldsymbol{R}_{\text{R},s}$ and $\boldsymbol{R}_{\text{R},p}$ align the polarization of the reference to the polarizations $\boldsymbol{s}$ and $\boldsymbol{p}$.

Assuming square law detectors with a photocurrent proportional to the incident field according to $i(\omega) = \mathcal{R}\,|\boldsymbol{E}|^2$, where $\mathcal{R}$ is the responsivity of the photodetector, the difference currents produced by the balanced photodetectors are easily seen to be sums of the transfer function elements $\hat{H}_{k,l}$ with different delays

$$i_s = \mathcal{R}\,|A|^2 \frac{\sqrt{\kappa}}{N}\frac{\sqrt{1-\kappa}}{\sqrt{2}} \sum_{k,l=1}^{N} \mathrm{Re}\Big[\left(s_1\hat{H}_{2k-1,2l-1} + s_2\hat{H}_{2k,2l-1}\right) \mathrm{e}^{-j\omega(t)(\tau_{\text{R}}-\tau_{\text{out},k}-\tau_{\text{in},l})} + \left(s_1\hat{H}_{2k-1,2l} + s_2\hat{H}_{2k,2l}\right) \mathrm{e}^{-j\omega(t)(\tau_{\text{R}}-\tau_{\text{out},k}-\tau_{\text{in},l}-\tau_{\text{P}})}\Big] \tag{11}$$

$$i_p = \mathcal{R}\,|A|^2 \frac{\sqrt{\kappa}}{N}\frac{\sqrt{1-\kappa}}{\sqrt{2}} \sum_{k,l=1}^{N} \mathrm{Re}\Big[\left(p_1\hat{H}_{2k-1,2l-1} + p_2\hat{H}_{2k,2l-1}\right) \mathrm{e}^{-j\omega(t)(\tau_{\text{R}}-\tau_{\text{out},k}-\tau_{\text{in},l})} + \left(p_1\hat{H}_{2k-1,2l} + p_2\hat{H}_{2k,2l}\right) \mathrm{e}^{-j\omega(t)(\tau_{\text{R}}-\tau_{\text{out},k}-\tau_{\text{in},l}-\tau_{\text{P}})}\Big]. \tag{12}$$

where s_i and p_i denote the components of $\boldsymbol{s}$ and $\boldsymbol{p}$ and stem from the inner product in Eq. (8).As the STL wavelength is swept, the different delays result in different wavelength offsets and thus the elements of the sums in Eqs. (11) and (12) appear at different frequencies in the spectra of i_s and i_p, allowing their extraction as discussed in the following section and thus allowing full characterization of the linear properties of the DUT.

2.2. Extraction of the device transfer function and linear parameters

The extraction of the complex time- and frequency domain transfer function matrices $\boldsymbol{h}(t)$ and $\boldsymbol{H}(\omega)$ from the recorded interferograms of Eqs. (11) and (12) requires a number of DSP steps as shown in Fig. 2 and discussed in sections 2.2.1 and 2.2.2. Further analysis of the transfer function matrix $\boldsymbol{H}(\omega)$ allows the extraction of a number of important linear parameters of the DUT, including insertion loss (IL), mode-dependent loss (MDL), differential modal group delay (DMD) and mode coupling [8, 21] and is discussed in section 2.2.3.

Optics EXPRESS

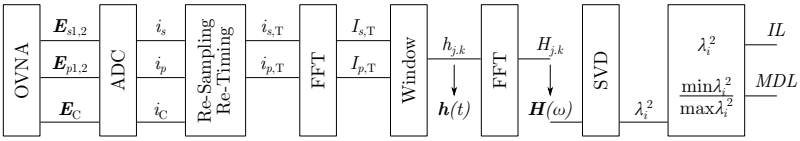

Fig. 2. Diagram of the signal processing flow for optical vector network analysis.

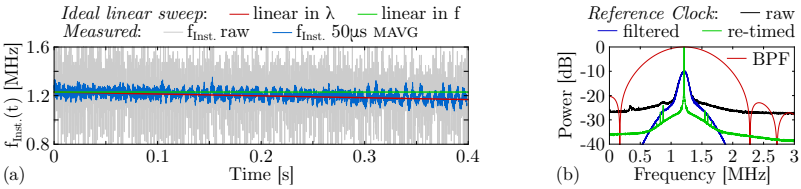

Fig. 3. Correction for sweep speed deviations and conversion from linear sweep in wavelength to linear sweep in frequency: (a) instantaneous frequency of the reference clock signal (MAVG: moving average), (b) normalized spectra of the reference clock signal before and after re-sampling and re-timing.

2.2.1. Linearization of the sweep

Prior to the extraction of the desired transfer function matrix elements from the interferograms of Eqs. (11) and (12), it is essential to correct for any deviations in the sweep speed during the linear wavelength sweep of the STL and to convert the latter into a linear sweep in frequency. The inclusion of the reference clock interferometer in the OVNA setup in Fig. 1 gives an additional signal

$$E_C = \sqrt{\frac{1-\kappa}{2}} A \left[e^{-j\omega(t)t} + e^{-j\omega(t)(t-\tau_C)} \right] \tag{13}$$

$$i_C = \mathcal{R} |A|^2 \, \mathrm{Re}\left[e^{-j\omega(t)\tau_C} \right], \tag{14}$$

where polarization alignment between the interferometer arms is assumed and polarization has thus been dropped in Eq. (13). This signal may be employed either as a clock signal for the analog to digital converter (ADC) [26], or as a reference signal to achieve linearization of the sweep in DSP, as discussed in this work.

A linear sweep in frequency would result in i_C containing only a single frequency, as the difference in fiber length between the two interferometer arms, and thus also the delay τ_C, is constant and known. In the experimentally acquired signal i_C, on the other hand, the sweep is linear in wavelength and the sweep speed is non-constant due to device limitations of the STL. Figure 3(a) shows the measured instantaneous frequency for a sweep across the optical C-band (1530 nm to 1570 nm) with a sweep speed of 100 nm/s and a path difference between the arms of the reference clock interferometer of 20 m. The obtained clock signal varies strongly in short time intervals, but with a moving average filter over 50 µs, falls within ±10 % of the calculated frequency resulting from an ideal linear sweep in wavelength.

Both the variation due to device imperfections and the frequency slope resulting from linear sweeping in wavelength may be corrected by upsampling the clock signal, selecting sampling points at given positions within each cycle—e.g., at all zero crossings—and subsequent re-timing of the selected samples to a constant sampling speed. Additionally filtering the clock signal around the desired frequency peak before re-sampling and re-timing improves the resulting

Optics EXPRESS

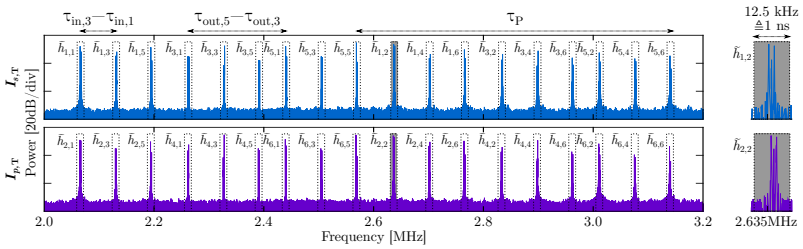

Fig. 4. Illustration of the windowing process, extracting the 36 elements $\tilde{h}_{k,l}(t)$ of the impulse response of a 3-mode DUT from the DFTs of the interferograms i_s and i_p.

signal. Figure 3(b) shows the normalized spectra of the reference clock signal before and after re-timing along with the applied filter. While in the spectrum of the raw signal the peak is spread into a wider peak due to the deviations from sweep speed, re-timing achieves a very narrow peak and thus good linearization of the sweep. Selecting samples of the interferograms of Eqs. (11) and (12) at the sampling points found from the reference clock signal and applying the same re-timing linearizes the underlying sweep and thus allows distortion-free extraction of the transfer function matrix elements.

2.2.2. Extraction of the device time and frequency response function matrices

Extraction of the complex time- and frequency domain transfer function matrices from the recorded interferograms is relatively straightforward, since, after linearization of the sweep, each delay results in a single, known frequency. Extracting the components of the sums at the different delays and combining them into 2×2 sub-matrices for each $\{k, l\}$ as

$$\begin{bmatrix} s_1\hat{H}_{2k-1,2l-1} + s_2\hat{H}_{2k,2l-1} & s_1\hat{H}_{2k-1,2l} + s_2\hat{H}_{2k,2l} \\ p_1\hat{H}_{2k-1,2l-1} + p_2\hat{H}_{2k,2l-1} & p_1\hat{H}_{2k-1,2l} + p_2\hat{H}_{2k,2l} \end{bmatrix} = \begin{bmatrix} s_1 & s_2 \\ p_1 & p_2 \end{bmatrix} \begin{bmatrix} \hat{H}_{2k-1,2l-1} & \hat{H}_{2k-1,2l} \\ \hat{H}_{2k,2l-1} & \hat{H}_{2k,2l} \end{bmatrix}$$
$$= \boldsymbol{R}_{s,p} \begin{bmatrix} \hat{H}_{2k-1,2l-1} & \hat{H}_{2k-1,2l} \\ \hat{H}_{2k,2l-1} & \hat{H}_{2k,2l} \end{bmatrix} = \begin{bmatrix} \tilde{H}_{2k-1,2l-1} & \tilde{H}_{2k-1,2l} \\ \tilde{H}_{2k,2l-1} & \tilde{H}_{2k,2l} \end{bmatrix}, \quad (15)$$

shows that the PBS and subsequent polarization-diverse detection may be regarded as another polarization rotation on top of those in Eqs. (4) and (5); as $\boldsymbol{s}$ and $\boldsymbol{p}$ are orthogonal unitary vectors, their elements s_1, s_2, p_1 and p_2 together form a unitary basis and thus the matrix $\boldsymbol{R}_{s,p}$ is a unitary matrix. To simplify discussion, this polarization rotation has further been combined with $\hat{\boldsymbol{H}}(\omega)$ by defining a matrix $\boldsymbol{R}_{\mathrm{N}s,p}$, similar in structure to $\boldsymbol{R}_{\mathrm{in}}$ and $\boldsymbol{R}_{\mathrm{out}}$ in Eqs. (4) and (5), i.e., being block-diagonal with N copies of $\boldsymbol{R}_{s,p}$, and defining $\tilde{\boldsymbol{H}}(\omega) = \boldsymbol{R}_{\mathrm{N}s,p}\boldsymbol{R}_{\mathrm{out}}\boldsymbol{H}(\omega)\boldsymbol{R}_{\mathrm{in}}$ with elements $\tilde{H}_{k,l}(\omega)$. These $\tilde{H}_{k,l}(\omega)$ differ from the elements $H_{k,l}(\omega)$ of the transfer function matrix of the DUT only by a series of polarization rotations, which have no impact on the linear parameters extracted from the transfer function matrix as discussed in section 2.2.3.

While the desired elements $\tilde{H}_{k,l}(\omega)$ appear in the interferograms of Eqs. (11) and (12), they can not be easily extracted in a direct manner. After performing a discrete Fourier transform (DFT) however, the elements $\tilde{h}_{k,l}(t)$ of the time domain transfer function, i.e., the impulse responses, may be directly extracted by simple windowing—provided the delays $\tau_{\mathrm{in},l}$, $\tau_{\mathrm{out},k}$ and τ_{P} were carefully selected to ensure sufficient separation to prevent any overlap of the impulse responses. Fig. 4 shows the windowing to extract the 36 elements $\tilde{h}_{k,l}(t)$ of the impulse response matrix from the DFTs of the two re-timed interferograms i_s and i_p of a 3-mode DUT.

Finally, the $\tilde{H}_{k,l}(\omega)$ are easily obtained by taking separate inverse DFTs of the $\tilde{h}_{k,l}(t)$ and thus the full time and frequency domain transfer function matrices $\tilde{\boldsymbol{h}}(t)$ and $\tilde{\boldsymbol{H}}(\omega)$ may be

reconstructed and further analyzed to derive the DUT linear parameters.

2.2.3. Calculation of the linear device parameters

Of the linear parameters associated with any SDM component or system, IL and MDL are likely the most important for SDM communication systems employing coherent detection and MIMO equalization [8]. The former determines power budgets thus limits available reach and the latter directly limits system capacity [7, 8]. Given the transfer function matrix $\tilde{\boldsymbol{H}}(\omega)$, both IL and MDL may be determined via singular value analysis [8]. The singular value decomposition (SVD) [28] decomposes $\tilde{\boldsymbol{H}}(\omega)$ into two unitary matrices $\boldsymbol{U}(\omega)$ and $\boldsymbol{V}(\omega)$ and a diagonal matrix $\boldsymbol{\Sigma}$ as

$$\tilde{\boldsymbol{H}}(\omega) = \boldsymbol{U}(\omega)\boldsymbol{\Sigma}(\omega)\boldsymbol{V}^{*}(\omega), \tag{16}$$

where * denotes the conjugate transpose and the diagonal elements $\lambda_1(\omega)$ to $\lambda_{2N}(\omega)$ of $\boldsymbol{\Sigma}(\omega)$ are the $2N$ singular values of $\tilde{\boldsymbol{H}}(\omega)$. The columns of the unitary input and output matrices $\boldsymbol{V}(\omega)$ and $\boldsymbol{U}(\omega)$ are the input and output eigenvectors of the system and describe the $2N$-dimensional polarization rotation (also referred to as mode-mapping, -mixing or -scrambling in the literature) between the launched input modes and the eigenmodes of $\tilde{\boldsymbol{H}}(\omega)$, and the latter and the received output modes respectively. Note that the singular values $\lambda_i(\omega)$ are the gains or losses associated with each eigenmode and their squares are equal to the eigenvalues of the phase-conjugate round-trip propagation matrix $\tilde{\boldsymbol{H}}(\omega)\tilde{\boldsymbol{H}}^{*}(\omega)$ [8, 11].

As the singular values $\lambda_i(\omega)$ are the gains/losses associated with the optical field, they directly relate to the insertion loss (IL) and mode-dependent loss (MDL) of the DUT. Defining the latter two in terms of optical power, IL is the mean of the squares of the singular values $\lambda_i(\omega)$, while MDL is the ratio between the maximum and minimum $\lambda_i^2(\omega)$:

$$IL = \overline{\lambda_i^2(\omega)} \qquad MDL = \frac{\max \lambda_i^2(\omega)}{\min \lambda_i^2(\omega)}. \tag{17}$$

Taking the SVD at each angular frequency ω yields the $\lambda_i(\omega)$ across the wavelength range of the STL sweep and thus allows wavelength resolved calculation of IL and MDL.

It should be noted that, for any unitary matrix, i.e., a lossless polarization rotation, the singular values are equal to 1 and thus the singular values of $\tilde{\boldsymbol{H}}(\omega)$ are the same as those of $\boldsymbol{H}(\omega)$, despite the series of polarization rotations the latter undergoes to become the former. The linear parameters derived via the SVD of $\tilde{\boldsymbol{H}}(\omega)$ are thus equal to those of the DUT.

Differential modal group delay (DMD) may impact system performance, given the presence of phase noise [15], and influences signal processing complexity as the maximum spread in group delays determines the minimum length of the MIMO equalizer [8]. DMD may be derived from $\tilde{\boldsymbol{H}}(\omega)$ by means of principle state of polarization analysis [11, 21, 29] where the principle delays are approximated by the eigenvalues of $\tilde{\boldsymbol{H}}(\omega + \Delta\omega)\tilde{\boldsymbol{H}}^{-1}(\omega)$ or by directly analyzing the impulse responses $\tilde{h}_{k,l}(t)$ [22, 25, 30]. In the latter case, distinct peaks for different mode groups $\tilde{h}_{k,l}(t)$ will be observed and DMD may be derived from the ratio of their respective spacing and the fiber length. Such analysis further allows the location and characterization of discrete events affecting mode-distribution along a fiber, by analyzing peaks at intermediate time instances [25]. Analysis of the impulse response is demonstrated in detail in section 3.2.

Finally, mode coupling may also be seen from analysis of the $\tilde{h}_{k,l}(t)$, where distributed mode coupling along the fiber will appear as plateaus between the peaks of the respective modes and mode coupling at discrete points generate additional peaks in the temporal response [22, 25, 30].

2.3. Optical vector network analyzer setup for reflective measurements

To characterize a single space division multiplexing (SDM) component, e.g., an SMUX, a transmissive measurement as shown in Fig. 1 may not be possible and a reflective measurement setup is

Optics EXPRESS

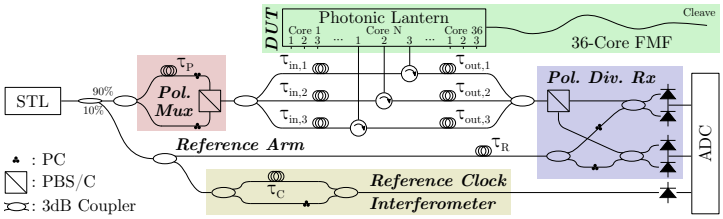

Fig. 5. SDM-OVNA setup for reflective measurement of the impulse response and transfer function of a 36-core 3-mode photonic lantern SMUX.

Table 1. Fiber configurations for the characterization of the photonic lantern and measurement of few-mode splice and cleaved fiber facet behavior.

Name	Pigtail	Splice	Fiber	Cleave	Angle
PL-CL0	0.3 m	–	–	CL0	0.7°
PL-SP1-CL1	1.3 m	SP1	8.8 m	CL1	0.4°
PL-SP2-CL1	0.3 m	SP2	8.8 m	CL1	0.4°
PL-SP2-CL2	0.3 m	SP2	8.7 m	CL2	0.9°

required. For such a measurement, the reflection from a cleaved fiber facet may be exploited, passing through the DUT a second time and being separated onto the output ports by circulators as shown in Fig. 5 for a 36-core 3-mode photonic lantern SMUX. For such a measurement, the measured response is the concatenation of the DUT, the fiber pigtail, the cleaved fiber facet (which for a good cleave is a weak mirror with a reflectivity of ca. 4 %), and again the fiber pigtail and DUT. While including the coupling to the fiber pigtail as part of the device response is usually desired, the effect of the reflection at the cleaved facet may be calibrated out of the measurement to allow measuring only the desired impulse response and complex transfer function of the fiber-coupled DUT.

3. Few-mode fiber, splice and component characterization

In this section we analyze a 3-mode multicore photonic lantern SMUX similar to that in [31], for with 36 cores. Based on the setup in Fig. 5, we show measurements results of system IL and MDL as well as fiber DMD and discuss the behavior of fusion splices in the 36-core FMF and that of the cleaved fiber facet itself. To this end a series of measurements was performed with different fiber configurations as shown in Table 1.

First, *PL-CL0* corresponds to measurement of the response of each of the photonic lanterns and serves as a base for comparison with the measurements with different splices and cleaves; the respective results are presented in section 3.1. *PL-SP1-CL1* additionally includes a fusion splice in the 36-core FMF and with different fiber lengths before and after the splice lends itself to analysis of the time-domain response; in section 3.2 the fiber DMD is calculated from the measured impulse responses and different degrees of mode-mixing are shown to be present at the splice for different cores. In *PL-SP2-CL1* the splice is replaced by another fusion splice, while maintaining the exact same configuration otherwise, including the cleave at which reflection takes place. This allows comparison of the system response with either splice to the base measurement and direct comparison of the system responses with the two splices; the respective results are discussed in section 3.3. Finally, *PL-SP2-CL2* introduces a different cleave to analyze the impact of cleave quality on the system response; this is discussed in section 3.4.

Optics EXPRESS

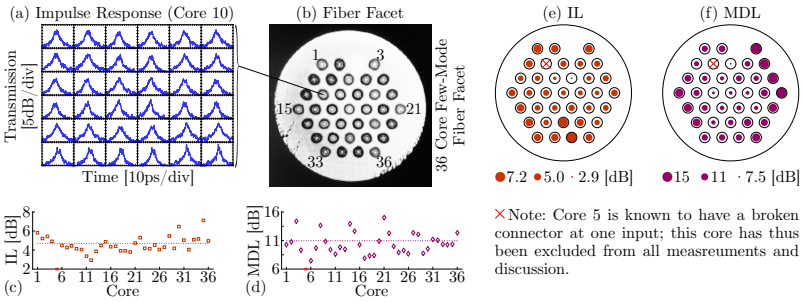

Fig. 6. Characteristics of the 36-core few-mode photonic lantern spatial multiplexer: (a) impulse response of core 10, (b) photograph of cleaved fiber facet with core numbering, (c) and (d) IL and MDL of all cores, (e) and (f) IL and MDL plotted across the fiber facet.

3.1. *Analysis of a 36-core 3-mode photonic lantern*

To characterize the 36-core photonic lantern SMUX, the full response for each of the 36 cores is measured separately, each yielding an impulse response matrix as shown in Fig. 6(a) for the exemplary case of core 10. While sufficient for the calculation of the complex transfer function and thus derivation of insertion and mode-dependent loss (IL and MDL), the impulse response hardly allows any differentiation of separate peaks due to the short fiber length of the pigtail, although it is significantly spread due to DMD.

Calculation of the complex transfer function and analysis of IL and MDL, as discussed in section 2.2, shows significant differences between cores for both IL and MDL as shown in Figs. 6(c) and 6(d), with the former ranging from 2.9 dB to 7.1 dB and the latter between 7.5 dB and 15.0 dB. It should be noted that the reported values are wavelength-averaged across the range of the optical C-band (1530 nm to 1570 nm) and that, in this and all of the following measurements of IL and MDL, the presented values have been corrected to account for the double-pass nature of the reflective measurement.

Analysis of the distribution of IL and MDL values of the fiber facet as shown in Figs. 6(e) and 6(f), shows the cores on the outer ring to have significantly higher IL and MDL as may be expected from increasing alignment error with increasing distance from the fiber center. Furthermore alignment between the photonic lantern chip and the output fiber pigtail seems to be optimum for cores slightly above and to the right of the center, rather than for the central cores, causing a generally increased misalignment.

3.2. *Few-mode fiber differential modal group delay*

Analysis of the impulse response matrix allows direct calculation of the DMD in the fiber, and in the presence of discrete mode-mixing points along the fiber, e.g., from fusion splices or the cleaved facet, further allows analysis of mode-mixing behavior at these points. Analyzing the impulse responses of measurement *PL-SP1-CL1*, which includes the SMUX, a 36-core FMF pigtail of 1.3 m length, a fusion splice and another 8.8 m of fiber, a number of well separated peaks can be seen in the impulse response matrices shown in Figs. 7(a)–7(c). In order to calculate the fiber DMD, the original of these peaks needs to be identified and once peaks corresponding to the mode-groups of interest have been selected, the DMD simply is the observed temporal spacing divided by the propagation distance in the fiber.

In the presence of discrete mode-mixing events, such as the fusion splice and cleave, additional peaks may arise due to different combinations of accumulated DMD before and after each mixing

Optics EXPRESS

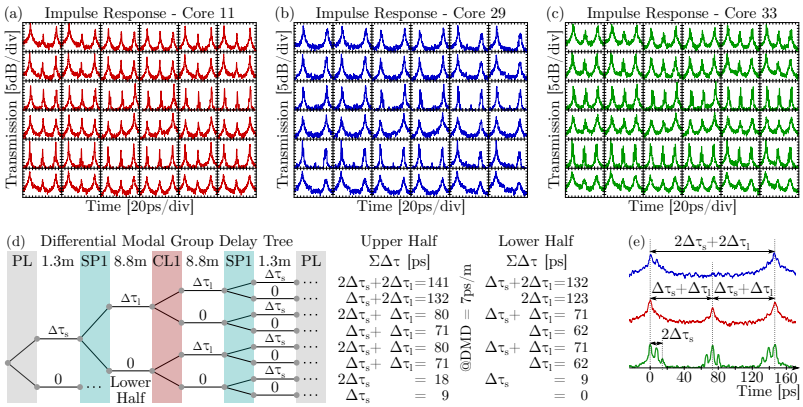

Fig. 7. Time domain analysis of the impulse responses from measurement *PL-SP1-CL1*. (a)–(c) Impulse response matrices of selected cores, showing different mode mixing behavior at the fusion splice and the cleave, (d) tree diagram of possible accumulated DMD assuming mode-mixing at discrete points and corresponding DMD values for all possible mode-mixing combinations, (e) comparison of the calculated values of accumulated DMD with experimentally obtained impulse responses.

event [25,30]. The impulse response matrices shown in Figs. 7(a)–7(c), corresponding to cores 11, 29 and 33 respectively, were selected as they represent three extreme cases in terms of mode-mixing at the splice and cleave. To interpret their differences, the possible accumulated delays with different mode mixing at the splice and cleave has to be considered.

Assuming a three-mode fiber supporting two mode groups with equal propagation constants within each mode group and different propagation constants between mode groups, Fig. 7(d) shows a tree diagram of all possible mode-mixing paths and associated accumulated relative delays. With the chosen fiber lengths, the delay $\Delta\tau_l$ is significantly larger than $\Delta\tau_s$ and thus three peaks around delays of 0, $\Delta\tau_l$ and $2\Delta\tau_l$ are expected. The outer peaks correspond to the two mode groups propagating without mixing, while the central peak corresponds to mixing at the cleave. The impulse response of core 11 in Fig. 7(a) shows such behavior with a strong central peak and thus significant mode mixing at the cleave. On the other hand, the impulse response of core 29 in Fig. 7(b) shows only two peaks, with the central peak missing, indicating that no mode mixing occurs at the cleave for this core. With no mode-mixing present, this core lends itself to simple calculation of the fiber DMD: the spacing of ca. 145 ps for the two cores and a total fiber distance of $2 \times (1.3\,\text{m} + 8.8\,\text{m})$ suggests a DMD of ca. 7 ps/m. Comparison of the impulse responses in Figs. 7(a) and 7(c), shows that in the latter case the three peaks are split into three sub-peaks each at a much closer spacing. Comparison of these spacings with the calculated spacings for a DMD of 7 ps/m in Fig. 7(d), confirms these spacings to result from mixing at the splice.

Comparing all the impulse responses as in Fig. 7(e), confirms a DMD of ca. 7 ps/m for the analyzed cores, which corresponds well with the DMD design of the fiber and previous measurements in [6, 24, 25], all of which suggest DMD values between 6.3 ps/m and 7.8 ps/m, depending on the core in question.

Besides providing a simple means to measure the fiber DMD parameters, time-domain analysis and comparison between the different impulse responses thus shows significantly different degrees of mode-mixing at the splice and cleave. While core 29 shows negligible mode-mixing at both the splice and cleave, core 11 shows significant mixing at the cleave, while showing none

Optics EXPRESS

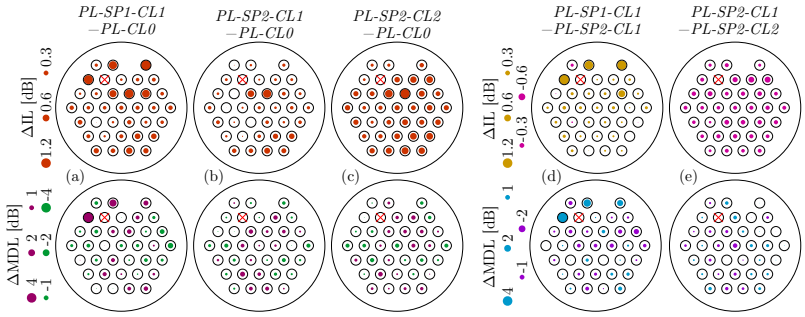

Fig. 8. Comparison of system IL and MDL with different splices and different cleaves: (a)–(c) ΔIL and ΔMDL for *PL-SP1-CL1*, *PL-SP2-CL1* and *PL-SP2-CL2* against *PL-CL0* respectively, (d) direct comparison of two splices, i.e., ΔIL and ΔMDL for *PL-SP2-CL1* against *PL-SP1-CL1*, (e) direct comparison of two cleaves, i.e., ΔIL and ΔMDL for *PL-SP2-CL1* against *PL-SP2-CL2*.

at the splice and finally core 33 shows strong mode-mixing at both. The remaining cores show less extreme behavior with varying degrees of mode-mixing at both points.

3.3. Few-mode fiber splice analysis

While some conclusions about the mode-mixing behavior at fusion splices in the 36-core 3-mode fiber may be drawn from analysis of the impulse response matrix as discussed in the previous section, analysis of their impact on system performance requires characterization of their influence on insertion and mode-dependent losses (IL and MDL). Two splices between the pigtail of the SMUX and an additional piece of 36-core FMF have been performed, resulting in measurements *PL-SP1-CL1* and *PL-SP2-CL1*. To directly show their impact on system IL and MDL, they are both compared to the measurement of the pigtailed SMUX alone (*PL-CL0*).

Figures 8(a) and 8(b) show the difference in wavelength-averaged IL and MDL for all cores for measurements with splice 1 and splice 2 compared to the measurement with only the SMUX. Both splices introduce significant IL, with a mean IL of 0.32 dB for splice 1 and 0.17 dB for splice 2. Δ_{IL} is below 0.5 dB for all cores, but cores 11 and 12 for both splices and additionally cores 2, 3, 4 and 13 for splice 1. By analyzing the mean difference in system MDL, we observe that the inclusion of a fiber splice may in fact reduce overall system MDL, i.e., have a negative ΔMDL, if the mode-mixing at the splice happens to de-align previously aligned MDL elements (e.g., the MDL caused by the SMUX) or itself introduces MDL which is not aligned with the principle MDL axes, similar to what was previously reported in [16, 17, 19]. Changes in MDL are within ±2 dB for all cores, with the exception of cores 2 and 4 for splice 1. On average, across all cores, the splices increase MDL by a mean of 0.13 dB for splice 1 and 0.05 dB for splice 2, showing splice 2 to be of higher quality both in regards of IL and MDL.

Finally, Fig. 8(d) shows a direct comparison between the splices, confirming splice 2 to have persistently lower IL for almost all cores. Their impact on MDL however is largely similar, with the notable exceptions of cores 2, 3 and 4, which were the cores with high IL for splice 1, but good IL for splice 2.

3.4. Reflectivity at cleaved fiber facet analysis

The impact of the cleaved fiber facet itself on the IL and MDL of the system has been analyzed in a similar manner to the analysis of the impact of the fusion splices. Again two measurements

(*PL-SP2-CL1* and *PL-SP2-CL2*) were performed with identical fiber configuration except the element under study, i.e., the fiber cleave. The two compared fiber cleaves both produced high quality fiber facets, free of cracks or scratches across the whole range occupied by the 36-cores, however with slightly differing cleave angles of 0.4° for cleave 1 and 0.9° for cleave 2.

Figures 8(b) and 8(c) show the difference in IL and MDL for the two measurements with different cleaves when compared to the measurement of the SMUX alone. Cleave 2 shows a higher IL across all cores, with an average difference of 0.2 dB, as clearly seen in the direct comparison between the measurements with the two cleaves in Fig. 8(e). The impact on MDL observed between the two measurements with different cleaves is small, with the average difference between the two measurements negligibly small.

3.5. Discussion

By providing a complete set of reflective measurements, characterizing the photonic lantern SMUX on its own and measuring the impact of different splices and cleaves, while maintaining all other system and fiber configuration parameters, the presented method allows direct analysis of the impact of fiber splices in SDM systems. While comparative analysis of the IL of measurements with and without a splice provides a direct measurement of the splice IL, any obtained value of MDL is always relative to the surrounding system and does not measure the MDL associated only with the splice. This may appear to be a shortcoming of the reflective SDM-OVNA measurement, but in fact provides the more relevant information, as any isolated MDL measurement of a splice holds little information about the impact on system MDL—and thus system capacity. This is due to a) the fact that the MDL of a concatenation of elements with MDL strongly depends on the relative alignment between the eigenmodes of the elements, potentially resulting in significantly lower MDL for the chain than for the separate elements, and b) the fact that in any system splices will appear between elements with MDL and thus their polarization rotation (or mode-mixing) may impact system MDL significantly more than the MDL associated with the splice. Both these facts are visible in the measurements of section 3.3 by the difference in impact on MDL and the presence of cores with reduced MDL when including a splice. Analysis of the impact of fiber splices thus has to be of a qualitative or statistical nature and by providing measurements of two splices over 36 cores, the presented measurements show splices to introduce significant mode-mixing and cause changes in system MDL that are not necessarily correlated with splice IL.

The measurements of the impact of the cleave show changes in system MDL and IL at a non-negligible scale and thus serve to highlight the potential for a measurement uncertainty in any reflective OVNA measurement, unless analysis is performed by comparing measurements with the same cleaved fiber facet. While the impact on IL was found to be strongly correlated with the cleave angle, the average difference in MDL between measurements with different cleave angles was negligible.

4. Conclusions

In this work, a comprehensive discussion of spatially diverse optical vector network analysis was given, including the setup, principle of operation and necessary DSP required to fully characterize a space division multiplexing (SDM) system or component. Experimental characterization of a 108-channel photonic lantern spatial multiplexer (SMUX) coupled to a 36-core 3-mode fiber is demonstrated and employed as basis for measurement of the impact of splices in the fiber.

From the measured impulse response and complex transfer function matrices of the SMUX, we calculated IL, MDL and DMD, and found the SMUX to have an average IL of 4.7 dB and an average MDL of 11.0 dB, while the fiber has a DMD of 7 ps/nm. Using the SMUX as a base, the mode-mixing behavior of two different splices in the few-mode multi-core fiber (FM-MCF) was analyzed, finding large differences in the degree of mode-mixing for the different cores in each splice and for different splices. Analysis of the impact of the splices on system IL and MDL shows splices to

Optics EXPRESS

introduce significant IL with the better of the two splices showing an average increase in IL of 0.17 dB. As splices introduce significant-mode mixing, system MDL may be reduced or increased when including a splice, finding a change of MDL by ±2 dB. A similar analysis was performed for the cleaved fiber facet present in any reflective OVNA measurement, finding only a small difference in IL and MDL for different cleaves.

The presented measurements confirm spatially diverse optical network analysis to be a powerful tool for accurate characterization of SDM systems and components. By providing characterization of the behavior of splices in FM-MCF, it contributes to an improved modeling and capacity estimation of SDM systems with a large spatial channel count.

Funding

Det Frie Forskningsråd, Teknologi og Produktion (mmW-SPRAWL project).

Appendix A

Distance, capacity and spectral efficiency data of recent millimeter-wave radio-over-fiber experiments

Table A.1 provides detail of the distance, capacity and SE data of the recent mmW RoF experiments included in Fig. 2.6.

Ref.	Date	Group*	Dist. [m]	Data Rate [¶]	RF Band	BW† [¶]	Pol. Mux	SE‡ [¶]	Complexity§
[68]	12/'11	DTU	1.2	100.0	W	25.0	Y	1.87	H
			2.0	50.0	W	25.0	N	1.87	M
[67]	12/'12	ZTE	1.0	108.0	W	54.0	Y	0.93	H
[62]	10/'13	DTU	15.0	16.0	W	16.0	N	0.93	M
[69]	11/'13	ZTE	1.5	24.0	Ka	9.2	N	2.44	L
[74]	03/'14	UDE	6.2	2.5	W	5.0	N	0.50	L
[79]	09/'14	ZTE	2.0	432.0	W	54.0	Y	1.87	xH
[61]	03/'15	ZTE	300.0	80.0	W	40.0	Y	0.93	xH
[60]	03/'15		2.5	20.0	W	10.0	Y	0.93	H
[77]	03/'15	ZTE	170.0	40.0	W	20.0	Y	0.93	H
			1700.0	20.0	W	10.0	Y	0.93	H
[59]	04/'15	ZTE	20.0	40.0	W	20.0	Y	0.93	H
			40.0	32.0	W	16.0	Y	0.93	H
			80.0	20.0	W	10.0	Y	0.93	H
PAPER3	10/'15	DTU	70.0	1.0	W	2.0	N	0.47	L
			70.0	2.5	W	5.0	N	0.47	L
[70]	10/'15	UDE	40.0	1.0	W	2.0	N	0.47	L

— **Table A.1** continued —

— **Table A.1** continued —

Ref.	Date	Group*	Dist. [m]	Data Rate [¶]	RF Band	BW† [¶]	Pol. Mux	SE‡ [¶]	Complexity§
PAPER4	11/'15	DTU	70.0	2.5	W	5.0	N	0.47	L
PAPER8	11/'15	DTU	2.0	4.0	Ka	4.0	N	0.93	L
PAPER6	03/'16	DTU	225.0	2.5	W	5.0	N	0.47	L
[78]	03/'16		1.2	5.0	V	3.0	N	1.56	M
			1.2	9.0	V	4.5	N	1.87	M
[75]	03/'16	UDE	1.0	8.8	V	2.0	N	4.11	L
			1.0	20.9	V	7.0	N	2.80	L
[76]	03/'16		3.0	0.3	W	0.1	N	2.12	H
PAPER5	05/'16	DTU	70.0	1.0	W	2.0	N	0.47	L
			70.0	2.5	W	5.0	N	0.47	L
[66]	10/'16	UDE	230.0	1.0	W	2.0	N	0.47	L
PAPER7	11/'16	DTU	225.0	2.5	W	5.0	N	0.47	L
PAPER15	11/'16	DTU	50.0	2.5	W	5.0	N	0.50	L
PAPER9	11/'16	DTU	50.0	15.0	W	15.0	N	0.93	M
			50.0	16.0	W	16.0	N	0.80	M
PAPER17	11/'16	DTU	50.0	2.5	W	5.0	N	0.47	L
PAPER16	01/'17	DTU	50.0	2.5	W	5.0	N	0.50	L
[71]	03/'17	UDE	0.7	60.0	W	20.0	N	2.80	M
			3.0	60.0	W	20.0	N	2.40	M
PAPER10	03/'17	DTU	50.0	46.8	W	23.4	N	1.87	M
PAPER11	03/'17	DTU	50.5	60.0	W	15.0	N	3.74	H
[72]	03/'17	ZTE	0.2	16.0	W	4.0	N	3.74	M
[65]	03/'17	ZTE	2500.0	54.0	W	18.0	Y	1.40	H
[73]	03/'17	ZTE/	0.2	352.0	D	44.0	Y	3.74	H
		DTU	0.6	352.0	D	44.0	Y	3.33	H
PAPER18	03/'17	DTU	40.0	2.5	W	5.0	N	0.50	L
PAPER12	07/'17	DTU	58.0	4.9	W	4.9	N	0.47	M
PAPER13	10/'17	DTU	50.0	15.0	W	15.0	N	9.93	M
PAPER14	10/'17	DTU	50.0	15.0	W	15.0	N	9.93	M

Table A.1: Distance, capacity and spectral efficiency data of recent mmW RoF experiments. Acronyms: BW: bandwidth, SE: spectral efficiency, RF: radio frequency, FEC: forward error correction, ED: envelope detection, Rx: receiver, LOS: line of sight.

*Three groups are discerned: 'DTU' is the Technical University of Denmark, works marked by 'ZTE' are collaborative efforts by Fudan University, ZTE and Georgia Institute of Technology, 'UDE' is the University of Duisburg-Essen.

†Actual occupied RF bandwidth, accounting for double sideband RF transmission where applicable.

‡Effective spectral efficiency, calculated from actual RF bandwidth occupation and accounting for FEC overheads.

§Complexity mostly regards complexity in the RF domain; generally experiments employing ED at the Rx are classified 'low' (L), such employing down-mixing at least 'medium' (M), while 'high' (H) is applied to links with polarization multiplexing and 'extra high' (xH) where multiple independent parallel LOS links are used.

¶Units: Data rate in [Gbit/s], BW in [GHz], SE in [bit/s/Hz/pol].

Bibliography

[1] M. Castells. *The Rise of the Network Society [The Information Age: Economy, Society, and Culture / Volume I]*. 2nd ed. Chichester, United Kingdom: Wiley-Blackwell, 2010. ISBN: 978-1-405-19686-4. DOI: 10.1002/9781444319514.

[2] C. Freeman and F. Louçã. *As Time Goes By: From the Industrial Revolutions to the Information Revolution*. Oxford, United Kingdom: Oxford University Press, 2002. ISBN: 978-0-19-925105-6. DOI: 10.1093/0199251053.001.0001.

[3] M. Hilbert and P. López. "The World's Technological Capacity to Store, Communicate, and Compute Information". In: *Science* 332.6025 (2011), pp. 60–65. ISSN: 1095-9203. DOI: 10.1126/science.1200970.

[4] R. Drath and A. Horch. "Industrie 4.0: Hit or Hype?" In: *IEEE Ind. Electron. Mag.* 8.2 (2014), pp. 56–58. ISSN: 1932-4529. DOI: 10.1109/MIE.2014.2312079.

[5] C. Humby. "Data is the new oil!" In: *Proc. ANA Sr. Marketer's Summit*. Evanston, IL, USA, 2006.

[6] M. Hermann, T. Pentek, and B. Otto. "Design Principles for Industrie 4.0 Scenarios". In: *Proc. 49th Hawaii International Conference on System Sciences*. Koloa, HI, USA: IEEE, 2016, pp. 3928–3937. ISBN: 978-0-7695-5670-3. DOI: 10.1109/HICSS.2016.488.

[7] J. Bloem, M. van Doorn, S. Duivestein, D. Excoffier, R. Maas, and E. van Ommeren. *The Fourth Industrial Revolution: Things to Tighten the Link Between IT and OT*. Sogeti VINT Research Report. 2014.

[8] S.-J. Hong, J. Y. L. Thong, J.-Y. Moon, and K.-Y. Tam. "Understanding the behavior of mobile data services consumers". In: *Inf. Syst. Front.* 10.4 (2008), pp. 431–445. ISSN: 1387-3326. DOI: 10.1007/s10796-008-9096-1.

[9] L. Kleinrock. "History of the Internet and its flexible future". In: *IEEE Wireless Commun.* 15.1 (2008), pp. 8–18. ISSN: 1536-1284. DOI: 10.1109/MWC.2008.4454699.

[10] C. Fuchs. *Internet and Society : Social Theory in the Information Age*. New York, NY, USA: Routledge, 2008. ISBN: 978-0-415-96132-5.

[11] P. DiMaggio, E. Hargittai, W. R. Neuman, and J. P. Robinson. "Social Implications of the Internet". In: *Annu. Rev. Sociol.* 27.1 (2001), pp. 307–336. ISSN: 0360-0572. DOI: 10.1146/annurev.soc.27.1.307.

[12] P. Mihailidis. "A tethered generation: Exploring the role of mobile phones in the daily life of young people". In: *Mob. Media Commun.* 2.1 (2014), pp. 58–72. ISSN: 2050-1579. DOI: 10.1177/2050157913505558.

[13] L. Leung. "User-generated content on the internet: an examination of gratifications, civic engagement and psychological empowerment". In: *New Media & Soc.* 11.8 (2009), pp. 1327–1347. ISSN: 1461-4448. DOI: 10.1177/1461444809341264.

[14] 5G PPP. *5G and the Factories of the Future*. Ed. by W. Harick and M. Gupta. Whitepaper. 2015.

[15] 5G PPP. *5G Vision*. Whitepaper. 2015.

[16] Ericsson. *5G Systems – Enabling the Transformation of Industry and Society*. Whitepaper. 2017.

[17] DIGI. *ANY-G TO 4G: The Top Five Considerations for Migrating to 4G LTE*. Whitepaper. 2014.

[18] Nokia. *5G Masterplan - five keys to create the new communications era*. Whitepaper. 2016.

[19] Cisco. *Cisco Visual Networking Index: Forecast and Methodology, 2016–2021*. Whitepaper. 2017.

[20] Cisco. *Cisco Visual Networking Index: Global Mobile Data Traffic Forecast Update, 2016–2021*. Whitepaper. 2017.

[21] GSM Association. *3GPP Low Power Wide Area Technologies*. Whitepaper. 2016.

[22] ITU-R M.2083-0. *IMT Vision – Framework and overall objectives of the future development of IMT for 2020 and beyond*. ITU Recommendation. 2015.

[23] F. Boccardi, R. Heath, A. Lozano, T. Marzetta, and P. Popovski. "Five disruptive technology directions for 5G". In: *IEEE Commun. Mag.* 52.2 (2014), pp. 74–80. ISSN: 0163-6804. DOI: 10.1109/MCOM.2014.6736746.

[24] A. Checko, H. L. Christiansen, Y. Yan, L. Scolari, G. Kardaras, M. S. Berger, and L. Dittmann. "Cloud RAN for Mobile Networks—A Technology Overview". In: *IEEE Commun. Surveys Tuts.* 17.1 (2015), pp. 405–426. DOI: 10.1109/COMST.2014.2355255.

[25] T. Pfeiffer. "Next Generation Mobile Fronthaul and Midhaul Architectures". In: *J. Opt. Commun. Netw.* 7.11 (2015), B38–B45. ISSN: 1943-0620. DOI: 10.1364/JOCN.7.000B38.

[26] J. G. Andrews, S. Buzzi, W. Choi, S. V. Hanly, A. Lozano, A. C. K. Soong, and J. C. Zhang. "What Will 5G Be?" In: *IEEE J. Sel. Areas Commun.* 32.6 (2014), pp. 1065–1082. ISSN: 0733-8716. DOI: 10.1109/JSAC.2014.2328098.

[27] P. Demestichas, A. Georgakopoulos, D. Karvounas, K. Tsagkaris, V. Stavroulaki, J. Lu, C. Xiong, and J. Yao. "5G on the Horizon: Key Challenges for the Radio-Access Network". In: *IEEE Veh. Technol. Mag.* 8.3 (2013), pp. 47–53. ISSN: 1556-6072. DOI: 10.1109/MVT.2013.2269187.

[28] W. Feng, Y. Wang, D. Lin, N. Ge, J. Lu, and S. Li. "When mmWave Communications Meet Network Densification: A Scalable Interference Coordination Perspective". In: *IEEE J. Sel. Areas Commun.* 35.7 (2017), pp. 1459–1471. ISSN: 0733-8716. DOI: 10.1109/JSAC.2017.2698898.

[29] M. Xiao, S. Mumtaz, Y. Huang, L. Dai, Y. Li, M. Matthaiou, G. K. Karagiannidis, E. Bjornson, K. Yang, C.-L. I, and A. Ghosh. "Millimeter Wave Communications for Future Mobile Networks". In: *IEEE J. Sel. Areas Commun.* 35.9 (2017), pp. 1909–1935. ISSN: 0733-8716. DOI: 10.1109/JSAC.2017.2719924.

[30] J. Wells. "Faster than fiber: The future of multi- G/s wireless". In: *IEEE Microw. Mag.* 10.3 (2009), pp. 104–112. ISSN: 1527-3342. DOI: 10.1109/MMM.2009.932081.

[31] P. Smulders. "Exploiting the 60 GHz band for local wireless multimedia access: prospects and future directions". In: *IEEE Commun. Mag.* 40.1 (2002), pp. 140–147. ISSN: 0163-6804. DOI: 10.1109/35.978061.

[32] J. J. Vegas Olmos and I. Tafur Monroy. "Reconfigurable Radio-Over-Fiber Networks". In: *J. Opt. Commun. Netw.* 7.11 (2015), B23. ISSN: 1943-0620. DOI: 10.1364/JOCN.7.000B23.

[33] J. Capmany and D. Novak. "Microwave photonics combines two worlds". In: *Nat. Photonics* 1.6 (2007), pp. 319–330. ISSN: 1749-4885. DOI: 10.1038/nphoton.2007.89.

[34] A. J. Seeds and K. J. Williams. "Microwave Photonics". In: *J. Lightw. Technol.* 24.12 (2006), pp. 4628–4641. ISSN: 0733-8724. DOI: 10.1109/JLT.2006.885787.

[35] J. Yao. "Microwave Photonics". In: *J. Lightw. Technol.* 27.3 (2009), pp. 314–335. ISSN: 0733-8724. DOI: 10.1109/JLT.2008.2009551.

[36] ITU-R SM.1045-1. *Frequency tolerance of transmitters*. ITU Recommendation. 1997.

[37] A. Kanno, P. T. Dat, T. Kuri, I. Hosako, T. Kawanishi, Y. Yoshida, and K. Kitayama. "Evaluation of frequency fluctuation in fiber-wireless link with direct IQ down-converter". In: *Proc. European Conference on Optical Communications*. Cannes, France: IEEE, 2014, We.3.6.3. ISBN: 978-2-9549-4440-1. DOI: 10.1109/ECOC.2014.6963972.

[38] U. Gliese, S. Norskov, and T. N. Nielsen. "Chromatic dispersion in fiber-optic microwave and millimeter-wave links". In: *IEEE Trans. Microw. Theory Tech.* 44.10 (1996), pp. 1716–1724. ISSN: 0018-9480. DOI: 10.1109/22.538964.

[39] H. Schmuck. "Comparison of optical millimetre-wave system concepts with regard to chromatic dispersion". In: *Electron. Lett.* 31.21 (1995), pp. 1848–1849. ISSN: 0013-5194. DOI: 10.1049/el:19951281.

[40] J. Yu, Z. Jia, L. Yi, Y. Su, G.-K. Chang, and T. Wang. "Optical millimeter-wave generation or up-conversion using external modulators". In: *IEEE Photon. Technol. Lett.* 18.1 (2006), pp. 265–267. ISSN: 1041-1135. DOI: 10.1109/LPT.2005.862006.

[41] W.-J. Jiang, C.-T. Lin, A. Ng'oma, P.-T. Shih, J. Chen, M. Sauer, F. Annunziata, and S. Chi. "Simple 14-Gb/s Short-Range Radio-Over-Fiber System Employing a Single-Electrode MZM for 60-GHz Wireless Applications". In: *J. Lightw. Technol.* 28.16 (2010), pp. 2238–2246. ISSN: 0733-8724. DOI: 10.1109/JLT.2010.2045341.

[42] C.-T. Lin, S.-P. Dai, J. Chen, P.-T. Shih, P.-C. Peng, and S. Chi. "A Novel Direct Detection Microwave Photonic Vector Modulation Scheme for Radio-Over-Fiber System". In: *IEEE Photon. Technol. Lett.* 20.13 (2008), pp. 1106–1108. ISSN: 1041-1135. DOI: 10.1109/LPT.2008.924176.

[43] G. Carpintero, K. Balakier, Z. Yang, R. C. Guzman, A. Corradi, A. Jimenez, G. Kervella, M. J. Fice, M. Lamponi, M. Chitoui, F. van Dijk, C. C. Renaud, A. Wonfor, E. A. J. M. Bente, R. V. Penty, I. H. White, and A. J. Seeds. "Microwave Photonic Integrated Circuits for Millimeter-Wave Wireless Communications". In: *J. Lightw. Technol.* 32.20 (2014), pp. 3495–3501. ISSN: 0733-8724. DOI: 10.1109/JLT.2014.2321573.

[44] T. Kuri and K.-i. Kitayama. "Long-term stabilized millimeter-wave generation using a high-power mode-locked laser diode module". In: *IEEE Trans. Microw. Theory Tech.* 47.5 (1999), pp. 570–574. ISSN: 0018-9480. DOI: 10.1109/22.763157.

[45] R. Yamanaka, R. Matsumoto, H. Sotobayashi, A. Kanno, and T. Kawanishi. "Highly frequency-stabilized millimeter-wave signal generation using optical phase-locked loop and flat optical frequency comb". In: *Proc. Conference on Lasers and Electro-Optics Pacific Rim.* Kyoto, Japan: IEEE, 2013, WPC–13. ISBN: 978-1-4673-6476-8. DOI: 10.1109/CLEOPR.2013.6600533.

[46] K.-i. Kitayama and R. A. Griffin. "Optical downconversion from millimeter-wave to IF-band over 50 km-long optical fiber link using an electroabsorption modulator". In: *IEEE Photon. Technol. Lett.* 11.2 (1999), pp. 287–289. ISSN: 1041-1135. DOI: 10.1109/68.740732.

[47] K. Prince and I. Tafur Monroy. "All-Optical Envelope Detection and Fiber Transmission of Wireless Signals by External Injection of a DFB Laser". In: *IEEE Photon. Technol. Lett.* 20.15 (2008), pp. 1317–1319. ISSN: 1041-1135. DOI: 10.1109/LPT.2008.926915.

[48] K. Prince and I. Tafur Monroy. "Multi-band radio over fiber system with all-optical halfwave rectification, transmission and frequency down-conversion". In: *Opt. Fiber Technol.* 17.4 (2011), pp. 310–314. ISSN: 1068-5200. DOI: 10.1016/j.yofte.2011.06.003.

[49] A. Bekkali, T. Kobayashi, K. Nishimura, N. Shibagaki, K. Kashima, and Y. Sato. "Real-Time 10GbE Data Transmission Over a Converged RoF Links and 96-GHz Wireless Bridge". In: *IEEE Photon. Technol. Lett.* 29.1 (2017), pp. 15–18. ISSN: 1041-1135. DOI: 10.1109/LPT.2016.2624339.

[50] X. Pang, A. Lebedev, J. J. Vegas Olmos, and I. Tafur Monroy. "Multigigabit W-Band (75–110 GHz) Bidirectional Hybrid Fiber-Wireless Systems in Access Networks". In: *J. Lightw. Technol.* 32.23 (2014), pp. 4585–4592. ISSN: 0733-8724. DOI: 10.1109/JLT.2014.2361957.

[51] T. S. Rappaport, S. Sun, R. Mayzus, Y. Azar, K. Wang, G. N. Wong, J. K. Schulz, M. Samimi, and F. Gutierrez. "Millimeter Wave Mobile Communications for 5G Cellular: It Will Work!" In: *IEEE Access* 1 (2013), pp. 335–349. ISSN: 2169-3536. DOI: 10.1109/ACCESS.2013.2260813.

[52] T. S. Rappaport, G. R. MacCartney, M. K. Samimi, and S. Sun. "Wideband Millimeter-Wave Propagation Measurements and Channel Models for Future Wireless Communication System Design". In: *IEEE Trans. Commun.* 63.9 (2015), pp. 3029–3056. ISSN: 0090-6778. DOI: 10.1109/TCOMM.2015.2434384.

[53] H. Xu, V. Kukshya, and T. S. Rappaport. "Spatial and temporal characteristics of 60-GHz indoor channels". In: *IEEE J. Sel. Areas Commun.* 20.3 (2002), pp. 620–630. ISSN: 0733-8716. DOI: 10.1109/49.995521.

[54] H. T. Friis. "A Note on a Simple Transmission Formula". In: *Proc. IRE* 34.5 (1946), pp. 254–256. ISSN: 0096-8390. DOI: 10.1109/JRPROC.1946.234568.

[55] M. Hata. "Empirical formula for propagation loss in land mobile radio services". In: *IEEE Trans. Veh. Technol.* 29.3 (1980), pp. 317–325. ISSN: 0018-9545. DOI: 10.1109/T-VT.1980.23859.

[56] C. E. Shannon. "A Mathematical Theory of Communication". In: *Bell Syst. Tech. J.* 27.3 (1948), pp. 379–423. ISSN: 0005-8580. DOI: 10.1002/j.1538-7305.1948.tb01338.x.

[57] R. Struzak. "On Spectrum Congestion and Capacity of Radio Links". In: *Ann. Oper. Res.* 107.1-4 (2001), pp. 339–347. ISSN: 0254-5330. DOI: 10.1023/A:1014975721176.

[58] C.-H. Li, M.-F. Wu, C.-H. Lin, and C.-T. Lin. "W-band OFDM RoF System with Simple Envelope Detector Down-Conversion". In: *Proc. Optical Fiber Communication Conference*. Los Angeles, CA, USA: OSA, 2015, W4G.6. ISBN: 978-1-55752-937-4. DOI: 10.1364/OFC.2015.W4G.6.

[59] Y. Xu, J. Yu, X. Li, J. Xiao, and Z. Zhang. "Experimental Investigation on Fiber-Wireless MIMO System With Different LO at W Band". In: *IEEE Photon. J.* 7.2 (2015), p. 7200907. ISSN: 1943-0655. DOI: 10.1109/JPHOT.2015.2411230.

[60] N. P. Diamantopoulos, S. Inudo, Y. Yoshida, A. Maruta, A. Kanno, P. T. Dat, T. Kawanishi, R. Maruyama, N. Kuwaki, S. Matsuo, and K.-i. Kitayama. "Mode-Division Multiplexed W-Band RoF Transmission for Higher-order Spatial Multiplexing". In: *Proc. Optical Fiber Communication Conference*. Los Angeles, CA, USA: OSA, 2015, W4G.2. ISBN: 978-1-55752-937-4. DOI: 10.1364/OFC.2015.W4G.2.

[61] X. Li, J. Yu, Z. Zhang, and Y. Xu. "Field Trial of 80-Gb/s PDM-QPSK Signal Delivery over 300-m Wireless Distance with MIMO and Antenna Polarization Multiplexing at W-Band". In: *Proc. Optical Fiber Communication Conference*. Los Angeles, CA, USA: OSA, 2015, Th5A.5. ISBN: 978-1-55752-940-4. DOI: 10.1364/OFC.2015.Th5A.5.

[62] X. Pang, J. J. Vegas Olmos, A. Lebedev, and I. Tafur Monroy. "A 15-meter multi-gigabit W-band bidirectional wireless bridge in fiber-optic access networks". In: *Proc. IEEE International Topical Meeting on Microwave Photonics*. IEEE, 2013, pp. 37–40. ISBN: 978-1-4673-6071-5. DOI: 10.1109/MWP.2013.6724013.

[63] C.-L. I, C. Rowell, S. Han, Z. Xu, G. Li, and Z. Pan. "Toward green and soft: a 5G perspective". In: *IEEE Commun. Mag.* 52.2 (2014), pp. 66–73. ISSN: 0163-6804. DOI: 10.1109/MCOM.2014.6736745.

[64] L. Dai, B. Wang, Y. Yuan, S. Han, C.-l. I, and Z. Wang. "Non-orthogonal multiple access for 5G: solutions, challenges, opportunities, and future research trends". In: *IEEE Commun. Mag.* 53.9 (2015), pp. 74–81. ISSN: 0163-6804. DOI: 10.1109/MCOM.2015.7263349.

[65] X. Li, J. Yu, K. Wang, Y. Xu, L. Chen, L. Zhao, W. Zhou, L. Zhao, and W. Zhou. "Bidirectional Delivery of 54-Gbps 8QAM W-Band Signal and 32-Gbps 16QAM K-Band Signal over 20-km SMF-28 and 2500-m Wireless Distance". In: *Proc. Optical Fiber Communication Conference*. Los Angeles, CA, USA: OSA, 2017, Th5A.7. ISBN: 978-1-943580-24-8. DOI: 10.1364/OFC.2017.Th5A.7.

[66] R. Chuenchom, X. Zou, N. Schrinski, S. Babiel, M. Freire Hermelo, M. Steeg, A. Steffan, J. Honecker, Y. Leiba, and A. Stöhr. "E-Band 76-GHz Coherent RoF Backhaul Link Using an Integrated Photonic Mixer". In: *J. Lightw. Technol.* 34.20 (2016), pp. 4744–4750. ISSN: 0733-8724. DOI: 10.1109/JLT.2016.2573047.

[67] X. Li, Z. Dong, J. Yu, N. Chi, Y. Shao, and G.-K. Chang. "Fiber-wireless transmission system of 108 Gb/s data over 80 km fiber and 2×2 multiple-input multiple-output wireless links at 100 GHz W-band frequency." In: *Opt. Lett.* 37.24 (2012), pp. 5106–5108. ISSN: 0146-9592. DOI: 10.1364/OL.37.005106.

[68] X. Pang, A. Caballero, A. Dogadaev, V. Arlunno, R. Borkowski, J. S. Pedersen, L. Deng, F. Karinou, F. Roubeau, D. Zibar, X. Yu, and I. Tafur Monroy. "100 Gbit/s hybrid optical fiber-wireless link in the W-band (75–110 GHz)". In: *Opt. Express* 19.25 (2011), p. 24944. DOI: 10.1364/OE.19.024944.

[69] J. Zhang, J. Yu, N. Chi, F. Li, and X. Li. "Experimental demonstration of 24-Gb/s CAP-64QAM radio-over-fiber system over 40-GHz mm-wave fiber-wireless transmission". In: *Opt. Express* 21.22 (2013), p. 26888. ISSN: 1094-4087. DOI: 10.1364/OE.21.026888.

[70] R. Chuenchom, X. Zou, V. Rymanov, B. Khani, M. Steeg, S. Dulme, S. Babiel, A. Stöhr, J. Honecker, and A. G. Steffan. "Integrated 110 GHz coherent photonic mixer for CRoF mobile backhaul links". In: *Proc. International Topical Meeting on Microwave Photonics*. IEEE, 2015, Tu–C2. ISBN: 978-1-4673-9368-3. DOI: 10.1109/MWP.2015.7356699.

[71] X. Li, J. Yu, Y. Xu, X. Pan, F. Wang, Z. Li, B. Liu, L. Zhang, X. Xin, and G.-K. Chang. "60-Gbps W-Band 64QAM RoF System with T-spaced DD-LMS Equalization". In: *Proc. Optical Fiber Communication Conference*. Los Angeles, CA, USA: OSA, 2017, M3E.2. ISBN: 978-1-943580-23-1. DOI: 10.1364/OFC.2017.M3E.2.

[72] X. Li, Y. Xu, J. Xiao, K. Wang, and J. Yu. "W-Band 16QAM-Modulated SSB Photonic Vector Mm-Wave Signal Generation by One Single I/Q Modulator". In: *Proc. Optical Fiber Communication Conference*. Los Angeles, CA, USA: OSA, 2017, M3E.6. ISBN: 978-1-943580-23-1. DOI: 10.1364/OFC.2017.M3E.6.

[73] R. Puerta, J. Yu, X. Li, Y. Xu, J. J. Vegas Olmos, and I. Tafur Monroy. "Demonstration of 352 Gbit/s Photonically-enabled D-Band Wireless Delivery in one 2x2 MIMO System". In: *Proc. Optical Fiber Communication Conference*. Los Angeles, CA, USA: OSA, 2017, Tu3B.3. ISBN: 978-1-943580-23-1. DOI: 10.1364/OFC.2017.Tu3B.3.

[74] A. Stöhr, O. Cojucari, F. van Dijk, G. Carpintero, T. Tekin, S. Formont, I. Flammia, V. Rymanov, B. Khani, and R. Chuenchom. "Robust 71-76 GHz Radio-over-Fiber Wireless Link with High-Dynamic Range Photonic Assisted Transmitter and Laser Phase-Noise Insensitive SBD Receiver". In: *Proc. Optical Fiber Communication Conference*. San Francisco, CA, USA: OSA, 2014, p. M2D.4. ISBN: 978-1-55752-993-0. DOI: 10.1364/OFC.2014.M2D.4.

[75] A. Stöhr, B. Shih, S. Abraha, A. Steffan, and A. Ng'oma. "High Spectral-Efficient 512-QAM-OFDM 60 GHz CRoF System using a Coherent Photonic Mixer (CPX) and an RF Envelope Detector". In: *Proc. Optical Fiber Communication Conference*. Anaheim, CA, USA: OSA, 2016, Tu3B.4. ISBN: 978-1-943580-07-1. DOI: 10.1364/OFC.2016.Tu3B.4. URL: https://www.osapublishing.org/abstract.cfm?URI=OFC-2016-Tu3B.4.

[76] P. Tien Dat, A. Kanno, N. Yamamoto, and T. Kawanishi. "High-Capacity and High-Spectral-Efficiency Seamless Fiber-Wireless System for High-Speed Trains". In: *Proc. Optical Fiber Communication Conference*. Anaheim, CA, USA: OSA, 2016, Tu3B.5. ISBN: 978-1-943580-07-1. DOI: 10.1364/OFC.2016.Tu3B.5.

[77] J. Xiao, J. Yu, X. Li, Y. Xu, Z. Zhang, and L. Chen. "20-Gb/s PDM-QPSK Signal Delivery over 1.7-km Wireless Distance at W-Band". In: *Proc. Optical Fiber Communication Conference*. Los Angeles, CA, USA: OSA, 2015, W4G.4. ISBN: 978-1-55752-937-4. DOI: 10.1364/OFC.2015.W4G.4.

[78] M. Xu, J. Zhang, F. Lu, L. Cheng, J. Wang, D. Guidotti, T. Kanesan, S. M. Mitani, and G.-K. Chang. "Multiband OQAM CAP Modulation in MMW RoF Systems with Enhanced Spectral and Computational Efficiency". In: *Proc. Optical Fiber Communication Conference*. Anaheim, CA, USA: OSA, 2016, Tu3B.3. ISBN: 978-1-943580-07-1. DOI: 10.1364/OFC.2016.Tu3B.3.

[79] J. Yu, X. Li, J. Zhang, and J. Xiao. "432-Gb/s PDM-16QAM signal wireless delivery at W-band using optical and antenna polarization multiplexing". In: *Proc. European Conference on Optical Communications*. Cannes, France: IEEE, 2014, We.3.6.6. ISBN: 978-2-9549-4440-1. DOI: 10.1109/ECOC.2014.6963945.

[80] R. D. Howson. "An Analysis of the Capabilities of Polybinary Data Transmission". In: *IEEE Trans. Commun. Technol.* 13.3 (1965), pp. 312–319. ISSN: 0096-2244. DOI: 10.1109/TCOM.1965.1089138.

[81] A. Lender. "Correlative Digital Communication Techniques". In: *IEEE Trans. Commun. Technol.* 12.4 (1964), pp. 128–135. ISSN: 0096-2244. DOI: 10.1109/TCOM.1964.1088964.

[82] A. Sekey. "An Analysis of the Duobinary Technique". In: *IEEE Trans. Commun. Technol.* 14.2 (1966), pp. 126–130. ISSN: 0096-2244. DOI: 10.1109/TCOM.1966.1089299.

[83] D. D. Falconer. *Carrierless AM/PM*. Bell Laboratories Technical Memorandum. 1975.

[84] P. A. Haigh, S. T. Le, S. Zvanovec, Z. Ghassemlooy, P. Luo, T. Xu, P. Chvojka, T. Kanesan, E. Giacoumidis, P. Canyelles-Pericas, H. L. Minh, W. Popoola, S. Rajbhandari, I. Papakonstantinou, and I. Darwazeh. "Multi-band carrier-less amplitude and phase modulation for bandlimited visible light communications systems". In: *IEEE Wireless Commun.* 22.2 (2015), pp. 46–53. ISSN: 1536-1284. DOI: 10.1109/MWC.2015.7096284.

[85] M. Iglesias Olmedo, T. Zuo, J. B. Jensen, Q. Zhong, X. Xu, S. Popov, and I. Tafur Monroy. "Multiband Carrierless Amplitude Phase Modulation for High Capacity Optical Data Links". In: *J. Lightw. Technol.* 32.4 (2014), pp. 798–804. ISSN: 0733-8724. DOI: 10.1109/JLT.2013.2284926.

[86] A. F. Shalash and K. K. Parhi. "Multidimensional carrierless AM/PM systems for digital subscriber loops". In: *IEEE Trans. Commun.* 47.11 (1999), pp. 1655–1667. ISSN: 0090-6778. DOI: 10.1109/26.803500.

[87] T. Zuo, A. Tatarczak, M. Iglesias Olmedo, J. Estaran, J. B. Jensen, Q. Zhong, X. Xu, and I. Tafur Monroy. "O-band 400 Gbit/s Client Side Optical Transmission Link". In: *Proc. Optical Fiber Communication Conference*. San Francisco, CA, USA: OSA, 2014, M2E.4. ISBN: 978-1-55752-993-0. DOI: 10.1364/OFC.2014.M2E.4.

[88] Q. Sun, L. Li, A. Tolli, M. Juntti, and J. Mao. "Optimal Energy Efficient Bit and Power Loading for Multicarrier Systems". In: *IEEE Commun. Lett.* 18.7 (2014), pp. 1194–1197. ISSN: 1089-7798. DOI: 10.1109/LCOMM.2014.2318300.

[89] C. Y. Wong, R. S. Cheng, K. B. Lataief, and R. D. Murch. "Multiuser OFDM with adaptive subcarrier, bit, and power allocation". In: *IEEE J. Sel. Areas Commun.* 17.10 (1999), pp. 1747–1758. ISSN: 0733-8716. DOI: 10.1109/49.793310.

[90] R. Puerta, J. J. Vegas Olmos, I. Tafur Monroy, N. N. Ledentsov, and J. P. Turkiewicz. "Flexible MultiCAP Modulation and its Application to 850 nm VCSEL-MMF Links". In: *J. Lightw. Technol.* 35.15 (2017), pp. 3168–3173. ISSN: 0733-8724. DOI: 10.1109/JLT.2017.2701887.

[91] R. Puerta, M. Agustin, L. Chorchos, J. Tonski, J.-R. Kropp, N. Ledentsov, V. A. Shchukin, N. N. Ledentsov, R. Henker, I. Tafur Monroy, J. J. Vegas Olmos, and J. Turkiewicz. "107.5 Gb/s 850 nm multi- and single-mode VCSEL transmission over 10 and 100 m of multi-mode fiber". In: *Proc. Optical Fiber Communication Conference*. Anaheim, CA, USA: OSA, 2016, Th5B.5. ISBN: 978-1-943580-08-8. DOI: 10.1364/OFC.2016.Th5B.5.

[92] O. Fresnedo, J. P. Gonzalez-Coma, M. Hassanin, L. Castedo, and J. Garcia-Frias. "Evaluation of Analog Joint Source-Channel Coding Systems for Multiple Access Channels". In: *IEEE Trans. Commun.* 63.6 (2015), pp. 2312–2324. ISSN: 0090-6778. DOI: 10.1109/TCOMM.2015.2427164.

[93] V. Tarokh, H. Jafarkhani, and A. R. Calderbank. "Space-time block coding for wireless communications: performance results". In: *IEEE J. Sel. Areas Commun.* 17.3 (1999), pp. 451–460. ISSN: 0733-8716. DOI: 10.1109/49.753730.

[94] A. Gorokhov and J.-P. Linnartz. "Robust OFDM Receivers for Dispersive Time-Varying Channels: Equalization and Channel Acquisition". In: *IEEE Trans. Commun.* 52.3 (2004), pp. 518–518. ISSN: 0090-6778. DOI: 10.1109/TCOMM.2004.823560.

[95] L. C. P. Cavalcante, J. J. Vegas Olmos, R. Dinis, L. G. d. Q. Silveira, I. Tafur Monroy, and L. F. d. Q. Silveira. "Wavelet-Coded OFDM for Next Generation Mobile Communications". In: *Proc. 84th Vehicular Technology Conference*. Montreal, Canada: IEEE, 2016. ISBN: 978-1-5090-1701-0. DOI: 10.1109/VTCFall.2016.7881967.

[96] Z. Chen, Z. Ding, X. Dai, and R. Zhang. "An Optimization Perspective of the Superiority of NOMA Compared to Conventional OMA". In: *IEEE Trans. Signal Process.* 65.19 (2017), pp. 5191–5202. ISSN: 1053-587X. DOI: 10.1109/TSP.2017.2725223.

[97] K. Higuchi and A. Benjebbour. "Non-orthogonal Multiple Access (NOMA) with Successive Interference Cancellation for Future Radio Access". In: *IEICE Trans. Commun.* E98.B.3 (2015), pp. 403–414. ISSN: 0916-8516. DOI: 10.1587/transcom.E98.B.403.

[98] A. Benjebbour, Y. Saito, Y. Kishiyama, A. Li, A. Harada, and T. Nakamura. "Concept and practical considerations of non-orthogonal multiple access (NOMA) for future radio access". In: *Proc. International Symposium on Intelligent Signal Processing and Communication Systems*. Naha, Japan: IEEE, 2013, pp. 770–774. ISBN: 978-1-4673-6361-7. DOI: 10.1109/ISPACS.2013.6704653.

[99] H. L. Resnikoff and R. O. Wells. *Wavelet Analysis: the Scalable Structure of Information*. New York, NY, USA: Springer, 1998. ISBN: 978-1-4612-6830-7. DOI: 10.1007/978-1-4612-0593-7.

[100] L. F. Q. Silveira, L. G. Q. Silveira, F. M. Assis, and E. L. Pinto. "Analysis and optimization of wavelet-coded communication systems". In: *IEEE Trans. Wireless Commun.* 8.2 (2009), pp. 563–567. ISSN: 1536-1276. DOI: 10.1109/TWC.2009.070978.

[101] M. A. Tzannes and M. C. Tzannes. "Bit-by-bit channel coding using wavelets". In: *Proc. Global Communications Conference*. Orlando, FL, USA: IEEE, 1992, pp. 684–688. ISBN: 0-7803-0608-2. DOI: 10.1109/GLOCOM.1992.276430.

[102] Z. Ding, X. Lei, G. K. Karagiannidis, R. Schober, J. Yuan, and V. K. Bhargava. "A Survey on Non-Orthogonal Multiple Access for 5G Networks: Research Challenges and Future Trends". In: *IEEE J. Sel. Areas Commun.* 35.10 (2017), pp. 2181–2195. ISSN: 0733-8716. DOI: 10.1109/JSAC.2017.2725519.

[103] 3GPP TR 36.859. *Study on Downlink Multiuser Superposition Transmission (MUST) for LTE*. Technical Report. 2015.

[104] F. Lu, M. Xu, L. Cheng, J. Wang, J. Zhang, and G.-K. Chang. "Non-Orthogonal Multiple Access With Successive Interference Cancellation in Millimeter-Wave Radio-Over-Fiber Systems". In: *J. Lightw. Technol.* 34.17 (2016), pp. 4179–4186. ISSN: 0733-8724. DOI: 10.1109/JLT.2016.2593665.

[105] F. Lu, M. Xu, L. Cheng, J. Wang, and G.-K. Chang. "Power-Division Non-Orthogonal Multiple Access (NOMA) in Flexible Optical Access With Synchronized Downlink/Asynchronous Uplink". In: *J. Lightw. Technol.* 35.19 (2017), pp. 4145–4152. ISSN: 0733-8724. DOI: 10.1109/JLT.2017.2721955.

[106] J. E. Mitchell. "Integrated Wireless Backhaul Over Optical Access Networks". In: *J. Lightw. Technol.* 32.20 (2014), pp. 3373–3382. ISSN: 0733-8724. DOI: 10.1109/JLT.2014.2321774.

[107] J. J. Vegas Olmos, T. Kuri, and K.-i. Kitayama. "Reconfigurable Radio-Over-Fiber Networks: Multiple-Access Functionality Directly Over the Optical Layer". In: *IEEE Trans. Microw. Theory Techn.* 58.11 (2010), pp. 3001–3010. ISSN: 0018-9480. DOI: 10.1109/TMTT.2010.2075490.

[108] S. E. Alavi, M. R. K. Soltanian, I. S. Amiri, M. Khalily, A. S. M. Supa'at, and H. Ahmad. "Towards 5G: A Photonic Based Millimeter Wave Signal Generation for Applying in 5G Access Fronthaul". In: *Sci. Rep.* 6.1 (2016), p. 19891. ISSN: 2045-2322. DOI: 10.1038/srep19891.

[109] H. Wang, M. M. A. Hossain, and C. Cavdar. "Cloud RAN architectures with optical and mm-Wave transport technologies". In: *Proc. 19th International Conference on Transparent Optical Networks*. Girona, Spain: IEEE, 2017, We.B2.4. ISBN: 978-1-5386-0859-3. DOI: 10.1109/ICTON.2017.8025007.

[110] K.-i. Kitayama, T. Kuri, H. Toda, and J. J. Vegas Olmos. "Radio over Fiber: DWDM Analog/digital Access Network and its Enabling Technologies". In: *Proc. 20th Annual Meeting of the IEEE Lasers and Electro-Optics Society*. IEEE, 2007, pp. 794–795. ISBN: 978-1-4244-0924-2. DOI: 10.1109/LEOS.2007.4382647.

[111] P. E. Green. "Fiber to the home: the next big broadband thing". In: *IEEE Commun. Mag.* 42.9 (2004), pp. 100–106. ISSN: 0163-6804. DOI: 10.1109/MCOM.2004.1336726.

[112] J. C. Attard and J. E. Mitchell. "Optical network architectures for dynamic reconfiguration of full duplex, multiwavelength, radio over fiber". In: *J. Opt. Netw.* 5.6 (2006), p. 435. ISSN: 1536-5379. DOI: 10.1364/JON.5.000435.

[113] J. M. Galve, I. Gasulla, S. Sales, and J. Capmany. "Reconfigurable Radio Access Networks Using Multicore Fibers". In: *IEEE J. Quantum Electron.* 52.1 (2016), p. 0600507. ISSN: 0018-9197. DOI: 10.1109/JQE.2015.2497244.

[114] Y. Luo, X. Zhou, F. Effenberger, X. Yan, G. Peng, Y. Qian, and Y. Ma. "Time- and Wavelength-Division Multiplexed Passive Optical Network (TWDM-PON) for Next-Generation PON Stage 2 (NG-PON2)". In: *J. Lightw. Technol.* 31.4 (2013), pp. 587–593. ISSN: 0733-8724. DOI: 10.1109/JLT.2012.2215841.

[115] M. Zhu, L. Zhang, S.-H. Fan, C. Su, G. Gu, and G.-K. Chang. "Efficient Delivery of Integrated Wired and Wireless Services in UDWDM-RoF-PON Coherent Access Network". In: *IEEE Photon. Technol. Lett.* 24.13 (2012), pp. 1127–1129. ISSN: 1041-1135. DOI: 10.1109/LPT.2012.2196427.

[116] M. P. Thakur, S. Mikroulis, C. C. Renaud, J. J. Vegas Olmos, M. C. R. Medeiros, and J. E. Mitchell. "Cost-efficient DWDM-PON/Mm-Wave wireless integration using coherent radio-over-fiber (CRoF)". In: *Proc. International Topical Meeting on Microwave Photonics*. Paphos, Cyprus: IEEE, 2015, TuP–19. ISBN: 978-1-4673-9368-3. DOI: 10.1109/MWP.2015.7356663.

[117] R. W. Heath and A. J. Paulraj. "Switching Between Diversity and Multiplexing in MIMO Systems". In: *IEEE Trans. Commun.* 53.6 (2005), pp. 962–968. ISSN: 0090-6778. DOI: 10.1109/TCOMM.2005.849774.

[118] L. Zheng and D. N. C. Tse. "Diversity and multiplexing: a fundamental tradeoff in multiple-antenna channels". In: *IEEE Trans. Inf. Theory* 49.5 (2003), pp. 1073–1096. ISSN: 0018-9448. DOI: 10.1109/TIT.2003.810646.

[119] W. Klaus, B. J. Puttnam, R. S. Luís, J. Sakaguchi, J. M. Delgado Mendinueta, Y. Awaji, and N. Wada. "Advanced Space Division Multiplexing Technologies for Optical Networks". In: *J. Opt. Commun. Netw.* 9.4 (2017), pp. C1–C11. ISSN: 1943-0620. DOI: 10.1364/JOCN.9.0000C1.

[120] J. Sakaguchi, W. Klaus, J. M. Delgado Mendinueta, B. J. Puttnam, R. S. Luís, Y. Awaji, N. Wada, T. Hayashi, T. Nakanishi, T. Watanabe, Y. Kokubun, T. Takahata, and T. Kobayashi. "Large Spatial Channel (36-Core × 3 mode) Heterogeneous Few-Mode Multicore Fiber". In: *J. Lightw. Technol.* 34.1 (2016), pp. 93–103. ISSN: 0733-8724. DOI: 10.1109/JLT.2015.2481086.

[121] B. J. Puttnam, R. S. Luis, W. Klaus, J. Sakaguchi, J. M. Delgado Mendinueta, Y. Awaji, N. Wada, Y. Tamura, T. Hayashi, M. Hirano, and J. Marciante. "2.15 Pb/s transmission using a 22 core homogeneous single-mode multi-core fiber and wideband optical comb". In: *Proc. European Conference on Optical Communication*. Valencia, Spain: IEEE, 2015, PD3.1. ISBN: 978-8-4608-1741-3. DOI: 10.1109/ECOC.2015.7341685.

[122] D. Soma, Y. Wakayama, S. Beppu, S. Sumita, T. Tsuritani, T. Hayashi, T. Nagashima, M. Suzuki, H. Takahashi, K. Igarashi, I. Morita, and M. Suzuki. "10.16 Peta-bit/s Dense SDM/WDM transmission over Low-DMD 6-Mode 19-Core Fibre across C+L Band". In: *Proc. 43rd European Conference on Optical Communications*. Vol. 20. 1. Gothenburg, Sweden, 2017, Th.PDP.A.1.

[123] I. Gasulla and J. Capmany. "Microwave Photonics Applications of Multicore Fibers". In: *IEEE Photon. J.* 4.3 (2012), pp. 877–888. ISSN: 1943-0655. DOI: 10.1109/JPHOT.2012.2199101.

[124] Y. Chen, J. Li, P. Zhu, H. Peng, J. Zhu, Y. Tian, Z. Wu, D. Ge, P. Zhou, K. Liu, Y. Xu, J. Chen, Y. He, and Z. Chen. "Cost effective wavelength reused MDM system for bidirectional mobile fronthaul". In: *Opt. Express* 24.20 (2016), pp. 22413–22422. ISSN: 1094-4087. DOI: 10.1364/OE.24.022413.

[125] L. Combi, A. Matera, A. Gatto, P. Parolari, P. Boffi, and U. Spagnolini. "Radio-over-modes for C-RAN architecture with smart optical resources assignment". In: *Proc. IEEE International Conference on Communications*. Paris, France: IEEE, 2017. ISBN: 978-1-4673-8999-0. DOI: 10.1109/ICC.2017.7997215.

[126] D. K. Gifford, B. J. Soller, M. S. Wolfe, and M. E. Froggatt. "Optical vector network analyzer for single-scan measurements of loss, group delay, and polarization mode dispersion". In: *Appl. Opt.* 44.34 (2005), pp. 7282–7286. ISSN: 0003-6935. DOI: 10.1364/AO.44.007282.

[127] G. VanWiggeren and D. Baney. "Swept-wavelength interferometric analysis of multiport components". In: *IEEE Photon. Technol. Lett.* 15.9 (2003), pp. 1267–1269. ISSN: 1041-1135. DOI: 10.1109/LPT.2003.816663.

[128] N. K. Fontaine, R. Ryf, M. A. Mestre, B. Guan, X. Palou, S. Randel, Y. Sun, L. Gruner-Nielsen, R. V. Jensen, and R. Lingle. "Characterization of Space-Division Multiplexing Systems using a Swept-Wavelength Interferometer". In: *Proc. Optical Fiber Communication Conference*. Anaheim, CA, USA: OSA, 2013, OW1K.2. ISBN: 978-1-55752-962-6. DOI: 10.1364/OFC.2013.OW1K.2.

[129] G. H. Golub and C. Reinsch. "Singular value decomposition and least squares solutions". In: *Numer. Math.* 14.5 (1970), pp. 403–420. ISSN: 0029-599X. DOI: 10.1007/BF02163027.

[130] B. L. Heffner. "Accurate, automated measurement of differential group delay dispersion and principal state variation using Jones matrix eigenanalysis". In: *IEEE Photon. Technol. Lett.* 5.7 (1993), pp. 814–817. ISSN: 1041-1135. DOI: 10.1109/68.229816.

[131] N. K. Fontaine. "Characterization of Space-Division Multiplexing Fibers Using Swept-wavelength Interferometry". In: *Proc. Optical Fiber Communication Conference*. Los Angeles, CA, USA: OSA, 2015, W4I.7. ISBN: 978-1-55752-937-4. DOI: 10.1364/OFC.2015.W4I.7.

[132] K.-P. Ho and J. M. Kahn. "Mode-dependent loss and gain: statistics and effect on mode-division multiplexing". In: *Opt. Express* 19.17 (2011), pp. 16612–16635. ISSN: 1094-4087. DOI: 10.1364/OE.19.016612.

[133] F. Ferreira, D. Fonseca, A. Lobato, B. Inan, and H. Silva. "Reach Improvement of Mode Division Multiplexed Systems Using Fiber Splices". In: *IEEE Photon. Technol. Lett.* 25.12 (2013), pp. 1091–1094. ISSN: 1041-1135. DOI: 10.1109/LPT.2013.2256120.

[134] S. Warm and K. Petermann. "Splice loss requirements in multi-mode fiber mode-division-multiplex transmission links". In: *Opt. Express* 21.1 (2013), pp. 519–532. ISSN: 1094-4087. DOI: 10.1364/OE.21.000519.

[135] M. Oishi, T. Hirasawa, K. Furuya, S. Akiba, J. Hirokawa, and M. Ando. "3.5-Gbit/s QPSK Signal Radio-Over-Fiber Transmission With 60-GHz Integrated Photonic Array-Antenna Beam Forming". In: *J. Lightw. Technol.* 34.20 (2016), pp. 4758–4764. ISSN: 0733-8724. DOI: 10.1109/JLT.2016.2551467.

[136] T. Hirasawa, K. Furuya, M. Oishi, S. Akiba, J. Hirokawa, and M. Ando. "Integrated photonic array-antennas in RoF system for MMW-RF antenna beam steering". In: *Proc. International Topical Meeting on Microwave Photonics*. Paphos, Cyprus: IEEE, 2015, TuP–14. ISBN: 978-1-4673-9368-3. DOI: 10.1109/MWP.2015.7356658.

[137] Z. Cao, Q. Wang, N. Tessema, X. Leijtens, F. Soares, and T. Koonen. "Beam steered millimeter-wave fiber-wireless system for 5G indoor coverage". In: *Proc. Optical Fiber Communication Conference*. Anaheim, CA, USA: OSA, 2016, TU2B.1. ISBN: 978-1-943580-07-1. DOI: 10.1364/OFC.2016.TU2B.1.

[138] J. Capmany and P. Munoz. "Integrated Microwave Photonics for Radio Access Networks". In: *J. Lightw. Technol.* 32.16 (2014), pp. 2849–2861. ISSN: 0733-8724. DOI: 10.1109/JLT.2014.2333369.

[139] S. Iezekiel, M. Burla, J. Klamkin, D. Marpaung, and J. Capmany. "RF Engineering Meets Optoelectronics: Progress in Integrated Microwave Photonics". In: *IEEE Microw. Mag.* 16.8 (2015), pp. 28–45. ISSN: 1527-3342. DOI: 10.1109/MMM.2015.2442932.

[140] P. T. Dat, A. Kanno, T. Umezawa, N. Yamamoto, and T. Kawanishi. "Millimeter- and terahertz-wave radio-over-fiber for 5G and beyond". In: *Proc. IEEE Photonics Society Summer Topical Meeting*. San Juan, Puerto Rico: IEEE, 2017, pp. 165–166. ISBN: 978-1-5090-6571-4. DOI: 10.1109/PHOSST.2017.8012702.

[141] H.-H. Cho, C.-F. Lai, T. K. Shih, and H.-C. Chao. "Integration of SDR and SDN for 5G". In: *IEEE Access* 2 (2014), pp. 1196–1204. ISSN: 2169-3536. DOI: 10.1109/ACCESS.2014.2357435.

[142] F. Z. Yousaf, M. Bredel, S. Schaller, and F. Schneider. "NFV and SDN - Key Technology Enablers for 5G Networks". In: *IEEE J. Sel. Areas Commun.* (2017). ISSN: 0733-8716. DOI: 10.1109/JSAC.2017.2760418. *(inpress)*.

[143] eCPRI Transport Network D0.1. *Common Public Radio Interface: Requirements for the eCPRI Transport Network*. Requirements Specification. 2017.

List of Acronyms

4G fourth generation (mobile network)

5G fifth generation (mobile network)

ADC analog to digital converter

BER bit error rate

BiF bend-insensitive fiber

BPSK binary phase shift keying

BW bandwidth

CAGR compound annual growth rate

CAP carrierless amplitude phase modulation

CO central office

C-RAN centralized radio access network

CU central unit (in a C-RAN)

CW continuous wave (i.e., a pure, un-modulated tone)

DMD differential modal group delay

DMUX de-multiplexer

DU distributed unit (in a C-RAN)

DUT device under test

DWDM dense wavelength division multiplexing

E/O electrical to optical conversion

ECL external cavity laser

ED envelope detector

FEC forward error correction

FFT fast Fourier transform

FMF few-mode fiber

FM-MCF few-mode multi-core fiber

FTTx fiber to the x

GEPL generic empirical path loss model

I in-phase signal component

IF intermediate frequency

IL insertion loss

IoT internet of things

ISI inter symbol interference

LD laser diode

LNA low noise amplifier

LO local oscillator

LOS line of sight

LPF low pass filter

LPWA low-power wide-area (connection)

M2M machine-to-machine (connection)

MCF multi-core fiber

MDL mode-dependent loss

MIMO multiple-input multiple-output

mmW millimeter wave (frequency range)

MOD modulator

MPA medium power amplifier

multiCAP multi-band carrierless amplitude phase modulation

MUX multiplexer

MWP microwave photonics

NFV network function virtualization

NG-PON next generation passive optical network

NOMA non-orthogonal multiple access

O/E optical to electrical conversion

OFDM orthogonal frequency division multiplexing

OOK on-off keying

OSC oscillator

OVNA optical vector network analyzer

PA power amplifier

PAM pulse amplitude modulation

PBC polarization beam combiner

PBS polarization beam splitter

PC polarization controller

PD photodiode

PON passive optical network

PSK phase shift keying

Q quadrature signal component

QAM quadrature amplitude modulation

QPSK quadrature phase shift keying (also: quaternary phase shift keying)

RAN radio access network

RAU radio access unit

RC raised cosine

RF radio frequency

RoF radio-over-fiber

RRC root raised cosine

RRH remote radio head

Rx receiver

SDM space division multiplexing

SDN software-defined networks

SDR software-defined radio

SE spectral efficiency (typically in [bit/s/Hz])

SFP+ enhanced small form-factor pluggable

SIC successive interference cancellation

SMF (standard) single mode fiber

SNR signal to noise ratio

STL swept tunable laser

SVD singular value decomposition

TS tone separation

Tx transmitter

UDWDM ultra dense wavelength division multiplexing

WCM wavelet coefficient matrix

WDM wavelength division multiplexing

Simon Rommel obtained his B.Sc. degree from the University of Stuttgart, Germany in 2011 and in 2014 obtained M.Sc. degrees in Photonic Networks Engineering from Aston University, Birmingham, UK and Scuola Superiore Sant'Anna, Pisa, Italy. His research interests include the fields of fiber-optic and wireless communications and the associated digital signal processing.
Dr. Rommel conducted his Ph.D. studies at the DTU Fotonik, Kgs. Lyngby, Denmark, combined with an additional research stay at the National Institute of Information and Communications Technology (NICT), Koganei, Tokyo, Japan.
This Ph.D. thesis was delivered in Ocotober 2017 and defended in November 2017 – the assessment committee consisted of Prof. Lars Dittmann, Prof.ir. A.M.J. (Ton) Koonen and Prof. Alwyn J. Seeds.

Simon Rommel
https://orcid.org/0000-0001-8279-8180

Department of Photonics Engineering
Ørsted Plads, Building 343
DK-2800 Kgs. Lyngby